The Proton Coulomb Form Factor from Polarized Inclusive $e-p$ Elastic Scattering at Q^2=0.5 (GeV/c)^2

Christopher Matthew Harris

Charlottesville, Virginia

B.S., University of Virginia, 1993

M.A., University of Virginia, 1998

A Dissertation Presented to the Graduate Faculty

of the University of Virginia in Candidacy for the degree of

Doctor of Philosophy

Department of Physics

University of Virginia

May, 2001

Acknowledgements

There are many people I would like to thank for supporting me and sticking with me through the long process of attaining my Ph.D. The list is far too long to name every name, and I hope those who remain unnamed will forgive me. Their support means just as much to me.

First and foremost, I would like to thank my friends and family. My parents, Joan and Jody Harris, and brothers, Jamey and Brian, have been a pillar of strength for me these past seven years. I owe them more than words can express. I also want to thank, in particular, my closest friends from my undergraduate days, my so-called "dunova" friends: Adam Cohen, Kevin England, James Freilich, Paul Glass, Mitch Harris, Matt Healy, Andy Poarch, Jack Sheppard, Mike Silberglitt, and all of their respective significant others, who have become like sisters to me. I want to thank them for their undying friendship and ability to fill my life with happiness. My girlfriend, Courtney Gaber, deserves much love and thanks for supporting me emotionally through these last painful months of graduate school.

I would like to thank all the staff at UVa for the many ways they make my life easier. I cannot name them all, but they are all very dear to me. I will especially miss hearing Bobby Floyd yell out: "Hey there, Chris!" every time I enter the stock room.

During my graduate school career, I was fortunate enough to spend some time running an experiment (E155) at the Stanford Linear Accelerator Center (SLAC). It was truly an honor to work with and learn from their top notch scientists and staff. I was also lucky to be able to spend a year in the San Francisco Bay area, one of the most beautiful this country has to offer. I will miss having lunch at SLAC cafeteria, surrounded by Nobel laureates, as much as I will miss the "theorists vs.

experimentalists" soccer match each year.

I cannot say many pleasant things about my experience at Jefferson Lab in 1998. My thesis experiment was a disaster, and Newport News is not of the same caliber as Palo Alto. However, many people worked hard to put my experiment on the floor of Hall C and run it. Most notably, I'd like to thank Earl of the RadCon group, and "them bone-heads" of the CEBAF Polarized Target group (they know who they are). Last, but not least, I'd like to thank Roger Carlini, then the Director of Hall C. For without his efforts, I could not have gotten such an early start on my analysis.

The people I'd most like to thank for my development as a physicist and a person, over the past several years, are my co-workers in the UVa Polarized Target group. I met Stephen Bueltmann in the Spring of 1996, and no one has had a bigger impact on my graduate school career. A brilliant scientist and a dear friend, I owe him much on a personal, as well as professional, level. Renee Fatemi, a.k.a. "Freak Girl", has kept me grounded and laughing for many years. I feel I can talk to her about anything and she will support me and be honest with me. She has really helped me keep things in perspective. I have never met a more dilligent worker than Paul McKee. He is hard-nosed, yet friendly, and is able to get more done per unit of time than I thought possible.

I would also like to thank the members of my defense committee: Oscar Rondon, Sergio Conetti, Larry Thomas, Don Crabb and Donal Day. Oscar was extremely helpful in teaching me the physics of my thesis experiment and always gave valuable comments in review of my thesis. Dr. Conetti served as my thesis review committee chairman and helped guide me through this whole process. I want to thank Dr. Thomas for remembering me from my undergraduate days and for reading my thesis on such short notice. Don Crabb has taught me everything I know about polarized targets, and for that I am grateful. And finally, I want to thank Donal for taking up the burden of being my advisor so late in the game.

So many more people deserve mention here, and I hope they understand how much they all meant to me. They have all made my graduate career memorable.

Abstract

The proton form factors provide information on fundamental properties of the proton and provide a test for models based on QCD. In 1998 at Jefferson Lab (JLAB) in Newport News, Va., experiment E93026 measured the inclusive e-p scattering cross section from a polarized ammonia ($^{15}NH_3$) target at a four momentum transfer squared of Q^2=0.5 (GeV/c)^2. Longitudinally polarized electrons were scattered from the polarized target and the scattered electron was detected. Data has been analyzed to obtain the asymmetry from elastically scattered electrons from hydrogen in $^{15}NH_3$. The asymmetry, A_p, has been used to determine the proton electric form factor, G_{Ep}. The result is consistent with the dipole model and data from previous experiments. However, due to the choice of kinematics, the uncertainty in the measurement is large.

Contents

List of Figures

List of Tables

Chapter 1 Introduction

1.1 Overview

In 1911, Rutherford's famous gold foil scattering experiment [1] showed that the positive charge in the gold atom was not evenly distributed but instead concentrated in a small region. This small region became known as the nucleus of the atom, and further experiments showed the nucleus to be made up of neutrons and protons. For over thirty years, neutrons, protons, and the electrons which surround the nucleus, were believed to be elementary point particles.

Rutherford scattering assumes scattering from a point-like charge, e, and mass m, with an infinitely heavy point charge, Ze [2]. In 1929, Mott [3] published a paper discussing the scattering of unpolarized fast electrons by atomic nuclei. In it, he derived a formula for such a cross section using Dirac electrons [4] (electrons whose definition include the notion of "spin"). This Mott cross section differed from the Rutherford equation by a factor of $\cos^2(\theta/2)$, where θ is the scattering angle.

In 1947, Rose [5] noticed that the finite size of the nucleus led to deviations from the Mott scattering equation when the electron wavelength was of the order of the size of the nucleus. He postulated that this could be exploited to provide a means for measuring the charge distribution of nuclei. Rosenbluth [6] took this a step further, incorporating the spin of the nucleon and showing that the internal structure of a nucleon could be parameterized by two form factors, F_1 and F_2, known as the Dirac and Pauli form factors respectively. Additional form factors, G_E and G_M, known as the Sachs form factors [7, 8], can be formed from linear combinations of F_1 and F_2 and represent the charge and magnetic moment distributions of the nucleon.

Since 1950, a large number of experiments have attempted to provide precise val-

ues of these form factors across a range of momentum transfer, using a variety of techniques. Until recently, the most common method used has been "Rosenbluth separation". In Rosenbluth separation, nucleon form factors are extracted from several measurements of the cross section at the same momentum transfer, Q^2, but at varying scattering angles, θ, and incident electron energies, E_0. Lately, new techniques which exploit the polarization of the electron and nucleon have also been used [9, 10].

Elastic electron scattering is the best way to determine the charge and magnetic moment distributions of nucleons. The electron is a good probe in elastic scattering as it interacts with the nucleon without disturbing the nucleon structure. To first order, the electron and proton interact by a single photon exchange. The electron-photon vertex is well understood from the theory of Quantum Electrodynamics (QED). Precise knowledge of this vertex allows for scrutiny of the $\gamma - N$ vertex, which is less well understood. The wavelength of the virtual photon is inversely proportional to Q^2. This property allows studies at different scales of the nucleon structure. At low Q^2, the virtual photon predominantly interacts with the nucleon by elastic collision. As $Q^2 \to 0$, the electron effectively interacts with a particle of point charge e and magnetic moment μ. At higher Q^2, the virtual photon interacts with individual quarks.

Nucleon form factors are fundamental quantities in physics. Measuring the charge and magnetic moment distributions of the nucleons provides information on the strong force that binds the quarks and gluons in the nucleons. Precise values of these form factors provide a test of any model based on Quantum Chromodynamics (QCD).

The primary objective of Jefferson Lab experiment E93026 was to use polarized electron-nucleon scattering to determine the Sachs Coulomb form factor of the neutron, G_{En} [11, 12]. A measurement of G_{Ep}, the proton charge form factor, was made in parallel. A precise measurement of the inclusive asymmetry for elastic $e - p$ scattering can be made using a target of polarized hydrogen nuclei in NH_3. No detection of the recoil nucleon is necessary, only the detection of elastically scattered electrons

from the longitudinally polarized beam incident on the polarized proton target is necessary. Alternating the helicity of the polarized electrons from positive to negative allows for the measurement of an asymmetry of the scattering rate. This asymmetry can be related to the form factors G_{Ep} and G_{M_p}. More importantly, choosing the polarization axes appropriately, the asymmetry can be related to the interference term of G_{Ep} and G_{Mp}. This allows for extraction of the electric form factor with less uncertainty than previous methods.

This experiment was run in Hall C at Jefferson Lab in the Fall of 1998. This thesis describes the experiment, E93026, the equipment associated with it, and the analysis performed in determining the proton charge form factor. In Chapter 2, the theoretical models will be laid out in some detail, and their predictions in our range of Q^2 will be presented. Chapter 3 will describe previous experimental data, including the different methods used to determine the form factors. Chapters 4 and 5 detail the equipment used during the experiment, including the polarized target (Chapter 5) and the steps taken to extract the nucleon target polarization. Chapter 6 outlines the process of event selection and details the cuts used on the data. Chapter 7 is devoted to the analysis of packing fraction and dilution factor for the experiment and will discuss the radiative corrections needed for this analysis. Chapter 8 outlines the method of data analysis and Chapters 9 and 10 present the results and conclusions.

Chapter 2 Theoretical Overview

2.1 Overview

In order to demonstrate the method used to determine the Sachs form factors in the experiment, a derivation of the elastic $e-p$ cross section and proton form factors is performed here. In addition, a variety of models, which attempt to describe the form factor dependence on kinematic variables, will be presented.

2.2 Elastic Scattering

In elastic electron-proton scattering the proton remains in its ground state, recoiling with momentum $\vec{q}$ and energy ω transferred in the scattering process. The virtual photon exchanged between the electron and proton probes the composition of the proton without modifying its initial state. The Feynman diagram shows this reaction (Figure 2.1). An electron with incident four momentum k and final four momentum k' scatters elastically from a proton initially at rest in the lab frame with four momentum p=M_N. The scattered proton four momentum is p'. The four momentum of the virtual photon, q, is the difference between the initial and final scattered electron four momenta, $k-k'$. The square of the four momentum transfer is a Lorentz invariant and, in the lab frame, can be described in terms of kinematic variables,

$$Q^2 \equiv -q^2 = 4EE' \sin^2(\frac{\theta}{2}) \ , \tag{2.1}$$

where E is the initial electron energy (beam energy), E' is the scattered electron energy, and θ is the scattering angle.

The differential cross section for this reaction can be written in terms of the

Lorentz invariant amplitude, M, which can be derived from the lepton and hadron currents for the reaction [13]. The basic expression for the cross section [14] is as follows:

$$d\sigma = \frac{|M|^2}{4[(k\cdot p)^2 - m_e^2 M_p^2]^{\frac{1}{2}}} \delta^{(4)}(k' + p' - k - p) \frac{d^3k'}{2E'} \frac{d^3p'}{2(M_p + \nu)} \ , \tag{2.2}$$

where

$$M = \frac{-e^2}{q^2}[j^\mu(k,k')] \cdot [J_\mu(p,p')] \tag{2.3}$$

and

$$|M|^2 = \frac{e^4}{q^4} L_e^{\mu\nu} W_{\mu\nu} \ . \tag{2.4}$$

$L_e^{\mu\nu}$ and $W_{\mu\nu}$ are the leptonic and hadronic tensors, respectively, composed of the the leptonic and hadronic currents, j^μ and J_μ. The electron current is defined by

$$j_\mu = \bar{u}(k')\gamma_\mu u(k) \ , \tag{2.5}$$

where $\bar{u}(k')$ and $u(k)$ are Dirac spinors and γ_μ are the Dirac gamma matrices. It can

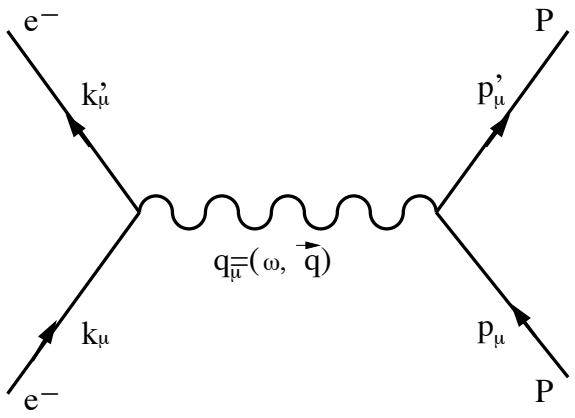

Figure 2.1: Feynman diagram of elastic electron-nucleon scattering.

then be shown [13] that the symmetric part of the lepton tensor is

$$L_e^{\mu\nu} = 2(k'^{\mu}k^{\nu} + k'^{\nu}k^{\mu} - (\vec{k}' \cdot \vec{k} - m^2)g^{\mu\nu}) \ . \tag{2.6}$$

The hadronic current, however, contains all the information about the hadronic initial state. Since the proton has internal structure, its coupling is more complex. The general form of the hadron current, after applying current and parity conservation, can be written in terms of Dirac and Pauli form factors,

$$J_{\mu} = \bar{u}(k') \left(F_1(Q^2)\gamma_{\mu} + \frac{i\kappa}{2M} F_2(Q^2)\sigma_{\mu\nu}q^{\nu} \right) u(k) \ . \tag{2.7}$$

where F_1 and F_2 are the Dirac and Pauli form factors, and κ is the anomalous magnetic moment. The symmetric part of the proton tensor is

$$W_{\mu\nu}^S = \frac{1}{2}\mathrm{Tr}(J_{\mu}J_{\nu}^{\dagger}) \ , \tag{2.8}$$

and can be fully evaluated [15] (See Appendix G for a full derivation of symmetric and antisymmetric terms). The differential cross section can be written in terms of these electron and proton tensors,

$$\frac{d\sigma}{d\Omega} = \frac{e^4}{64\pi^2 M_p^2 Q^4} \left(\frac{E'}{E} \right)^2 L_S^{\mu\nu} W_{\mu\nu}^S \ , \tag{2.9}$$

where $d\Omega$ is a solid angle of the scattered electron which is derived from the d^3k' term. Contracting the two tensors, the cross section becomes,

$$\frac{d\sigma}{d\Omega} = \sigma_{\mathrm{Mott}} \left[\left(F_1^2 + \frac{\kappa_p^2 Q^2}{4M_p^2} F_2^2 \right) + \frac{Q^2}{2M_p^2} (F_1 + \kappa_p F_2)^2 \tan^2(\theta/2) \right] \ , \tag{2.10}$$

where σ_{Mott} is the cross section for a structureless target. Written in terms of the

Sachs form factors, $G_{E_p}(Q^2)$ and $G_{M_p}(Q^2)$, where

$$G_{M_p}(Q^2) = F_1(Q^2) + \kappa_p F_2(Q^2) \qquad G_{Ep}(Q^2) = F_1(Q^2) - \kappa_p \tau F_2(Q^2) \ , \quad (2.11)$$

and writing the ratio of $Q^2/4M_p^2$ as τ, the cross section is

$$\frac{d\sigma}{d\Omega} = \sigma_{Mott} \left(\frac{G_{E_p}^2(Q^2) + \tau G_{M_p}^2(Q^2)}{1+\tau} + 2\tau G_{M_p}^2(Q^2) \tan^2(\theta/2) \right) \ . \quad (2.12)$$

This is the elastic unpolarized free $e-p$ cross section. Note that unlike Equation (2.10), Equation (2.12), which utilizes the Sachs form factors, has no interference term.

When scattering a polarized electron beam from a polarized target, the $e-p$ cross section can then be written as the sum of an unpolarized part, Σ, which is related to the elastic cross section $\frac{d\sigma}{d\Omega}$ and a polarized part, Δ, that is dependent upon the helicity, h, of the polarized electron,

$$\sigma^{\pm} = \Sigma + h\Delta \ ; \qquad h = \pm p_{beam} \ . \quad (2.13)$$

The polarized part of the cross section (Δ) comes from the antisymmetric parts of the lepton and hadron currents. Mixtures of symmetric and antisymmetric terms cancel so we are only left with the antisymmetric lepton tensor contracted with the antisymmetric hadron tensor. These antisymmetric tensors are written as follows:

$$L_A^{\mu\nu} = -2i\epsilon^{\mu\nu\rho\sigma} q_\rho s_\sigma \ , \quad (2.14)$$

$$W_{\mu\nu}^A = \frac{1}{2} \mathrm{Tr}[J_\mu (\vec{\sigma} \cdot \hat{n}) J_\nu^\dagger] \ , \quad (2.15)$$

where s_σ is the spin of the electron ($\pm$ 1/2), $\hat{n}$ is the direction of proton polarization and $\vec{\sigma}$ is the set of Pauli matrices. The contraction of these two antisymmetric tensors

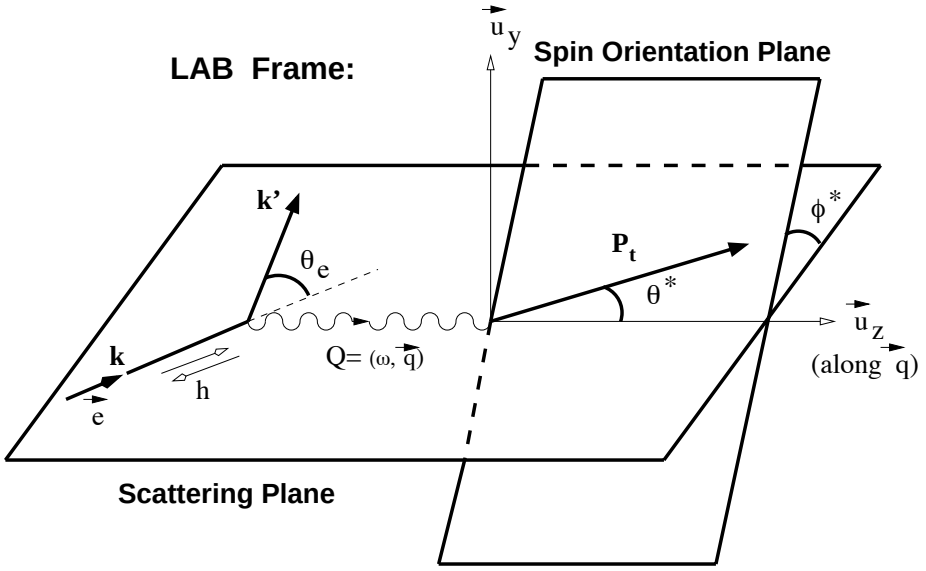

Figure 2.2: Polarized electron scattering from a polarized target.

can be taken in a similar fashion to the symmetric contraction, resulting in

$$L_A W^A = 2Q^2 \left[2MqG_E G_M \frac{\cot(\theta/2)}{\sqrt{1+\tau}} \sin\theta^* \cos\phi^* + Q^2 G_M^2 \sqrt{1 + \frac{\cot^2(\theta/2)}{1+\tau}} \cos\theta^* \right] . \tag{2.16}$$

Angles θ^* and ϕ^* describe the orientation of the nucleon polarization. Specifically, θ^* is the angle from the z-direction in the x-z plane (where the z-direction is the direction of $\vec{q}$) and ϕ^* is the angle from the x-direction in the x-y plane (see Figure 2.2).

If Equation (2.9) is rewritten, replacing the symmetric tensors with the antisymmetric contraction, we arrive at the cross section difference:

$$\Delta \equiv \frac{d\Delta\sigma}{d\Omega} = \frac{e^4}{64\pi^2 M_p^2 Q^4} \left(\frac{E'}{E} \right)^2 L_A^{\mu\nu} W_{\mu\nu}^A \ . \tag{2.17}$$

Using the results from Equation (2.16) for the antisymmetric terms, the cross section difference is written

$$\frac{d\Delta\sigma}{d\Omega} = 2\sigma_{Mott}\left(\frac{E'}{E}\right)\tan(\theta/2)\sqrt{\frac{\tau}{1+\tau}} \cdot \left[G_E G_M \sin\theta^* \cos\phi^* + G_M^2\sqrt{\tau(1+(1+\tau)\tan^2(\theta/2))}\cos\theta^*\right] \quad (2.18)$$

If the direction of polarization is chosen such that it is in the scattering plane ($\phi^* = 0$), and perpendicular to $\vec{q}$ ($\theta^* = \pi/2$), Δ is only dependent upon the interference term, $G_E G_M$ and kinematic variables.

This interference term can be isolated experimentally by measuring an asymmetry of the scattering of polarized electrons from polarized protons,

$$A_p = \frac{\sigma_+ - \sigma_-}{\sigma_+ + \sigma_-} = \frac{\Delta}{\Sigma} \ . \quad (2.19)$$

Keeping the same choice of polarization axes, the asymmetry reduces to

$$A_p = \frac{-2\sqrt{\tau(1+\tau)}\tan(\theta_e/2)G_{E_p}G_{M_p}}{G_{E_p}^2 + \tau(1+2(1+\tau)\tan^2(\theta_e/2))G_{M_p}^2} \ . \quad (2.20)$$

2.3 Theoretical Models

A variety of models have attempted to describe the Q^2 dependence of the Sachs nuclear form factors. Simple parameterizations, such as the dipole approximation, have shown good agreement with the data. At low Q^2, models typically describe the electron-nucleon interaction as being mediated by a vector meson. This description, however, breaks down at higher momentum transfer where perturbative QCD inspired models are more successful.

The quantity *isospin*, I, is used to describe the proton (p) and neutron (n) as different states of the same particle, the nucleon (N) [16]. Nucleons can then be described in Dirac notation using the magnitude (I) and third component (I_3) of the

isospin vector, $|I, I_3>$, where,

$$n = |1/2, -1/2> \quad \text{and} \quad p = |1/2, 1/2> \ . \tag{2.21}$$

In many models, Dirac and Pauli form factors are constructed as linear combinations of their isoscalar (IS), which have net isospin equal to zero, and isovector (IV) components, which have non-zero isospin,

$$F_1 = \frac{1}{2}(F_1^{IS} + F_1^{IV}) \qquad F_2 = \frac{1}{2}(F_2^{IS} + F_2^{IV}) \ . \tag{2.22}$$

Different authors have used a slightly different notation, but for the sake of consistency here, I uniformly report them in this stated notation.

2.3.1 Dipole Model

The dipole approximation is the simplest description of the Q^2 dependence of the nucleon form factors. This model is valid in the non-relativistic limit ($\omega \ll m_N$), where the approximation $Q^2 = q^2 - \omega^2 \approx q^2$. An exponential spatial distribution is assumed for both charge and magnetic moment. The charge density can be written in terms of the proton radius, r_0, and a normalization constant, ρ_0:

$$\rho(r) = \rho_0 e^{-r/r_0} \ . \tag{2.23}$$

The nucleon form factors are related to the Fourier transform of this charge (or magnetic moment) distribution. The dipole form factor can be written as

$$G_D(Q^2) = \int \rho(r) e^{-i\vec{q}\cdot\vec{r}} d^3\vec{r} = \frac{1}{(1 + Q^2 r_0^2)^2} \ . \tag{2.24}$$

The fit to previous data from unpolarized experiments [14] has determined r_0^2 to be $\frac{1}{0.71}$ GeV^{-2}. For $qr << 1$, the exponential can be expanded to become

$$G_D(Q^2) = 1 - \frac{1}{6}Q^2 < r_E^2 > + \frac{Q^4}{120} < r_E^4 > + \ldots \ , \tag{2.25}$$

where $< r_E^2 >$ is the mean square radius. As Q^2 approaches zero, the higher order terms can be ignored and the slope of $G_D(Q^2)$ can be related to the mean square radius:

$$\frac{dG_D}{dQ^2} = -\frac{1}{6} < r_E^2 > \ . \tag{2.26}$$

The item of interest is the root mean square (rms) radius,

$$\sqrt{< r_E^2 >} = \sqrt{-6 \left(\frac{dG_D(Q^2)}{dQ^2} \right)_{Q^2=0}} \ . \tag{2.27}$$

The mean square radius of the proton can be found from the slope of G_{Ep} near Q^2=0 (GeV/c)^2.

In terms of this dipole form factor, the charge and magnetic moment form factors for the proton can be written

$$G_{E_p} = G_D \qquad G_{M_p} = \mu_p G_D \ .$$

The dipole approximation has been shown to be an excellent parameterization of the electric and magnetic form factors at low Q^2, as can be seen in Figure 2.3 [23, 41, 36, 17, 43], where the ratio of the form factor to the dipole parameterization is given against the momentum transfer squared.

2.3.2 Vector Meson Dominance Models

Vector Meson Dominance (VMD) models describe the interaction between electrons and nucleons via a photon-vector meson interaction (see Figure 2.4), rather than a

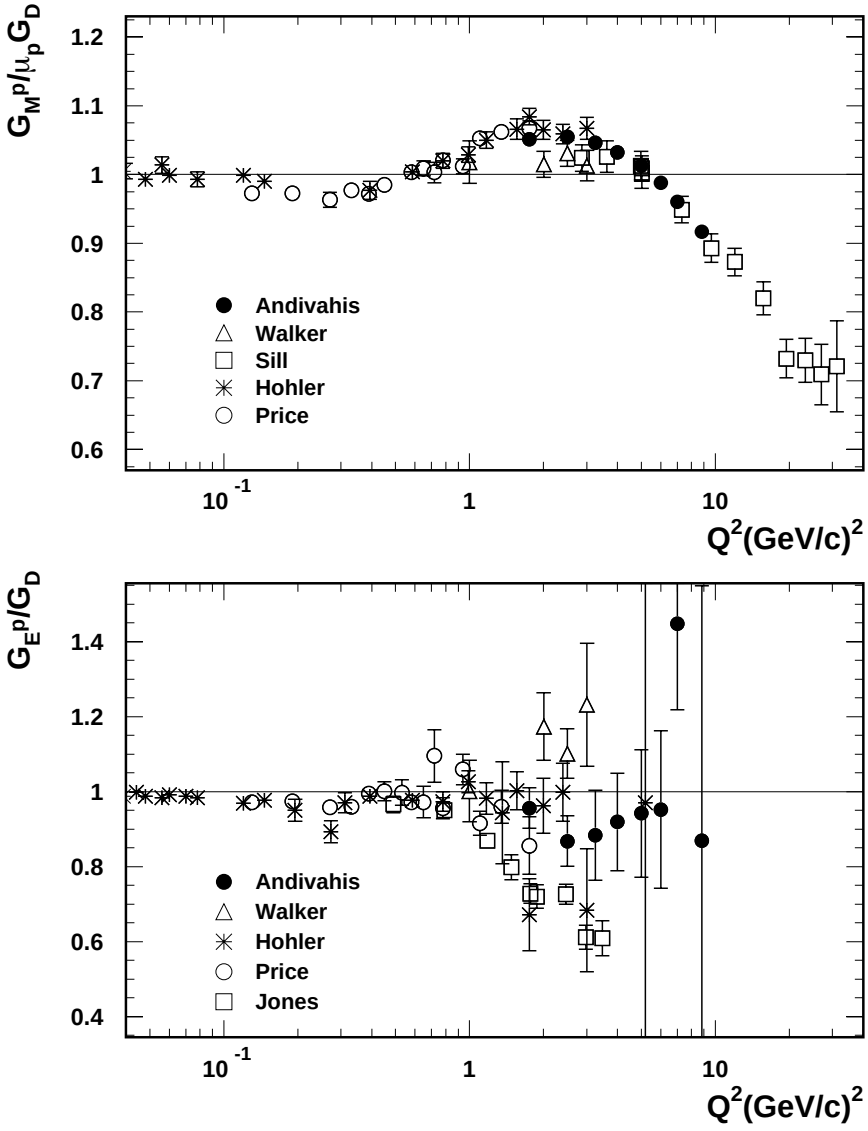

Figure 2.3: Ratio of $G_{Ep}/\mu_p G_D$ (top) and G_{Ep}/G_D (bottom) as a function of Q^2. Data from Andivahis [23], Walker [41], Sill [36], and Hohler [17] is from Rosenbluth separation. The data from Jones [43] utilizes recoil polarimetry.

simple virtual photon exchange [18, 19]. It assumes that the hadronic part of the vacuum polarization is made up of vector mesons [20]. VMD models have both isovector and isoscalar form factors which are composed of meson propagators times a meson-nucleon coupling term,

$$F \sim \frac{\alpha(Q^2)}{Q^2 + M_V^2} \ , \tag{2.28}$$

where $\alpha(Q^2)$ represents the coupling term, the meson propagator is of the form $1/Q^2$, and M_V is the mass of the vector meson.

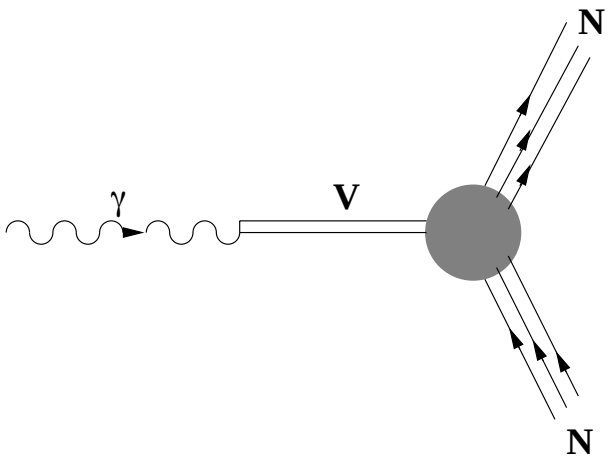

Figure 2.4: Photon-nucleon coupling in the vector meson dominance model.

Several such models exist, each including different vector mesons with different forms of coupling. Some include higher mass mesons and/or widths of mesons. Two such models will be outlined in this work.

Hohler Model

Hohler et al. [17] incorporate ρ and ω mesons as well as higher terms related to ϕ, ρ', and ω', but exclude the ρ'' contributions. Widths of all mesons are excluded in this model. The masses and coupling strengths of the higher mesons were left as free parameters in the fit to previous data. The isoscalar and isovector form factors are

written:

$$F_1^p(Q^2) = F_{1\rho}^p + \frac{a_1(\omega)}{M_\omega^2+Q^2}\sum_V \frac{a_1(V)}{M^2(V)+Q^2} \ , \tag{2.29}$$

$$\kappa_p F_2^p(Q^2) = F_{2\rho}^{IV}(Q^2) + \frac{a_2(\omega)}{M_\omega^2+Q^2}\sum \frac{a_2(V)}{M^2(V)+Q^2} \ , \tag{2.30}$$

$$2F_{1\rho}^{IV} = \frac{0.955+0.090(1+Q^2/0.355)^{-2}}{1+Q^2/0.536} \ , \tag{2.31}$$

$$2F_{2\rho}^{IV} = \frac{5.335+0.962(1+Q^2/0.268)^{-1}}{1+Q^2/0.603} \ . \tag{2.32}$$

Here V refers to the heavier meson states. Parameters from the best fit to proton data alone (fit 5.3) were as follows:

$$\begin{aligned} a_1(\omega) &= 0.67 & a_2(\omega) &= 0.04 \\ a_1(V_1) &= -0.39 & a_2(V_1) &= -1.88 \\ a_1(V_2) &= -0.54 & a_2(V_2) &= 0.24 \\ M_1(V_1) &= 0.96\,\mathrm{GeV} & M_2(V_1) &= 1.14\,\mathrm{GeV} \\ M_1(V_2) &= 1.66\,\mathrm{GeV} & M_2(V_2) &= 3.19\,\mathrm{GeV} \ . \end{aligned}$$

The mass of the ω meson was fixed at 0.7826 GeV.

Iachello, Jackson, and Lande (IJL) Model

Iachello, Jackson, Lande [21] use the ρ, ω, and ϕ mesons, and also include the width of the ρ, Γ_ρ. Widths of other mesons were not included. This model uses an intrinsic proton form factor, $g(Q^2)$, which has a dipole form, $1/(1+\gamma Q^2)^2$, where γ is a free parameter. Masses are fixed in this model, but the coupling strengths are left as free parameters to be fit to existing proton and neutron form factor data. In this model, the form factors are:

$$F_1^{IS} = g(Q^2)\left[(1-\beta_\omega-\beta_\phi)+\beta_\omega\frac{M_\omega^2}{M_\omega^2+Q^2}+\beta_\phi\frac{M_\phi^2}{M_\phi^2+Q^2}\right] \ , \tag{2.33}$$

$$F_1^{IV} = g(Q^2)\left[(1-\beta_\rho)+\beta_\rho\frac{M_\rho^2+8\Gamma_\rho M_\pi/\pi}{M_\rho^2+Q^2+(4M_\pi^2+Q^2)\Gamma_\rho\alpha(Q^2)/M_\pi}\right] , \quad (2.34)$$

$$\kappa_p F_2^{IS} = g(Q^2)\left[(-0.12-\alpha_\phi)\frac{M_\omega^2}{M_\omega^2+Q^2}+\alpha_\phi\frac{M_\phi^2}{M_\phi^2+Q^2}\right] , \quad (2.35)$$

$$\kappa_p F_2^{IV} = g(Q^2)\left[3.706\frac{M_\rho^2+8\Gamma_\rho M_\pi/\pi}{M_\rho^2+Q^2+(4M_\pi^2+Q^2)\Gamma_\rho\alpha(Q^2)/M_\pi}\right] . \quad (2.36)$$

The function $\alpha(Q^2)$ is defined as:

$$\alpha(Q^2) = \frac{2}{\pi}\left(\frac{Q^2+4M_\pi^2}{Q^2}\right)^2 \ln\left(\frac{(Q^2+4M_\pi^2)^{1/2}+(Q^2)^{1/2}}{2M_\pi}\right) . \quad (2.37)$$

The best fit parameters to existing proton and neutron form factor data are as follows:

$$\Gamma_\rho = 112\,\mathrm{MeV} \qquad \beta_\rho = 0.672$$
$$\gamma = 0.25\,(\mathrm{GeV}/c)^{-2} \qquad \beta_\omega = 1.102$$
$$\alpha_\phi = -0.052 \qquad \beta_\phi = 0.112 .$$

Masses of the mesons were fixed at M_ρ=0.765 GeV, M_ω=0.784 GeV, and M_ϕ=1.019 GeV.

2.3.3 Dimensional Scaling

Dimensional scaling [22] is a technique wherein the Q^2 dependence of a reaction can be determined by counting the number of interacting particles or fields that are present.

$$\frac{d\sigma}{dQ^2}(AB \to CD) \sim (Q^2)^{2-n} , \quad (2.38)$$

where n is the sum of particles in the interaction. For $e-p$ scattering, n=8 (three quarks and one electron in both the initial and final states). The cross section is

dominated by the F_1 term at high Q^2 and its change with Q^2 becomes

$$\frac{d\sigma}{dQ^2} = \frac{F_1^2(Q^2)}{Q^4} \ . \tag{2.39}$$

Equating Equation (2.38) for n=8, with Equation (2.39), we find that $F_1 \propto 1/Q^4$ in the limit of high Q^2. Likewise, due to an extra quark helicity flip in the helicity non-conserving part of the scattering amplitude, $F_2 \propto 1/Q^6$ [22]. Therefore the combination $Q^2(F_2^P/F_1^P)$ should approach a constant value, as evidence from SLAC experiment NE11 [23] would suggest (see Figure 2.5). Unfortunately, data taken during E93026 is not at a high enough momentum transfer to test this prediction as "high Q^2" is generally 4 (GeV/c)^2 or higher [22].

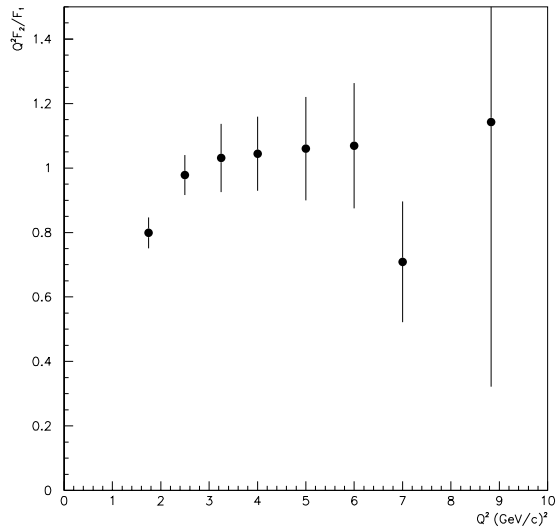

Figure 2.5: Asymptotic behavior of $Q^2F_2^p/F_1^p$ from NE11 [23]. Values approach a constant value of approximately 1.0 (GeV/c)^2.

2.3.4 QCD Sum Rules

At low Q^2, form factors can be determined from non-perturbative techniques. QCD sum rule techniques are based on quark-hadron duality, which states that the charac-

teristics of the hadron spectrum can be described in terms of either quark or hadron fields. In QCD, both hard scattering and soft wave function overlap contribute to the proton form factors. Hard scattering is mediated by exchange of virtual gluons. The argument is that higher order QCD terms are suppressed by a factor of $(\frac{\alpha_S}{\pi})$ for each gluon exchange in the limit of low Q^2 [24]. So in the low Q^2 regime, the proton form factors can be determined from the lowest order diagrams in QCD. QCD sum rules predict that the ratio of the form factors is proportional to $1/Q^2$,

$$\frac{F_2^P}{F_1^P} \sim \frac{\mu^2}{Q^2}, \tag{2.40}$$

where μ^2 is the value approached asymptotically with increasing Q^2 ($\mu^2 \sim 1$ GeV^2) [25].

2.3.5 Hybrid Models

Several models have been created to try to reconcile the low Q^2 behavior of the proton, which follows VMD models quite well, with the high Q^2 form predicted by pQCD. These models use scaling parameters from fits to previous data, and are therefore more of a parameterization than a true fundamental theory, but have in the past shown rather good agreement to the data in the interpolated region. The model proposed by Gari and Krümpelmann [26] tries to synthesize the meson dynamics at low Q^2 with pQCD at high Q^2. This model incorporates only the ρ and ω mesons. Heavier mesons are suppressed by their coupling constants. Form factors are similar to VMD models in that they are written in terms of pole terms times meson-nucleon form factors. These meson-nucleon form factors are assumed to be the same for all vector mesons (i.e. $F_1 = F_1^\rho = F_1^\omega = F_1^\gamma$, and $F_2 = F_2^\rho = F_2^\omega = F_2^\gamma$). The Dirac and Pauli form factors are combinations of the isoscalar and isovector form factors:

$$F_1^{IS}(Q^2) = \left[\frac{m_\omega^2}{m_\omega^2 + Q^2}\frac{g_\omega}{f_\omega} + \left(1 - \frac{g_\omega}{f_\omega}\right)\right] F_1(Q^2) \tag{2.41}$$

$$F_1^{IV}(Q^2) = \left[\frac{m_\rho^2}{m_\rho^2+Q^2}\frac{g_\rho}{f_\rho} + \left(1-\frac{g_\rho}{f_\rho}\right)\right] F_1(Q^2) \quad (2.42)$$

$$\kappa_S F_2^{IS}(Q^2) = \left[\frac{m_\omega^2}{m_\omega^2+Q^2}\frac{\kappa_\omega g_\omega}{f_\omega} + \left(\kappa_S-\frac{\kappa_\omega g_\omega}{f_\omega}\right)\right] F_2(Q^2) \quad (2.43)$$

$$\kappa_V F_2^{IV}(Q^2) = \left[\frac{m_\rho^2}{m_\rho^2+Q^2}\frac{\kappa_\rho g_\rho}{f_\rho} + \left(\kappa_V-\frac{\kappa_\rho g_\rho}{f_\rho}\right)\right] F_2(Q^2)\ . \quad (2.44)$$

Here $\kappa_V = \kappa_p - \kappa_n$ and $\kappa_S = \kappa_p + \kappa_n$ (where κ_p and κ_n are the proton and neutron anomalous magnetic moments). The factors $\frac{g_\alpha}{f_\alpha}$ and κ_α are free parameters. $\frac{g_\alpha}{f_\alpha}$ is a coupling factor between the vector meson and the nucleon, while κ_α is the ratio of tensor to vector coupling known from pion-nucleon scattering [27]. The functional form of F_1 and F_2, interpolated between low and high Q^2 regions, is:

$$F_1(Q^2) = \frac{\Lambda_1^2}{\Lambda_1^2+\hat{Q}^2}\frac{\Lambda_2^2}{\Lambda_2^2+\hat{Q}^2}\ , \quad (2.45)$$

$$F_2(Q^2) = \frac{\Lambda_1^2}{\Lambda_1^2+\hat{Q}^2}\left[\frac{\Lambda_2^2}{\Lambda_2^2+\hat{Q}^2}\right]^2\ , \quad (2.46)$$

where

$$\hat{Q}^2 = Q^2 \log\left(\frac{\Lambda_2^2+Q^2}{\Lambda_{QCD}^2}\right) \Big/ \log\left(\frac{\Lambda_2^2}{\Lambda_{QCD}^2}\right)\ . \quad (2.47)$$

The Λ terms are scale factors for the parameterization in the different regions encompassed by the model.

Using masses of $m_\rho = 0.776$ GeV and $m_\omega = 0.784$, $\kappa_p = 1.79$ and $\kappa_n = -1.91$, the best fit to data came from the following values for the free parameters:

$$\Lambda_1 = 0.795 \text{ GeV} \quad \Lambda_2 = 2.27 \text{ GeV} \quad \Lambda_{QCD} = 0.29 \text{ GeV}$$
$$\frac{g_\rho}{f_\rho} = 0.377 \qquad \frac{g_\omega}{f_\omega} = 0.411$$
$$\kappa_\rho = 6.62 \qquad \kappa_\omega = 0.163\ .$$

The GK parameterization has successfully described $Q^4 G_{M_p}$ as a function of Q^2

up to high Q^2 (20 (GeV/c)^2) from previous data [26]. It also predicts G_{E_p} quite well up to Q^2=1.5 (GeV/c)^2. This Q^2 limit comes from a lack of data to be fit at the time the Gari and Krümpelmann paper was written.

2.3.6 Lattice Calculation

The most modern technique for predicting the nucleon form factors is lattice calculations. In their paper, Dong et al. [28] perform lattice calculations of the strangeness contribution to the form factors. The strangeness content of the nucleon is of considerable interest since polarized deep inelastic scattering experiments found large, negative polarizations from the strange quark [29, 30, 31].

Dong et al. calculated s, u, and d quark contributions to the electric and magnetic form factors of the nucleon. They found that magnetic moment and electric form factors from the different quark flavors in the sea were sizeable. The net effect of the sea, however, was small as there were large cancellations among the quark flavors due to the difference in electric charges.

2.3.7 Model Comparison

Several of these models can be tested by our experiment, most notably the Dipole model, the Hohler model, the IJL model, the model by Gari and Krümpelmann, and the lattice calculation (LC) model. G_{Ep} or G_{Mp} could be extracted from the asymmetry and compared directly the those values predicted by these models. For G_{Ep} the Hohler, IJL, and GK models all predict a similar deviation from the dipole in the region of $Q^2 \leq 1.0$ (Figure 2.6), but the magnitude of the departure varies for each model. It is clear that the lattice calculation deviates from these models, having a value larger than the dipole for all values of $Q^2 \leq 1.0$ (GeV/c)^2. A plot of G_{Mp} divided by the dipole form factor and the proton magnetic moment (Figure 2.7) shows the Hohler, IJL, and GK models behaving in similar manners with all three models starting below the dipole value but crossing over the dipole towards higher Q^2.

However, the IJL model has its crossing at much higher Q^2 (~ 0.54 (GeV/c)^2) than either the Hohler model (~ 0.30) or the GK model (~ 0.35). The lattice calculation model deviates significantly lower with its lower proton magnetic moment.

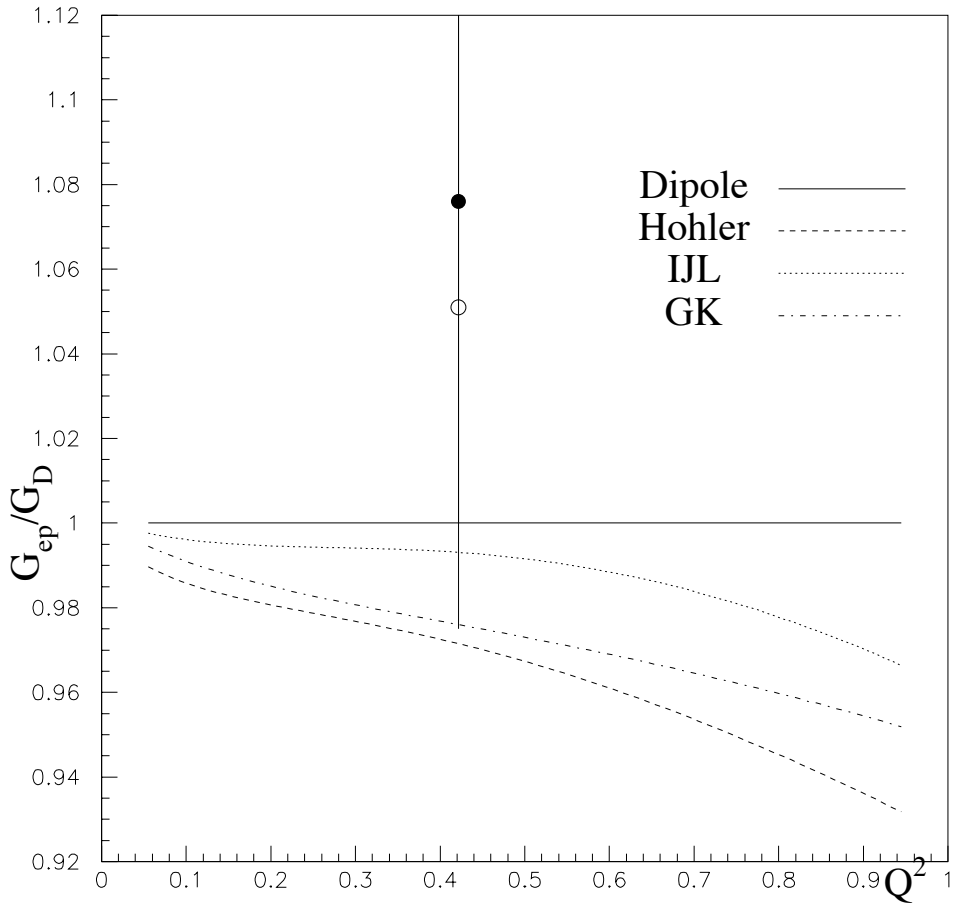

Figure 2.6: Theoretical models for the proton Coulomb form factor from Hohler [17], Iachello, Jackson and Lande [21], and Gari and Krümpelmann [26]. Values of G_{Ep} with (solid circle) and without (open circle) contributions from the sea are included from lattice calculations [28].

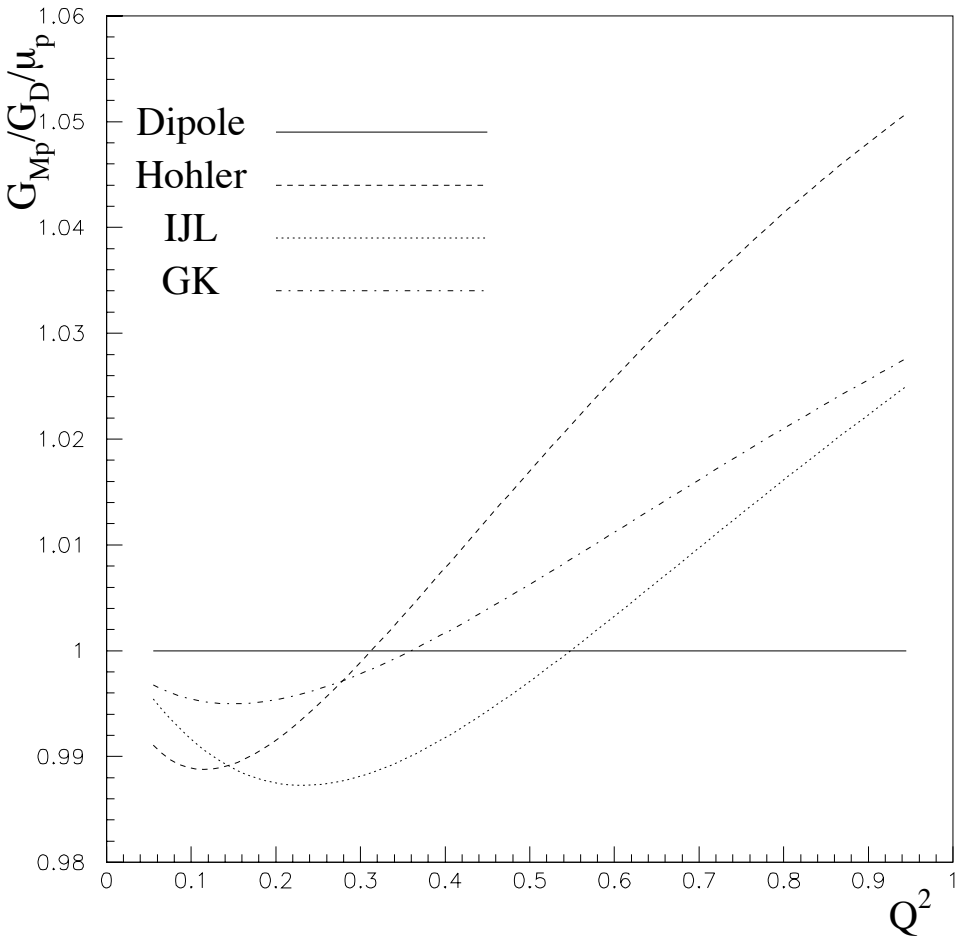

Figure 2.7: Theoretical models for the proton magnetic form factor from Hohler [17], Iachello, Jackson and Lande [21], and Gari and Krümpelmann [26].

Chapter 3 Previous Experimental Data

3.1 Overview

There are different methods available for determination of proton form factors from elastic electron scattering. Until recently, the most common method was Rosenbluth separation, which uses unpolarized cross sections at several angles (and corresponding incident energies) for a fixed Q^2. As shown in Chapter 2, it is also possible to extract the form factors using polarized scattering. The method of E93026 is to measure an asymmetry in polarized scattering related to the product of the form factors. Other experiments have determined the form factors through recoil polarimetry. Both of these polarized methods are seen as an improvement since they yield an interference term rather than sums of form factors squared, which is more difficult to decouple when one is small. An outline of several experiments which have used these methods follows. A brief description of each experiment and their kinematic ranges will be given and the data will be compared to theory.

3.2 Unpolarized Scattering

Important unpolarized experiments designed to determine proton form factors took place as early as the 1960's. These experiments typically used liquid hydrogen targets and generally used the method of Rosenbluth separation to determine values for the form factors. Recall Equation (2.11), called the Rosenbluth equation, the equation for the unpolarized cross section. With unpolarized scattering, this is the measured cross section from which the form factors are obtained. At fixed Q^2, this cross section

is essentially an equation of the form,

$$\frac{d\sigma}{d\Omega} = A(\tau,\theta)G_{Ep}^2 + \tau G_{Mp}^2 \ . \tag{3.1}$$

If at least two measurements are made of the cross section at the same Q^2 point, but with varying θ and E' values, the two unknowns, G_{Ep} and G_{Mp}, can be determined. This method is subject to large systematic errors mainly due to the necessity of measuring absolute cross sections, sometimes using different spectrometers at different angles. These uncertainties are large especially at high Q^2 where the magnetic form factor dominates, making extraction of G_{Ep} more difficult. As Q^2 (and thus τ) increases, $A(\tau,\theta)$ decreases, making the magnetic term far larger than the electric term. For example, at Q^2=3.0 (GeV/c)^2 and θ=15°, $A(\tau,\theta)G_{Ep}^2$=0.0010, whereas τG_{Mp}^2=0.0089.

Janssens (1966) [32]

Data for this experiment were taken at the Stanford Mark III accelerator, using a liquid hydrogen target. Data were taken for many Q^2 points ranging from 0.15 to 0.86 (GeV/c)^2. Three to five measurements per Q^2 were taken at angles between 45° and 145°, allowing for reasonable Rosenbluth separation. Uncertainties in the cross section were quoted at 5.0% with a normalization uncertainty of 1.6%.

Litt (1970) [33]

This experiment used the SLAC 8 GeV spectrometer, in End Station A (ESA) and also used a liquid hydrogen target. Incident electron energy, between 3 and 10 GeV, was higher than the Janssens experiment, as was the Q^2 range, from 1.00 to 3.75. Again, roughly 3-5 points per Q^2 were taken, each at different scattering angles, with a cross section uncertainty of 1.5-2.0% and a normalization uncertainty of 4.0%.

Berger (1971) [34]

At the Physikalisches Institut of the University of Bonn, elastic data were also taken using a liquid hydrogen target. As many as 14 points were taken at a single Q^2 across the broad range of scattering angles, $25^\circ \leq \theta \leq 111^\circ$. The Q^2 range falls across the ranges of Janssens and Litt, $0.1 \leq Q^2 \leq 1.95$ $(\mathrm{GeV}/c)^2$. Cross section uncertainties ranged from 2-6% with a normalization uncertainty of 4%.

Bartel (1973) [35]

At DESY, a slightly different experimental setup was used. Instead of a rotatable spectrometer, 3 different spectrometers were used at fixed angles to measure cross sections. Two of the spectrometers detected electrons, at 12° and 86°. The third spectrometer was set up to detect recoil nucleons corresponding to the 86° electrons. This experiment covered a range of $0.67 \leq Q^2 \leq 3.00$ $(\mathrm{Gev}/c)^2$. Uncertainties were 2-4% in the cross section and 2.1% in the normalization.

Sill (1986) [36, 37, 38]

A new series of SLAC ESA experiments began in 1986. The purpose of this experiment was to measure G_{Mp} at high Q^2. Beam energies ran from 5.5 GeV to 21 GeV while limiting the scattering angle to between 21° and 33°. Most of this data is above the range of our interest.

Katramatou (1987) [39, 40]

Another experiment at the SLAC ESA used two new spectrometers, a 180° back angle spectrometer and a 0° nucleon recoil spectrometer. At these kinematics, the magnetic form factor dominates the cross section to the extent that any contribution by G_{Ep} is negligible. Therefore, Rosenbluth separation was not necessary for this experiment, as the cross section was only a function of G_{Mp}. The Q^2 range for this experiment

was 0.5 to 1.8 $(\mathrm{GeV}/c)^2$. Uncertainties in the cross sections were in the 2-3% range, with a normalization uncertainty of 1.8%.

Walker (1989) [41, 42]

SLAC experiment E140 provided another measurement of G_{Ep} and G_{Mp} from elastic scattering. Several measurements of the form factors were made across a range of momentum transfer from 1.0 to 3.0 $(\mathrm{GeV}/c)^2$ using initial electron energies of 1.6 to 8.3 GeV and scattering angles from 11.7° to 46.6°. Data from E140 was compared to the previous data cited here, falling in line, generally, with Berger [34], Litt [33], and Katramatou [39], but deviating from Bartel [35]. In addition to the analysis of E140 data, Walker did a reanalysis of the previous data to generate a world fit to the entire set of data including E140. The resulting world fit to G_{Mp} was in line with the data prior to E140, but the fit to G_{Ep} was not. The plot of G_{Ep}/G_D for the world fit is consistent with the dipole parameterization or even slightly above the dipole. This is in contrast to the previous data which had indicated that G_{Ep}/G_D had a slight decrease with increasing Q^2 above Q^2=1.0 $(\mathrm{GeV}/c)^2$. Figure 3.1 shows the Walker reanalysis on the same axes as the previous data shown in Figure 2.3, so as to be easily compared and contrasted.

3.3 Polarized Scattering

Recently, polarized scattering experiments have been used to determine the proton form factors. In Hall A at Jefferson Lab, Jones et. al. [43] have used the method of recoil polarimetry in elastic $\vec{e}p \rightarrow e\vec{p}$ scattering. The ratio of the electric to magnetic form factor is obtained by measuring the transverse and longitudinal polarization of the scattered proton while detecting the scattered electron in coincidence. Neither the beam polarization nor the analyzing power of the polarimeter must be known. For one-photon exchange, the ratio of the form factors can be written in terms of the

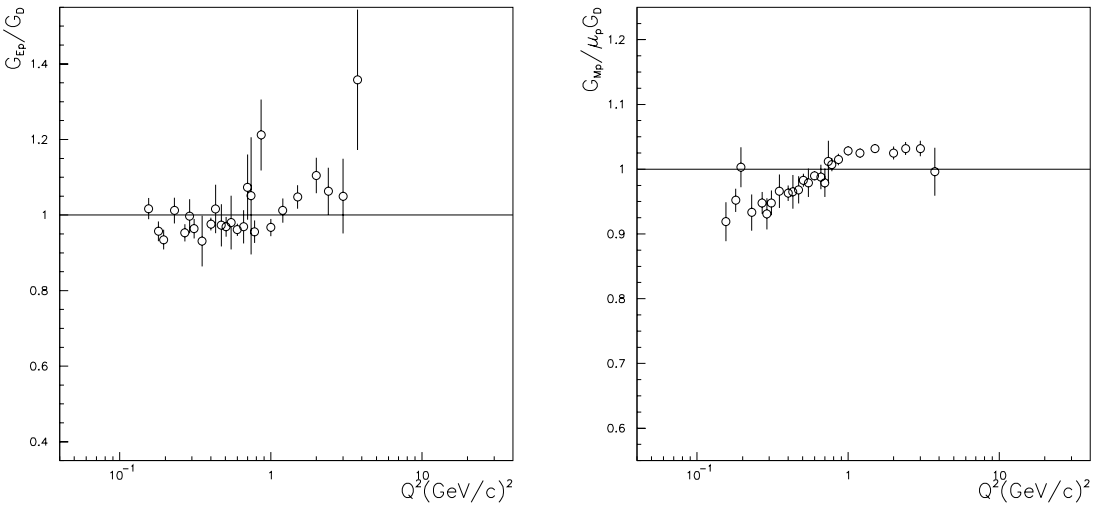

Figure 3.1: World fit from Walker's reanalysis. The left hand plot is of G_{Ep}/G_D vs. Q^2 from Walker's reanalysis [42]. The right hand plot is of $G_{Mp}/\mu_p/G_D$ vs. Q^2. The flat line in both plots at a ratio of 1.0 represents the dipole approximation. By comparing to Figure 2.3, it is clear that Walker's world fit is in line with previous data for the magnetic form factor, but in conflict with previous data for the charge form factor.

transverse (P_t) and longitudinal (P_l) recoil polarizations and kinematic factors:

$$\frac{G_{Ep}}{G_{Mp}} = \frac{-P_t}{P_l}\frac{E+E'}{2M}\tan\left(\frac{\theta_e}{2}\right) \quad . \tag{3.2}$$

The results of this experiment showed a sharp decline in the ratio of form factors with an increase in Q^2, which is a serious deviation from the dipole approximation. This indicates that G_{Ep} falls off faster with Q^2 than G_{Mp}. This is in direct conflict with Walker's world fit results. In addition, a plot of Q^2F_2/F_1 appears not to level off as expected from pQCD and earlier experiments.

3.4 Summary

In the last 30 years, elastic electron scattering has been utilized in a variety of ways to determine the form factors, G_{Ep} and G_{Mp}. Unpolarized scattering is relatively

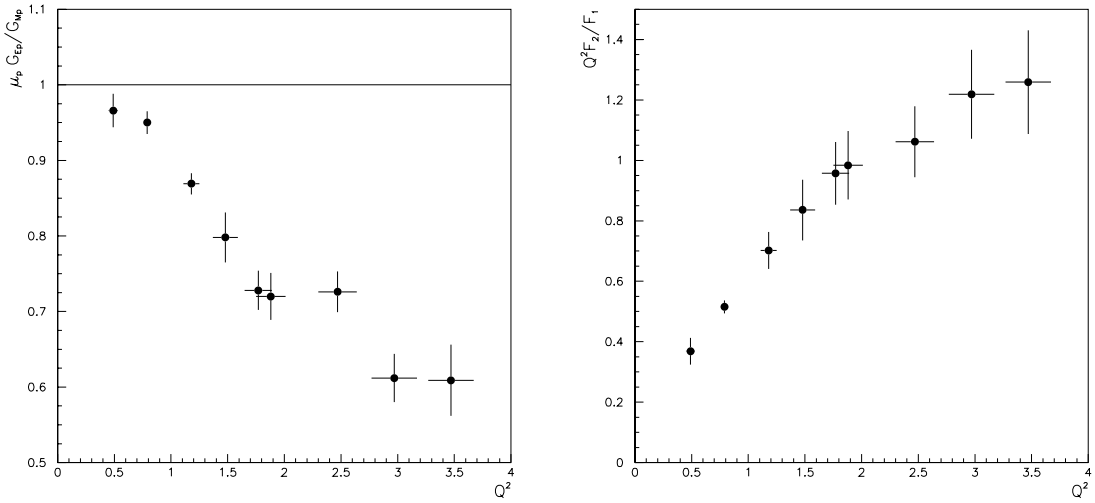

Figure 3.2: The left hand plot is of $\mu_p G_{Ep}/G_{Mp}$ vs. Q^2 from the Jones experiment [43] in Hall A at Jefferson Lab. The flat line at a ratio of 1.0 represents the dipole approximation. The right hand plot is of Q^2F_2/F_1 vs. Q^2.

easy to do since it does not require a polarized beam or target, but the method for extracting the form factors, by Rosenbluth separation, introduces large systematic uncertainties. Polarized scattering is an improved method and is starting to provide data that could shed new light on the behavior of the form factors across a broad range of Q^2.

Some of the above experiments had Q^2 ranges above our region of interest. However, the Janssens experiment, Berger experiment, and Bartel experiment all had data around the region of $Q^2 = 0.5$ (GeV/c)^2. The Jones experiment had one point at $Q^2 = 0.49$ (GeV/c)^2. Plots of G_{Ep}, G_{Mp}, G_{Ep}/G_D, and $\mu_p G_{Ep}/G_{Mp}$ can be found in Figures 3.3- 3.6, respectively. In all plots, the data from unpolarized scattering is represented by open circles, whereas the data from the Jones experiment is represented by an open square. One can see from Figure 3.6 that the ratio of the form factors is different for the polarized scattering than for the unpolarized scattering, but not outside the range of statistical agreement with the dipole model at this momentum transfer. The models shown in Figure 3.5 and Figure 3.6 show no clear trends in the

data. The data is scattered across all the models, giving no clear indication of favoring one model over the others with the current uncertainties in the measurements. Table 3.1 summarizes the kinematics for each experiment discussed in this chapter. Table 3.2 lists the values of G_{Ep} and G_{Mp}, with their associated uncertainty, for the data points shown in Figures 3.3-3.6.

Experiment	Q^2 Range $(\mathrm{GeV}/c)^2$	E_0 Range GeV	θ Range degrees
Janssens [32]	0.15-0.86	0.25-1.00	45-145
Litt [33]	1.00-3.75	3.0-10.0	12-42
Berger [34]	0.10-1.95	0.66-1.91	25-111
Bartel [35]	0.67-3.00	0.80-6.50	12,86
Sill [36]	2.80-31.3	5.5-21.0	21-33
Katramatou [39]	0.50-1.80	0.50-1.30	180
Walker [41]	1.00-3.00	1.60-8.25	11-46
Jones [43]	0.49-3.47	0.93-4.09	45

Table 3.1: Summary of previous experiments: Janssens [32], Litt [33], Berger [34], Bartel [35], Sill [36], Katramatou [39], Walker [41], and Jones [43].

Experiment	Q^2 $(\mathrm{GeV}/c)^2$	$G_{Ep} \pm \Delta G_{Ep}$	$G_{Mp} \pm \Delta G_{Mp}$
Janssens	0.3894	0.40755 ± 0.00714	1.12436 ± 0.02098
Janssens	0.4282	0.39812 ± 0.00991	1.05740 ± 0.02763
Janssens	0.4674	0.36293 ± 0.00722	0.99232 ± 0.02020
Janssens	0.5064	0.35067 ± 0.00958	0.91065 ± 0.02545
Janssens	0.5452	0.31586 ± 0.00700	0.88261 ± 0.01616
Janssens	0.5837	0.30739 ± 0.00960	0.82807 ± 0.02114
Janssens	0.6229	0.27137 ± 0.00655	0.78554 ± 0.01272
Berger	0.3894	0.39360 ± 0.00415	1.14871 ± 0.02500
Berger	0.5842	0.29367 ± 0.00172	0.82982 ± 0.00603
Bartel	0.6700	0.26915 ± 0.00351	0.71387 ± 0.01351
Jones	0.4900	0.33817 ± 0.00770	1.01107 ± 0.02303

Table 3.2: Summary of previous experimental data: Janssens [32], Berger [34], Bartel [35], and Jone [43]. Values of G_{Ep} and G_{Mp} for the Jones data were obtained from the ratio of $\mu_p G_{Ep}/G_{Mp}$, using the dipole value for one to determine the other. Errors listed are statistical only.

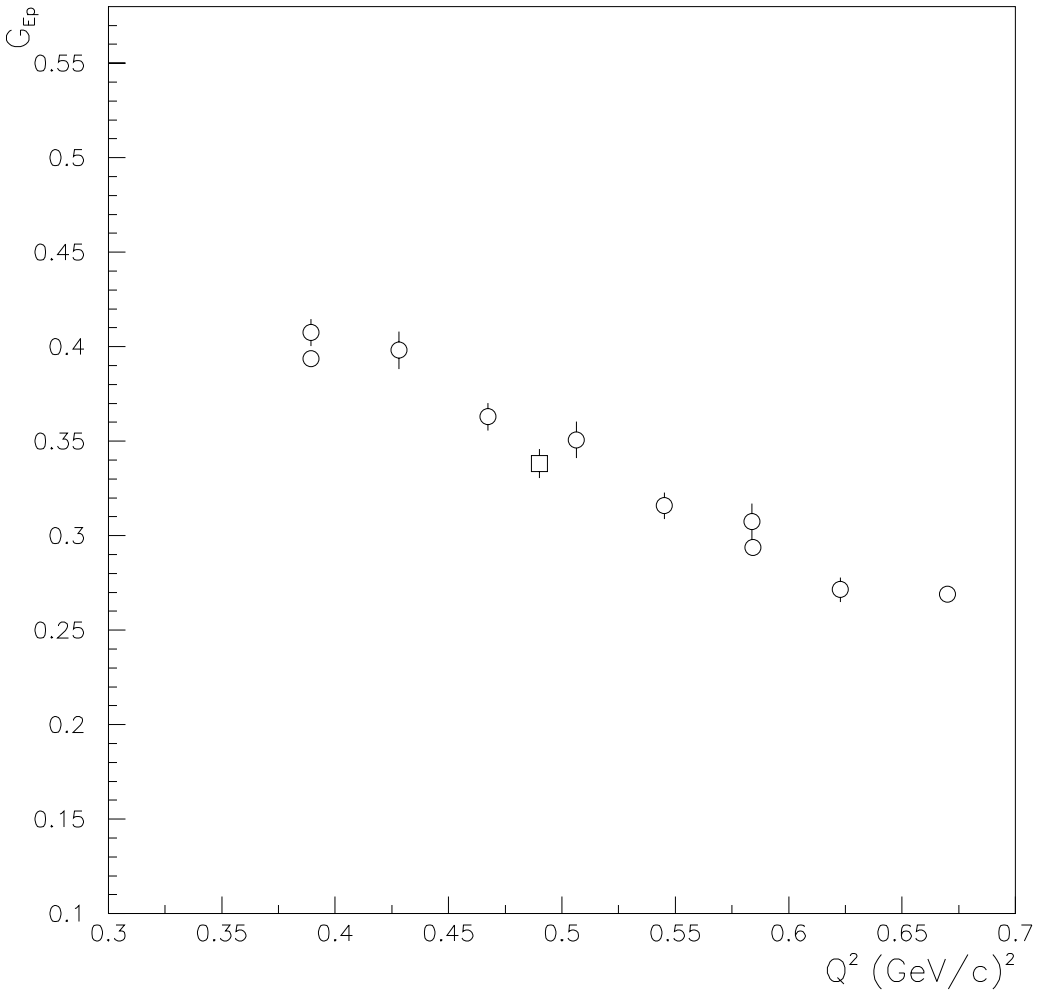

Figure 3.3: G_{Ep} from previous experiments. The open circles are from Rosenbluth separation (Janssens [32], Berger [34], and Bartel [35]) and the open square is from recoil polarimetry (Jones) [43].

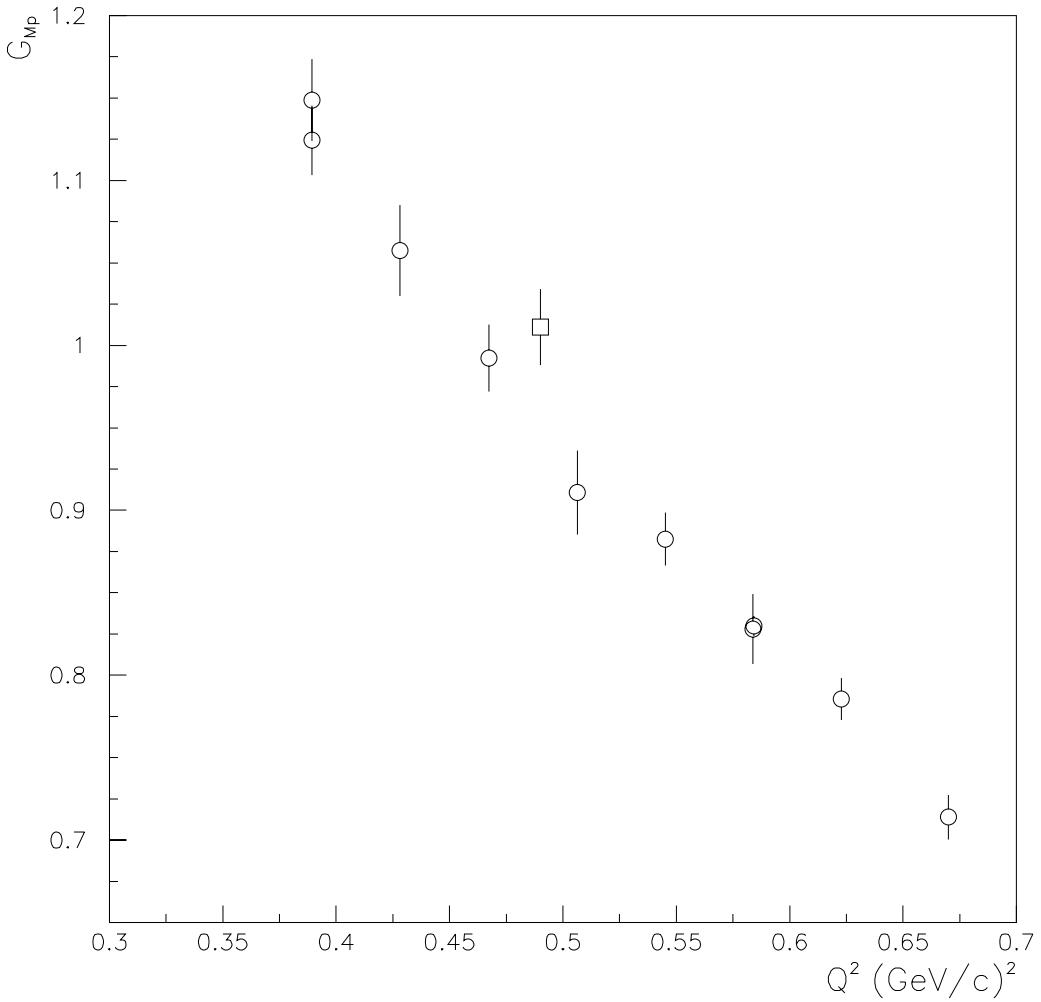

Figure 3.4: G_{Mp} from previous experiments. The open circles are from Rosenbluth separation (Janssens [32], Berger [34], and Bartel [35]) and the open square is from recoil polarimetry (Jones) [43].

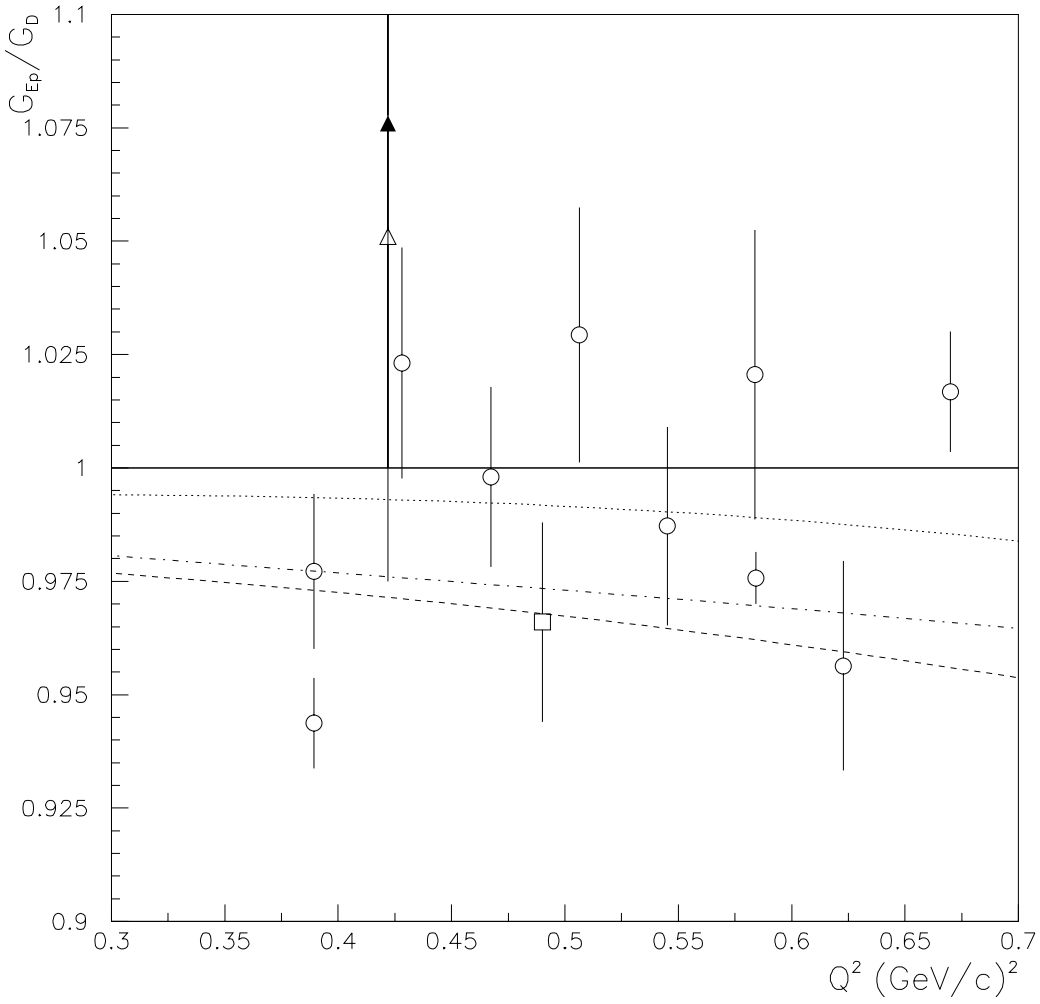

Figure 3.5: G_{Ep}/G_D from previous experiments [32, 34, 35, 43] with models. The solid line represents the dipole value. The IJL model [21] is represented by the dotted line, the dot-dash line is the GK model [26], the dashed line is from Hohler [17] and the open and solid triangles represent the LC model [28] with and without sea contributions, respectively. The open circles represent data from Rosenbluth separation (Janssens [32], Berger [34], and Bartel [35]), while the open square is data from polarized scattering [43].

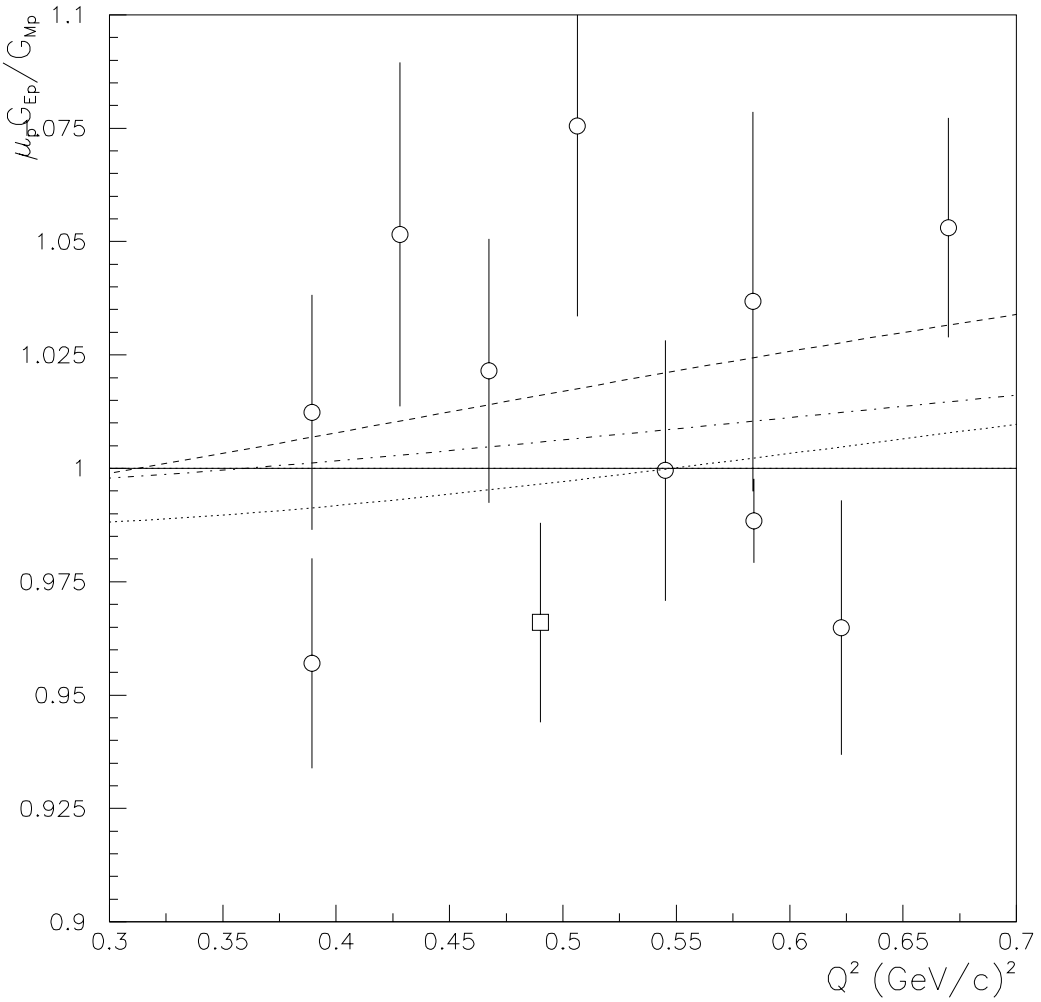

Figure 3.6: $\mu_p G_{Ep}/G_{Mp}$ from previous experiments [32, 34, 35] with models. The open circles are from Rosenbluth separation (Janssens [32], Berger [34], and Bartel [35]) and the open square is from recoil polarimetry [43]. The solid line represents the dipole value. The IJL model [21] is represented by the dotted line, the dot-dash line is the GK model [26], and the dashed line is from Hohler [17].

Chapter 4 Experimental Apparatus

4.1 Overview

Hall C at Jefferson Lab housed much of the necessary apparatus to perform experiment E93026 in the fall of 1998. Continuous wave (CW) longitudinally polarized beam was provided to the hall at our desired energies. A Møller polarimeter was used to determine the magnitude of the beam polarization. Instrumentation along the beamline in Hall C measured the beam current and position in the beampipe. A raster system spread the beam out over the face of our target, and a set of chicane magnets compensated for the downward bend of our target magnetic field. The polarized target provided nucleons polarized in the scattering plane. The Hall C High Momentum Spectrometer (HMS) was used to detect scattered electrons and a collaboration-built neutron detector captured the recoiling nucleon in coincidence. Electronics in the counting house created triggers for both the HMS and neutron detector, and a data acquisition system provided a graphical interface for the user and saved the data to disk. A schematic of the Hall C floor layout can be seen in Figure 4.1.

4.2 Choice of Kinematics

Measurements were taken at two different four momentum transfers of Q^2=0.5 $(\mathrm{GeV}/c)^2$ and 1.0 $(\mathrm{GeV}/c)^2$. As outlined in Chapter 2, the measurement of the asymmetry, which is related to the interference term, $G_E G_M$, depends on the orientation of the polarization axes. The contribution of the G_M^2 term is minimized by keeping the direction of nucleon polarization as close to perpendicular to the direction of $\vec{q}$ as possible.

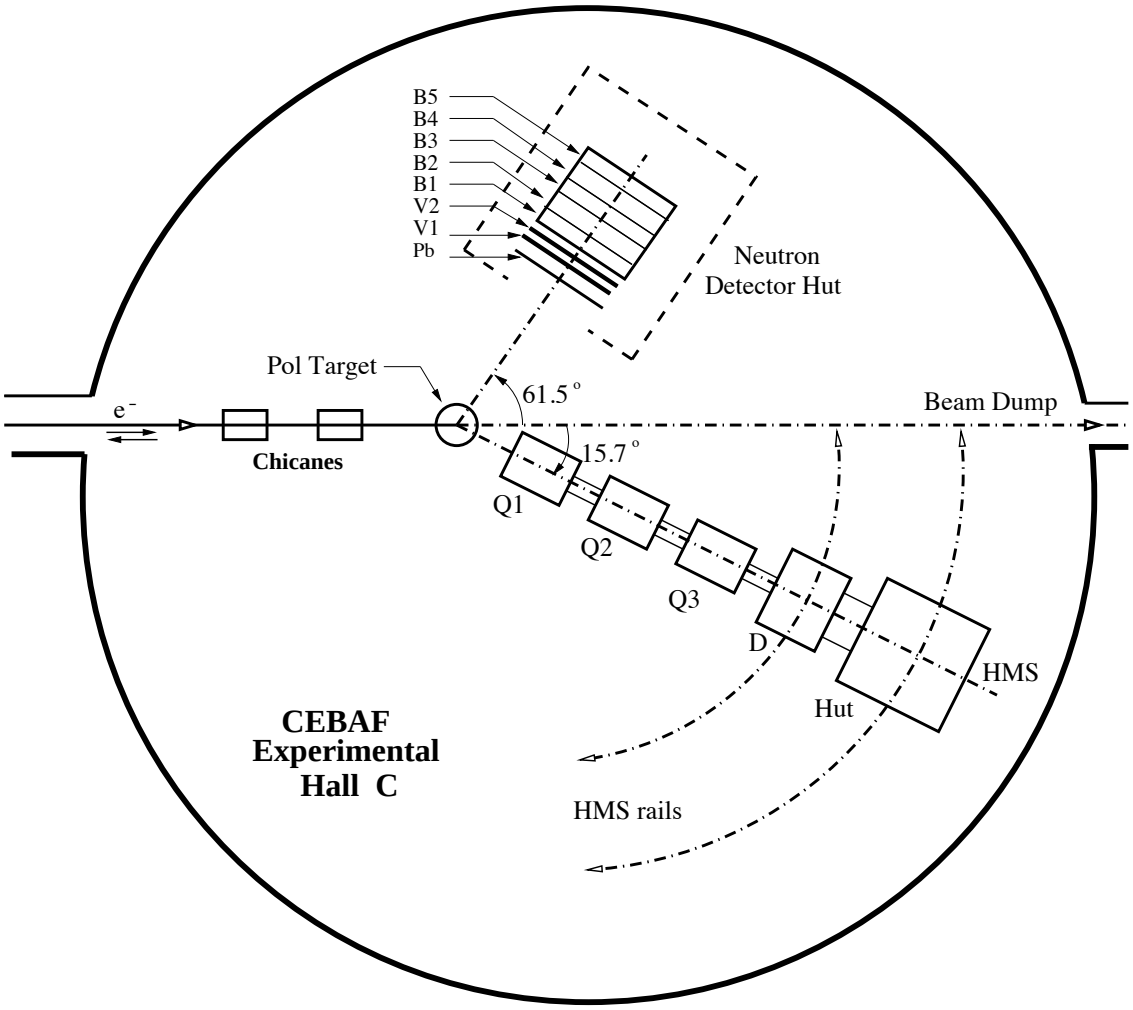

Figure 4.1: Layout of equipment on Hall C floor for experiment E93026.

The first step in choosing kinematics is to select the values of Q^2 where the form factors are to be measured. The choices of energy and scattering angle are then selected which provide the desired Q^2. For given values of initial electron energy and scattering angle, θ_e, the nucleon scattering angle, θ_q, can be determined by conservation of momentum perpendicular to the direction of the beam,

$$\sin\theta_q = \frac{E'}{p_n}\sin\theta_e \ , \tag{4.1}$$

where $p_n = |\vec{q}|$, and E' is determined from $Q^2 = 4E_\circ E'\sin^2(\frac{\theta_e}{2})$. To minimize the contribution of the G_M^2 term, the angle of the magnetic field axis is set perpendicular to θ_q, so that

$$\theta^* = \theta_B - \theta_q \sim \frac{\pi}{2} \ . \tag{4.2}$$

The choice of kinematics was further restricted by the dimensions of the magnet, which sets limits on the range of valid values of θ_B. In addition, the use of a rastered beam 2 cm in diameter required further clearance from the coil package. The following is a list of our kinematics and the corresponding scattering angles.

Table 4.1: G_{En} kinematics and scattering angles

Q^2 (GeV/c)^2	E_o (GeV)	E' (GeV)	θ_e (deg.)	θ_q (deg.)
0.5	2.724	2.456	15.7	61.6
1.0	4.238	3.694	14.5	54.5

Further constraints were imposed as well, such as available beam energies provided by the lab, and the physical limit of 13.6° for the minimum HMS angle achievable in the existing Hall C configuration.

4.3 Polarized Electron Beam

Experiment E93026 made use of the polarized, CW electron beam provided by the CEBAF machine at Jefferson Lab. In coordination with the other halls, beam energies

of 2.724 GeV and 4.238 GeV were provided over our four months of running at currents ranging from 80 nA to 150 nA. Higher beam currents were provided for Møller running.

4.3.1 Polarized Electron Source

Polarized electrons were produced by near bandgap photoemission from a strained gallium arsenide crystal using a circularly polarized laser. GaAs is an efficient photoemitter in the infrared range using the $P_{3/2}$ valence band to $S_{1/2}$ conduction band transition. Unstrained GaAs has a maximum achievable polarization of 50% due to the 4-fold degeneracy of the $P_{3/2}$ state and the 2-fold degeneracy of the $S_{1/2}$ state. The transition probabilities are determined from Clebsch-Gordon coefficients. Strained GaAs has an electric field in the material that breaks the degeneracy of the valence band. The electric field splits the degenerate levels in the $P_{3/2}$ state, allowing the selection of only one of the transitions. Switching the direction of the circularly polarized light switches the helicity of the emitted electrons. The pattern of electron helicity was determined by a pairwise randomized helicity scheme with a flip rate of 1 Hz.

4.3.2 Accelerator

The first phase of acceleration is the injector which supplies 45 MeV of energy to the emitted electrons. It is here that the initial polarization orientation is set. As an electron travels through magnets in the arcs and Hall C beamline, its spin precesses, resulting in a different polarization orientation at the experimental hall. By selecting the beam energy and injector angle appropriately, and by taking into account the magnets in the Hall C beamline, nearly longitudinally polarized electrons can be delivered to the target.

The precession angle into Hall C is determined from

$$\theta_C = \frac{E_l}{m_e}\frac{(g-2)}{2}[2n_C^2 - n_C(1-2\alpha+1/2.4) - \alpha(1+1/4.8)]\pi \ , \tag{4.3}$$

where E_l is the linac energy, n_C is the number of recirculation passes before entering Hall C, and α is the ratio of injector energy to linac energy. g is the gyromagnetic ratio of the electron which has a value of 2.00232. At the time of running, the value of α was 0.1125. The energy of the beam that enters the hall is the sum of all linacs plus the injector energy,

$$E_C = (2n_C + \alpha)E_l \ . \tag{4.4}$$

To maintain as much longitudinal polarization of the electrons as possible, it is desirable to have a total precession angle that is an integral number of π radians.

After the beam moved through the injector, it passed into the north linac section of the accelerator. Here the beam was accelerated by superconducting radio frequency cavities. At the end of the north linac, the beam was sent through the east arc.

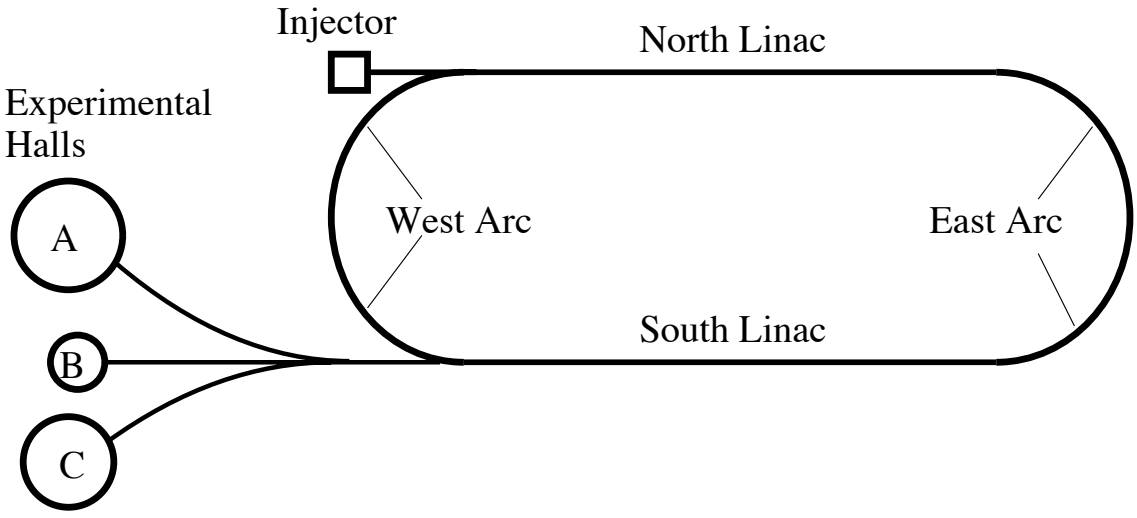

Figure 4.2: Overhead diagram of accelerator and experimental halls.

Beams at different energies follow separate paths since higher energies required higher magnetic fields to bend it around the turn. At the end of the arc, where it meets

the south linac, the beams were recombined and were accelerated further. The total energy gained in one complete pass around the accelerator was nominally 800 MeV (400 MeV per linac). At the end of the south linac the beam could be extracted into the beam switchyard, which then delivered the beam to the appropriate hall. All three halls could run simultaneously at three different energies if necessary. All halls had the capability to run with polarized beam, however the magnitude of the longitudinal component of the polarization differs between halls. In order to maintain longitudinal polarization for all halls, the difference between spin precession angles for each hall had to be an integral multiple of π. For most combinations of energy and injector angle, this was not possible and one or more halls received beam with only a fraction of the full longitudinal polarization. More than one hall could run with 5-pass beam, but no two halls could have the same less than 5-pass beam [44].

4.4 Hall C Beamline

After the electron beam was deflected into the Hall C beamline at the appropriate energy, it was transported into the hall by way of the Hall C arc and beamline. The arc contained bending magnets, steering magnets, quadrupoles, and hardware to monitor the position of the beam. The beamline within the hall was equipped with monitors of current and position, raster magnets, as well as a set of chicane magnets to compensate for the effect of the large target magnetic field. The layouts of both arc and beamline are shown in Figure 4.3 and Figure 4.4 respectively. BPM stands for beam position monitor. Likewise, beam current monitors are shown as BCMs. The BPMs, BCMs, superharps, Unser, and fast raster system will all be discussed in greater detail later in this chapter.

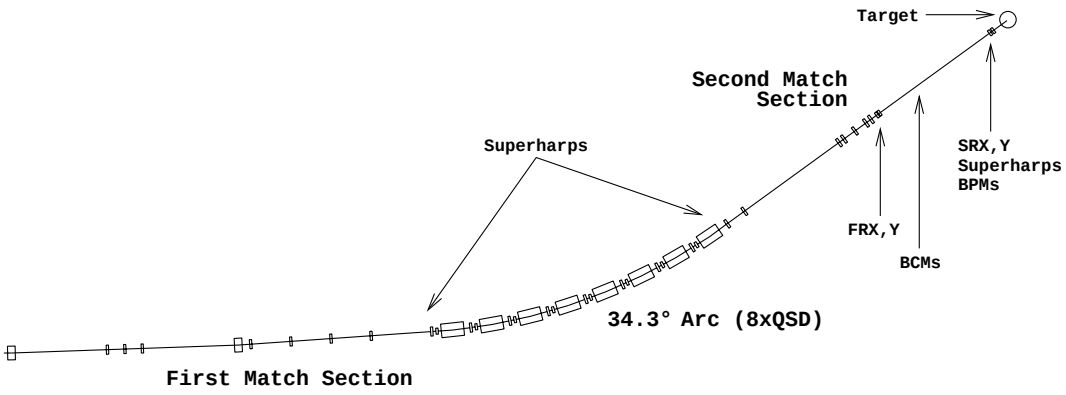

Figure 4.3: Diagram of Hall C arc.

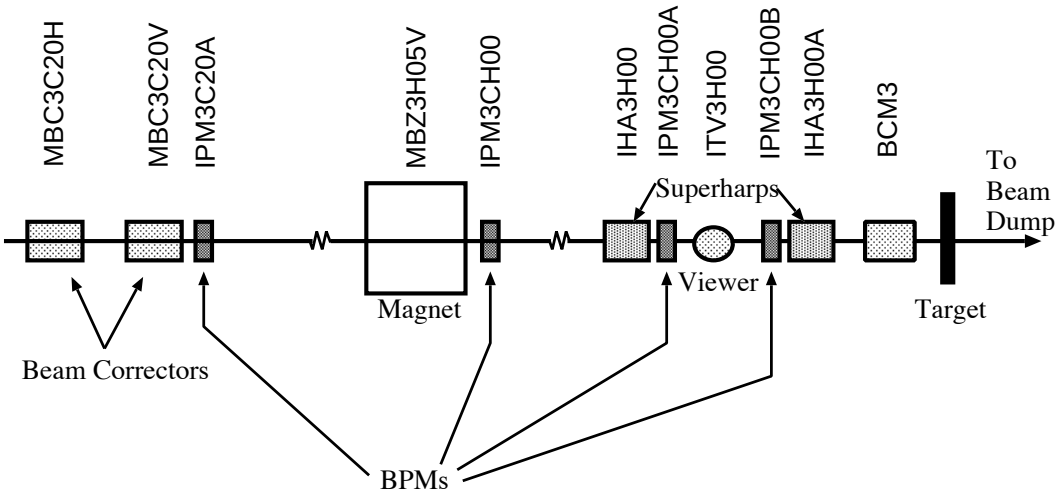

Figure 4.4: Diagram of Hall C beamline and components. For experiment E93026, the viewer was removed and BCM3 was replaced with the SEM (discussed later).

4.4.1 Møller Polarimeter

Møller polarimetry was used to measure the electron beam polarization [45]. The polarimeter consisted of a thin target foil of pure iron (4-10 μm thick) placed in a 4 Tesla superconducting solenoid[1]. Two quadrupoles, Q1 and Q2, were used to bend the scattered and recoil electrons away from the beamline and into the two coincidence detectors. Since the detectors were fixed in space, the quadrupoles were implemented for flexibility in kinematics, allowing coincidence measurements to be made at a wide range of beam energies. The detectors were total absorption counters made of SF2

[1]Typically the Møller magnet was only run at 3 Tesla.

lead glass. A 5" photo tube was connected to each block of lead glass. The incoming beam was focused on the thin target foil which was positioned perpendicular to the beam.

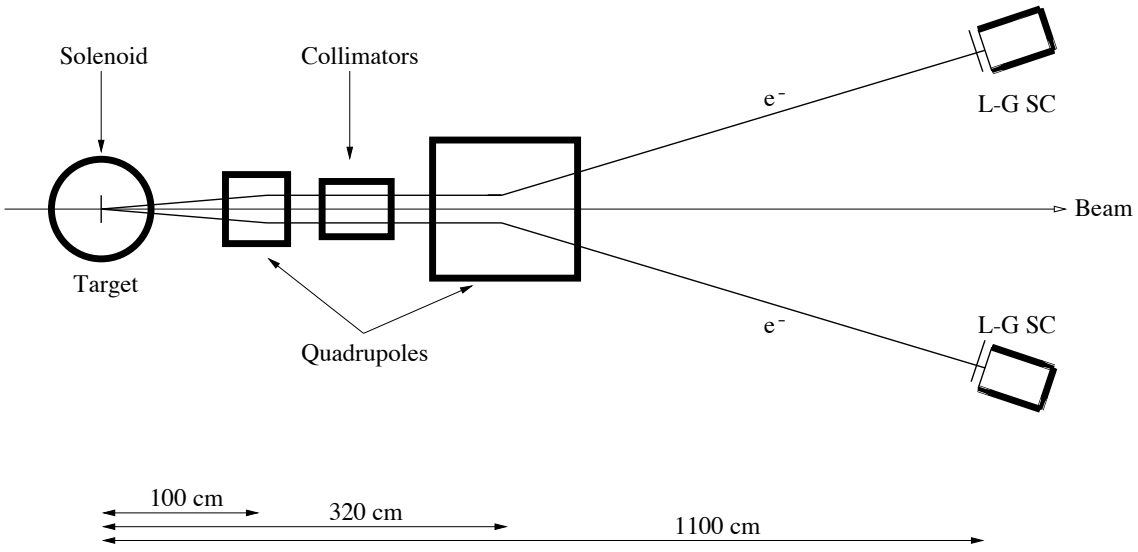

Figure 4.5: Layout of the Hall C Møller polarimeter.

Møller scattering is based on $\vec{e} + \vec{e} \rightarrow e + e$ scattering. Since this is a pure QED process, the cross section can be calculated to high precision. When the beam is longitudinally polarized and the helicity of the electron is reversed, the asymmetry of longitudinally polarized electrons scattered from longitudinally polarized target electrons is related to the analyzing power and the beam and target polarizations,

$$\epsilon = \frac{N_L - N_R}{N_L + N_R} = A_{zz}(\theta) P_z^B P_z^T \ , \tag{4.5}$$

where ϵ is the count rate asymmetry between positive (N_L) and negative (N_R) helicity electrons, $A_{zz}(\theta)$ is the analyzing power as a function of θ, P_z^B is the beam polarization in the z-direction, and P_z^T is the target polarization in the z-direction. The analyzing power is

$$A_{zz}(\theta) = -\sin^2\theta \frac{(8 - \sin^2\theta)}{(4 - \sin^2\theta)^2} \ . \tag{4.6}$$

A_{zz} is a maximum at $\theta = 90^\circ$ in the center of mass frame, and has a value of $A_{zz} =$

$-\frac{7}{9}$. The target foil polarization is determined from the number of unpaired valence electrons in the material. The pure iron target has 2 of its 26 valence electrons unpaired for an 8% polarization. The method of polarization was brute force, placing the iron foil in a high magnetic field to reach magnetic saturation. Under these conditions, electron polarization in pure iron is known to an uncertainty of 0.25% [45].

In the past, the smallest uncertainty for a Møller measurement [46] of beam polarization was 3% (dominated by the contribution from the target polarization). However, with the Hall C Møller polarimeter, much of this uncertainty can be reduced. Magnetic saturation of the target foil minimizes the uncertainty in the foil polarization. The coincidence detection helps to eliminate the Mott scattering background. Also, the large acceptance for detection of the scattered electrons allows for minimization of the effect of atomic motion of the electrons in the target material, known as the Levchuk effect [47]. For a nominal beam polarization of 70% and a beam current of 1 μA, it took only five minutes to obtain enough statistics for a 1% measurement [45]. During the experiment we typically used a lower beam current (500 nA) and took longer runs (40 minutes) for better statistics (.5%).

Demagnetization of the target from beam heating can be a problem in such a setup. However, tests were done at 1 μA using foils of different thicknesses to determine if this would impact our target polarization. Measurements of beam polarization were taken at several beam currents and using foils of different thicknesses to investigate any possible polarization dependence on beam current. The measured polarization was consistent up to currents of 1 μA (the upper limit of our current range for these tests and well above the 100 nA for data taking) [48].

Beam provided to Hall C ranged in polarization from 34.4% to 78.2%. The majority of data on $^{15}ND_3$ for our Q^2=0.5 (GeV/c)^2 point was taken with beam polarization $> 70\%$. However, due to beam polarization problems early in our running, the data taken on $^{15}NH_3$ at this momentum transfer was taken with an average beam polarization of only 40.4%. The typical total error on the measurement of beam polarization

was less than 2%.

4.4.2 Harps and Superharps

The beam profile was measured by a system of harps throughout the accelerator, and by superharps in Hall C. A harp is a device which consists of a movable frame and three sensor wires, two vertically aligned and one horizontally aligned. This frame was moved in and out of the beam by a stepper motor. An Analog-to-Digital Converter (ADC) recorded the signal on each wire. Using information from a position encoder attached to the stepper motor, and the ADC values, the beam position and profile was determined. Superharps in Hall C are the same as harps but have been fiducialized and surveyed into place with greater precision to allow accurate absolute position measurements. Superharps were positioned along the Hall C arc and in front of the polarized target (See Figures 4.3 and 4.4). Using position information from the superharps in the arc and field maps of the arc bend, beam energy was determined to an uncertainty of $\sim 10^{-3}$ [49]. In this experiment, the superharps in front of the target were not used due to the adverse effects of the target magnetic field. In addition, the dimensions of the superharp were not sufficient to accurately measure the beam profile with the use of the 2 cm rastered beam.

4.4.3 Chicanes

The Hall C chicane system was laid out as follows: a dipole, BE, bent the incoming beam down, into the primary chicane magnet, BZ1, which then bent the beam back up enough to compensate for the effective target field. A second chicane, BZ2, was placed after the target magnet to steer the outgoing beam into the beam dump. BE is located 18.71 m upstream, while BZ1 and BZ2 are 4.84 m upstream and downstream, respectively. A stylized diagram can be seen in Figure 4.6.

The chicane system was necessary to compensate for the target magnetic field which bent the beam electrons downward. The polarized target magnet had a central

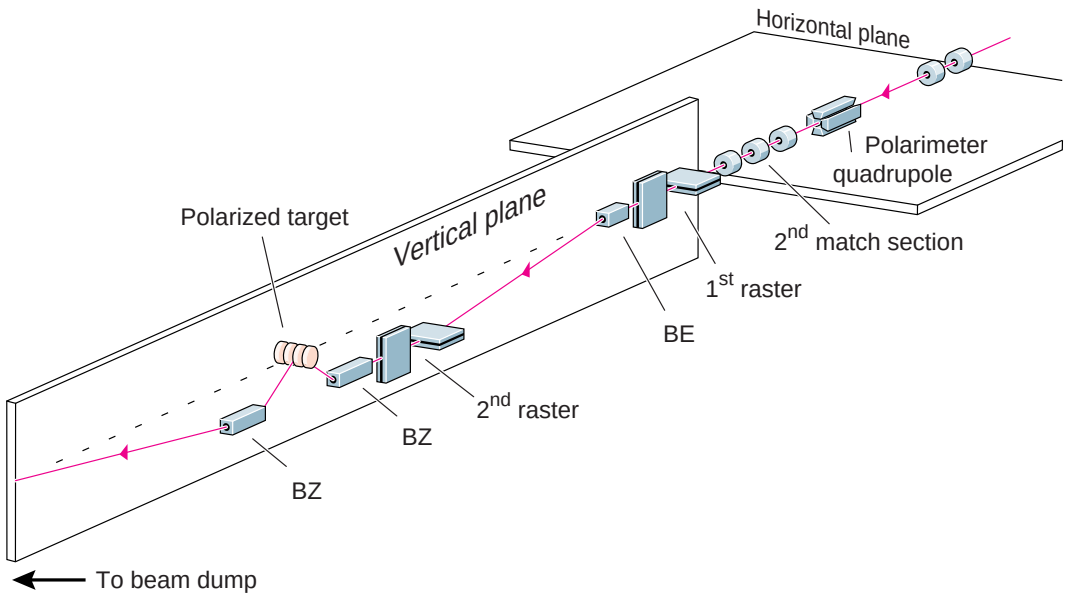

Figure 4.6: Hall C chicane layout.

field value of 5.1 Tesla, with significant stray field. To theoretically determine the amount of bend compensation needed by the chicanes, a sharp-cut-off model [50] was used for the radial and longitudinal B-field components taken from the standard G_{En} magnet field map. This method approximates the field strength as a function of distance as a cylinder of effective radius and effective length containing a uniform 5.1 Tesla within the cylinder. For B_0=5.1 Tesla, the field had an effective radius, R_0=15.92 cm and effective length, L_0=54.40 cm. Different Q^2 values required different target magnet orientations where θ_B, the angle between the direction of the coil's magnetic field and the direction of the beam in the lab frame, was non-zero. In these cases the solenoid field can be simplified as a uniform field perpendicular to the beam direction with a reduced effective B-field and a reduced effective radius by a factor of $\cos\theta_B$ [50].

The initial chicane settings, however, were determined from Runge-Kutta integra-

tion of the theoretical field map. The precise settings of the chicanes were fixed from studies early in the experiment. The chicane specifications, including effective length (L_{eff}), gap width (G), current (I), field strength (B), and bending angle (Φ), can be found in Table 4.2.

Magnet	L_{eff}	G(inch)	I(A)	B(kG)	Φ(deg)
BE	1.0	1.0	108.40	2.2006	1.3887
BZ1	2.0	1.7	216.20	4.2462	5.3552
BZ2	2.0	3.0	354.02	3.4765	4.3844

Table 4.2: Chicane magnet specifications for experiment E93026 at Q^2=0.5 (GeV/c)^2.

To allow a range of Q^2 values, BZ1 and BZ2 were mounted on movable pillars which could be raised or lowered to accomodate different amounts of magnetic deflection.

4.4.4 Beam Rastering

A beam rastering system was designed to distribute the beam uniformly across the face of the target cell [51]. The raster needs of the polarized target are two-fold. A focused beam spot on our frozen ammonia bead target would introduce too much heat to a localized point resulting in loss of polarization, incorrect NMR measurements, and possibly the destruction of target material. Also, due to the size of our target and the method for measuring the target polarization, it is necessary to spread the beam out evenly over the target. Since $^{15}NH_3$ and $^{15}ND_3$ have polarization characteristics that change with radiation dose, it was important to provide an even distribution of charge across the face of the target. For these reasons, two separate raster systems were used. A fast raster, which is standard Hall C equipment, spread the beam spot over a 1-2 mm diameter. A slow raster, specially designed for E93026, was used in addition to the fast raster to spread the beam over a 1 cm radius, evenly distributing charge throughout the cavity yet avoiding the edges of the target cup (See Figure 6.5 for a plot of the raster distribution).

Each raster system consisted of two raster magnets (one for the x direction and

one for the y direction), power resonance loops, and a pattern generator. The driving frequency of the fast raster was set to 24.2 kHz for both x and y directions, with the y raster phase-shifted by 90 degrees. Each raster magnet was amplitude modulated at a frequency of 47 Hz to produce a pseudo-spiral pattern. The slow raster was given a driving frequency of 100 Hz with a 90° phase shift in the y direction to produce a circular pattern with a constant linear velocity. ADC values of the raster magnet currents for each event were recorded and used to determine the position of the beam spot on the face of the target.

4.4.5 Beam Position Monitors

The Hall C beamline had several Beam Position Monitors (BPMs) placed to determine the relative position of the beam in the beampipe. Each BPM was a cavity with four antennae rotated 45 degrees from the horizontal and vertical axes. These antenna detect the resonant transverse electromagnetic (TEM) mode frequency. The intensity of the signal at each antennae determines the relative beam position at that BPM. Because the position is determined from relative signal strengths, the measurement is independent of the beam current. However, it is subject to small non-linearities in the electronics due to current shifts, yielding a position uncertainty of < 1.0 mm. The BPMs are only effective in measuring an average beam position, so for our rastered beam, the event-by-event beam position had to be determined by other means. Details of the operation of the BPMs can be found in Reference [52].

4.4.6 Secondary Electron Monitor

The Secondary Electron Monitor (SEM) was designed to determine the absolute electron beam position just in front of the target [53]. It measured the beam position for each trigger and helped determine the interaction point for each event. It is based on the principle of Secondary Electron Emission (SEE), where a low-energy electron is ejected from a solid surface as the result of energetic electron bombardment. The

solid surface used by the SEM was an array of 34 1 mm wide metal strips, 17 in the horizontal x-direction and 17 in the vertical y-direction (however, only 14 of each were read out). Each strip was made of stainless steel and had a thickness of 8 μm. Two anode foils were placed on the opposite ends of the planes of metal strips and were set at a positive voltage of typically 100 V. These anode foils collected the secondary electrons produced at the metal strips. These small secondary electron currents were integrated differentially for pairs of strips equally spaced from the center, over a set integration time of 40 μs. This differential integration helped to suppress noise. Integrated currents above threshold were added up over a position sensitive resistor ladder to determine location of charge differential in both x- and y-planes. The output for both planes was sent to an ADC in the counting house.

The SEM had a coverage range of $\pm$ 14 mm in both x- and y-directions, covering the entire target face (and more than covering the 10 mm raster radius). It was run at low beam currents with short integration times and with the fast raster on (smearing the beam out over a 1 mm radius). The fast raster caused the beam to be spread out over more than one foil, reducing the sensitivity. Since the fast raster had a diameter of 1-2 mm, this caused an uncertainty in the hit position. The measurement had difficulties when two foils equally spaced from the origin possessed equal amounts of charge. This often occurred near the origin (see Figure 4.7).

In order to obtain an absolute position measurement, the slow raster ADC values were calibrated to the SEM x and y hit positions. During the experiment the beam was aligned by observing a plot of the scattering rate as a function of the raster x and y positions, looking for where the edge of the target cup was hit. Thus, a relative target center was determined and the relative raster measurements could be used to steer the beam properly onto the face of the target, provided there were no changes made to the beamline or target configuration. However, the SEM could provide an absolute calibration as the center of the SEM was surveyed to be at the center of the beam pipe.

For calibration of the raster current to the SEM, a short replay was done where

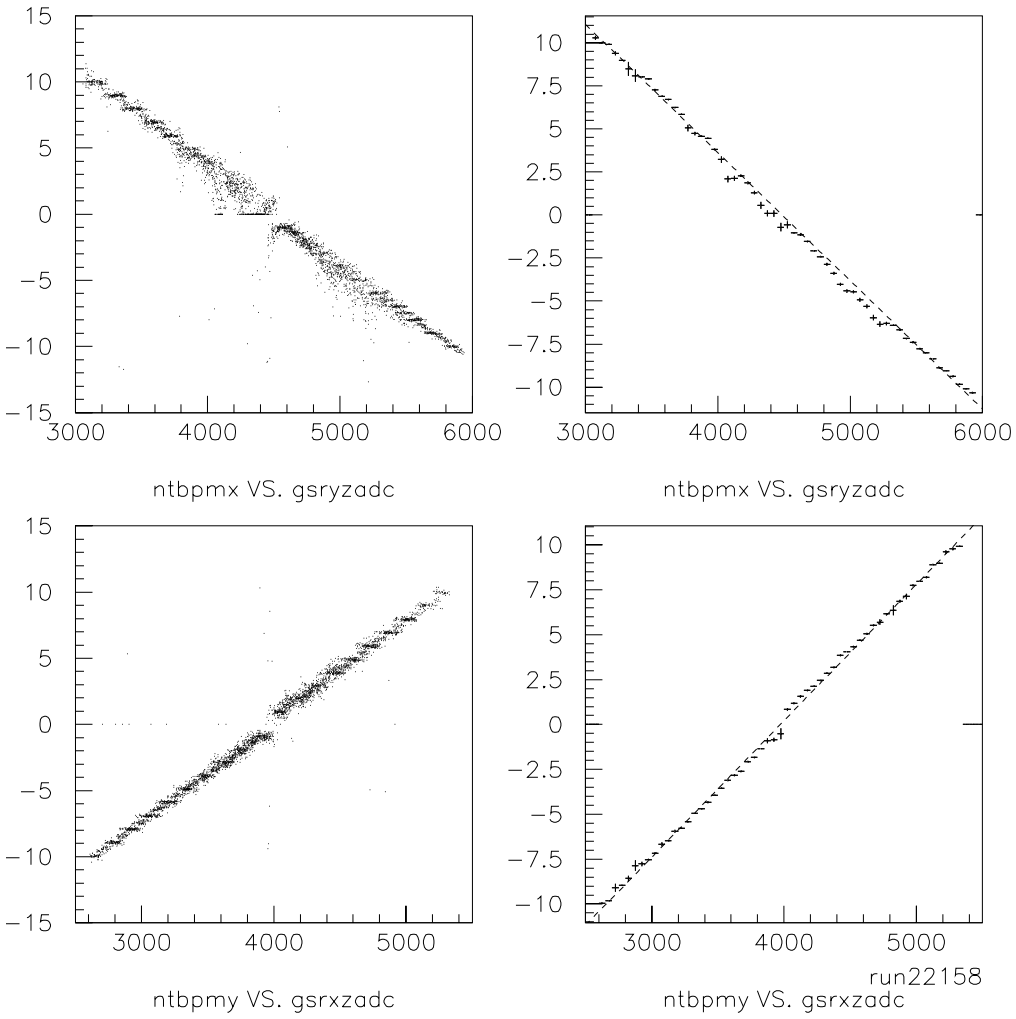

Figure 4.7: Slow raster calibration to the SEM with no cuts to eliminate noise. The scatter of points off the diagonal in the left hand plots reduced the accuracy of the fits (right hand plots) and thus introduced an error into the determination of the beam position. "ntbpmx" and "ntbpmy" are the SEM x and y coordinates. "gsrxzadc" and "gsryzadc" are the slow raster x and y ADC values.

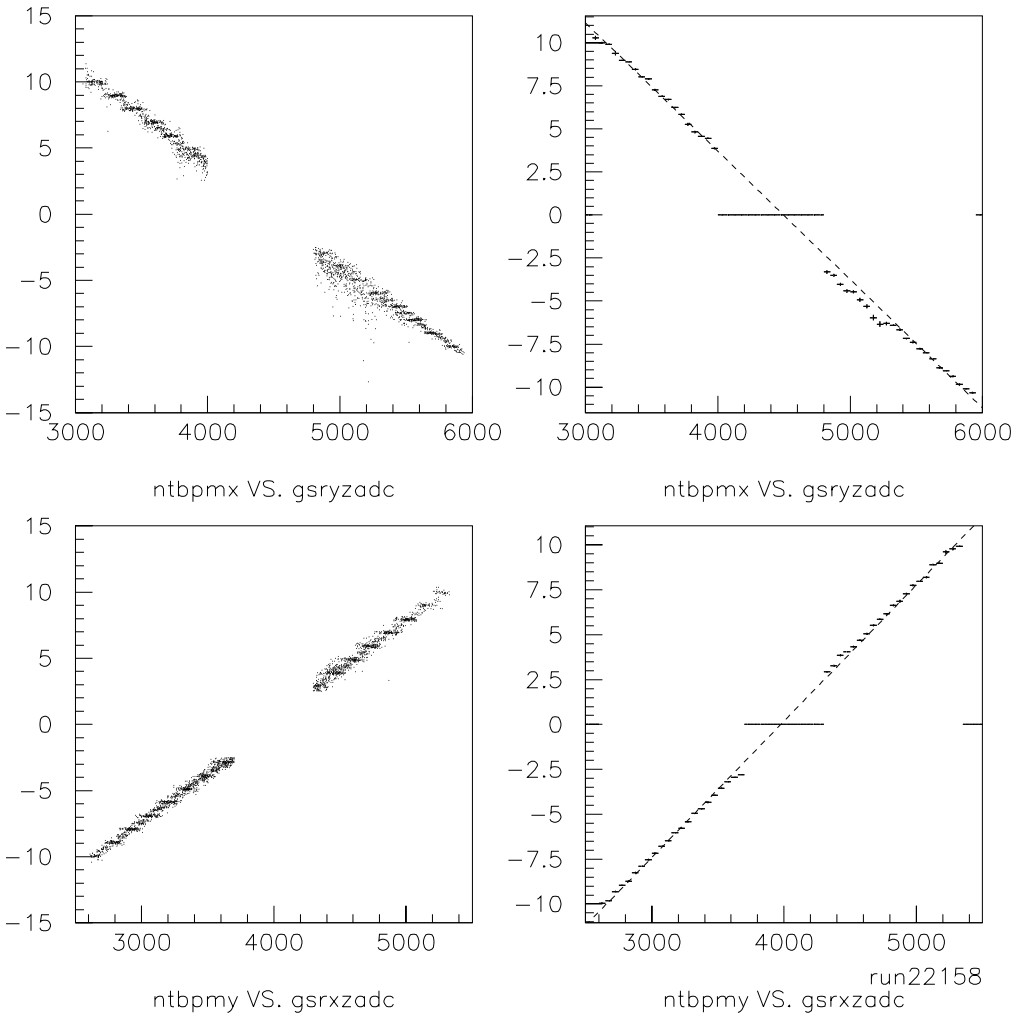

Figure 4.8: Slow raster calibration to the SEM with cuts to eliminate noise. The cuts, which eliminated data from within 2 mm of the center of the SEM, were implemented to reduce the noise, which improved the fit to the data. "ntbpmx" and "ntbpmy" are the SEM x and y coordinates. "gsrxzadc" and "gsryzadc" are the slow raster x and y ADC values.

20,000 events were analyzed for each run, which produced slow raster ADC values and the x and y coordinates of the SEM. The SEM and the slow raster had different coordinate systems, so the +X-axis for the SEM was plotted against the -Y-axis for the slow raster ADC. The +Y-axis of the SEM was plotted against the +X-axis of the slow raster ADC. Cuts were made to hits near the origin ($\pm$ 2 mm) of the SEM to eliminate noise (see Figure 4.8). After applying these cuts, both plots were fit with a straight line to determine a slope and intercept for each run. Elimination of noise resulted in a difference in calibrated beam position of up to 0.6 mm, or 6% of the raster radius. The slope and offset of these fits were written to file and used by the analyzer as calibration parameters in determining the center position of the slow raster on a run-by-run basis. Errors in these calibrations could result in significant errors in the measured scattered electron energy, since an offset in vertical direction is indistinguishable from an offset in momentum. For this reason, great care was taken in calculating the raster calibrations.

4.4.7 Beam Current Measurement

There are three current measuring devices that are used in conjunction to determine the beam current in Hall C. Located between BCM1 and BCM2 (see Figure 4.3), the Unser monitor [54, 55] measures the absolute value of the current to a high degree of precision (2 parts in 10^4), but suffers from sizeable drifts in the zero offset. This makes it less than optimum for regular beam current measurements. Therefore, it is used to calibrate the gain of the Beam Current Monitors BCM1 and BCM2.

Located upstream of the fast raster system in the Hall C arc, the BCMs are RF cavities which have stable gains and stable zero offsets. Calibration measurements, taken before and after the running of E93026, were made with the Unser monitor within a small span of time and at varying currents to obtain a cross calibration between the Unser and the BCMs. The BCMs could then be used during data taking and be counted on to provide accurate current measurements to within 10% [56]. The

value of the current from BCM2 during the experiment compares very well with the value of the current from BCM1 using the post-experiment calibration [56]. The beam current measured by BCM1, with the calibration completed after the experiment, was used for the data analysis.

BCM1 with the post-experiment calibration was the standard BCM used for the data analysis of this experiment.

4.5 Target

The polarized target used in E93026 was the first of its kind to be used at Jefferson Lab. It was by far the most complex target used in Hall C, consisting of a 5 Tesla superconducting magnet cooled by liquid helium, a high frequency microwave system, a ^{4}He evaporation refrigerator to cool the target material, and a Nuclear Magnetic Resonance (NMR) system for detection of the target polarization [57]. The target insert was designed to provide a $^{15}NH_3$ target, a $^{15}ND_3$ target, a large diameter solid carbon target, a small diameter solid carbon target, and a hole for "no target" running. The details of construction, operation, and analysis of the target can be found in Chapter 5.

4.6 High Momentum Spectrometer

The High Momentum Spectrometer (HMS) is a magnetic spectrometer with large solid angle and momentum acceptance. Three quadrupole magnets and one dipole comprise the magnet package, mounted on a common carriage which is rotatable about a central pivot. All magnets and detector packages are mounted directly on this carriage so that distances between elements remained fixed. In front of the first quadrupole (Q1) a slit system is installed. Different slits could be inserted or removed to carry out different tasks. The HMS sieve slit (see Figure 4.6) has an array of uniform and regularly spaced holes and was used for optics studies. The center

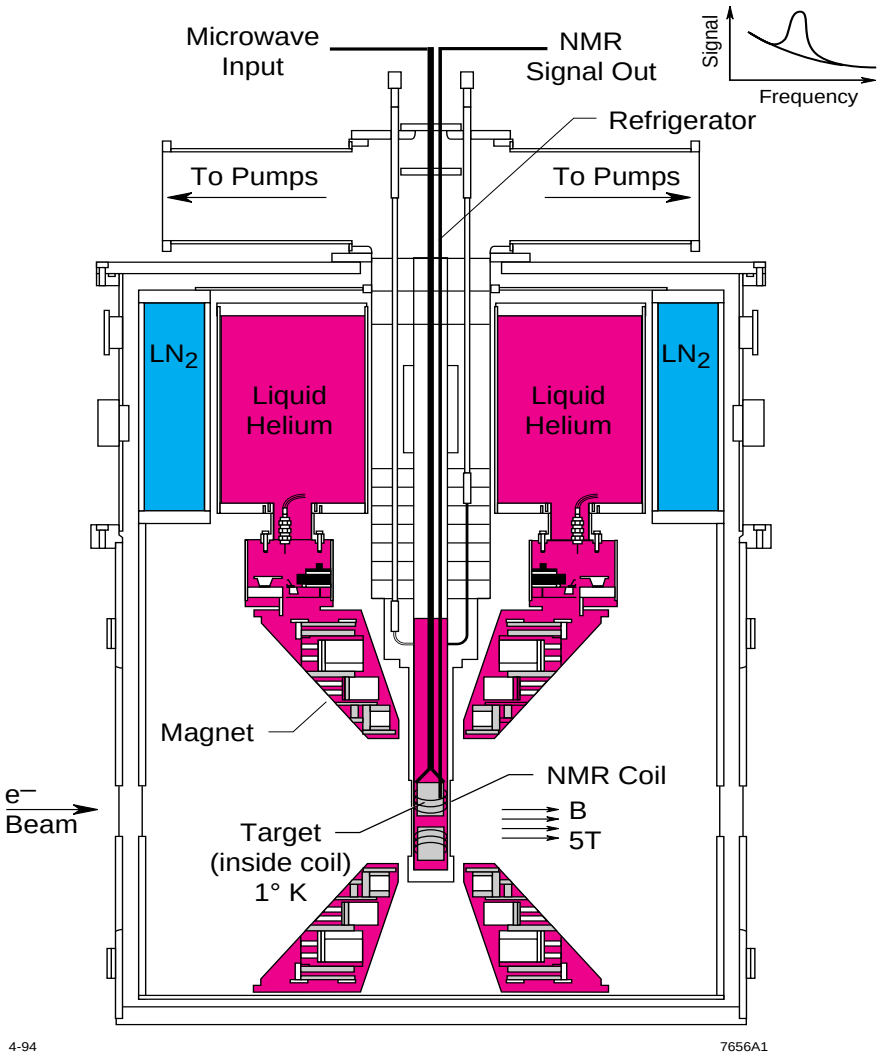

Figure 4.9: Cross-sectional view of the polarized target.

hole is smaller than the uniform size in order to test reconstruction resolution, and two diagonal holes are missing as a check on orientation of the reconstructed data. The pion collimator is octagonal and is designed to limit the solid angle acceptance of the HMS. With the dimensions given in the figure and spaced 166.37 cm from the center of the target, the pion collimator had a solid angle acceptance of 7.25 msr. Both slits were made of Tungsten with 10% CuNi.

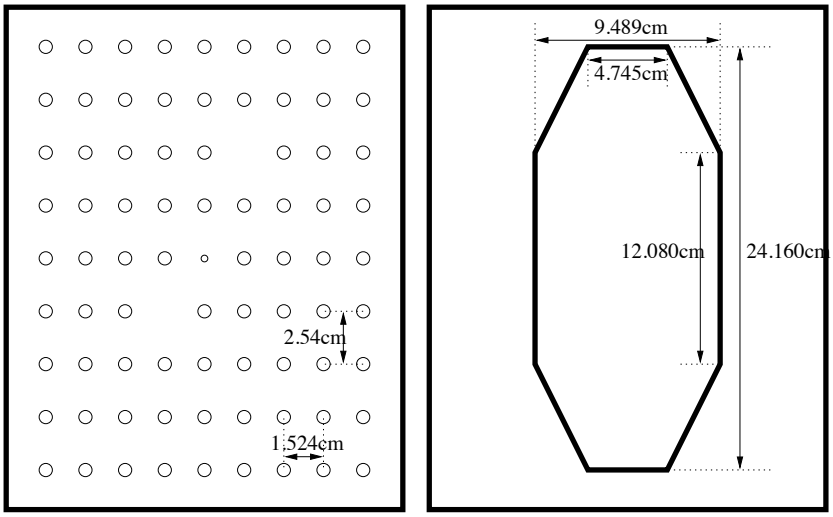

Figure 4.10: Sieve slit (3.175 cm thick with uniformly spaced holes 0.508 cm in diameter) and pion collimator (6.35 cm thick).

4.6.1 HMS Magnets

The four spectrometer magnets are arranged in a QQQD formation on the rotating carriage (see Figure 4.11). The quadrupoles are superconducting coils surrounded by soft iron to enhance the central field and reduce the stray field. In addition, each quadrupole has numerous correction coils producing a field uniformity on the order of 10^{-4}. Current for each quadrupole magnet is supplied by Danfysik System 8000 power supplies, which provide 1250 Amps at 5 Volts. Quadrupoles Q1 and Q3 focus in the dispersive (vertical) direction, while Q2 focuses in the non-dispersive direction.

The HMS dipole is also a superconducting magnet with a bend radius of 12.06 m and a 25 degree bend angle. The effective field length of the dipole is 5.26 m. Power is supplied by a similiar Danfysik 8000 power supply, providing 3000 Amps at 10 Volts. The 10^{-4} field stability was monitored by a NMR probe [58].

Alignment of the magnets was done with respect to their optical axis, which differed from their physical axis. The point to point tune in both dispersive and non-dispersive directions provided the large momentum acceptance and solid angle, and enables reconstruction of extended target lengths. Field settings for all magnets

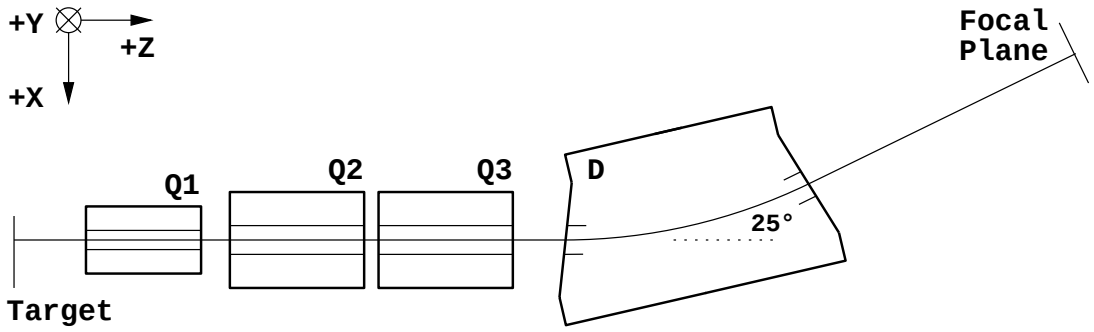

Figure 4.11: HMS magnetic elements. The Y-direction is into the page.

were determined by the COSY INFINITY program provided by MSU [59].

4.6.2 HMS Detectors

The HMS detector package included two drift chambers, two sets of hodoscopes, a gas Čerenkov detector, and a lead-glass shower counter array. The detectors were arranged as shown in Figure 4.12. The drift chambers provided position and trajectory information used in building particle tracks. Hits detected in the hodoscopes were used to build fast triggers. The Čerenkov detector and shower counter identified particles through particle velocity and energy deposition data. All detector high voltage was supplied by CAEN power supplies monitored and controlled by EPICS [60] software through a VME CAEN-net controller card in the detector hut.

Drift Chambers

The first drift chamber is mounted directly behind the exit window of the HMS dipole. The second drift chamber is located 81.2 cm behind the first and both had an aluminum frame wrapped in mylar. Each chamber had 6 wire planes, two measuring x position (x,x′), two measuring y position (y,y′), and two (u,v) measuring on a diagonal oriented 15° from the x-axis. The wire planes are spaced 1.8 cm apart and contain

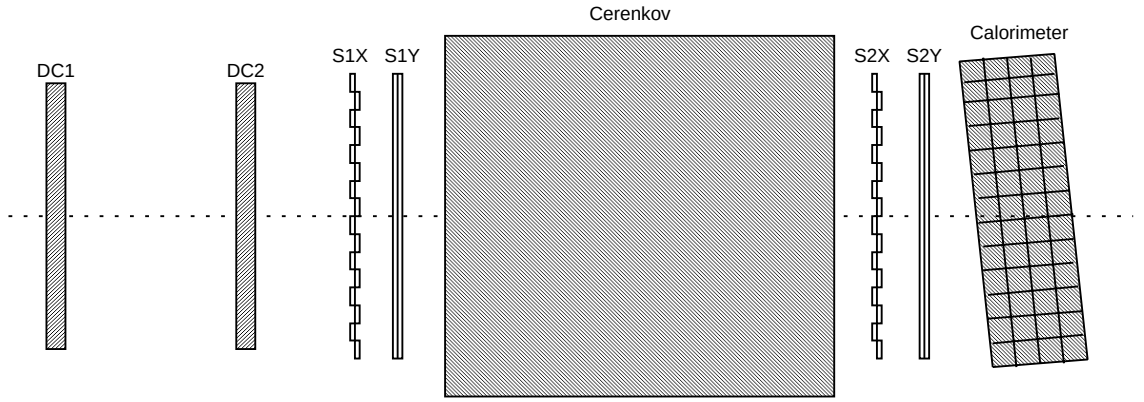

Figure 4.12: Side view of the HMS detector package.

both field (cathode) and sense (anode) wires. Field wires are 150 μm gold plated copper-beryllium wires maintained at a negative high voltage. Sense wires are 25 μm gold plated tungsten. Wires in each plane are spaced 1 cm apart. A grid of 113 x and x$'$ wires and 52 y and y$'$ wires provide a detection area of 113 cm $\times$ 52 cm, with 107 u and v wires which helps resolve multiple hits and provide improved accuracy in position.

Each chamber was filled with an argon and ethane gas mixture equal in amounts by weight, with a 1% isopropyl alcohol additive to help dissolve organic compounds formed by the irradiation of the ethane [61]. The gases were mixed in a gas shed outside the experimental hall and delivered to each chamber by a MKDS 1259c proportional mass flow control system.

When a charged particle enters the drift chamber, it ionizes the gas along its path through the chamber. The negative voltage on the field wires accelerates the ionized electrons towards the nearest sense wire. Sense wires are read out by amplifier/discriminator cards. Information on position from each of the planes are accumulated and used to reconstruct the trajectory of a particle.

Hodoscopes

Behind the second drift chamber and in front of the Cerenkov detector is the first hodoscope set, an x-plane and a y-plane. The x-plane contains 16 paddles made of Bicron BC404 plastic scintillator 1 cm thick and 8 cm wide. Each paddle is wrapped in one layer of light tight aluminum foil and two layers of Tedlar. At the end of each paddle is a Phillips XP2282B eight-stage photomultiplier tube attached to the paddle through a UVT lucite light guide. Each paddle has a 0.5 cm overlap with its neighboring paddles, so the row of 16 paddles in the x-plane covers an area 120.5 cm long. The y-plane is similiar but only has 10 paddles for a total length of 75.5 cm.

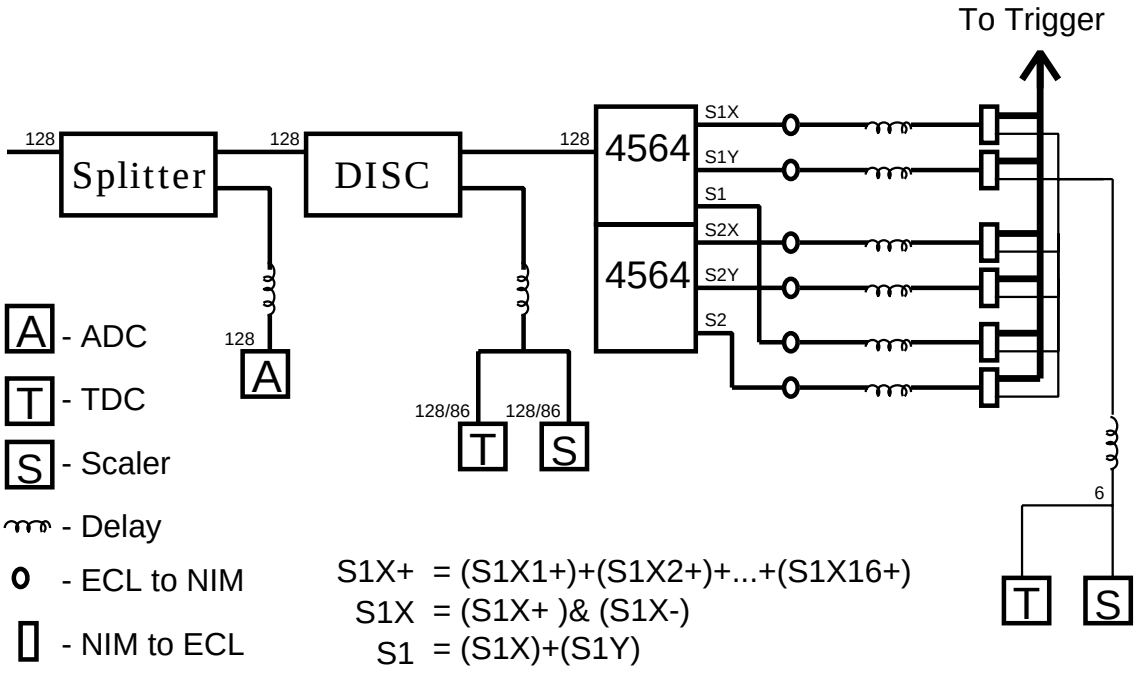

Figure 4.13: HMS hodoscope electronics logic.

Signals from the photomultipliers are sent to the counting house on RG58 cables. There the signal was split. One-third of the signal amplitude was transmitted along delay lines to an ADC. The other two-thirds were sent to a PS7106 leading edge discriminator. This discriminator had two ECL outputs. The first went through a logical delay to Fastbus TDCs and VME scalers. The other ECL output went to the

Lecroy 4654 logical unit which ORed all signals from one side of a given plane to be used in the trigger. Figure 4.13 shows the details of the hodoscope electronics. Trigger information from the hodoscopes is used with information from the drift chambers to determine the electron trigger.

Čerenkov

The Čerenkov detector sits between the pairs of hodoscope planes. When particles travel faster than the speed of light in a medium, they emit Čerenkov radiation. By adjusting the index of refraction of the gas within the detector, a momentum threshold can be set whereby particles heavier than electrons will require much greater momentum in order to emit Čerenkov light. In this way we discriminate between electrons and pions. The critical momentum is determined from the following equation:

$$p_{critical} = \frac{m}{\sqrt{n^2 - 1}} \ , \tag{4.7}$$

where m is the mass of the particle and n is the index of refraction of the medium. The index of refraction used for this G_{En} experiment was set to 1.0011 using 0.79 atm of Perfluorobutane (C_4F_{10}, n=1.00143 at 1 atm and 300 K). The momentum threshold for electrons to emit Čerenkov radiation is 11 MeV/c, whereas the threshold for pions is nearly 3000 MeV/c.

The Hall C Čerenkov detector is 165 cm in length (120 cm of effective length) and has an inner diameter of 150 cm. The hydroformed entrance and exit windows to the Čerenkov detector are made of 0.1016 cm Al (.27 g/cm^2). The windows were made as thin as possible to help minimize the production of knock-on electrons from pions. Energetic pions can produce knock-on electrons in the windows which could be detected if they have sufficient energy (however pions detected in the shower counter rarely produced more than one photoelectron above discriminator threshold, so a cut on the number of photoelectrons detected eliminated pion contamination). Two mirrors were fixed at the back of the tank to focus the reflected light onto two 5" Burle

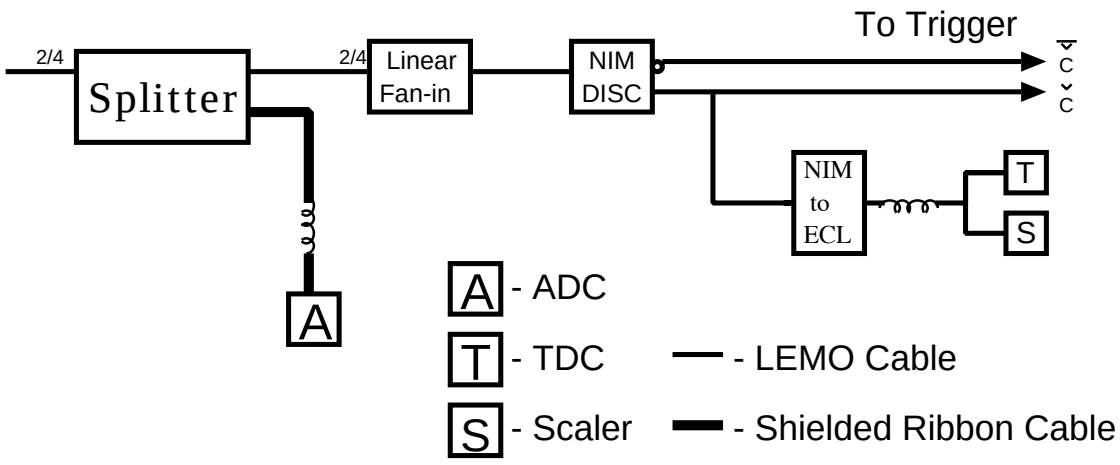

Figure 4.14: HMS Čerenkov detector electronics logic.

8854 photomultiplier tubes (PMTs). The phototube entrance windows are opaque below 200 nm causing a loss of UV sensitivity. Therefore, the front surface of each PMT was coated with a wavelength shifting material (para-Terphenyl, protected by 25 nm of MgF_2) to increase the quantum efficiency in the ultraviolet region [62]. The addition of the wavelength shifting material converts all light below 320 nm into a fluorescence at 360 nm where the PMT window is transparent.

Signals from the photomultipliers were sent to the counting house on RG58 and RG8 cables. There the signal was split with one part delayed and then sent to an ADC (see Figure 4.14). The other signal was summed by a Phillips 740 linear fan and discriminator to generate signals for the trigger, TDC, and scalers. Čerenkov efficiency, defined as the number of times the Čerenkov fired divided by the number of good tracks, was typically better than 99.9%, showing that at our kinematics there was a pure sample of electrons.

Calorimeter

Behind the Cerenkov and behind the last layers of hodoscopes lay the shower counter calorimeter. The shower counter identified electrons and rejected pions based on the total energy deposited. The shower counter was constructed from blocks of TF1 lead

glass, 10 cm × 10 cm × 70 cm in dimension, with a photomultiplier tube at one end of the block. The blocks were arranged 4 layers deep and 13 blocks high for a coverage area of 130 cm × 70 cm. TF1 has a radiation length of 2.54 cm, giving the calorimeter a total thickness of nearly 16 radiation lengths. The entire calorimeter was rotated by 5° relative to the optical axis to eliminate the possibility of particles passing through the cracks between blocks. Gains of each module were calibrated and monitored by a laser system.

An energetic electron will emit photons through Bremsstrahlung which generates e^+e^- pairs which emit photons creating a cascading shower of particles. Čerenkov light emitted by this cascade of particles was detected and the signal size was related to the track length of the shower. This track length was proportional to the energy of the initial electron.

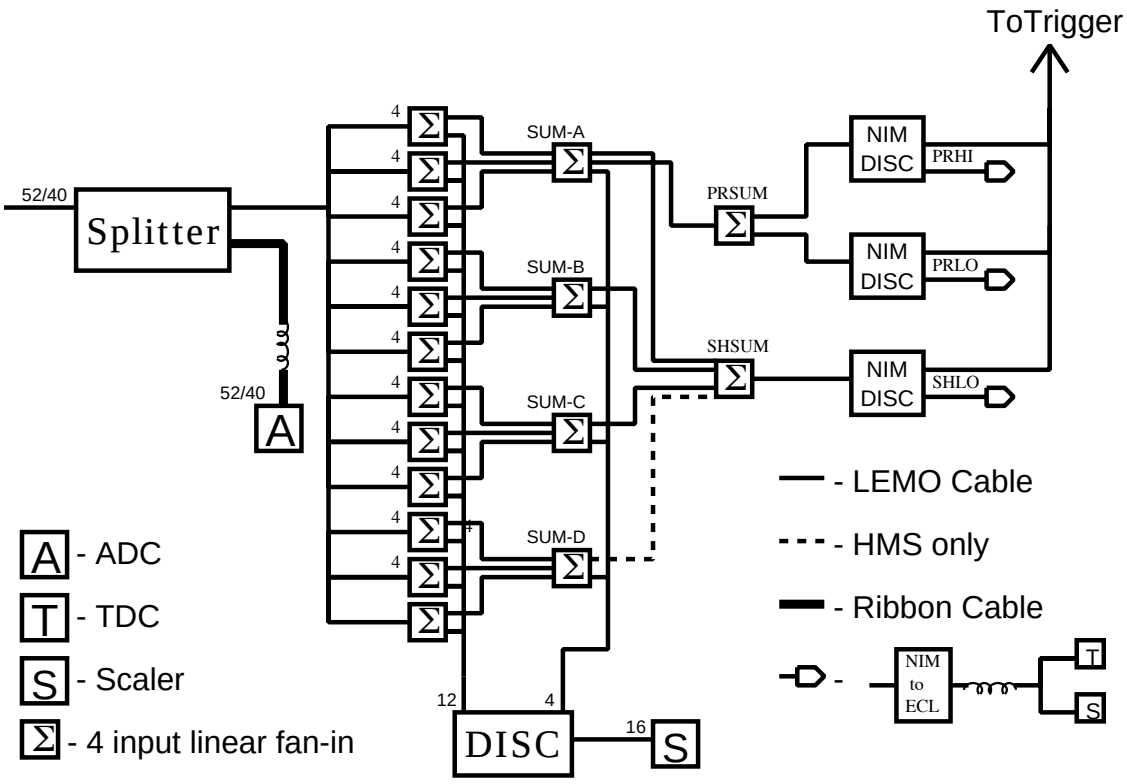

Figure 4.15: HMS shower counter electronics logic.

Photomultiplier signals sent to the counting house were split, with one output sent through a delay to an ADC. The other outputs were summed by a 740 linear fan and discriminated for the trigger. Details of the electronics logic can be seen in Figure 4.15.

4.7 Neutron Detector

For a coincidence measurement, we needed to provide a detector to complement the HMS which would provide information about the recoiling nucleon. Requirements for this detector included a large effective counter area to match the HMS acceptance, good energy and angular resolution, and a high detection efficiency. For this G_{En} experiment, we had to be able to detect recoiling neutrons and protons from quasielastic $e-p$ or $e-n$ scattering at the target in coincidence with a scattered electron.

4.7.1 Coverage Area

The large counter area was accomplished by using large Bicron 408 plastic scintillators in a wall covering the scattering cone of the recoiling nucleon. Each scintillator had the dimensions of 10 cm $\times$ 10 cm $\times$ 160 cm and the detector was arranged in a scintillator stack roughly 16 bars high and five layers deep (see Figure 4.16). The coverage area was dictated by the solid angle acceptance of the electron arm and the Fermi broadening of the deuteron quasielastic peak. Monte Carlo simulation using proposal values for the HMS solid angle and momentum bite ($\pm$ 10%) verified analytical calculations which indicated that the d(e,e'n) process required a coverage area of 1.6 m $\times$ 1.6 m, when placed 4.03 m from the target (for Q^2=0.5 (GeV/c)^2). The center of the stack was also placed 20 cm below the initial beam height to take into account the tilt of the scattering plane resulting from the deflection of the outgoing electron by the target magnetic field. In addition to the five layers of scintillator bars, there were also two layers of veto paddles. All bars and paddles were equipped with

photomultiplier tubes on both ends.

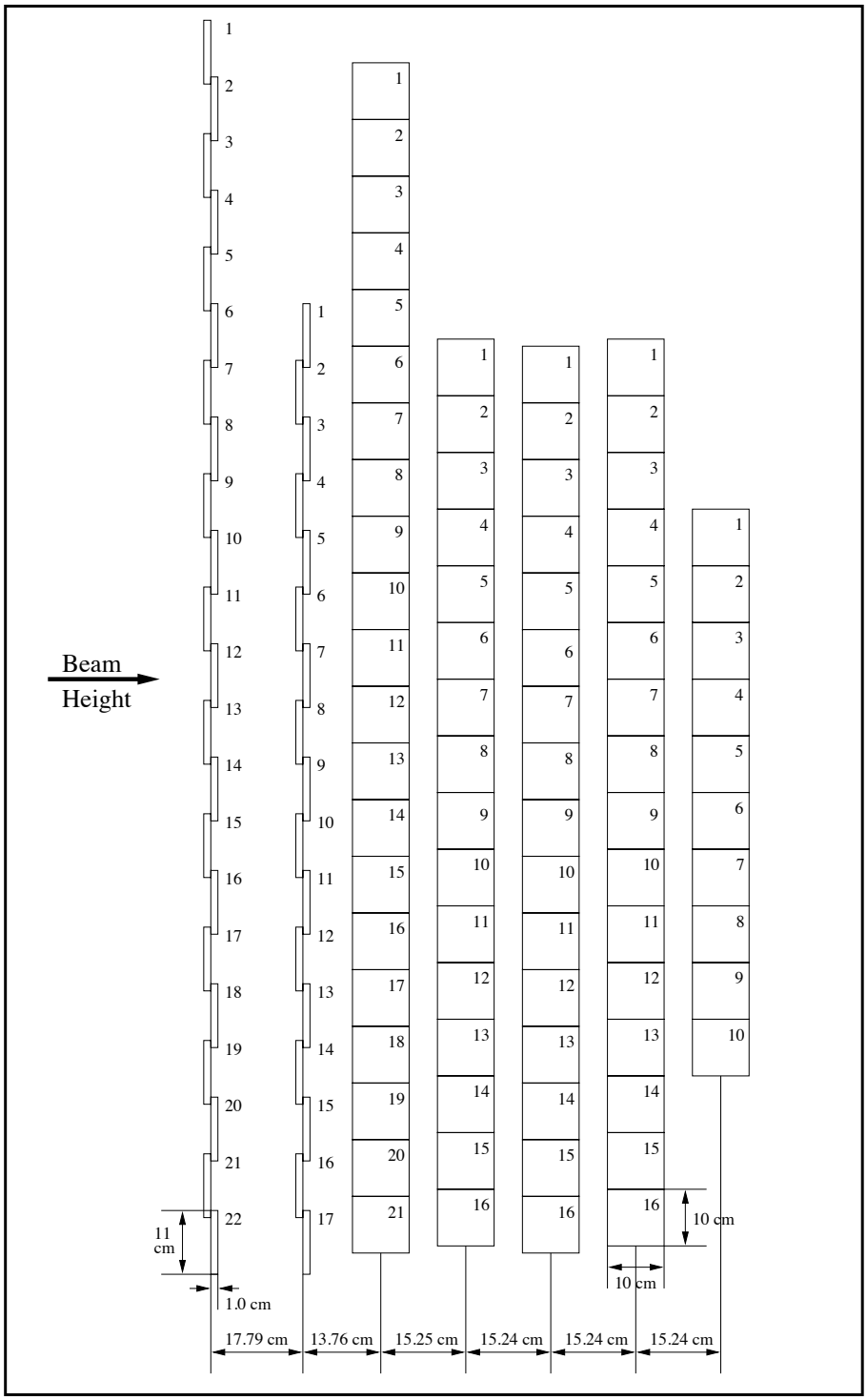

Figure 4.16: Side view of E93026 neutron detector.

4.7.2 Detector Efficiency

The neutron detection efficiency is about 10% for each 10 cm of scintillator [63, 64]. For this reason the 79 neutron detector bars were arranged most effectively in a grid five layers deep. The two front layers of veto paddles (also Bicron 408 plastic scintillator, with dimensions 1 cm $\times$ 11 cm $\times$ 160 cm) were used to discriminate between neutrons and charged particles such as protons and pions. In front of the veto paddles were layers of CH_2 and lead, used for shielding of soft X-rays from the target [65].

4.7.3 Energy and Angle Resolution

The energy and angle resolution of the neutron detector bars were determined from the time and position resolution of each hit in the bars. Energy resolution is dependent upon the time of flight of the detected particles. For fixed uncertainties in path length and timing resolution, energy resolution improves linearly with increased flight path [64]. Therefore, the neutron detector was placed far enough from the target to minimize the role of the timing resolution in the energy uncertainty. To obtain energy resolution, the timing resolution as well as the uncertainty in path length due to the thickness of the neutron bar had to be taken into account. The fractional energy resolution $\Delta T/T$ is given by

$$\frac{\Delta T}{T} = \gamma(\gamma+1)\left[\left(\frac{\Delta x}{x}\right)^2 + \left(\frac{\Delta t}{t}\right)^2\right]^{1/2} , \tag{4.8}$$

where T is the kinetic energy, ΔT is the resolution of the kinetic energy, γ is the Lorentz factor, x is the nominal path length of the recoiling nucleon, Δx is the uncertainty in path length due to the thickness in the bar, t is the time of flight of that particle, and Δt is the timing resolution of the coincidence signal.

The timing resolution measured during the experiment was actually larger than expected. Using the measured timing resolution of 450 ps, our energy resolution

became 16.5 MeV, which was similar to, but slightly larger than, the proposed value of 15.4 MeV.

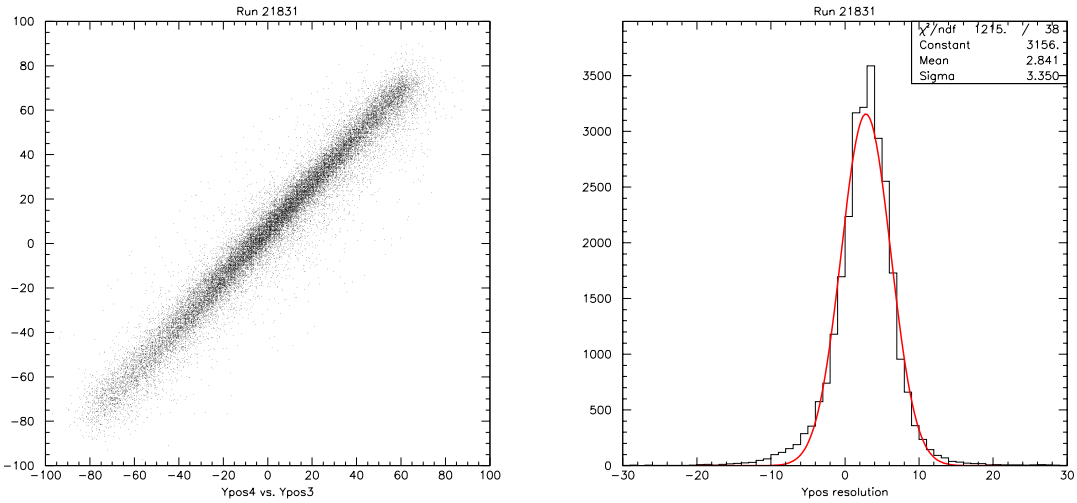

Figure 4.17: Neutron detector position resolution. The difference between hit positions in successive bar planes provided an improved position resolution [48]. The left hand plot shows the "ypos" of hits in plane 3 vs. hits in plane 4 (the first and second bar planes). The right hand plot shows the difference between the ypos values from plane 3 to plane 4 and represents the width of the diagonal line in the left hand plot.

The position resolution was determined by comparing the hit position in successive layers of neutron bars. By comparing the "*ypos*" of hits in plane 3, versus hits in plane 4, we can see from Figure 4.17 that the position resolution is 33.50 mm [48]. Using the value of 4.03 m as the distance of the neutron detector from the target, the angle resolution is determined to be $\sim$ 8.3 mrad.

4.8 Electronics

Experiment E93026 had an electronics setup designed to accept triggers from both the electron and nucleon detector arms. Individual spectrometer triggers were formed by their respective electronics based on signals from their individual spectrometer components. These individual triggers were sent to the trigger supervisor (TS) which

would then accept, reject, or scale the different trigger types and then initiate further processing.

4.8.1 Electron Triggers

Electron triggers were initiated by the hodoscope signals. Whenever a charged particle passed through the spectrometer and was detected by a hodoscope plane an electron pretrigger was logged. A charged particle was "detected" by the hodoscope when both the left and right PMTs fired in coincidence. The four planes of hodoscopes allow for different levels of hodoscope triggers. A trigger labelled STOF was formed if there was a hit in one of the front hodoscope planes and in one of the back planes, whereas the trigger labelled SCIN required that three out of four hodoscope planes found a hit. Each hodoscope plane had an efficiency of greater than 99%. If a hodoscope trigger was present, then the particle identification was made from the information from the Čerenkov and the shower counter. A hodoscope trigger with no Cerenkov signal indicated a pion. A hodoscope trigger with a Cerenkov or a large shower counter signal indicated an electron. The shower counter threshold was set such that $> 90\%$ of electrons were detected with good pion rejection. The Cerenkov triggered if the Cerenkov sum signal was above its threshold of 1 or 2 photoelectrons.

Two types of electron triggers existed, ELLO and ELHI. ELLO was the coincidence of a hodoscope trigger and a Cerenkov signal. ELHI was formed from hodoscope triggers plus a large calorimeter signal. The final electron trigger was formed by an OR of these two electron triggers. Figure 4.18 shows the full schematic of the electron trigger logic.

4.8.2 Nucleon Triggers

There were four types of nucleon triggers coming from the Neutron Detector: neutron bar (BAR), paddle (PAD), cosmic (CT), and laser triggers (LT). A BAR was formed from the OR of all 79 bars in the 5 planes of neutron bars. Likewise, a PAD was

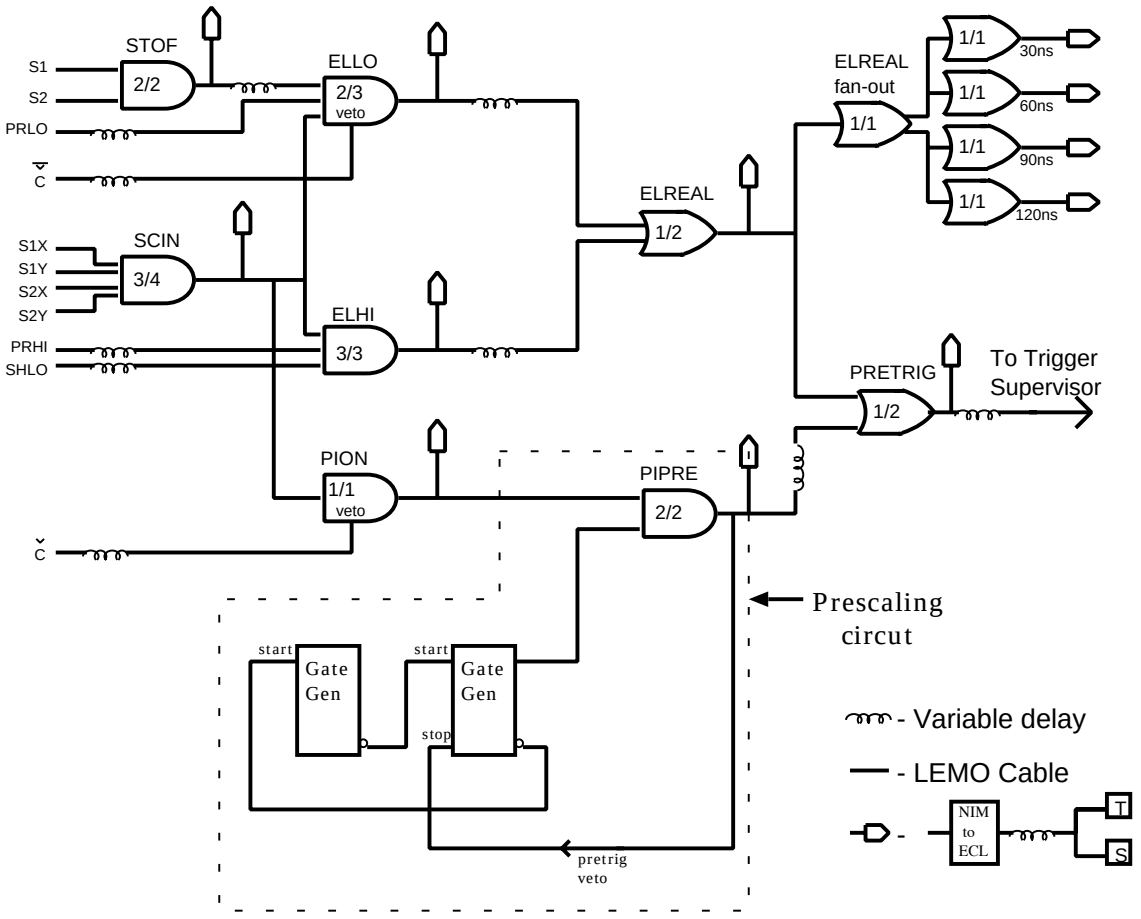

Figure 4.18: Hall C electron trigger logic. The trigger logic for E93026 was modified slightly whereby the output of ELREAL was the trigger, not the pretrigger, and was routed to the trigger supervisor.

formed from the OR of all 39 veto paddles. Thresholds in each were set to maximize the signal to noise ratio (75 mV for bars, 30 mV for paddles) while maintaining efficiency. The cosmic trigger was formed from a coincidence of a hit in a top bar with a hit in a bottom bar. The laser system, triggered by LT, was used to calibrate and monitor the PMT gains in the bars. Figure 4.8.1 shows the nucleon trigger logic.

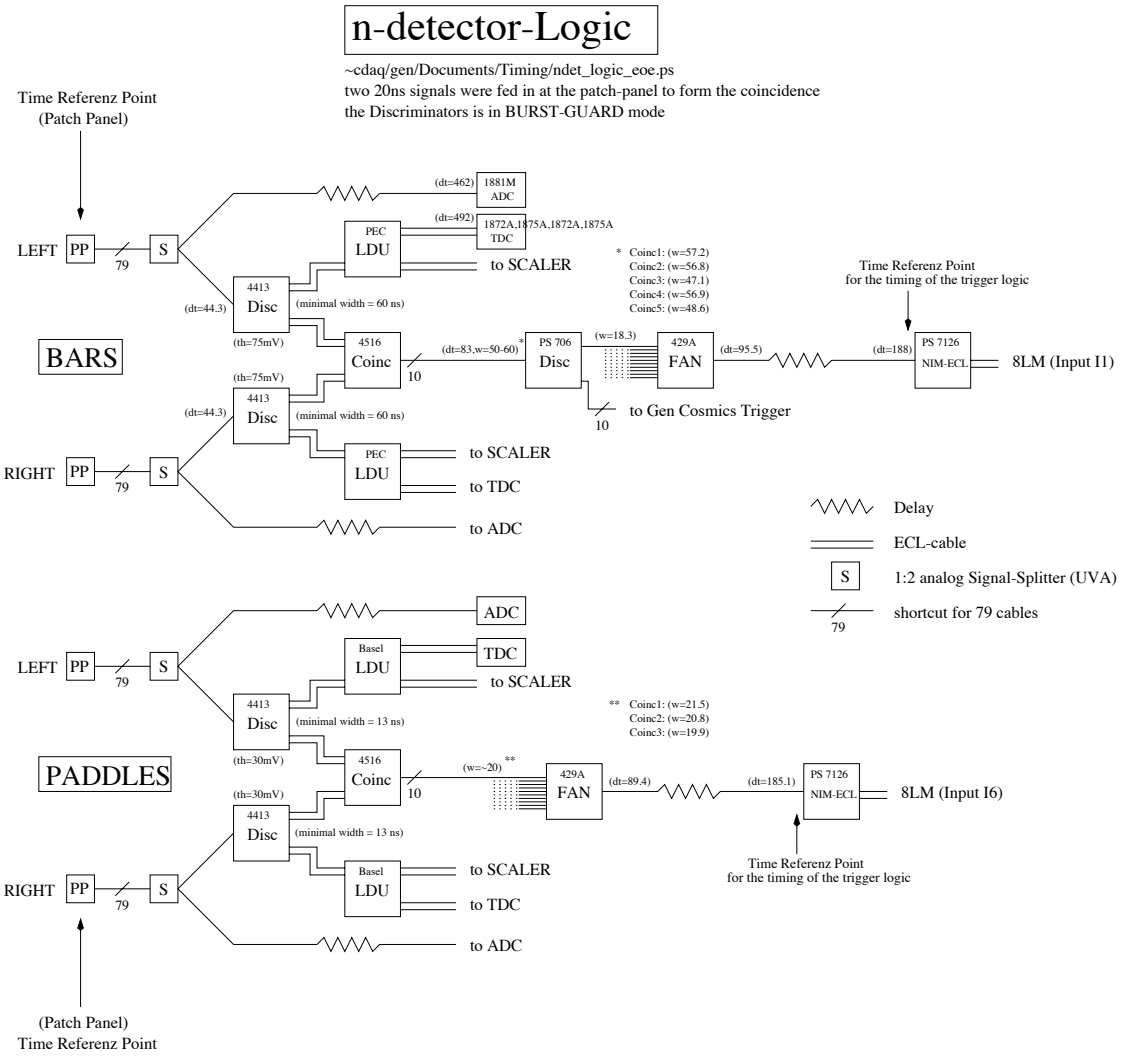

Figure 4.19: E93026 nucleon trigger logic.

4.8.3 Triggers and Event Types

Individual triggers from the electron and nucleon arms were fed into two octal logical units which produced outputs based on logic combinations of the inputs (see Figure 4.8.3). During E93026 there were 2 main trigger types: electron "single" and electron-neutron bar coincidence. The electron "single" trigger was actually an electron-NOTneutron bar coincidence trigger. The combination of this "single" trigger and the coincidence trigger formed the true singles rate (which is discussed in great detail in Section 8.2). Other trigger types included scaler, laser, cosmic, and

pedestal triggers. These triggers were passed to the Trigger Supervisor (TS) which generated events from the triggers. The TS matched input trigger data to event type via a lookup table (see Table 4.3). Physics triggers were disabled during the first 1000 events in each run for pedestal measurement. Physics triggers were also turned off during each period of potential helicity transition (1 Hz) for $\simeq 600$ μs. Helicity gated scalers were read out during this period. All other scalers were read every five seconds.

0: Asynchronous scaler readout
1: HMS Single
3: eB coincidence
4: Pedestal
5: Helicity gated scaler readout
6: Laser
7: Cosmics
8: Illegal Trigger pattern

Table 4.3: E93026 event types.

4.9 Data Acquisition

CODA, the CEBAF Online Data Acquisitions System, version 2.0, was implemented as the standard Hall C data acquisition system, starting with this experiment. The hardware associated with this system included eight FASTBUS and VME crates run by Read Out Controllers (ROCs) on embedded CPUs. The main run control program resided on a single Sun workstation (CDAQS1). In addition to receiving data from the ROCs, CDAQS1 was also linked to a HP-UX machine (CDAQH1) which read slow controls such as magnet currents and high voltages through Input-Output Controllers (IOCs). CDAQS1 also exchanged information with the target computer in the counting house. A schematic of the data acquisition system can be seen in Figure 4.9.

The trigger supervisor determines the event type from trigger information and

passes this event type to the ROCs, which read out ADC and TDC modules specified by the user in readout lists. The ROC CPU stored the data and shipped the event fragments to the Event Builder (EB). The EB built the event (essentially added header information to the event fragment) and put the data into a common event format. Events were then written to data disk by the Event Recorder (ER). Four 17 GB disks comprised the data disk system. A background process backed up the data to tape. Scalers were read every five seconds, slow controls were read every 30 seconds. Target data was sent to CODA from the target DAQ at a frequency dictated by the polarization measurement intervals (usually around every 40 seconds).

ADC "sparsification" (ignoring ADC events that were below a certain threshold thereby reducing the event size) was turned on for the HMS, but turned off for the neutron detector. Typical event size was $\sim$ 2.3 kB. The event rate varied with the prescale factor for the singles triggers. For prescale of four, event rate was 450 Hz (for 100 nA), but dropped to 300 Hz for a prescale of eight. Computer dead time also varied slightly with the prescale factor, but was roughly 11%.

Figure 4.20: E93026 combined trigger logic.

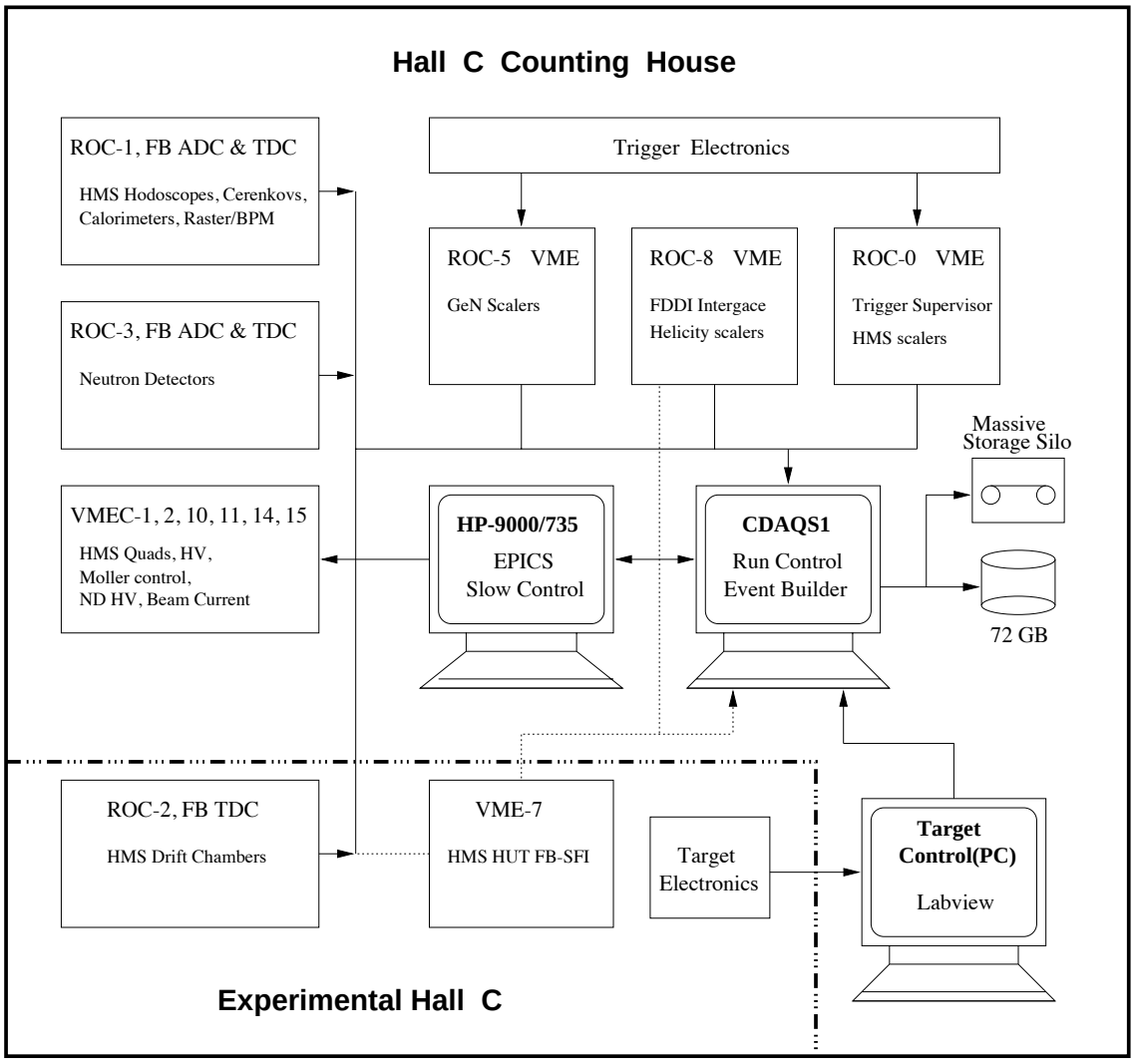

Figure 4.21: E93026 data acquisition system schematic.

Chapter 5 Polarized Target

5.1 Introduction

Polarized electron-polarized nucleon scattering requires a target in which the nucleons are polarized and a technique for determining the magnitude of the resulting polarization. For E93026, a solid polarized target system was used. It consisted of five major sub-systems: a large magnet to provide a preferred orientation for the nucleon spins, a ^{4}He evaporation refrigerator to cool the target material to approximately 1 K, a target insert in which the target material was located and could be mounted or extracted with ease, a microwave system to dynamically polarize the target spins, and a Nuclear Magnetic Resonance (NMR) system to determine the level of polarization in the target.

The choice of target material was critical as the experiment required high target polarization over an extended period of time. The target material had to be able to withstand large doses of radiation without losing a significant portion of its polarization. The target material also needed to have relatively quick buildup and thermalization time constants. The faster the target could reach its maximum polarization or reach thermalization, the less of an impact it had on the experiment's beam usage time. The target material was chosen to provide a high density of protons or neutrons while also containing a paramagnetic dopant. The technique of Dynamic Nuclear Polarization (DNP) used this paramagnetic dopant, a material with an unpaired or quasi-free electron, to enhance the nuclear polarization. The ^{4}He evaporation refrigerator was capable of handling the large heat load deposited by both the microwaves and electron beam on the 3 cm thick target. The NMR system provided a way to measure the degree of orientation of the nucleon spin states without destroying

a large portion of that polarization.

5.2 Dynamic Nuclear Polarization

The DNP technique uses a microwave field to transfer the polarization of the electron spins to the nuclear spins, to obtain a high nuclear polarization. The reason for implanting paramagnetic centers in the target material was so that they can be used to transfer polarization from the electrons to the nucleons via the electron-nucleon spin-spin interaction [66, 67].

The target material was doped with free radicals, materials with an unpaired electron, and placed in a high magnetic field at low temperature. In the high magnetic field, the free electron spins are nearly 100% anti-aligned with the magnetic field axis. At sufficiently large ratios of field to temperature, there is an alignment of the nuclear spins which is small, but measureable.

The Hamiltonian of the system, $\mathcal{H}_0$, is composed of the two separate Zeeman transitions for the electron and nucleon spin states, and $\mathcal{H}_{ss}$, which is the contribution to the Hamiltonian from the spin-spin interaction,

$$\mathcal{H}_0 = \vec{\mu}_e \cdot \vec{B} + \vec{\mu}_n \cdot \vec{B} + \mathcal{H}_{ss} \ . \tag{5.1}$$

$\vec{\mu}_e$ and $\vec{\mu}_n$ are the electron and nucleon magnetic moments, respectively, and $\vec{B}$ is the magnetic field vector. The radio-frequency (RF) fields applied to the spin system can induce transitions between spin states. In absence of the spin-spin interaction, transitions are called "allowed" transitions. If the $\mathcal{H}_{ss}$ term is included, transitions are called "forbidden" transitions [68].

Allowed transitions, also called pure spin transitions, allow spins to move from one energy level to another. If the applied RF field has a frequency $\nu = \nu_e$, it will induce transitions in the electron spin (from upper to lower energy level, or vice versa). For $\nu = \nu_n$, similar transitions will be made by the nucleon spin. Forbidden

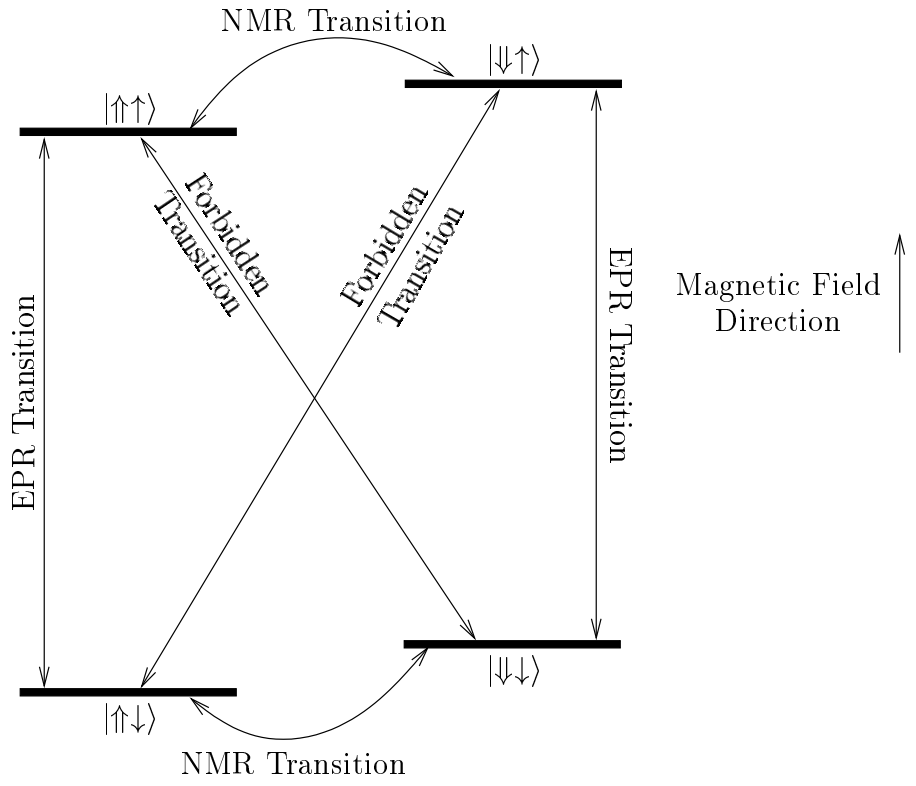

Figure 5.1: Energy level diagram for Zeeman splitting in a magnetic field.

transitions allow both electron and nucleon spins to flip simultaneously, provided the RF frequency is equal to $\nu_e + \nu_n$ or $\nu_e - \nu_n$. The probability of these forbidden transitions is smaller than the allowed transitions by a factor of the square of the dipolar mixing coefficient, ϵ. ϵ^2 is small, only 10^{-4} for nucleons 3 Å away from the unpaired electron, dropping off with the sixth power of distance, but is not zero [68].

The essential feature of Dynamic Nuclear Polarization (DNP) is that while polarization is built up through this interaction between the electron and nucleon, it does not generally decay via this mechanism. Electron spins have a strong interaction with the thermal motions of solids and decay rapidly (and radiationless) through spin-lattice relaxation. Conversely, nucleon spins are weakly coupled to the lattice and therefore decay much more slowly than the electron. Transition probabilities for spin-lattice relaxation are very different for electrons and nucleons, and differ by a factor of magnetic moment squared (433188 for protons) [66]. This disjoint in spin

relaxation times allows nucleon spins to accumulate in the desired energy level while electron spins are reused to build polarization.

Species	Magnetic Moment
electron	$\mu = 1.001\ \mu_B$
proton	$\mu = 2.793\ \mu_N$
neutron	$\mu =$ -1.913 μ_N
deuteron	$\mu = 0.857\ \mu_N$
Bohr magneton	$\mu_B = 5.788 \times 10^{-11}$ MeV $\cdot$ T^{-1}
nuclear magneton	$\mu_N = 3.152 \times 10^{-14}$ MeV $\cdot$ T^{-1}

Table 5.1: Relevant magnetic moments.

There are on the order of 10^7 nucleons per unpaired electron (or 10^{19} unpaired electrons/cm^3). Further enhancement of polarization must take place through what is known as spin diffusion, which is the transfer of nucleon polarization via the nucleon-nucleon spin-spin interaction. The unpaired electrons sparsely populate the target material, so the fraction of nucleons that are in close proximity to this agent of polarization buildup is small. Only nucleon spins near an unpaired electron are polarized by the electron-nucleon spin-spin interaction. However, when a nucleon spin relaxes, it can transfer its polarization to a neighboring nucleon spin. This interaction is energy conserving and occurs frequently (10^4 times/second) [68]. The initially polarized nucleon spin can then be "repolarized" by the free electron in its close proximity. This allows the nucleon ordering created near the electron to propagate out from the paramagnetic centers.

5.2.1 Radiation Damage

During the normal running of the experiment, the target is placed in a beam of high energy electrons. These electrons produce additional paramagnetic radicals in the course of their collisions. These additional centers can be valuable in aiding polarization to a degree, but after a point, they only serve to depolarize the target. The probability of reverse relaxation via the electron-nucleon interaction remains small only when the number of local electrons is small. The more unpaired electrons

in the vicinity, the greater the chance one will flip a nucleon spin back. So there are actually two modes of spin relaxation for nucleons. The first, which is always present and is temperature dependent, is relaxation via spin-lattice relaxation. The second is relaxation through the electron-nucleon spin-spin interaction, which is proportionally small as long as the density of paramagnetic centers remains small.

When the buildup of paramagnetic centers becomes so great that the level of polarization is degraded below acceptable levels, an anneal must be performed. Annealing is the process of heating the target material to the temperature at which it was initially radiated (nominally 80 K) for a period of 15-20 minutes (or whatever is deemed experimentally successful for a given target material). This serves to allow extra paramagnetic centers to recombine, decreasing the density of centers (or producing different centers) and diminishing the effect of relaxation through the electron-nucleon interaction. In some materials, such at $^{15}NH_3$, after a certain amount of radiation damage (typically the level of the target's initial radiation dose), annealing no longer has any benefit and the target material must be replaced.

5.3 Nuclear Magnetic Resonance

The magnitude of the target polarization is determined by NMR which works on the principle that the spin system's magnetic susceptibility will change as the polarization changes. These changes in susceptibility can be measured in a calibrated way. The main element of the NMR system was the Liverpool Q-meter [69]. The Q-meter measured the Q of the RLC circuit formed by the NMR coil and the resistive and capacitive elements housed within the Q-meter box. This circuit could be tuned to series resonance using a tuning capacitor within the Q-meter. The voltage output of the Q-meter was roughly parabolic (see Figure 5.3a) as the frequency was swept across resonance. The components of the Q-meter circuit are selected so as to operate in the frequency range of the resonance of the nucleon system. The resonant frequency

peak of the Q curve is dictated by the nuclear energy level splitting (Figure 5.1):

$$\nu = \frac{\Delta E}{h} \ . \tag{5.2}$$

ΔE is the energy difference between energy levels and h is Planck's constant. The energy level splitting is dictated by the magnitude of the magnetic field and the spin of the nucleon,

$$\Delta E = \frac{-\mu_N \Delta m B}{I} \ . \tag{5.3}$$

B is the magnitude of the magnetic field, μ_N is the magnetic moment of the nucleon, I is the spin of the particle and Δm describes the change in orientation of the spin of the particle[1].

A radio frequency generator produced radio waves at the resonant frequency (213 MHz for protons in a 5 T field), flipping the spin-state of a small sample of nucleon spins. This caused a change in induction which was detected by the Q-meter as a change in circuit voltage. The Q-meter provided the output voltage as a function of frequency when modulated about this resonant frequency. This output voltage is a function of circuit impedance,

$$Z = i\omega L - \frac{i}{\omega C} + R \ , \tag{5.4}$$

where the imaginary part of the impedance affects the phase of the resonant peak, and the real part of the impedance affects the resistance of the circuit. When the nucleon polarization is enhanced, the susceptibility of the material is changed which in turn changes the inductance by

$$L = L_0(1 + 4\pi\eta\chi) \ , \tag{5.5}$$

where L is the inductance, L_0 is the free space inductance of the coil, χ is the sus-

[1] m can have $2I$+1 values ranging from -I to +I.

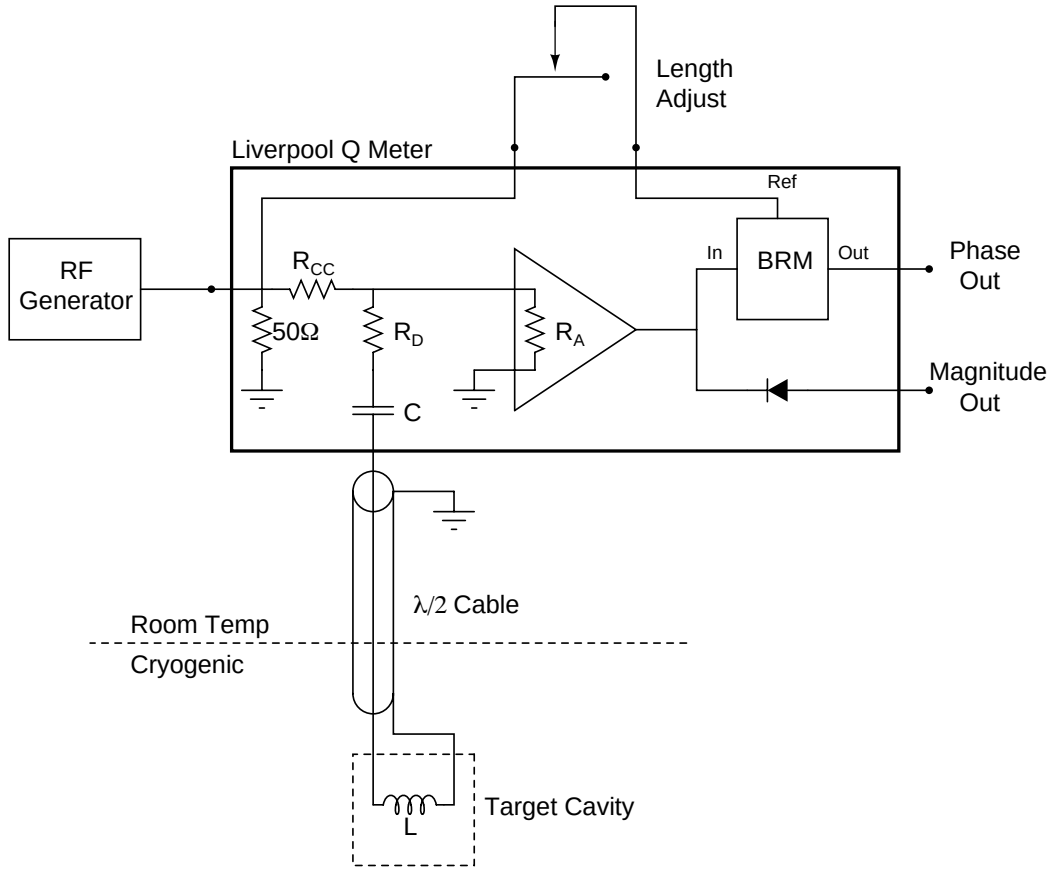

Figure 5.2: Liverpool Q-meter schematic. The Balanced Ring Modulator (BRM) is the key component of the Q-meter, measuring the phase between the input and the reference signal.

ceptibility, and η is a filling factor. Using this equation, we can modify our original equation for the impedance to read:

$$Z = i\omega(L_0(1 + 4\pi\eta\chi_1) - \frac{1}{\omega^2 C}) + R + 4\pi\omega\eta\chi_2 \ , \tag{5.6}$$

where χ_1 is the real part and χ_2 is the imaginary part of the susceptibility. In the region of the resonant frequency, χ_1 becomes very small in comparison to χ_2. Therefore, we can see that the dispersive part of the impedance does not change but the absorptive part of the impedance does change. The absorptive part of the signal

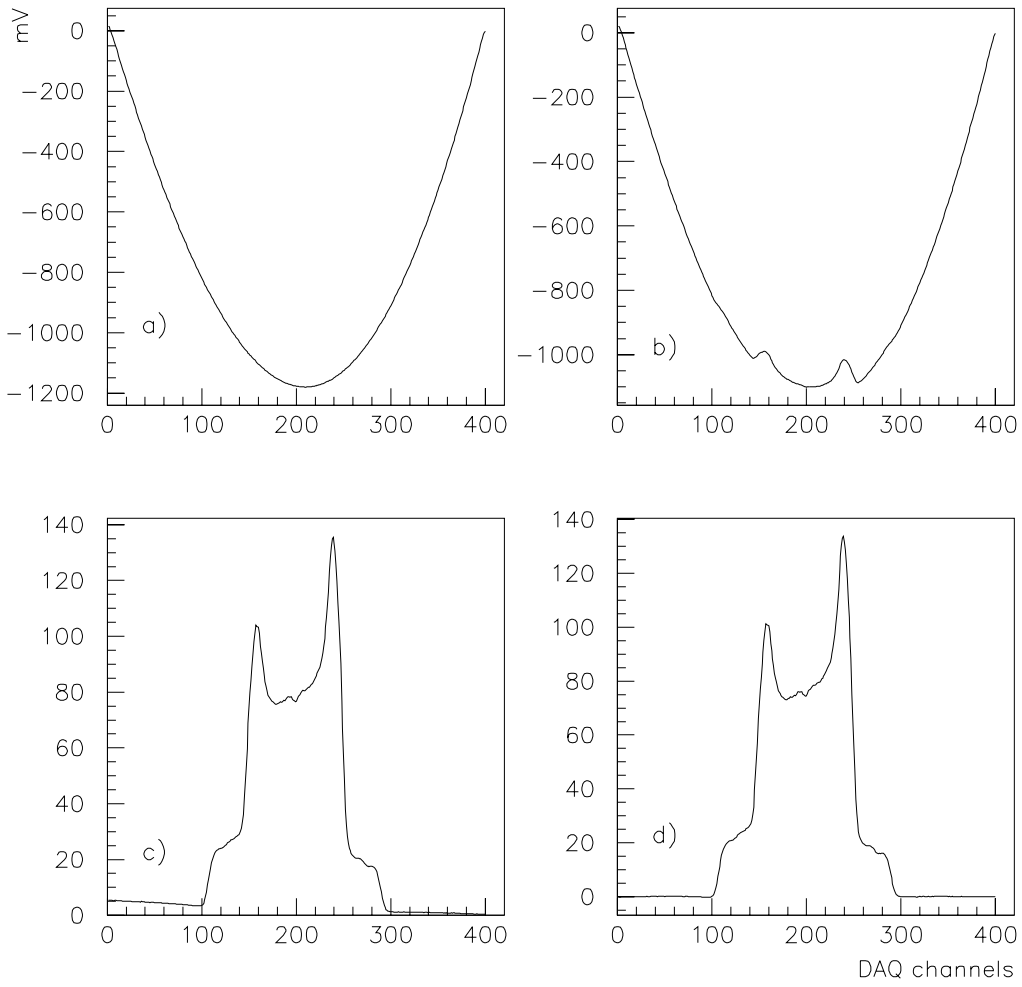

Figure 5.3: Evolution of enhanced deuteron signal acquisition: (a) Baseline signal is taken off-resonance;(b) Raw signal is taken on-resonance;(c) Raw signal after baseline subtraction; and (d) Poly-subtracted signal.

is detected by measuring the phase rf, using a phase sensitive detector (in this case, a balanced ring modulator in the Liverpool Q-meter) [69]. At resonance, we can write the Q value as

$$Q = \frac{\omega L}{(R + 4\pi\eta\chi_2)} \ . \tag{5.7}$$

For a positive value of χ_2, Q is reduced. This is observed in the peak on the Q curve. (Figure 5.3b)

A baseline signal, taken off-resonance, was subtracted from the signal to provide a flat background. Because the presence of the polarization signal distorts the shape of the Q-curve slightly, there was always a small residual curve left over from the baseline subtraction (see Figure 5.3c). Changes in temperature and the disturbance from the beam caused tuning changes as well. Therefore, a quadratic was fitted to the wings and then subtracted from the baseline-subtracted signal to produce a poly-subtracted signal (Figure 5.3d). This poly-subtracted signal should be completely flat on the wings. The poly-subtracted signal was integrated and the integrated area is proportional to the magnitude of the polarization,

$$P \propto \int_0^\infty \chi_2(\omega) d\omega \ . \tag{5.8}$$

To find the constant of proportionality, a measurement of the nucleon polarization at thermal equilibrium had to be made. Thermal equilibrium is reached by allowing the target material to sit in a bath of liquid helium at a stable temperature and constant magnetic field. The resulting NMR signal at thermal equilibrium (TE signal) had a polarization which could be calculated from Boltzmann statistics. In the case of a spin-1/2 system, the polarization is the difference between the spin-up and spin-down particles, divided by the total number of spins,

$$P = \frac{N_\uparrow - N_\downarrow}{N_\uparrow + N_\downarrow} \ , \tag{5.9}$$

where

$$N_{\uparrow} = \frac{e^{\frac{\mu B}{kT}}}{e^{\frac{-\mu B}{kT}} + e^{\frac{\mu B}{kT}}} \tag{5.10}$$

and

$$N_{\downarrow} = \frac{e^{\frac{-\mu B}{kT}}}{e^{\frac{-\mu B}{kT}} + e^{\frac{\mu B}{kT}}} \ . \tag{5.11}$$

This can be simplified to produce an equation for the polarization in terms of known quantities:

$$P(1/2) = \tanh(\frac{\mu B}{kT}) \ . \tag{5.12}$$

For spin 1 systems, the analogous result is,

$$P(1) = \frac{4\tanh(\frac{\mu B}{2kT})}{3 + \tanh^2(\frac{\mu B}{2kT})} \ . \tag{5.13}$$

The calibration constant (CC) was then just the TE polarization divided by the measured TE area, because signal area increases linearly with polarization,

$$CC = \frac{\text{Polarization}_{TE}(B,T)}{\text{Area}_{TE}} \ . \tag{5.14}$$

In addition to the above "area method", other methods of determining the target polarization were employed to provide redundant measurements or to provide an alternative method in the event that no reliable calibration constant was available. Two such methods, the "midpoint method" and the "peak height" method, are described in some detail in Appendix H.

5.4 Target Hardware and Performance

To achieve the goals of the experiment it was necessary to maintain a high level of polarization and determine accurately its value. To reach this end, several key pieces of hardware were needed.

5.4.1 Magnet

The target magnet used in this experiment was a 5 Tesla superconducting Helmholtz split pair coil from Oxford Instruments. The homogeneous field region for this magnet was uniform to a part in 10^4 over an oblate spheroid of greater than 3 cm in diameter, and was sufficient to encompass our target cell. The magnet had a 20 cm bore with an opening angle of 100°, and a coil split of 8 cm and opening angle of 34°. This large bore opening angle was essential to the running of this experiment allowing for flexibility in the choice of kinematics.

As discussed in Chapter 4, the target field was aligned such that the direction of the magnetic field was perpendicular to $\vec{q}$ in order to maximize the sensitivity to G_{Ep}. Any misdetermination of the field direction allows the G_M^2 term to contribute to the asymmetry in an unforeseen manner. This makes exact determination of the direction of the field extremely important. This was accomplished by use of a Hall probe inserted into the refrigerator to the central field region with an external vernier. The Hall probe was specially machined and surveyed into place for this target system. The magnetic axis was found to be consistent with the geometrical direction of the field to within one-tenth of a degree. For details on the determination of the target field direction, please see Reference [70].

5.4.2 Evaporation Refrigerator

The polarization, and thus signal size, at thermal equilibrium varies inversely with temperature, so it was important to achieve as low a temperature as reasonably possible. Thermalization time increases as the temperature decreases, so an intermediate low temperature was sought which produced a large signal size but did not take several hours to thermalize. Historically, the ratio of field to temperature has been the most important aspect of the magnet and refrigerator combination. Experiments using a dilution refrigerator are capable of temperatures much lower than 1 K, but have less cooling power than an evaporation refrigerator. The heat load on the refrigera-

tor comes from two sources, the energy deposited by the electron beam in the 3 cm target and the microwave radiation used to build polarization. Heat load from the microwaves, estimated from helium boil-off rates in the target cavity, was about 1 W and the electron beam deposited an estimated 0.5 W. Because of this large heat load, it was important to have a system capable of an even greater amount of cooling power. For this we used a ^{4}He evaporation refrigerator, which cooled the target by evaporation of ^{4}He. Liquid helium was forced to evaporate by pumping on the liquid in the cryostat "nose" by a large pumping system. Three 2060H Alcatel mechanical pumps in parallel with each other were the backing pumps in a series of roots blowers (an Alcatel 1000, an Alcatel 3000, and a Balzers 12000), which provided a total of 12000 m^3/hr pumping speed, able to remove $\sim$1.5-2.0 Watts of heat from the target.

Liquid helium was drawn from the magnet dewar through a small transfer line to the separator which, when pumped on, separated liquid and gas phases of helium through a sintered plate, and allowed the liquid to drain into the target chamber as shown in Figure 5.4. Two separate valves were available for filling the target chamber from the separator. In the initial cooldown phase, it was advantageous to deposit the cold gas and any available liquid directly into the target chamber. This was done by the "bypass valve", which ran directly from the separator to the target chamber. The cold gas drawn through the bypass valve cooled the separator, the perforated plate heat exchangers, and the radiation baffles as it was drawn out of the target cavity by the pumps. Once in the normal mode of operations, when some liquid already existed in the chamber, the bypass valve was closed and the "run valve" was used to continue filling and maintaining a liquid level. The run valve connected the separator and the target chamber through a system of heat exchangers which cooled the liquid as it flowed down to the target. Opening the run valve allowed liquid to flow through a tube soldered to the perforated plate heat exchangers. The cold evaporating gas being pumped from the liquid in the nose cooled the plates, which in turn cooled the tube and the incoming helium liquid.

The refrigerator was also equipped with a helium level probe and several temper-

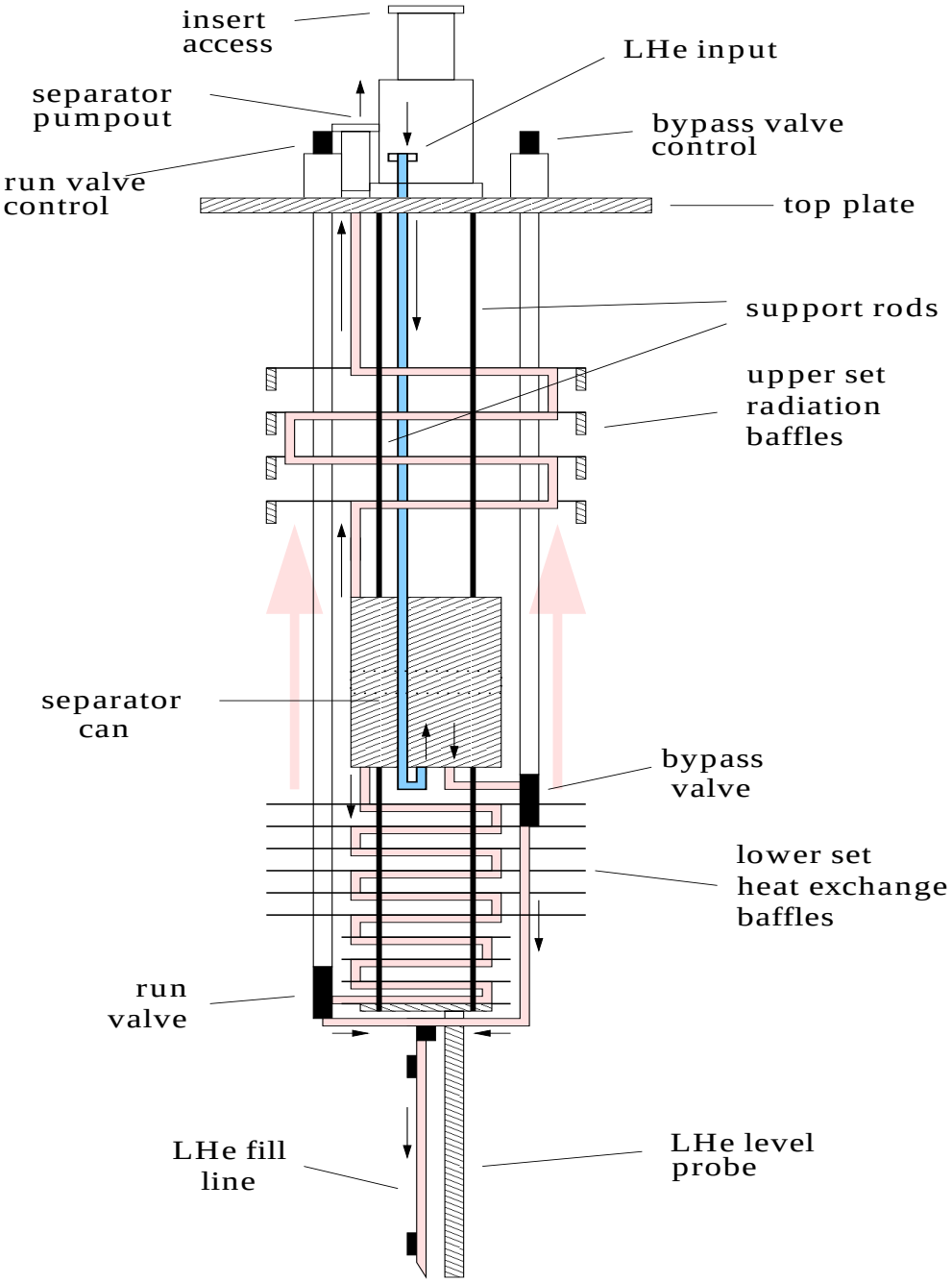

Figure 5.4: Target ^{4}He evaporation refrigerator. Black arrows show the direction of flow of liquid helium through the separator and into the target chamber. The large grey arrows show the direction of gaseous helium as it is pumped out of the refrigerator.

ature indicating devices, including a ^{4}He manometer and RuO_2 chip resistors of 1kΩ, in an assortment of key locations.

5.4.3 Target Insert

The target insert contained the target cavities, into which the target material was loaded. It could be inserted or removed from the system with relatively little disturbance to the magnet and refrigerator. It was inserted into the central bore of the refrigerator, positioning the target cups within the central field region of the magnet. The insert was equipped with microwave waveguides which were used to transmit microwave power, and NMR transmission cables which connected to the Q-meters outside of the refrigerator. The insert also contained copper heat sinks to reduce heat flow to the 1 Kelvin target chamber from the room temperature top plate. Temperature sensors were located throughout the insert for diagnostics.

At the bottom of the insert was the target ladder. This aluminum ladder held a total of five targets: two polarized target material holders, a full sized solid target, a small solid target, and a hole target (See Figure 5.5). Wrapped around the target ladder were two coils of heater wires, a primary and a back-up heater wire, used during the annealing process.

Inside the target cups were the NMR coils. In each target cup there were two coils, a single loop "proton" coil, and a 4-turn "deuteron" coil. The coils were oriented 90 degrees from the field direction for maximum coupling of the RF to the magnetic field. The coils were aligned along the axis of rotation of the magnet so as to maintain this maximum coupling at all magnet orientations. Also located within the target cups were thermocouple junctions. These thermocouple junctions were used to measure the temperature of the material during an anneal. The cups themselves were made of a fluorinated material (PCTFE - Poly-Chloro-Trifluoro Ethylene [71]), called Kel-F, which has no free protons (which would provide an unwanted background proton signal to our NMR signals), is moderately radiation damage resistant, and is easily

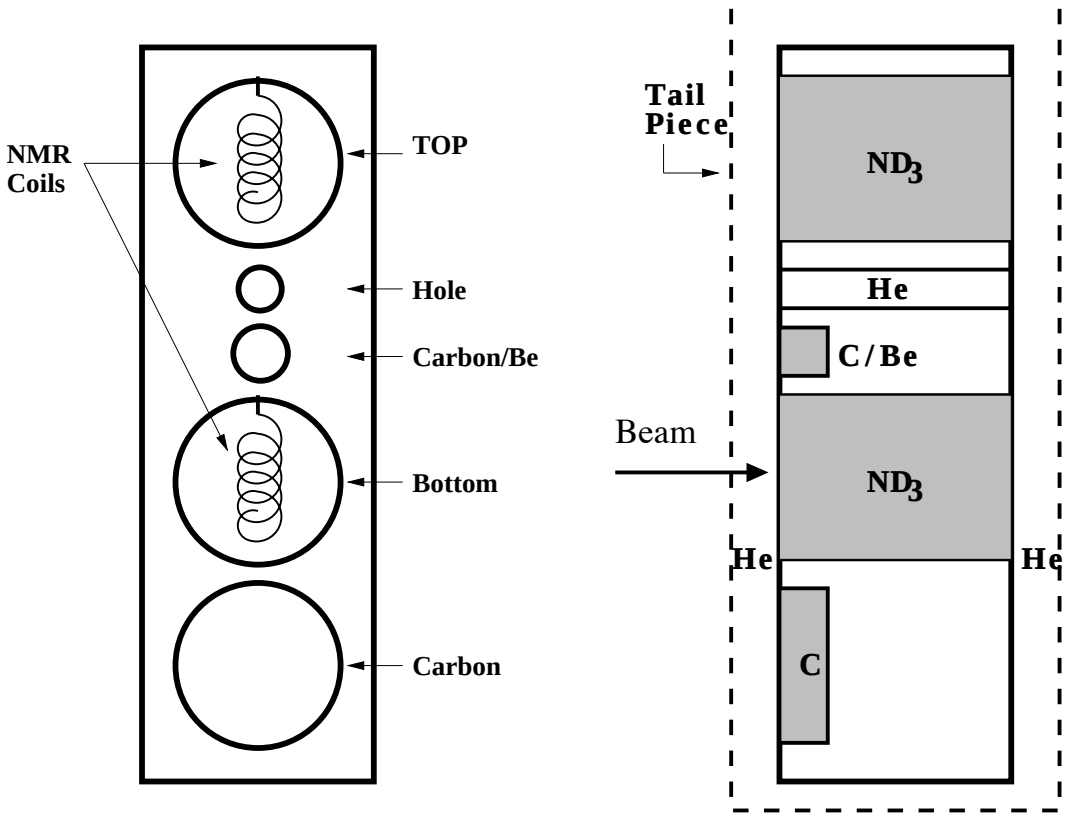

Figure 5.5: Target insert used in E93026

machinable.

A ^{3}He manometer provided the primary temperature measurement as the vapor pressure/temperature characteristics of ^{3}He are well known. A ^{4}He manometer provided redundancy in temperature measurement. As a monitor of target temperature, resistors were placed along the target ladder, outside, but near the target cups.

The insert was attached to the refrigerator by a collar apparatus and a pneumatic powered piston which could raise and lower the target position by raising or lowering the entire insert and microwave table using a stepper motor. A target position encoder, attached to this stepper motor, read the target position to 1/100th of a millimeter.

5.4.4 Microwaves

The microwaves were generated by an Extended Interaction Oscillator (EIO) tube which oscillated at frequencies around 140 GHz (the Larmor frequency of electrons at 5 Tesla) and was tunable over a range of $\pm$ 2 GHz.

The primary method of measuring the microwave frequency of the EIO was by a frequency counter. As a backup for frequency measurement, a harmonic mixer, which sampled the EIO tube frequency with the tenth harmonic of a 14 GHz reference oscillator was also used. The difference between the 10th harmonic of this oscillator and the sampled EIO frequency gave an accurate measurement of the EIO frequency. Attenuators controlled the amount of power into the mixer and into the target cavity, and the power of the microwave radiation was measured by a thermistor. The dimension of the resonant cavity of the EIO was mechanically changed to vary the frequency.

5.4.5 Target Material

Ideally, the target material should be able to polarize as high as possible, have the largest possible fraction of polarizable materials, and be able to withstand large doses of radiation. The target material chosen for this experiment was in the form of frozen ammonia crystals. $^{15}NH_3$ was chosen as the proton material and $^{15}ND_3$ was used as the neutron target material. Frozen ammonia offers several advantages over other target material candidates and is well suited to the experimental environment at Jefferson Lab. First, and one of the most important reasons, is that both $^{15}NH_3$ and $^{15}ND_3$ achieve high levels of polarization. Protons can be polarized to nearly 100%, while deuterons in $^{15}ND_3$ reach well over 40% polarization. Also, frozen ammonia offers a higher dilution factor[2] than other possible polarized target materials by virtue of having a higher percentage of polarizable nucleons.

[2]The dilution factor is the ratio of polarizable materials in the target to all materials in the target. Calculation of the dilution factor will be explained in Chapter 6.

Other candidates for target materials were ^{6}LiD, recently used at SLAC during experiment E155 [72], and alcohols, chemically doped with paramagnetic radicals [73]. In order to achieve high levels of polarization, the target material must contain unpaired electrons which are used to build nucleon polarization. There are two main approaches to implanting radicals in the target material, by chemically doping the material or radiating it with and electron beam. Chemically doped alcohols, such as butanol, used at CERN during SMC [57], have fallen out of favor for use in high intensity beams, because they have much less resistance to radiation, causing their polarization to drop off rapidly and resulting in a lower average polarization over time. Solid ammonia targets are more resistant to radiation damage. Typically, a given target of $^{15}NH_3$ can withstand a dose of 10^{15} e^-/cm^2 before needing to be annealed (a process which "refreshes" the nucleon polarizability), and a dose of 10^{17} e^-/cm^2 before needing to be replaced. $^{15}ND_3$ is even more resistant to radiation and has never needed to be replaced. One of the advantages of ^{6}LiD is that it offers an even higher dilution factor than $^{15}ND_3$. The assumption made at higher energies is that the ^{6}Li nucleus can be approximated as a deuteron plus an alpha particle [74], providing an additional deuteron. However, it has drawbacks in its long thermalization and buildup times. Also, at the energies available at Jefferson Lab, nuclear effects in the ^{6}Li nucleus are a concern as the nuclear properites of lithium are not well understood.

The target material was produced from high purity ammonia gas, slow frozen in a teflon tube cooled by liquid nitrogen. Once the gas was frozen into a solid cylinder, it was removed from the teflon tube and crushed through mesh sieves to get an average crystal size of 1-3mm in diameter. The details of the production process, including freezing, crushing, and storing of the material, can be found in Reference [75]. As provided by the manufacturer, purity of the gas was measured to be greater than 98% ^{15}N and greater than 99% deuteron [76]. Once frozen, the target material was measured to have a density of 1.056 g/cm^3 for $^{15}ND_3$ and 0.917 g/cm^3 for $^{15}NH_3$ [77].

Once the material was prepared, paramagnetic centers must be introduced in order for it to polarize to a high degree. Irradiation by an electron beam creates $^{15}NH_2^-$

radicals when an electron knocks out a proton from an ammonia molecule. The unpaired electron in NH_2^- acts as a paramagnetic center (provided the temperature stays low enough to prevent it from recombining too rapidly). Earlier results showed reasonable success irradiating frozen ammonia targets to achieve high polarization. It has been demonstrated that irradiation under liquid argon for an accumulated dose of up to approximately 10^{17} electrons/cm^2 gives the best results [57, 78].

In March of 1998, both proton and deuteron materials were irradiated at the Jefferson Lab Free Electron Laser (FEL) facility, which was the first ever outside use of the facility. An irradiation cryostat which contained the material immersed in liquid argon, was placed in the beamline. Liquid nitrogen temperature is desired, but it has been shown that irradiating liquid nitrogen with a high intensity beam can cause explosions [79]. A 38 MeV beam of electrons of 2-4 μA, and a circular raster of 0.75 inches in diameter was impinged on the target until the approximate full target dose of 10^{17} electrons/cm^2 was reached. Each target load took approximately 4 to 8 hours to reach this optimum dose [80].

5.4.6 Target Data Acquisition

The target polarization was measured by the NMR system and accompanying computer data acquisition system. As discussed earlier, the main element of the NMR system was the Q-meter RLC circuit. In a 5 Tesla field the resonant frequency for protons is 213 MHz.

The output of the Q-meter was sent to the STAC interface module, which is part of the Q-Curve Acquisition component of the target data acquisition system (see Figure 5.6). The STAC, which stands for Stand-Alone CAMAC Microprocessor System [81], was an intelligent module capable of autonomous operation upon receipt of a set of parameters and commands. The core of the STAC module is an analog to digital converter which adds up the total number of individual sweeps (designated by the operator at the polarization display panel in the counting house) in each frequency

bin. The STAC then sends the sum of the voltages for each bin from all individual sweeps to the target data acquisition computer, which then averaged the signal over the known number of individual sweeps. The total amplification of the NMR system was also divided out so that the result was independent of gain.

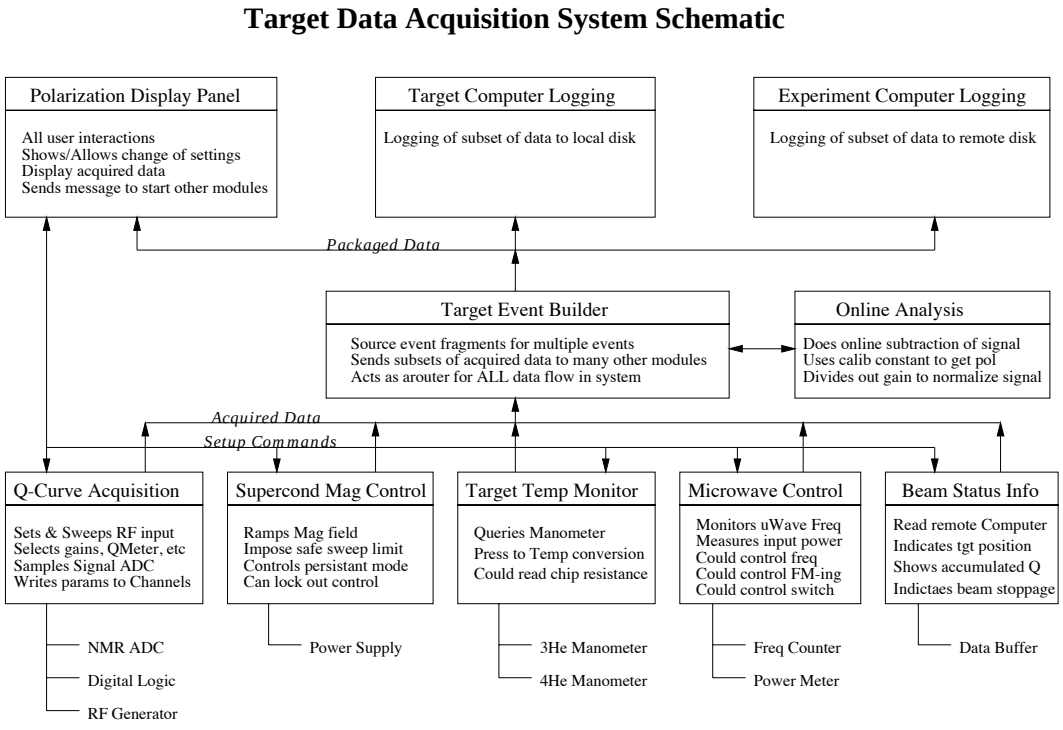

Figure 5.6: Flowchart of target data acquisition system.

Signal amplification occurred in two stages. The signal conditioning (referred to as Yale) cards, which performed the first stage of amplification, were contained in the Q-meter housing and received the phase, diode, and DC level signals directly from the Q-meter. These signals represented the absorptive part of the signal, the total signal, and the DC level of the signal. The Yale cards, before amplification, subtracted a pedestal voltage from the signal to increase the range of possible amplification. This pedestal voltage was obtained by measuring the voltage at a set time after the start of the frequency sweep, optimized to center the response function around zero. The second stage of amplification took place in a NIM amplifier, between the Yale Cards

and the STAC module. Yale gain was set to either 1, 20, or 50, while the NIM amplifiers could add an additional factor of 0.5, 1, 2, 5, or 10. Amplification was set as large as possible for TE signals, with the limiting factor being the ADC range of $\pm$ 5.0 Volts in the STAC. However, a gain setting used for the small TE calibrations could not be used for the enhanced signals, as the enhanced signals would quickly exceed the 5 Volt limit. The uncertainty in the total gain of the system was estimated at less than 0.5%.

The target data acquisition computer ran code generated by Paul McKee [82], written in the software package from National Instruments called LabVIEW. This code received information about each set of frequency sweeps from the STAC. It was more than a passive recorder of data, however. The entire NMR measurement was controlled from this software by setting the frequency, number of sweeps, selecting which NMR coil to activate, and choosing the gain values to amplify the signal. This information, chosen by the operator, was sent to the STAC module and the Rohde & Schwarz RF generator. Upon completion of the designated set of sweeps, the STAC relayed the output to the computer, which then divided out the selected gain, averaged the signal over the number of sweeps, subtracted a baseline signal, performed an online quadratic fit to the residual curve, and then integrated the resulting signal.

The program was also designed to read several other instruments associated with the target. The ^{3}He and ^{4}He manometers were read out and the program computed the temperature from the vapor pressure, displayed it on the front panel of the program, and wrote the values to the data stream. Resistor values, Q-meter temperatures (monitored for stability), microwave frequency, power, and temperature, and many other NMR and target related measurements were read routinely and stored for later analysis and online trouble shooting.

5.4.7 Target Performance

Prior to the start of experiment E93026 in Hall C of Jefferson Lab, both $^{15}NH_3$, and the deuterated form, $^{15}ND_3$, were given a pre-irradiation of 10^{17} e-/cm^2, but still required some "cold dose" to achieve their highest polarization. Pre-irradiation is obtained at liquid argon temperatures, however irradiation *in situ* at 1 K also has a positive impact on the polarization behavior. Without cold dose, deuteron polarization topped out around 15%. Proton polarization could possibly reach the same maximum polarization of 90% or greater with or without cold dose, but the buildup times for material without cold dose were much slower, so the effective level of polarization achieved was lower. The deuteron target, after several cycles of cold irradiation and annealing, achieved polarization above 40%, but this polarization fell when the beam was turned on, due to the added heat load. For the experiment as a whole, the average proton polarization was on order of 80%, however data taken for the $Q^2 = 0.5(\mathrm{GeV}/c)^2$ point averaged only 55%. The average deuteron polarization was 21%. The average polarization was lower than expected due to DAQ problems that coincided with high polarization. Unfortunately, during these times, the beam was left on target, reducing the polarization while no valuable data was being taken. The polarization was also reduced by the heat from high beam currents, sometimes as high as 150 nA. Maximum polarization was normally obtained within 30 minutes, although times varied with the amount of pre-dose the sample had received and with the timing of the beam being turned on.

After approximately 10^{16} electrons, the target polarization decayed to the acceptable lower limit[3], and an anneal of the material had to be performed. The annealing procedure involved the use of an Oxford Intelligent Temperature Controller (ITC-4), which measured the temperature on the outside of the target cavity via platinum resistors. The ITC-4 also provided the current source for the heater wires and used

[3]The lower limit of the target polarization was determined by a figure of merit (FOM), where FOM=(beam current)·(avg. polarization)^2·(data hours), using observed and historical rates of decay for the polarization.

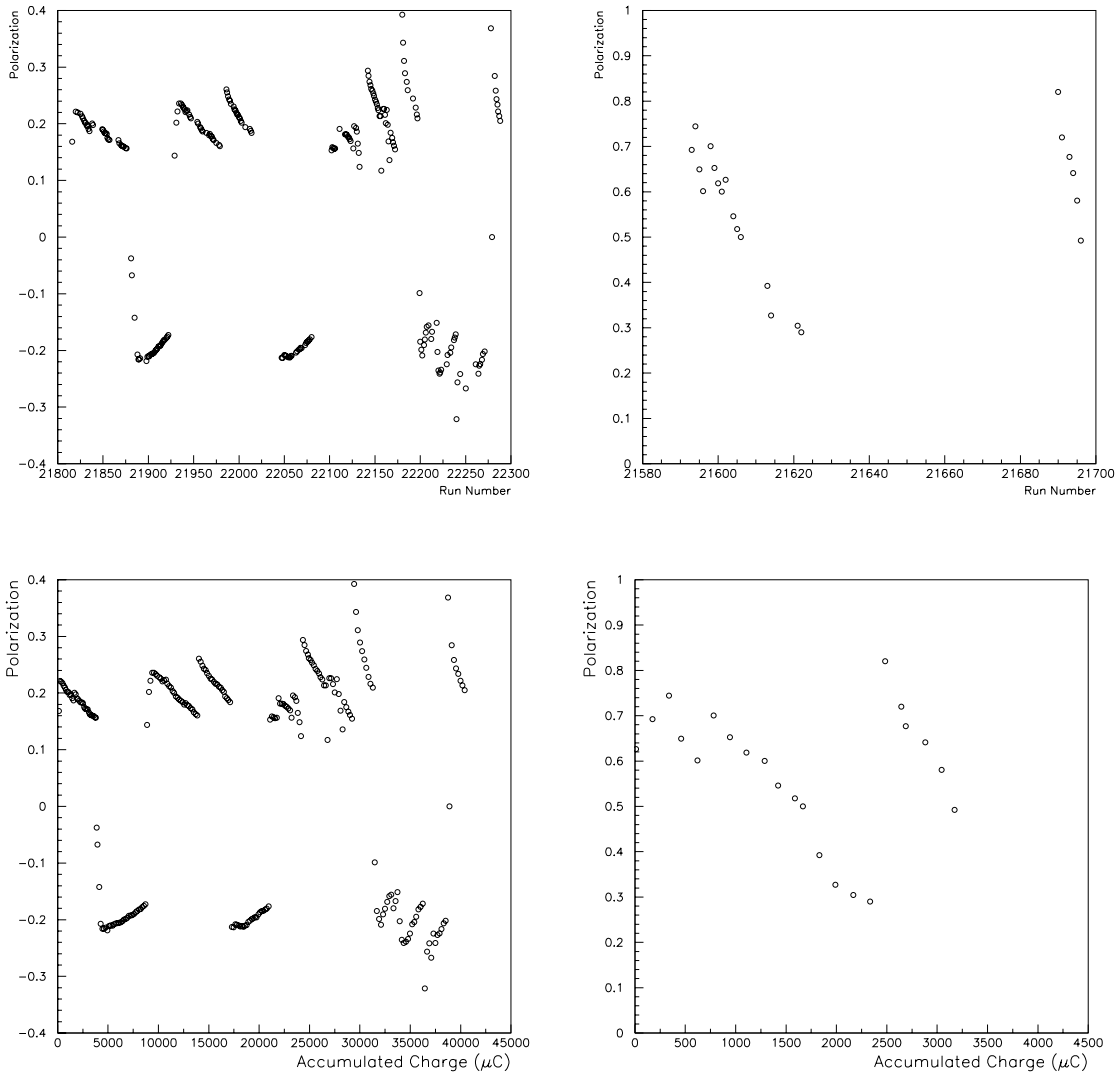

Figure 5.7: History plot of all $^{15}ND_3$ and $^{15}NH_3$ data at Q^2=0.5 $(GeV/c)^2$ as a function of run number and accumulated charge. The top left plot is of $^{15}ND_3$ polarization history, the top right plot is $^{15}NH_3$ polarization history. The two bottom plots are of the deuteron and proton polarization as a function of accumulated charge.

a feedback loop to control the rate of heating according to operator input parameters. For the early part of the experiment, anneals were very successful and produced increasingly higher maximum polarization. When equipment failure required us to replace the ITC-4 with another model, temperature calibrations also changed and were less reliable. This unfortunately resulted in less successful anneals. Annealing at the wrong temperature, whether too high or too low, had undesired effects on the target material. Too high an anneal temperature caused recombination of some (or all) of the original paramagnetic centers, making the material very difficult to polarize. Too low an anneal temperature did not get rid of the excess centers and did not refresh the nucleon polarization. Ideal anneal temperatures were 80 K for proton material and slightly higher, 85 K, for deuteron. Experimentally it was found that annealing at these temperatures for approximately 15-20 minutes yielded the best results.

5.4.8 Target Radiation Characteristic

Solid ammonia has been used in polarized targets since the 1980s. The combination of high polarization, radiation hardness, and density of nucleons has made frozen ammonia a desirable target. Previous experiments at SLAC have put large electron doses on these targets. The behavior of $^{15}NH_3$ and $^{15}ND_3$ in beam has been examined and a quantitative analysis of decay rates has been done [83]. Precise knowledge of decay rates can aid in the planning of an experiment, as the average polarization has a significant impact on the amount of effective data taken per hour of beam time.

The measure of decay used was the radiation characteristic (RC) as defined by Crabb & Meyer [73]. It is the flux of 10^{14} particles/cm^2 through the target which reduces the polarization by e^{-1} of its initial value:

$$P = P_0 \cdot exp(\frac{-\Delta Q}{RC}) \ . \tag{5.15}$$

Qualitatively, $^{15}NH_3$ is known to have two separate decay periods, an early fast decay, and a late slow decay (see Figure 5.9). Over successive anneals, the rates of both decay

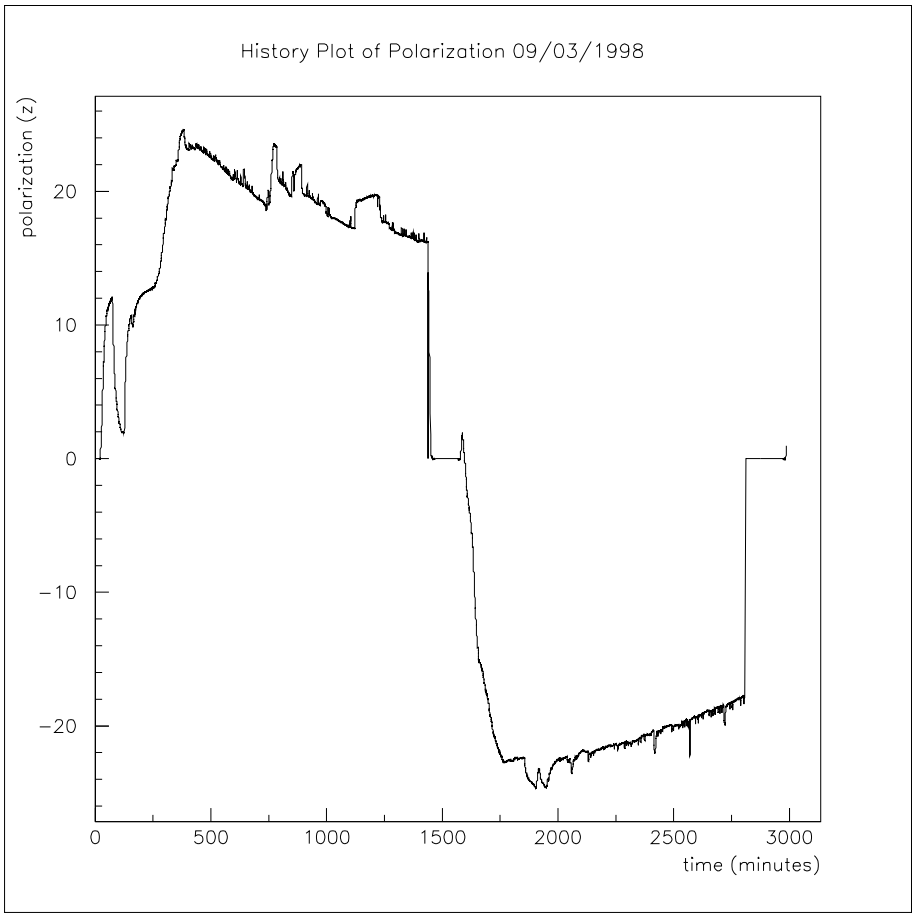

Figure 5.8: Buildup and decay of positive and negative deuteron polarization. Sudden jumps in the polarization were caused by intermittent beam on/beam off conditions where the target polarization reacts quickly to the change in temperature.

regions increase as a function of accumulated charge, until the polarization can no longer be recovered by annealing. Using recent data from experiment E155x at SLAC, values for these early and late decays were determined over a range extending out to $800 \cdot 10^{14}$ electrons of accumulated charge. The value for the radiation characteristic for both the early and late periods dropped linearly over this range (a drop in RC indicates an increase in the decay rate). The values for the radiation characteristics for both periods can be found in Table 5.2. It is interesting to note that the late RC is roughly twice the value of the early RC throughout the range of accumulated charge. The values compare favorably to the values stated by Crabb & Meyer, whose

values fall almost exactly in line with the data from E155x [84].

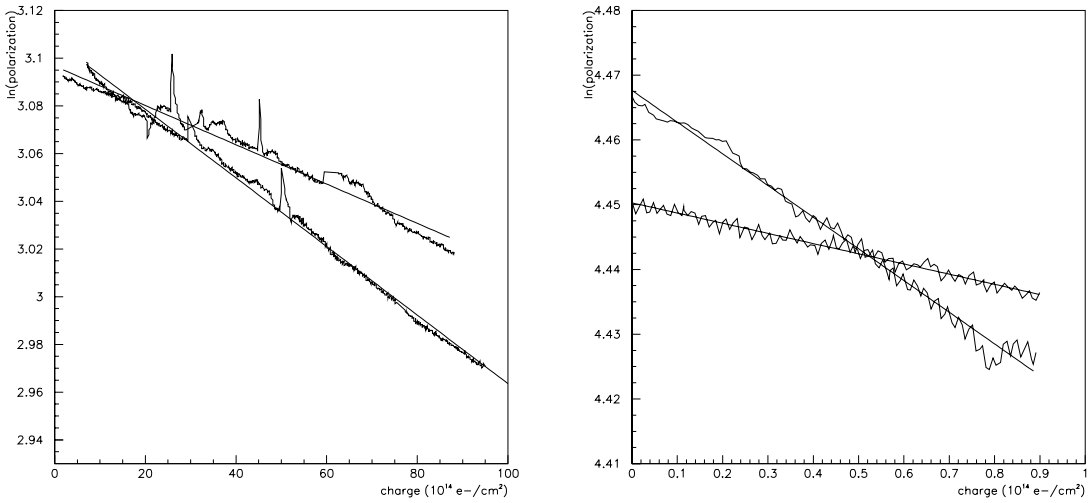

Figure 5.9: Deuteron and proton decay rates. The decay of negative deuteron polarization (above left) is two times slower than the decay of positive deuteron polarization. Proton polarization (above right) from the early period is two times faster in decay rate than late period proton decay. In the plot of the proton polarization decay, the late period decay has been shifted to overlap the early period data for comparison sake.

The decay of $^{15}ND_3$ in beam is well approximated by a single exponential decay. To date, $^{15}ND_3$ has never failed to recover its polarization after many anneals despite the accumulation of charge in excess of that for which $^{15}NH_3$ is unrecoverable. In fact, $^{15}ND_3$ seemed to show a slight radiation hardening with accumulated dose. However, deuterated ammonia exhibited an intriguing behavior in that the decay of positive polarization was much faster than the decay of negative polarization (Figure 5.9). It is unclear why this was so, but the difference was nearly a factor of two. At Jefferson Lab, a range of high electron currents, from 80 nA to 150 nA was used, and the decay rate showed a definite dependence on beam current. At 150 nA, the RC for both positive and negative polarization dropped by 30% from their values at 80 nA. This current dependence, as well as the difference between positive and negative polarization, must be taken into account in determining running conditions for an

experiment. The values for deuteron positive and negative decay rate are listed in table 5.3 and also compared favorably to the results of Crabb & Meyer.

Table 5.2: $^{15}NH_3$ radiation characteristics

Data Source	Early RC	Late RC
Crabb&Meyer	70	175
E155x 'fresh'	150	300
E155x 'used'	50	100

Table 5.3: $^{15}ND_3$ radiation characteristics

Current Range	Positive RC	Negative RC
Crabb&Meyer (80-90 nA)	130	260
80-95 nA	159 ± 22	249 ± 19
95-115 nA	153 ± 11	262 ± 8
115-125 nA	143 ± 8	————
140-155 nA	110 ± 24	175 ± 30

5.5 Off-line Signal Analysis

After the experiment, the thermal equilibrium data, which determined our calibration constants for the run, were studied in detail. The small signal to noise ratio under TE conditions requires very stable operating conditions in order to perform the measurement within acceptable uncertainty. Due to the unpredictable nature of running conditions, this experiment did not always adhere to these necessary standards, resulting in a less than ideal collection of TE measurements. A software routine (a "vi" in the LabView package) was written to view each individual TE signal to look for signs of aberrant noise or obvious misfitting of the signal. Signals that could not be fit with the standard fit parameters were eliminated from the set of data used to determine the calibration constant. Different fits to the wings of the subtracted signals were tried against the set of data, using different limits of integration and fit orders in the fit to the wings of the signal. The set of fit parameters which produced the

lowest χ^2 per degree of freedom on the fit (while also visibly fitting the proper region) were chosen for the set of data in question. The value of χ^2 per degree of freedom for a good fit, using a quadratic fit equation, was consistently below 1.0. Using these parameters, each polysubtracted signal was integrated and the area and temperature were recorded. With this new set of offline analyzed signals, a new calibration constant was calculated. Fluctuations in calibration constant from these different fits were small (and negligible when compared to the statistics of this experiment). Correction factors for each run (see Appendix D) were stored in a database file used by the analyzer.

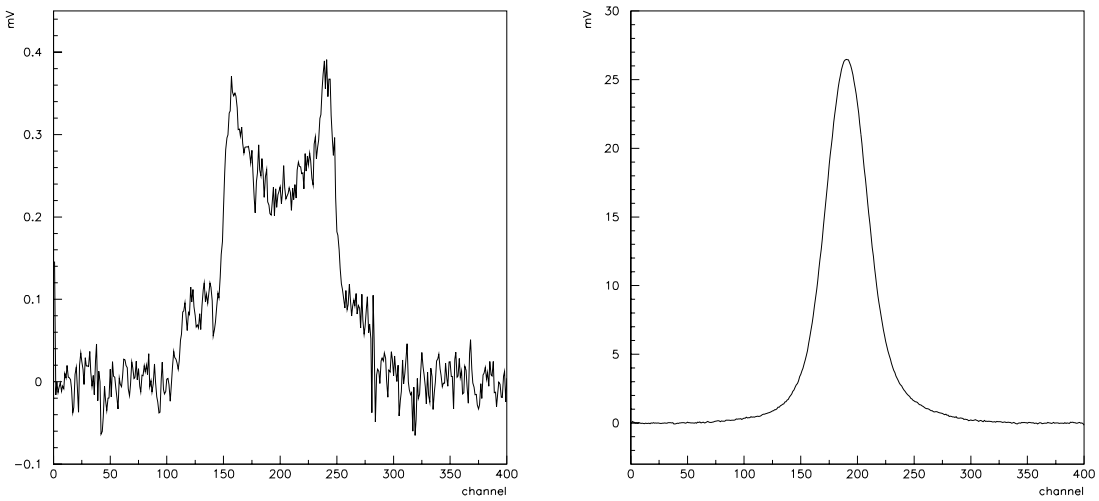

Figure 5.10: Deuteron and proton TE signals. The signal size of the proton TE makes it much easier to measure with great accuracy.

While corrections to the TE calibrations are linear and easily corrected, there were also non-linear effects that needed to be considered. The tune of the NMR system was susceptible to drifts due to temperature change in system components which could result in poor subtraction of raw signal from the baseline signal. This in turn could lead to a potentially poor polynomial fit to the wings of the subtracted signal which could yield incorrect polarization measurements for enhanced signals. A closer

analysis of the baseline subtractions was performed and better (and more rigorous) fit parameters were chosen to reduce this error. A Labview vi was created to read in the original data files and refit the enhanced signals with the same fit parameters as the TE and reintegrate the resulting polysubtracted signals. The correction due to refitting of these enhanced signals was less than 1%, well within both the statistical and systematic uncertainties in the target polarization.

5.5.1 Target Polarization Uncertainty

The statistical error for each calibration constant can easily be calculated. The equation for the calibration constant (Eqn. 5.14) is a function of area and temperature, so contributions from both temperature and area add in quadrature:

$$\left(\frac{(\Delta CC)_{stat}}{CC_{stat}}\right)^2 = \left(\frac{\Delta T}{T}\right)^2 + \left(\frac{\Delta A}{A}\right)^2 . \tag{5.16}$$

This error is between 1 and 2% for most deuteron TE calibrations, and less than 1% for proton TEs since the uncertainty is area is much smaller in the large proton TE signals (see Figure 5.10).

However, there is another factor that must be included to represent the change in packing density around the coils that can change the filling factor. This change in filling factor can alter the area to polarization ratio determined at thermal equilibrium. This filling factor can change at any time and affect the polarization during a run. A single calibration constant cannot capture this effect. More detailed studies need to be done to help determine how the calibration constant changes over time and what affects the filling factor the most (beam, anneal, time, etc). Studies done during E143 point to a 2-3% uncertainty due to the change in filling factor [78]. However, there is insufficient calibration data from this experiment to perform such systematic studies of the in-beam behavior of the target material. For this reason, it was decided to calculate an overall polarization error based on the fluctuation of individual TE

calibrations taken over time. This method captures the statistical and systematic effects sufficiently.

The first step in this process was to pare down all of our calibration constants to those that were the most stable and most accurate, excluding points that were clearly not yet thermalized. Each set of calibration data was examined to observe rate of change of area and temperature. In most cases the remaining calibrations were all sufficiently thermalized. However, there were some cases where the temperature, and thus area, was fluctuating due to the nature of the filling cycle of the magnet helium supply. This was an unavoidable consequence of the filling method and equipment in Hall C. Due to time constraints, some data points which represented our only measure of the target polarization for a large set of runs were taken under less than optimal conditions. We could not exclude this data however, since it was our only measure of the polarization.

Grouping	CC	CC error
Sept	0.9153	0.0081
	1.0057	0.0057
	1.0921	0.0090
Oct.	1.0052	0.0098
	0.9598	0.0207
	1.0032	0.0090

Table 5.4: $^{15}ND_3$ calibration constants and associated error are renormalized to the mean of each grouping.

To estimate fluctuations in calibration constants, the two sets of deuteron data taken wholly within a single day without the interruption of beam or annealing were initially examined. Each of these groups was normalized to the weighted average value of the group. The weighted averages were normalized to 1.0 and the fluctuation about 1.0 was used to determine the standard deviation (see Table 5.4). Data taken with the VXI system had unknown sources of noise which disrupted TE signal measurements. These TEs were not used during data taking and subsequently the measurements were not included in the estimation of uncertainty. The error in any one point in

the remaining group is the standard deviation of the entire sample. The standard deviation of these six renormalized points was 0.0588. This 5.88% standard deviation could then be taken as the total uncertainty on the deuteron polarization, which accounted for both statistical and systematic error in the data.

Grouping	CC	CC error
Jul.	1.0184	0.0010
	0.9998	0.0001
Aug.	0.9884	0.0009
	1.0065	0.0007
Nov.	1.0045	0.0005
	1.0174	0.0005
	0.9973	0.0004
	0.9733	0.0006

Table 5.5: $^{15}NH_3$ calibration constants and associated error are renormalized to the mean of each grouping.

Data for the proton target, $^{15}NH_3$, was slightly more plentiful and allowed for better analysis of systematics (see Table 5.5). A total of eight data points were used in three groupings to determine the total uncertainty of the proton target. Using the same method outlined above for the deuteron target, a total uncertainty in the proton polarization was determined to be 1.49%. Table 5.6 summarizes the polarization uncertainty for each spin species for experiment E93026.

Species	Polarization Uncertainty
Deuteron	5.88 %
Proton	1.49 %

Table 5.6: Target polarization uncertainty

Appendix D contains the final TE values and the corresponding correction factors. Appendices E and F contain the individual area and temperature measurements that make up each deuteron and proton TE measurement.

Chapter 6 Event Selection

6.1 Introduction

This chapter will discuss the process of reducing the raw data files into ntuples from a set of selected runs. Details of the cuts placed on the data will be included, as will explanations of the corrections applied to the data. A summary of the final set of cuts is included at the end of this chapter and a list of all good runs for each target type is provided in Appendix B.

6.2 Data Reduction

Raw data tapes were analyzed directly and the results were written to scaler files and PAW[1] ntuples. Various cuts could be applied to the data without having to reanalyze the raw data tapes when ntuples were used. The analysis code wrote in ntuples event information such as focal plane coordinates and reconstructed quantities. It also wrote to scaler files run averaged information, including the charge-weighted average target polarization, accumulated charge, and deadtime information.

Experiment E93026 did not have a pure single arm counter. Events were registered as coincidence events or non-coincidence events. However, a true singles rate was the combination of these two subsets of events. Unfortunately, triggers for each event type were handled differently and therefore had different deadtimes and prescale factors. Handling this was further complicated by the necessity of separating events of positive and negative helicity. Instead of one rate for the singles, with one deadtime and

[1]PAW, developed at CERN, is an interactive utility for analyzing experimental data on a computer graphics display. An ntuple is a database containing common data structures for each event in the data.

one charge measurement, there were four separate rates that needed to be added together properly: coincidence/positive helicity, coincidence/negative helicity, non-coincidence/positive helicity, non-coincidence/negative helicity.

6.3 Run Selection

Not all data runs recorded were deemed usable for this analysis. Runs were excluded for a variety of reasons, including data acquisition problems, poor HMS or neutron detector performance, poor beam quality, and target data acquisition problems. Restriction of the pool of available runs to those which did not have uncorrectable problems left less than 30 runs of $^{15}NH_3$ data. After all cuts to the data, this collection of runs provided 1458015 non-coincidence events and 2435539 coincidence events from 3636.7 μC of charge through the target.

6.4 Event Analysis

Reconstruction of electrons in the HMS allowed us to eliminate events that did not originate in or near (within our resolution) the target. A cut on the raster radius allowed us to restrict the incident electrons to those which fell well within the edges of our target cup. Particle ID cuts let us remove pions (π^-) from our data sample.

6.4.1 Coordinate Systems

There are two coordinate systems of interest in this analysis: the coordinate system of the laboratory frame, and the HMS transport coordinate system. These coordinate systems are illustrated in Figure 6.1. In the lab frame, the z axis is chosen to be along the incident beam direction, with the x axis in the vertical direction ($+x$ points down toward the floor) and the y axis in the horizontal direction (with $+y$ pointing left when looking downstream, governed by $\hat{y} = \hat{z} \times \hat{x}$). The HMS coordinate system

is rotated about the x axis of the lab frame to have the z' axis pointing along the central optical axis of the HMS. The x' axis again points down and $\hat{y}' = \hat{z}' \times \hat{x}'$.

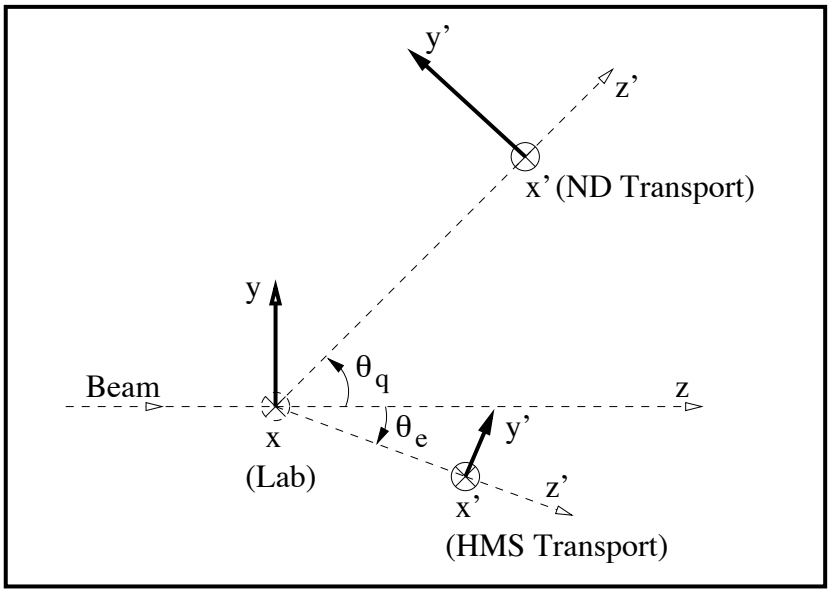

Figure 6.1: E93026 coordinate systems. The neutron detector transport coordinate system was used in the double-arm analysis [85], but was not used in the single-arm analysis.

6.4.2 Event Reconstruction

Reconstruction of charged particles through the HMS was accomplished by transporting the known focal plane quantities to the target through the spectrometer magnets and the field of the target magnet. The standard HMS reconstruction had to be modified to account for the effect of the beam raster and the E93026 target magnet.

Standard HMS Reconstruction

Events that passed through the focal plane of the HMS, defined as the midpoint between the two wire chambers, had location and direction information in the form of focal plane quantities x_{fp}, y_{fp}, x'_{fp}, and y'_{fp}. x_{fp} and y_{fp} are the coordinates of the hits, and x'_{fp}, and y'_{fp} give trajectory information. x'_{fp} and y'_{fp} are often referred

to as angles but are actually the rate of change of x_{fp} and y_{fp} with respect to z_{fp}. From these values, information about the interaction point could be determined from reconstruction through the HMS magnets. Target quantities y_{tar}, y'_{tar}, x'_{tar}, and δ, which is the percent difference of the reconstructed momentum from the spectrometer central momentum, can be expressed in terms of the focal plane quantities and the reconstruction matrix coefficients $\mathbf{M}_{jklm}$ [86].

$$q^i_{tar} = \sum_{jklm} \mathbf{M}^i_{jklm} (x_{fp})^j (x'_{fp})^k (y_{fp})^l (y'_{fp})^m \ , \tag{6.1}$$

where $q^{1,2,3,4}_{tar}$ are the reconstructed quantities x'_{tar}, y_{tar}, y'_{tar}, and δ respectively, and

$$\mathbf{M}^i_{jklm} = < q^i_{tar} | x^j_{fp} x'^k_{fp} y^l_{fp} y'^m_{fp} > \ . \tag{6.2}$$

In the standard reconstruction, the assumption of no vertical beam offset is necessary to obtain δ. These reconstruction coefficients were calculated using COSY INFINITY which was used to model magnetic components of the spectrometer. Calibration of these matrix elements was done by using the sieve slit during elastic scattering from a carbon target. These calibrations were done previous to E93026 and the details can be found in the thesis of D. Dutta [86].

Treating the Vertical Beam Offset

The standard HMS reconstruction assumes no vertical beam offset. However, the slow raster in E93026 gave vertical offsets in the beam position at the target of up to 1 cm. Since the HMS is vertically dispersive, offsets in the vertical direction cannot be distinguished from shifts in δ, where a 1 cm offset results in about a 1% shift in δ. This was corrected by a scheme that uses slow raster position information to correct the focal plane quantities for this offset. After this correction, the standard HMS reconstruction could be performed.

The correction of the vertical beam offset is as follows:

1) Apply the standard reconstruction matrix, $\mathbf{M}$, to the focal plane quantities to get a first estimate of the target quantities:

$$|x_{tar}=0, x'_{tar}, y_{tar}, y'_{tar}, \delta >_{i=1} = \mathbf{M}|x_{fp}, x'_{fp}, y_{fp}, y'_{fp} > \ . \tag{6.3}$$

2) Apply the forward transport matrix, $\mathbf{F}$, to the target quantities for x_{tar}=0 and x_{tar}=$x_{raster} - zx'_{tar}$ to get the *deviation* in focal plane quantities caused by the vertical beam offset.

$$\begin{aligned} |dx_{fp}, dx'_{fp}, dy_{fp}, dy'_{fp} >_i \ &= \ \mathbf{F}|x_{tar} = x_{raster} - zx'_{tar}, x'_{tar}, y_{tar}, y'_{tar}, \delta >_i \\ &\quad -\mathbf{F}|x_{tar}=0, x'_{tar}, y_{tar}, y'_{tar}, \delta >_i \ . \end{aligned} \tag{6.4}$$

The correction zx'_{tar} is applied to the raster position to account for the offset due to the z coordinate of the intersection point.

3) Apply $\mathbf{M}$ to the corrected focal plane quantities for a better estimate of the target quantities:

$$|x_{tar}=0, x'_{tar}, y_{tar}, y'_{tar}, \delta >_{i+1} = \mathbf{M}|x_{fp} - dx_{fp}, x'_{fp} - dx'_{fp}, y_{fp} - dy_{fp}, y'_{fp} - dy'_{fp} > \ . \tag{6.5}$$

4) Repeat steps 2 and 3 until δ converges:

$$|\delta_i - \delta_{i+1}| < \epsilon \ , \tag{6.6}$$

where $\epsilon = 0.0005$. This procedure is referred to as $\mathbf{V}$, the vertical beam offset procedure, in later sections.

This procedure has drawbacks which include having to use the forward map $\mathbf{F}$, which is not a standard part of the HMS reconstruction package. Also, this procedure is only valid in a field free region. Reconstruction through the target field will be discussed in the next section.

Reconstruction through the Target Magnetic Field

The following procedure was developed to reconstruct the events through the target magnetic field. It also includes the effect of the vertical beam offset by incorporation of the routine **V** described above.

1) Apply the procedure **V** to obtain the first estimate for the target quantities:

$$|x_{tar} = x_{tar_0}, x'_{tar}, y_{tar}, y'_{tar}, \delta >_{V,i=1} = \mathbf{V}|x_{fp}, x'_{fp}, y_{fp}, y'_{fp}, x_{tar_{0,i=1}} = x_{raster} > \quad . \tag{6.7}$$

2) Drift out to the field free region (z=100 cm), since **V** is only valid in field free regions.

3) Transport through the target field to the intersection with the beam to get the first estimate for real target quantities:

$$|x_{tar}, x'_{tar}, y_{tar}, y'_{tar}, z_{tar}, \delta >_{i=1} = \mathbf{RK}|x_{tar} - zx'_{tar}, x'_{tar}, y_{tar} - zy'_{tar}, y'_{tar}, z_{tar}, \delta >_{V,i=1} \ , \tag{6.8}$$

where **RK** represents the Runge-Kutta integration performed to transport the event through the target magnetic field.

4) Transport to the z_{tar}=0 plane to get a better estimate of the beam offset:

$$x_{tar_{0,i=1}} = (x_{raster} - (x_{tar_i} - x_{raster})) - z_{tar_i} x'_{tar_i} \ . \tag{6.9}$$

5) Apply **V** to get corrected focal plane quantities with corrected beam offsets to get an estimated set of target coordinates.

$$|x_{tar} = x_{tar_{0,i+1}}, y_{tar}, y'_{tar}, \delta >_{V,i+1} = \mathbf{V}|x_{fp}, x'_{fp}, y_{fp}, y'_{fp}, x_{tar_{0,i+1}} > \quad . \tag{6.10}$$

6) Drift out to z=100 cm and transport back into target field (by **RK**) to get a

better estimate for the real target quantities:

$$|x_{tar}, x'_{tar}, y_{tar}, y'_{tar}, z_{tar}, \delta >_{i+1} = \mathbf{RK}|x_{tar} - z x'_{tar}, x'_{tar}, y_{tar} - z y'_{tar}, y'_{tar}, z_{tar}, \delta >_{V,i+1} \ , \tag{6.11}$$

7) Repeat steps 4-6 until the reconstructed value for the target x position converges to the input raster x position,

$$|x_{tar_{i+1}} - x_{raster}| < \epsilon \ , \tag{6.12}$$

where ϵ in this routine is 0.2 mm.

More detail on these procedures for treating the vertical beam offset and target magnetic field can be found in reference [87]. Tests of these procedures were performed by Markus Muehlbauer in Monte Carlo, previous to the experiment. Events were generated across the entire phase space of the HMS and the entire target volume. Resolution was determined by comparing the original target coordinates with the reconstructed coordinates. The resolutions in δ, x_{tar}, y_{tar}, z_{tar}, x'_{tar}, and x'_{tar} are listed in Table 6.1. It is important to note that the resolutions listed in the table do not take into account the effects of radiation or variation in beam energy.

Variable	Resolution (FWHM)
δ	0.1%
x_{tar}	0.1 mm
y_{tar}	2.0 mm
z_{tar}	5.0 mm
x'_{tar}	0.20°
y'_{tar}	0.04°

Table 6.1: Resolution of reconstructed target quantities.

A possible problem in the reconstruction through the target field was discovered after the experiment. The reconstruction of the invariant mass, in the data, was dependent upon the position of the raster. Invariant mass is a measure of the mass of the particle from which the electron is scattered, and therefore should not be

dependent upon raster position. Invariant mass is determined by the mass of the nucleon (or other scattered particle), the electron energy loss, and the scattering angle, $W^2 = M^2 + 2M\omega - Q^2$. Events in the bottom of the raster were reconstructed in a sharper peak and at a slightly lower value of invariant mass (see Figure 6.2). Events from the top of the target had a wider distribution and were shifted higher in W. The target field, which bends outgoing electrons down, could be creating a bias between events from the top and bottom of the target. Only the higher momentum electrons from the bottom of the target make it to the collimator, whereas lower momentum electrons from the top of the target cleared the slit to enter the spectrometer. This possibly explains the *shape* difference (although attempts to use Monte Carlo routines to predict this effect are inconclusive). The shift in *energy* between the top and bottom of the target may be explained by the raster calibration. Calibration of the raster ADC by the SEM is imperfect and small variations in the slope of the calibration (please refer to Section 4.4.6) lead to shifts in the reconstructed invariant mass. This procedure should be improved for the next running of this experiment.

6.4.3 Tracking Cuts

A cut on the physical dimension of the target cavity was applied in the form of a cut on the raster radius (discussed later) and a cut on y_{tar}, the horizontal component of the target position. If the scattering angle were 0°, then the HMS views the 26 mm horizontal dimension of the target cup, however, at 15.7°, the HMS saw 27 mm of the target in the y-direction. Therefore, a cut of $|y_{tar}| <3$ cm was applied to the data. The vast majority of events come from within 1 cm of center of the target, so the 3 cm cut was applied to eliminate any events that originated far from the target, without losing the good events originating from the target. Figure 6.3 shows the y_{tar} distribution for run 21596. Of the 444188 hits in this run, 97.5% of them fall within the $\pm$ 3 cm cut. Of the other 11070 hits, 7949 of the events were pathological, reconstructing at $y_{tar} = 100.0$ cm. The other 3121 hits (or 0.7% of the total hits)

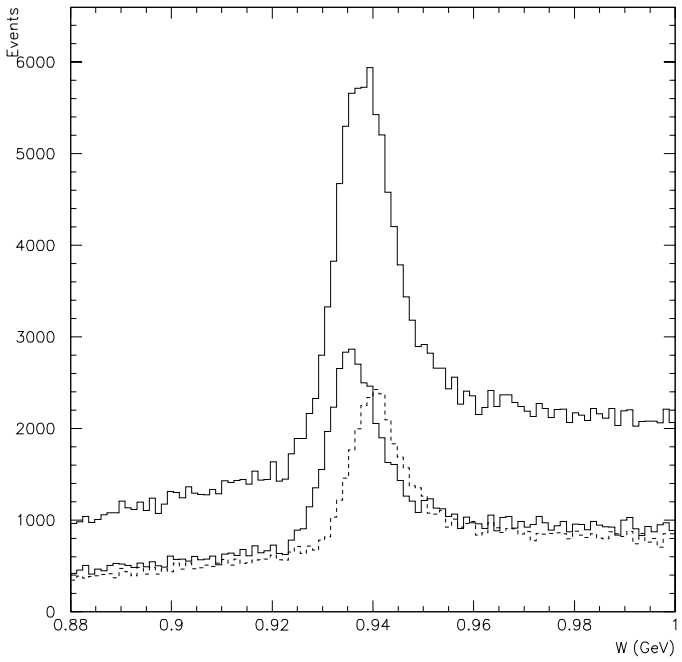

Figure 6.2: Difference in reconstructed invariant mass with raster position. The W peak from the top of the target (dashed line) is wider and shifted higher in W than the peak from the bottom of the target (small peak with solid line). The large solid line peak is the sum of the top and the bottom.

came from the extended wings of the y_{tar} distribution.

The quantities y'_{tar} and x'_{tar} are often referred to as the in-plane and out-of-plane scattering angles. This is true in the small angle approximation, however, they are really the rate of change of the horizontal and vertical target components with the z-direction, $\frac{dy_{tar}}{dz}$ and $\frac{dx_{tar}}{dz}$. The aperture of the HMS collimator is octagonal and the extremes of the opening were 4.74 cm in the horizontal direction and 12.08 cm in the vertical direction (as shown in Chapter 4). The cuts on scattering angle were chosen to exclude any events that come from outside this region. The target field bent all negatively charged particles towards the floor. Particles that otherwise would have had trajectories above the acceptance of the collimator were bent into the HMS by the field of the target magnet. The net effect was a shifting the centroid of x'_{tar} away from

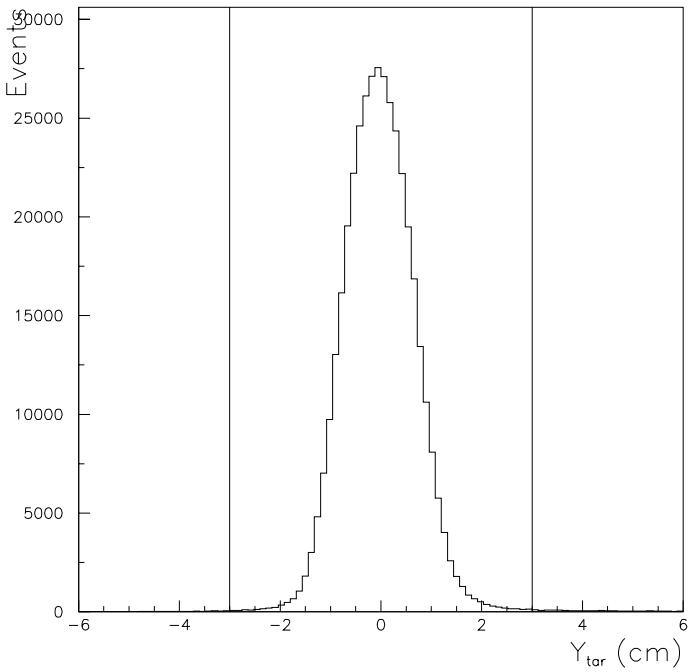

Figure 6.3: Distribution of events in y_{tar}. The distribution of events shown is with all cuts from this chapter applied to the data.

zero by 5 mrad (see Figure 6.4). Cuts on this variable were therefore also asymmetric about zero.

6.4.4 Trigger Efficiency

Hodoscope inefficiencies in the HMS could have led to missed triggers. Each plane of hodoscopes had an inefficiency which could cause the plane to not fire. The efficiency of each scintillator was determined by taking tracks that point to the center of the paddle and determining how often each paddle fired. The requirement for a trigger was that at least 3 of 4 planes must have fired. Individual efficiency of each plane was roughly 99%, giving this 3 of 4 cut an efficiency of approximately 97%. Values for this efficiency factor ranged from 96% to 99% on a run-by-run basis. The effect of trigger efficiency was included in an overall efficiency factor for each run, folded in

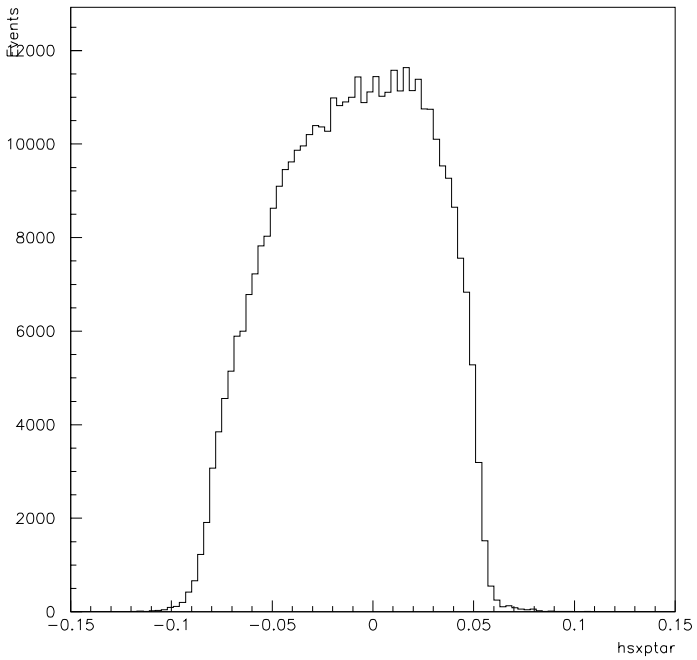

Figure 6.4: Distribution of events in x'_{tar}. The centroid of the events is shifted away from zero by the target field. The distribution of events shown is with all cuts from this chapter applied to the data.

with computer deadtime and fiducial efficiency.

6.4.5 Fiducial Efficiency

When a trigger was generated, all of the information from the HMS was stored and used to determine several things about the event, such as momentum, direction, and particle identification. This information was used to track the particle back to the target. However, not all triggers could be adequately tracked back to the target. The tracking efficiency was the ratio of the number of events for which a track could be found to the number of "good" electrons. "Good" events were a subset of all triggers for which the particle was forward-going (not a cosmic) and had less than 15 hits in the wire chambers. A chamber with more than 15 hits was assumed to

be a good event with additional "noise" which makes tracking difficult. If both wire chambers had more than 15 hits, the "noise" was generated by electrons scraping against the spectrometer magnets, which were outside the acceptance. These events were not considered in the tracking efficiency. However, since the hodoscope planes were larger than the wire chambers, events that qualified as a trigger may not have had a valid track. We therefore could not use tracking efficiency, as defined above, as a measure of how effectively we formed tracks from our given hits. The hit in the hodoscope could lie outside the wire chambers and never form a track, even though it was associated with a trigger. By limiting the number of triggers to those electrons that also passed through the wire chambers, we effectively made a fiducial cut that restricted the geometry of events that entered the spectrometer. If our wire chambers worked at 100% efficiency then we would have found a track for every trigger that passed through them. However, this was not the case. Fiducial efficiency was then defined as the number of tracks found divided by the number of "good" triggers, the triggers that also passed through the wire chambers. The fiducial efficiency varied between 95-98 % over the experiment.

6.4.6 Raster Cuts

Unlike most Hall C experiments, this experiment required a large raster radius. To preserve the target material and limit damage from an intense beam spot, two rasters were applied to the beam before it hit the target. A fast raster spread the beam over a 2 mm diameter to blur the beam spot (see Section 4.4.4). In addition, a slow raster spread the beam across the face of the target, out to a radius of 1cm, at a rate of 1Hz. During the experiment there were some concerns of incorrect steering of the beam and/or misalignment of the target cavity, as evidenced by clipping of the edge of the target cavity with the beam. Figure 6.5 is a plot of events in x_{tar} vs. y_{tar} which shows possible signs of clipping on the upper left-hand side of the target cell. The event rate at the large radius limits of the raster were ordinarily higher than the middle,

however, the disparity in event rate between left and right sides of the cavity indicate more than the normal raster pattern (overall underweighting of rates at the top of the target is due to settling of the target material). This was confirmed by visual inspection of the target cell which showed radiation damage on the upper left-hand edge. For this reason, cuts to the x and y amplitude of the slow raster were applied, so that events which originated from electrons hitting the cell wall are excluded from the data set.

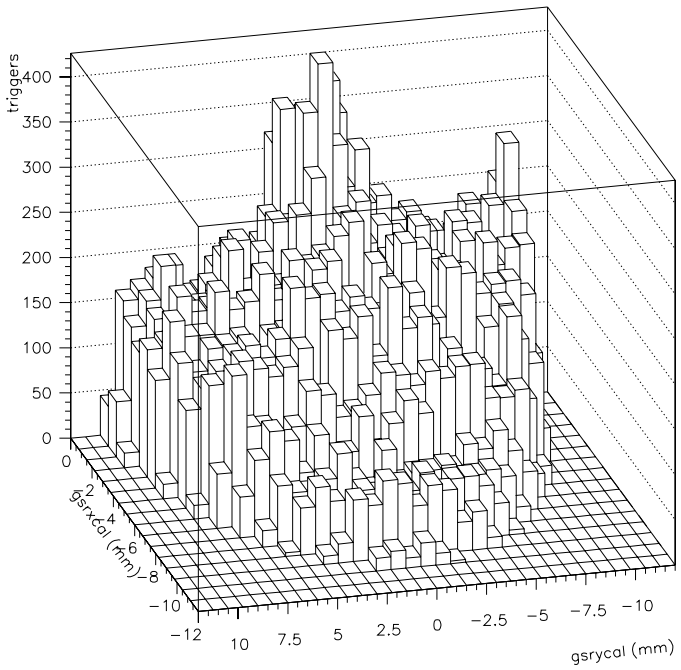

Figure 6.5: Evidence of rastered beam clipping the edge of the target cavity. The top half of the target raster is shown. The edge of the raster on the right hand side of the plot is higher than the left hand side. In general, the outer edge of the target and the center of the target received a disproportionate amount of the beam. The top most section of the raster distribution is depleted due to settling of the target material. The raster trigger distribution shown is from data run 21593.

6.4.7 Particle ID

To eliminate pion contamination in the event sample, a cut on the number of photoelectrons detected in the Čerenkov was implemented in software. Pions can produce a Čerenkov signal if they produce knock-on electrons with sufficient energy. Detected knock-on electrons from pions are created in the window of the Čerenkov detector. A cut at 3 photoelectrons, with a cut on the shower counter energy at one-quarter of the scattered electron energy, was sufficient to reduce pion contamination to effectively zero. The Čerenkov cut was responsible for eliminating 1 in every 1000 events, while the shower counter cut 8 in every 1000 events. The effect of these cuts can be observed in Figure 6.6. With these cuts, events with small deposited energy in the calorimeter and few photoelectrons are eliminated from the data.

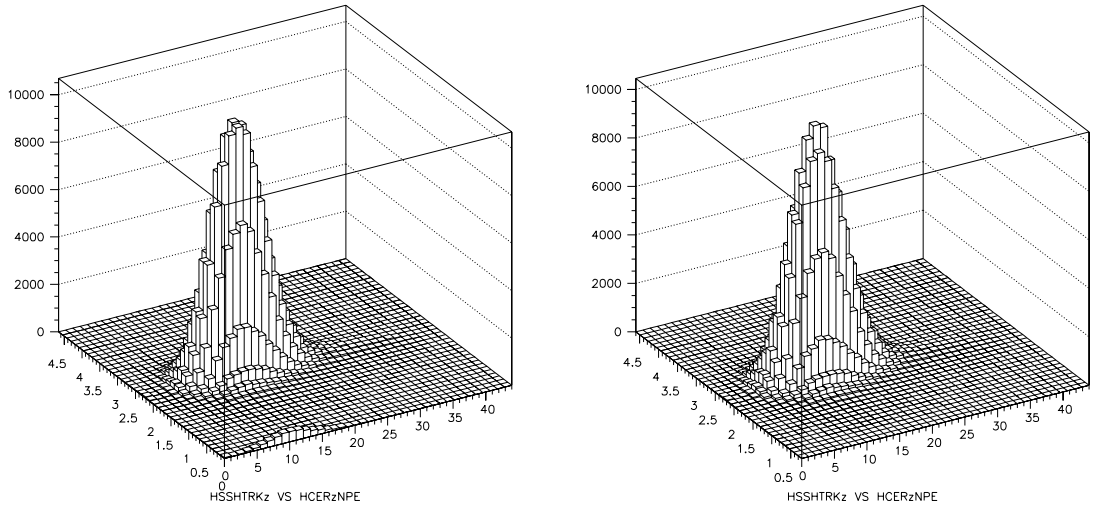

Figure 6.6: Energy deposited in the shower counter (HSSHTRKz) vs. number of photoelectrons in the Čerenkov (HCERzNPE), without cuts (left) and with cuts (right).

6.5 Computer and Electronics Corrections

Limitations in the rate capacity of our data acquisition system played a role in detection of events. Inefficiencies and deadtimes are rate dependent, but these are measurable and correctable inefficiencies and should have little or no impact on the final results.

6.5.1 Electronics Deadtime

Electronics deadtime occurs when the electronics is busy processing a previous trigger and is unable to accept the new trigger. This deadtime is dependent upon the event rate and the electronics gate width. If we assume that events follow a Poisson distribution, then the probability distribution for the mean time between events is $P(t) = Re^{-Rt}$, where R is the event rate and t is time. The number of events that fall at a time less than the gate width, τ, is the number of events lost due to busy electronics. The rate of missed events is the integral of the probability distribution from time zero to τ, since all events occurring at these times will not be processed by the electronics. Likewise, the rate of all events is the same integral evaluated over all time,

$$R_{missed} = \int_0^{\tau} Re^{-Rt} dt \ , \tag{6.13}$$

$$R_{total} = \int_0^{\infty} Re^{-Rt} dt \ , \tag{6.14}$$

To get the deadtime, we divide the number of missed triggers by the total number of triggers,

$$\text{Deadtime} = \frac{R_{missed}}{R_{total}} = 1 - e^{-Rt} \ . \tag{6.15}$$

During the experiment, we experienced rates in the neutron detector of 4 MHz, on average, sent over ten lines to the discriminator, with each line carrying 400 kHz. Hall C gate widths were 50-60 ns, so electronics deadtime was estimated at 2%. A post-experiment study [89, 90] measured a deadtime rate dependence of 0.5% deadtime for

every MHz of full data rate, which would predict exactly 2.0% electronics deadtime for our stated rate.

The electronics deadtime for the HMS, in contrast, is negligible. With an event rate peaking around 500 Hz, and gate widths less than 120 ns, the deadtime is effectively zero. For the inclusive measurement, the neutron detector does not determine the event trigger, but rather only categorizes which type of event, coincidence or non-coincidence, was seen in the HMS. For this reason, only the HMS electronics deadtime will affect the event rate. Since this deadtime is zero, it is neglected in the analysis.

6.5.2 Computer Deadtime

Computer deadtime arises when the computer data acquisition system is busy processing an event when the next event occurrs. In this situation, the new event is lost. Computer deadtime, unlike electronics deadtime, is not negligible. Events recorded by the electronics were logged as pretriggers. The pretriggers that were processed successfully by the trigger supervisor were recorded as triggers. The ratio of triggers to pretriggers gives a measure of the computer deadtime. On average, the deadtime was approximately 10% for both helicities. Coincidence triggers had a slightly lower deadtime, on average, than singles triggers, due to lower event rate.

Table 6.2 gives a summary of all the cuts applied to the data in the PAW ntuples. Once these cuts are made to the data, the refined data set is used to determine the packing fraction, and is ultimately used to determine asymmetries for each run. Further cuts in E' and θ_{scat} are placed on the data to determine the packing fractions and asymmetries. The details and reasoning for these cuts will be discussed in the next 2 chapters.

% cut	Cut Name	Cut on Data	Description
	EvTyp	=1	Singles Events
	EvTyp	=3	Coincidence Events
	Helicity	$4096 \leq h < 16385$	Negative Helicity
	Helicity	$h \geq 16385$	Positive Helicity
2.5 %	y_{tar}	$\lvert y_{tar} \rvert < 3.0$	Cuts out events with bad tracks
14.2 %	Raster	$X^2_{raster}+Y^2_{raster} < 100$	Cuts out events outside target cavity
9.0%	x'_{tar}	$\lvert x'_{tar}+0.005 \rvert < 0.055$	Limits events to the flat part of x'_{tar}
0.2%	Cerenkov	hcer_npe > 3.0	Cut on low number of photoelectrons
0.7%	Calorimeter	$E_{shower}/E' > 0.25$	Eliminates events with small shower

Table 6.2: Summary of the cuts on the raw data. The variable h represents the helicity flag "gtslatch" which signifies the helicity of each event (2^{13} is negative helicity and 2^{14} is positive helicity). X_{raster} and Y_{raster} are the calibrated raster positions, gsrx_calib and gsry_calib determined in the raster calibration to the SEM (see Section 4.4.6). E_{shower} is the energy deposited in the shower counter by the detected particle. All other variables are described in this chapter.

Chapter 7 Packing Fraction and Dilution Factor

7.1 Overview

The packing fraction of the target, *pf*, is the ratio of target thickness containing target material traversed by the beam, to the total target thickness. The packing fraction takes into account the fact that target material, in the form of small beads or crystals, does not fill up the entire volume of the target cavity, and therefore scattering from within the cell is not only from the target material. Rather, there is a significant probability that the electron scattered from a liquid helium nucleus, which filled the gaps between target beads. Other materials in the target cell, such as NMR coils, also have to be taken into account. In addition, not all scattering at the target made it into the spectrometer. An acceptance function of the HMS had to be determined. If the acceptance function and the contributions from other materials within the target cell are known, the true target thickness can be determined.

The dilution factor is the ratio of scattering rates from polarized target materials to the scattering rate from all materials in the target cavity. If the packing fraction is known, then the dilution factor can be calculated from the material properties (such as thickness, density, and molecular weight) and modelled cross sections.

7.2 Acceptance Corrections

The Monte Carlo program, MCEEP [88], which includes radiation, the target raster, and the effects of the target magnetic field, produced an acceptance function for the

HMS at a momentum transfer of 0.5 $(\mathrm{GeV}/c)^2$. This acceptance function described the distribution of events, in E' and θ, which originated at the target and passed all the way through the HMS to the focal plane. The acceptance function was parameterized in E' and θ and incorporated into the model for target rates. For each bin in E' and θ, the normalized acceptance value for that bin was multiplied by the value of the modelled rate to produce an acceptance weighted rate,

$$\mathrm{Rate}'(E',\theta) = F(E',\theta) \cdot \mathrm{Rate}(E',\theta) \ , \tag{7.1}$$

where $\mathrm{Rate}'(E',\theta)$ is the acceptance weighted rate and $F(E',\theta)$ is the parameterized acceptance function from MCEEP. $\mathrm{Rate}'(E',\theta)$ can then confidently represent the data scattering rate. Figure 7.1 shows the acceptance functions in both θ and E' for scattering on a 3 cm carbon target (used to represent our 3 cm $^{15}ND_3$ target). The acceptance functions for other target materials were nearly identical.

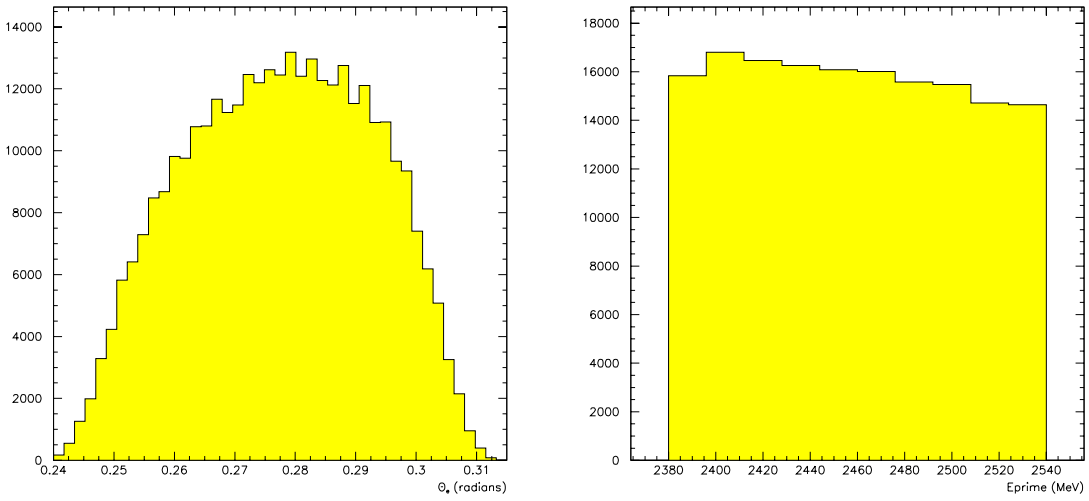

Figure 7.1: Acceptance functions from MCEEP. The left plot is the population of events by scattering angle (in radians). The right plot is the population of events in scattered electron energy (in MeV). No cross section weighting has been applied in either figure.

7.3 Calculating Packing Fraction

The method of determining packing fraction was by comparison of data rates between the polarized target[1] and a target of known thickness. The target of known thickness was solid ^{12}C specially machined to be 0.6858 cm in thickness.

Scattering rates used for packing fraction were taken from the central region of the spectrometer acceptance which was identical for all materials[2]. For these studies, only rates within $\pm\ 0.5^{\circ}$ of the central angle (15.72°) were included. Rates determined from the model were determined over this restricted angular range. All rates, from both data and model, were binned in E' and θ and were integrated over the scattering angle to provide rates as a function of scattered electron energy only. Here we define rate as the number of counts detected per unit charge per second,

$$\mathrm{Rate}(E',\theta) = \frac{d\sigma(E',\theta)}{d\Omega dE'} \cdot \Delta E' \cdot \Delta\Omega \cdot \mathcal{N} \cdot \mathrm{I}\ , \tag{7.2}$$

where $\frac{d\sigma}{d\Omega dE'}$ is the scattering cross section, $\Delta E'$ is the scattered energy bin width, $\Delta\Omega$ is the solid angle of the spectrometer, and I is the measured beam current. E_0 is a supressed variable as it is constant. $\mathcal{N}$ is the number of scattering centers in a given area, and is defined by the density, thickness and atomic number of the material:

$$\mathcal{N} = \frac{N_A \rho t}{A}\ , \tag{7.3}$$

where N_A is Avogadro's number, ρ is the density, t is the material thickness, and A is the atomic number. ΔE and $\Delta\Omega$ are the same for all materials and can therefore supressed as they are divided out in the rate ratio. The rate summed over all θ bins

[1] For the duration of this chapter, references to rates from the "polarized target" is meant to indicate rates from the materials within the target cavity including $^{15}NH_3$ (or $^{15}ND_3$), liquid helium, NMR coils, and aluminum endcap windows.

[2] MCEEP was used to generate acceptance functions for all materials in the target, showing them to be identical.

is then written:

$$\text{Rate}(E') = \sum_{\theta_i} \frac{d\sigma(E',\theta)}{d\Omega dE} \cdot \mathcal{N} d\theta \ . \tag{7.4}$$

Scattering rates from carbon runs were compared to polarized target runs, providing the data rate ratio (RR),

$$RR_{data}(E') = \frac{\text{Rate}_{tgt}(E')}{\text{Rate}_{carbon}(E')} \ , \tag{7.5}$$

where $\text{Rate}_{tgt}(E')$ is the rate from all the components of the polarized target, as a function of the scattered electron energy[3], and $\text{Rate}_{carbon}(E')$ is the rate from all components in the carbon target. This rate ratio was then compared to a model of radiated rates from the polarized target and from the carbon target, with packing fraction left as a variable for the polarized target (pf for the carbon target was fixed).

$$RR_{model} = \frac{R_X \cdot pf + R_{^{15}N} \cdot pf + R_{tgthe} \cdot (1 - pf) + R_{NMR} + \Sigma R_{unpol}}{R_{^{12}C} + R_{ctgthe} + \Sigma R_{unpol}} \ . \tag{7.6}$$

Here X refers to either proton or deuteron, depending on the polarized target. The subscripts ^{15}N, $tgthe$, NMR, ^{12}C, $ctgthe$, and $unpol$ refer to rates from nitrogen-15, helium within the target cavity, NMR coil material (copper and nickel), carbon-12, helium from within the 3cm cavity space not taken up by carbon, and other unpolarized materials outside the cavity (helium and aluminum), respectively. This procedure required a model of cross sections for all the materials present. In addition, since the rates obtained from data are naturally radiated, the data rates had to be corrected for radiation (in the form of a radiative correction factor).

Equating equation (7.4) with this Born rate ratio, the packing fraction is determined.

$$pf = \frac{RR_{Born}(R_{^{12}C} + R_{ctgthe} + \Sigma R_{unpol}) - (R_{tgthe} + \Sigma R_{unpol} + R_{NMR})}{R_X + R_{^{15}N} - R_{tgthe}} \tag{7.7}$$

[3]All rates discussed in this chapter from this point should be assumed to be a function of scattered electron energy only, unless otherwise noted.

The subscript *hex* denotes the helium outside the target cavity through which the beam had to travel. Copper and Nickel are included because the NMR coils are composed of CuNi tubing. The rates of each of these materials was assumed[4] to be the product of the Born cross section and the number density, N. Since all rates were charge normalized, it was assumed that any factor involving the amount of charge through the target, used in computing the rate, would cancel from both numerator and denominator. Each number density was computed as follows:

$$N = conc \cdot \mathcal{N} \ , \tag{7.8}$$

where *conc* is the relative concentration of the material, which was 1.0 for everything with the exception of deuteron (proton) which was 3.0, ignoring impurities, since there are 3 deuterons (protons) for every nitrogen in $^{15}ND_3$ ($^{15}NH_3$).

A value for packing fraction at each scattered energy could then be determined. Since the packing fraction is a physical quantity describing the thickness of the target, it should be constant across E' (as shown in Figure 7.14). Therefore, it was reasonable to average the values from each energy bin, weighted by rate, to obtain a more precise value for packing fraction. To reduce statistical uncertainty even further, a composite carbon run was created by combining rates from like carbon runs. Since spectrometer conditions (such as ADC thresholds and high voltage settings) changed occasionally, and few carbon runs were taken during the majority of data taking, this proved a difficult task. Only a dozen runs could confidently be combined to produce a composite carbon run. (See Appendix B for a listing of these runs).

7.4 Cross Section Model

In order to obtain cross sections for various nuclei, the O'Connell & Lightbody [91] code, QFS, was used. QFS models the A(e,e') cross sections, building the total cross

[4]Rates are a function of scattered electron energy, integrated over the scattering angle, for the center of the spectrometer where the acceptance functions of all materials are taken to be equal.

section from five individual reaction mechanisms: quasielastic scattering, scattering from two interacting nucleons, Delta production, higher resonances, and deep inelastic scattering. It was intended to predict cross sections within 20% over a range of 0.5 to 5.0 GeV incident electron energy. QFS uses as its input the fermi momentum and average separation energy of the target material. The Fermi momentum value is used by QFS to determine the width of the Gaussian shape of the cross section. The average separation energy influences the position of the centroid of that Gaussian. Initial values of κ_F and E_s for materials used in the E93026 target were obtained from measurements made by Whitney *et al.* [92]. Their data showed that the Fermi momentum of a material is a function of the atomic number. A parameterization of the Whitney data was used to interpolate between A values. These initial values were refined after comparison with previously taken data (see Figures 7.2-7.5). A list of the final input parameters is given in Table 7.1.

A	κ_F (MeV)	E_s (MeV)
4	180	20
9	200	20
12	221	20
15	240	20
27	250	25
59	260	35
64	260	35

Table 7.1: Input parameters for QFS. κ_F is the Fermi momentum and $\bar{E}_s$ is the average separation energy. The parameter ϵ_D, representing the delta separation energy, is set to 13 MeV for all materials.

The broadening of the quasielastic peak by the Fermi momentum provided an accurate model of the Born cross sections for nuclei with A$\geq$4, at our momentum transfer. However, consistent results for the deuteron could not be obtained by this method. This model does not accurately describe the deuteron system, which is composed of only one proton and one neutron. Therefore, a momentum distribution [93] was used for the deuteron (see Figure 7.2 for the comparison of the model to exist-

subroutine	variable	value (units)	comment
SIGX	SIG0	0.01 (nb)	
SIGX	SIG1	5.40 (nb MeV)	
SIGX	GAM0	610 (MeV)	
SIGR1	GAMSPRD	0.00 (MeV)	
SIGR1	AR	920 (MeV/c)	for A<2
SIGR2	GAMSPRD	0.00 (MeV)	
SIGR2	AR	980 (MeV/c)	for A<2
SIG2N	A2	550 (MeV/c)	for A<12
SIG2N	A2	570 (MeV/c)	for A≥12
SIG2N	SIG2N	0.7*SIG2N	for A≤27
SIGDEL	AD0	774 (MeV/c)	
SIGDEL	AD1	774 (MeV/c)	
SIGDEL	GAMSPRD	20 (MeV)	
SIGDEL	GAMR	100 (MeV)	
SIGDEL	GAMPI	50 (MeV)	
SIGDEL	AD	700 (MeV/c)	for A<2

Table 7.2: Updated strength parameters and resonance widths for QFS. In general, variables listed here that start with "A" are scale parameters reflecting the dependence on atomic number. Variables that start with "GAM" are generally peak widths, and those that start with "SIG" are related to cross sections.

ing deuteron data). The inelastic cross section for the proton compared well with the Brasse parameterization [61, 94]. The finite experimental resolution of the spectrometer gives the delta function cross section for the proton a Gaussian shape. A resolution parameter was included to account for this effect. This resolution parameter defined the standard deviation of the Gaussian. The value varied as a function of Q^2 but scaled with incident beam energy. For beam energies of less than 5 GeV, the resolution parameter=0.00238*E_0(MeV) was used. The Q^2=0.5 (GeV/c)^2 beam energy of 2729 MeV resulted in a standard deviation of 6.50 MeV for a FWHM of 16.5 MeV.

A modified version of QFS was created to include the updated Fermi momenta and average separation energies, the resolution parameter for the proton, and updated values of strength parameters and resonance widths. The code was modified so that a call to a subroutine for the deuteron momentum distribution was called instead of the Gaussian shape distribution for $n(k)$. A list of the modified strength parameters and resonance widths is provided in Table 7.2.

This updated version of QFS was then tested against data from the same spectrometer but from a different experiment. Proton data from experiment E89008 [95] at Q^2=1.0 (GeV/c)^2 with beam energy of 4.032 GeV and a central scattering angle of 15.00° was compared to the model with these same input values. A θ range of $\pm$ 2.0° was included and the measured E' ranged from 3.2 to 3.7 GeV. The data from E89008 had not been corrected for effects of radiation, so the model had to be radiated to properly compare the two (the details of radiating the data will be discussed in greater detail later in this chapter). The result of the radiated model was a distribution of events nearly identical to the E89008 data (See Figure 7.6). This comparison provides assurance that the model accurately represents the scattering cross sections and the effects of the radiation.

As another test of the model, absolute rates were calculated using the experimental values of $\Delta E'$, $\Delta\Omega$, and beam current. The results were compared to experimental rates as a function of both E' and θ (See Figures 7.7 and 7.8). As can be seen from the

plots, the modelled rate is considerably higher than the experiment rates. However, this is consistent with the results from the same test of the exclusive rates from this experiment [85].

The Born cross sections provided by QFS were used as input into code that incorporated the effects of radiation. This code generated internal radiative corrections in the peaking approximation and full external radiative corrections [96, 97]. The output was a data file containing Born, internal, and external cross sections for each material in the target composition file, at each energy in the runplan file. The target composition file contained the list of all materials traversed by the beam as it travelled through the target together with the thickness, density, concentration, mass, and atomic number for each material (A sample target composition file can be found in Appendix C). The runplan file contained the nominal incident beam energy, electron scattering angle, and a range of scattered electron energy values that covered our range of interest.

Each radiated cross section at each scattered energy was weighted by the material's relative density per molecular weight to produce a radiated rate for each scattered energy bin. Taking the acceptance function of all the materials to be equal, this rate was equivalent to the real scattering rate. This radiated rate was then compared to the Born rate at each scattered energy to give the correction factor at that energy. This was done for both the ammonia target and the carbon target. The resultant radiative correction was then simply,

$$R_{corr} = \frac{\mathrm{CORFAC}_{tgt}}{\mathrm{CORFAC}_{carbon}} = \frac{\frac{R_{tgt_{Born}}}{R_{tgt_{rad}}}}{\frac{R_{carbon_{Born}}}{R_{carbon_{rad}}}} \ , \tag{7.9}$$

which could be used to convert the data rate ratio (RR_{data}) to a ratio of Born rates (RR_{Born}),

$$RR_{Born} = R_{corr} \cdot RR_{data} \ . \tag{7.10}$$

Figure 7.9 shows the Born and radiated rates of the full target and the individual

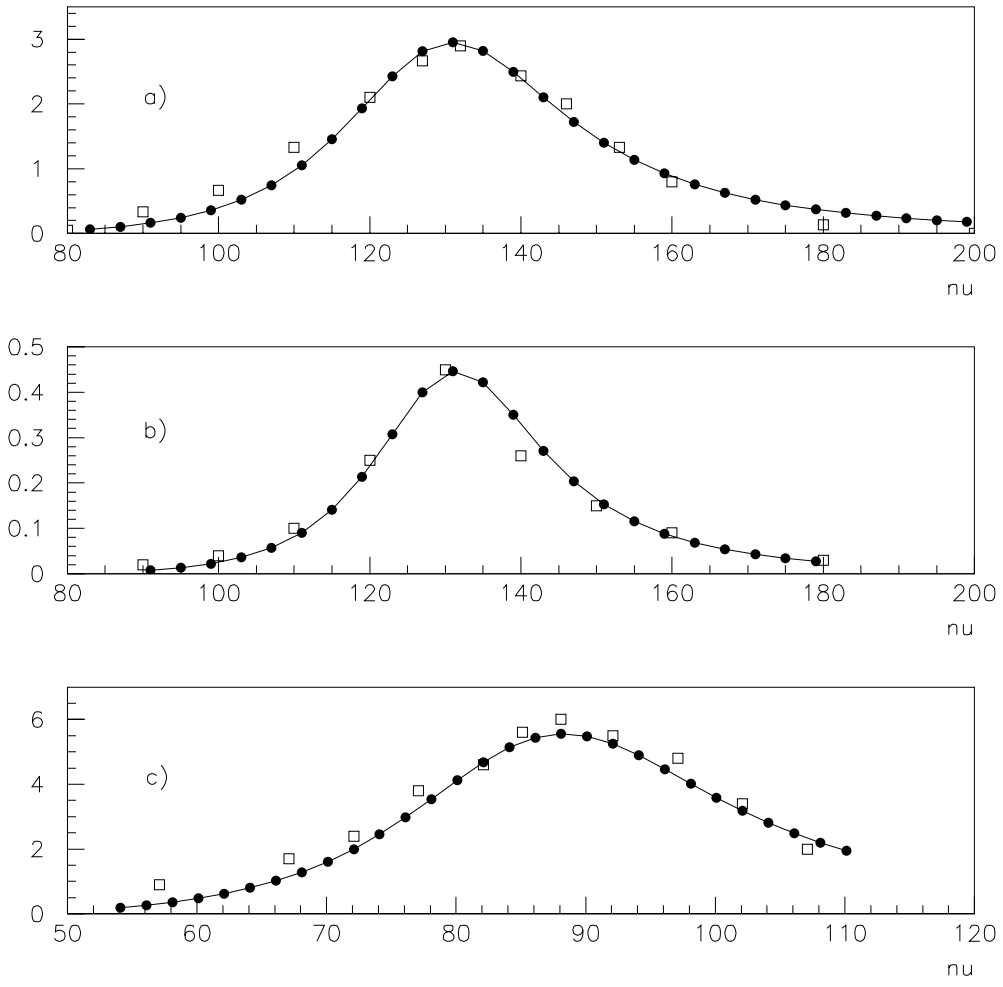

Figure 7.2: Deuteron cross sections. a) Data from inelastic electron-deuteron scattering a)[98] at Q^2=0.24 (GeV/c)^2 (E_0=600 MeV, θ=55°), b) [99] at 180° (Q^2=0.24 (GeV/c)^2, E_0=320 MeV), and c) [100](Q^2=0.16 (GeV/c)^2, E_0=447.1 MeV, θ=60°). The open squares represent data, solid circles connected by the solid curve represent the model. The model compares well to all three sets of data.

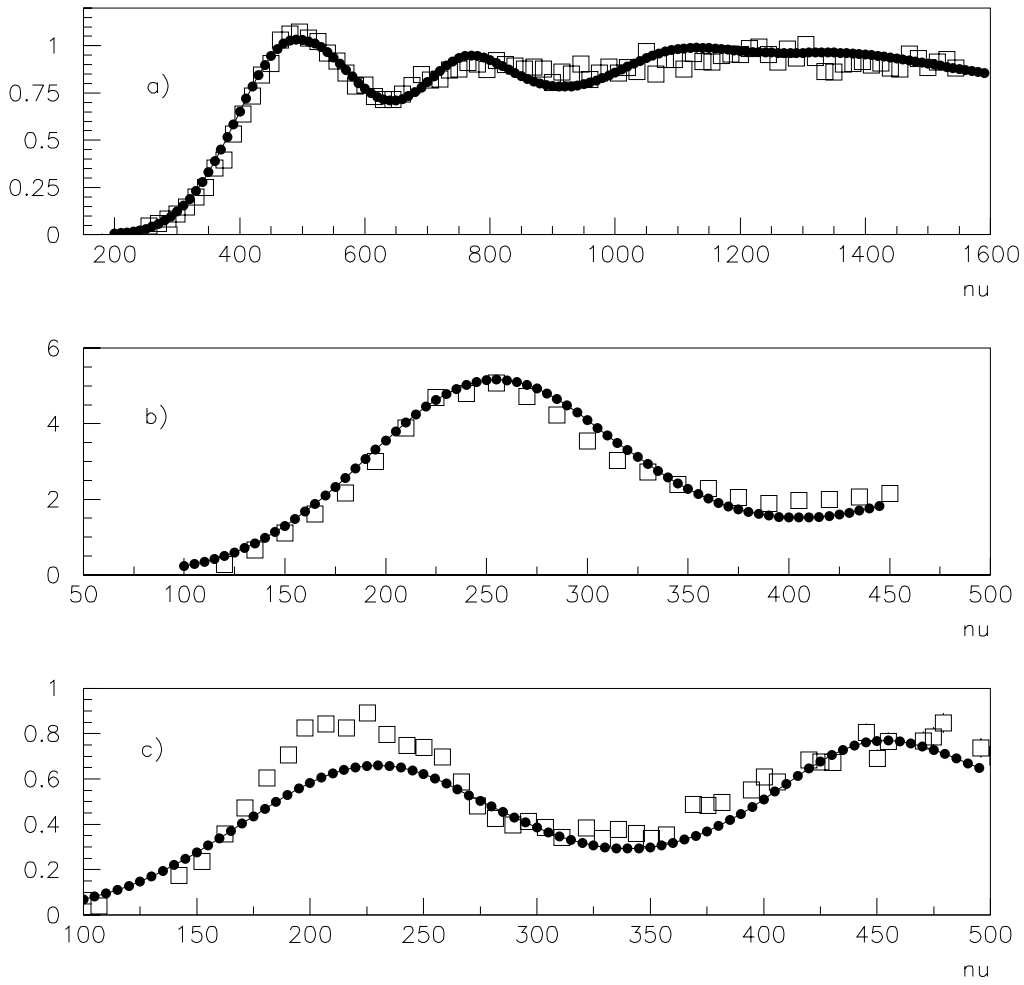

Figure 7.3: Comparison of QFS to helium data [101] at Q^2 values of a) 0.86 (GeV/c)^2 (E_0=3595 MeV, θ=16.02°), b) 0.43 (GeV/c)^2(E_0=2020 MeV, θ=20.02°), and c) 0.36 (GeV/c)^2 (E_0=723.6 MeV, θ=60°). At the lowest Q^2 point, the model does not fit well at the peak, but in our Q^2 region it fits very well. Error bars are included for the data but are smaller than the marker size.

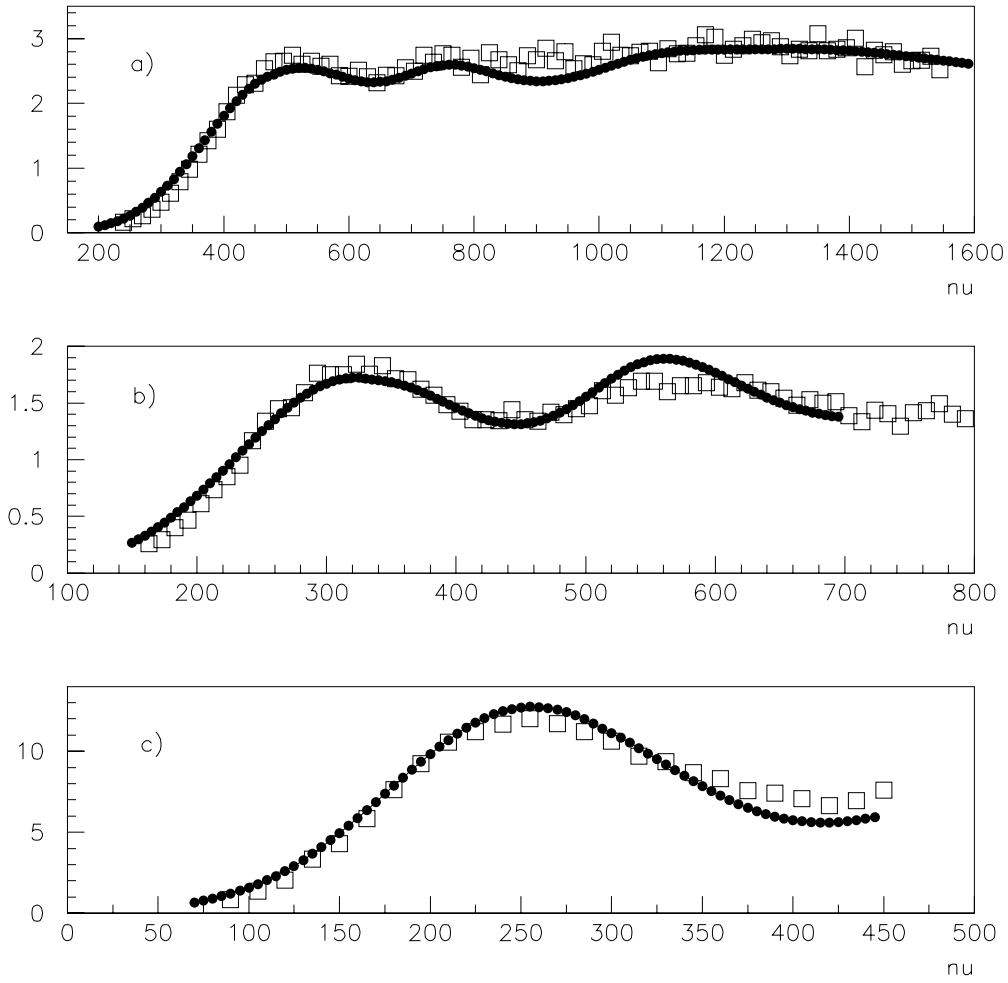

Figure 7.4: Comparison of QFS to carbon data [101]at Q^2 values of a) 0.86 (GeV/c)^2 (E_0=3595 MeV, θ=16.02°), b) 0.53 (GeV/c)^2 (E_0=1299 MeV, θ=37.5°), and c) 0.43 (GeV/c)^2 (E_0=2020 MeV, θ=20.02°). Error bars are included for the data but are smaller than the marker size.

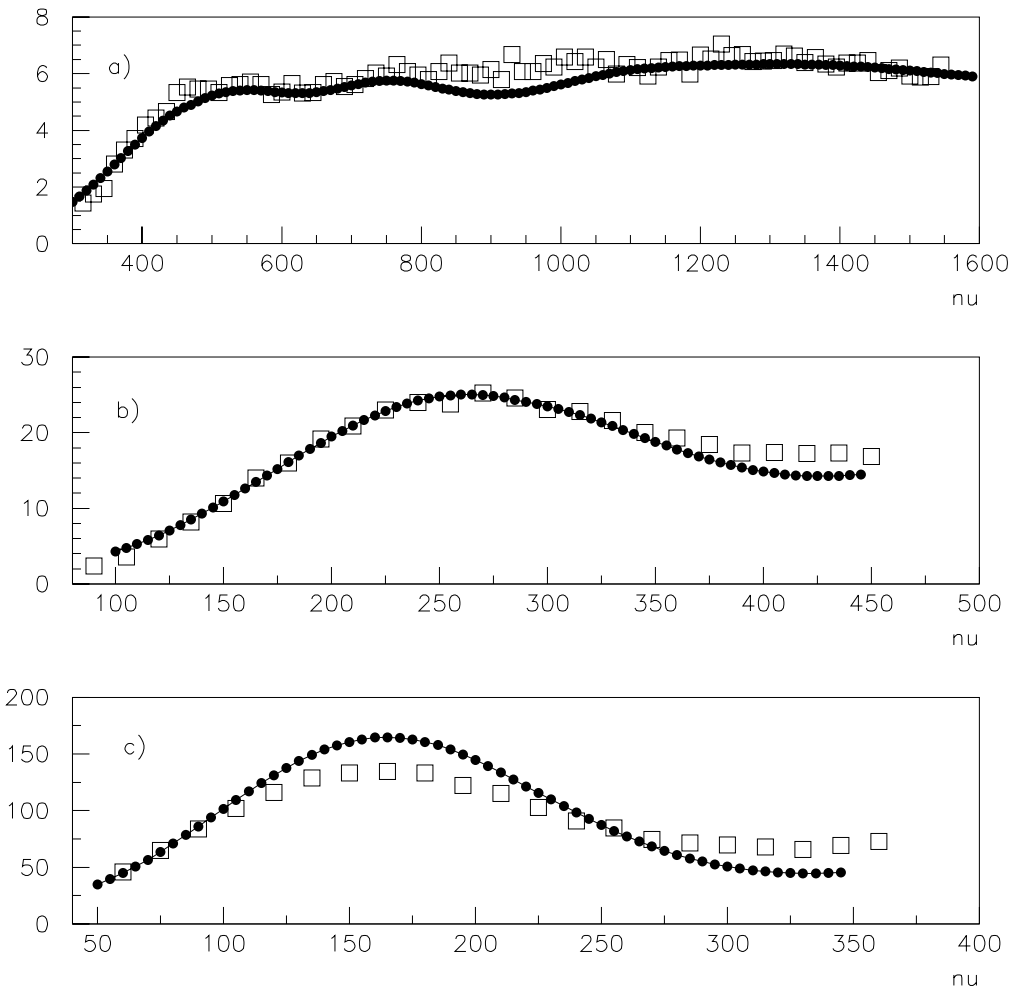

Figure 7.5: Comparison of QFS to aluminum data [101]at Q^2 values of a) 0.86 (GeV/c)^2 (E_0=3595 MeV, θ=16.02°), b) 0.43 (GeV/c)^2 (E_0=2020 MeV, θ=20.02°), and c) 0.26 (GeV/c)^2 (E_0=2020 MeV, θ=15.02°). Again, at the low Q^2 point, the fit is poor at the peak, but in our Q^2 range the fit is better. Error bars are included for the data but are smaller than the marker size.

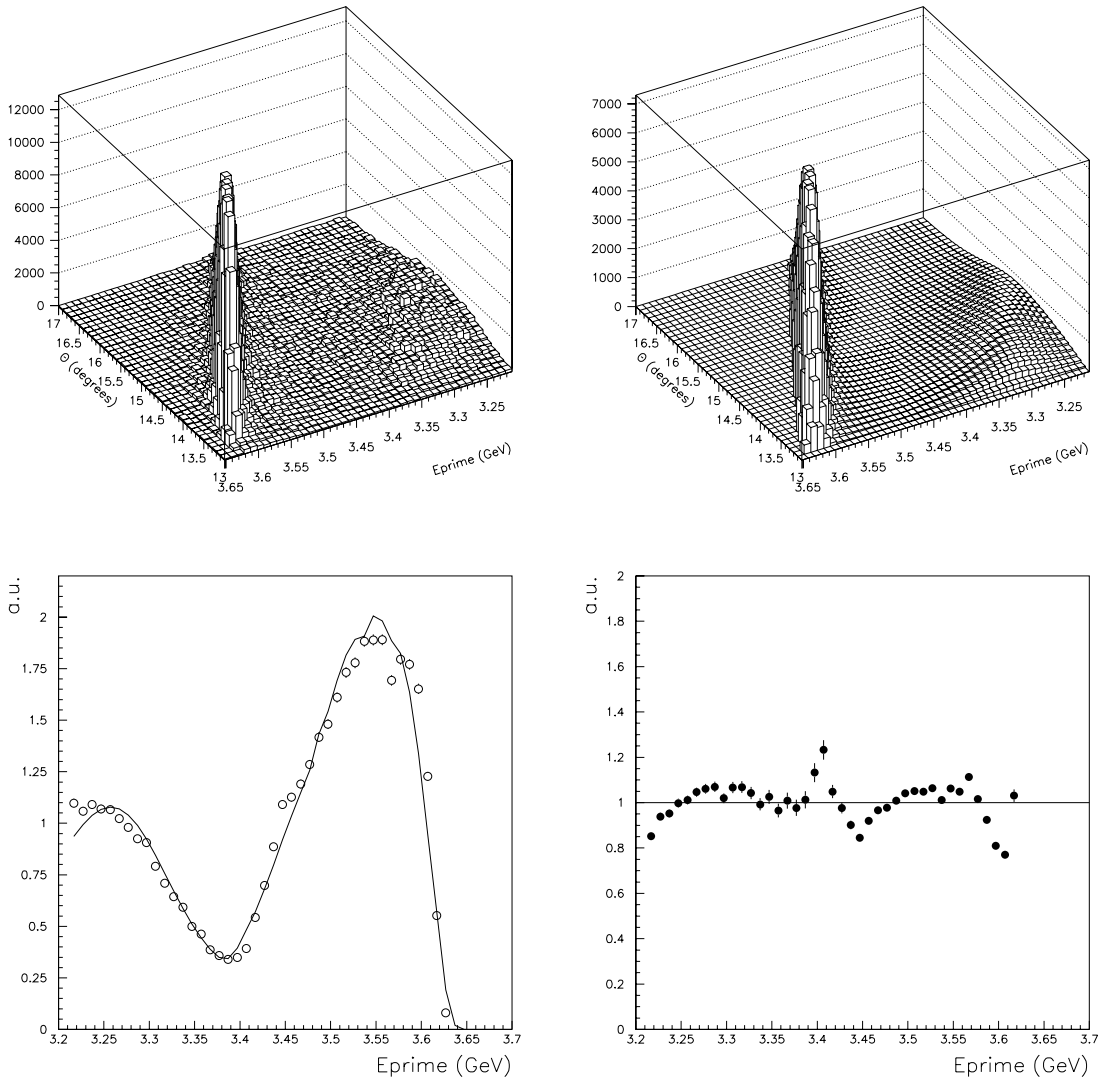

Figure 7.6: Comparison of QFS model to data from experiment E89008 [95]. The top left plot is the data from E89008 and the top right plot is the model at the same energy (4.032 GeV) and angle (15.00°). For both top plots the axes are scattered electron energy (GeV), angle (degrees), and counts. The number of counts differs between the two plots, but the units are arbitrary and we are only interested in the shape. The bottom left plot illustrates the fact that the shape of both distributions, integrated over the scattering angle, are virtually identical. The bottom right plot shows the ratio between data and model. Statistical error bars on both bottom plots are typically smaller than the marker size.

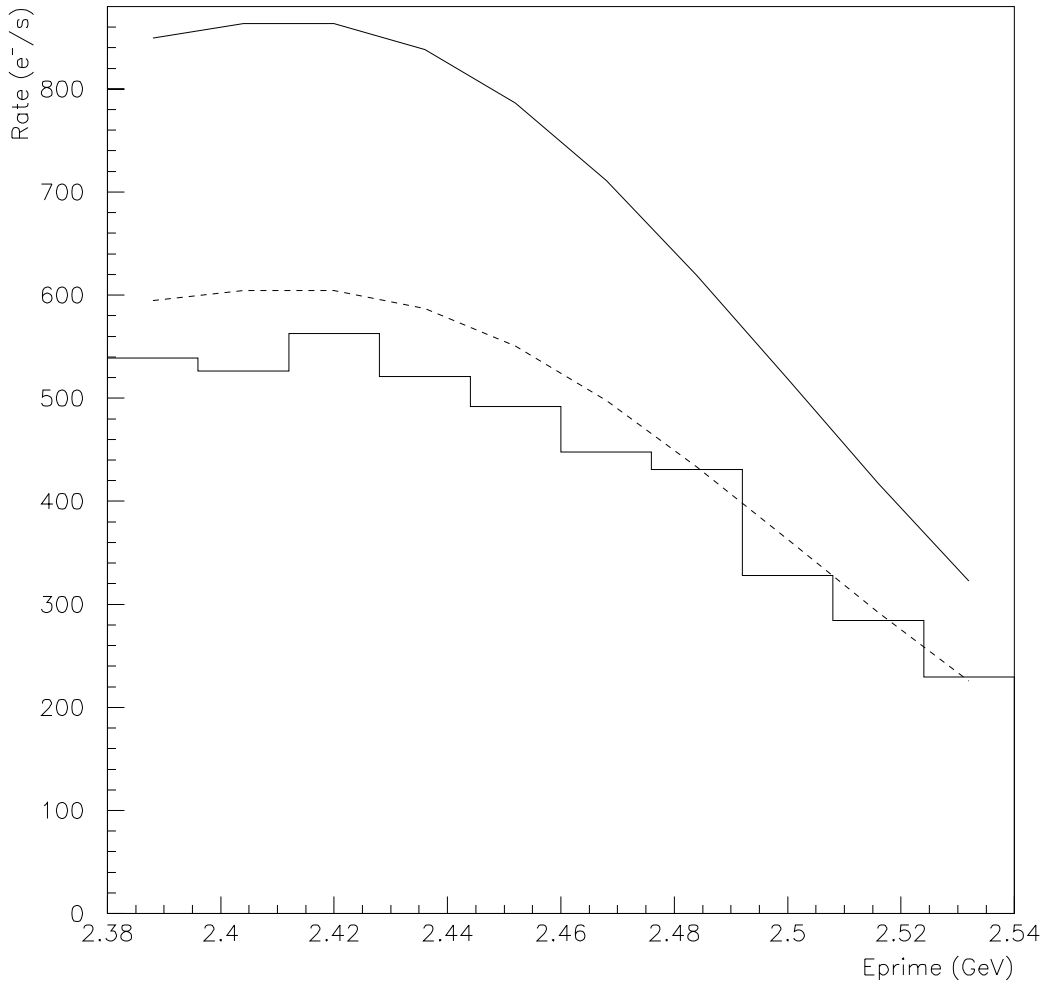

Figure 7.7: Comparison of QFS model absolute rates in E' to data from experiment E93026. The solid line represents the model and the histogram is the data from carbon run 22279. The dashed line represents 70% of the model value. Both data and model were subject to the full set of cuts described in the previous chapter with and angular range of $\pm$ 0.5 degrees from the central scattering angle.

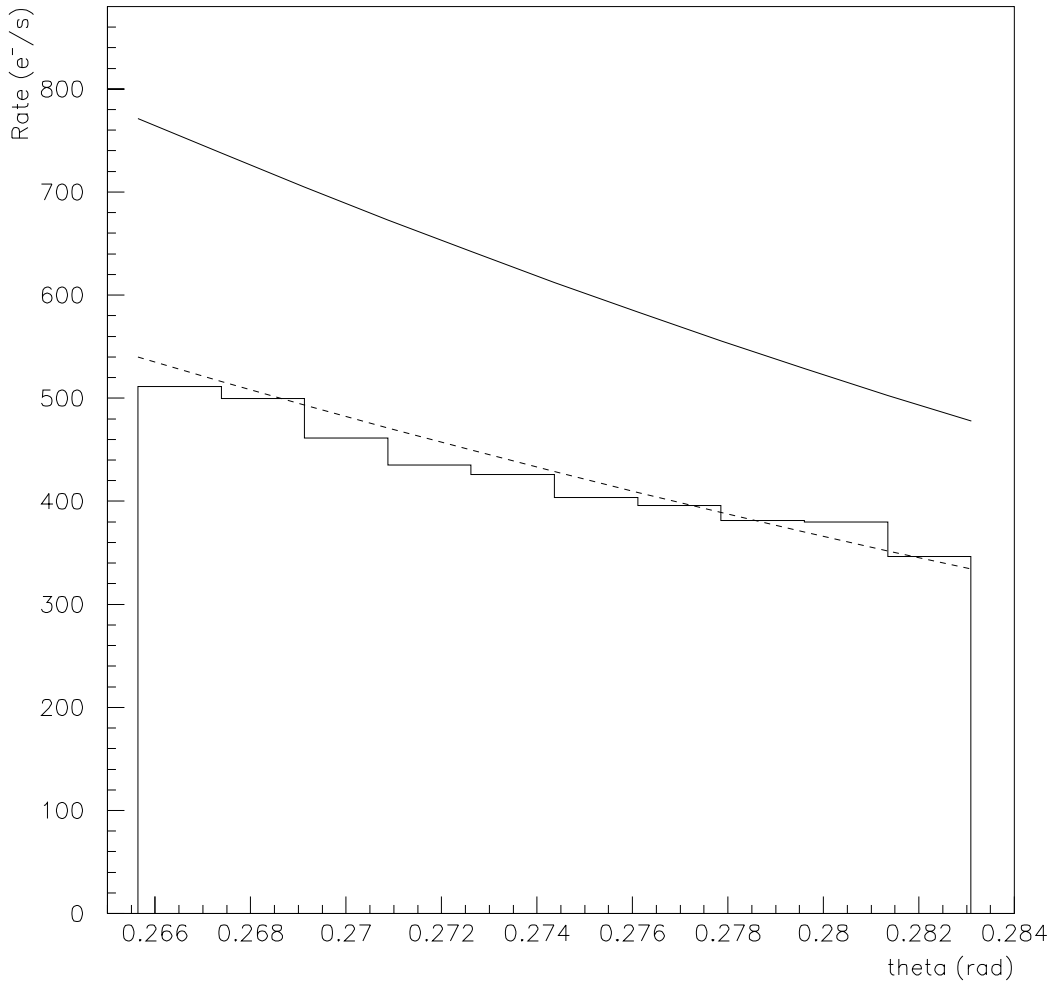

Figure 7.8: Comparison of QFS model absolute rates in θ to data from experiment E93026.The solid line represents the model and the histogram is the data from carbon run 22279. The dashed line represents 70% of the model value. Both data and model were subject to the full set of cuts described in the previous chapter with and angular range of $\pm$ 0.5 degrees from the central scattering angle.

components of the target. Figures 7.10 and 7.11 show the radiated model compared with the data, with a cut on the central angle of $\pm$ 0.5° applied to both. It is clear from both figures that the model fits the data extremely well.

7.5 Radiative Corrections

The single-photon exchange diagram, shown in Figure 2.1, in fact never occurs. Electrons radiate via bremsstrahlung along the path of travel, and also radiate through several processes at the scattering vertex. Scattering which does not follow the single-photon exchange diagram affects the shape of the measured cross section. The electron is a good probe of nuclear structure since it has only an electromagnetic interaction and is only weakly interacting, thus it does not disturb the system being studied. However, it does radiate profusely and these processes must be accounted for. If an electron radiates before scattering from the target, the energy of the electron at the scattering vertex will be lower than the measured beam energy. Likewise, if the electron radiates after it has scattered, the detected scattered electron energy will be less than it could be if it had not radiated. Either or both of these processes occur. *Internal* radiation occurs at the scattering vertex through internal bremsstrahlung, two photon exchange, vacuum polarization, and vertex corrections. *External* radiation occurs as a result of the electron's interaction with the material through which it traverses. Figure 7.12 shows the Feynman diagrams of these radiative processes.

In elastic scattering, the effects of internal and external radiation can be accounted for by a radiative correction factor which relates the Born and radiated cross sections,

$$\frac{d\sigma}{d\Omega}_{rad} = (1 + \delta_{corr})\frac{d\sigma}{d\Omega}_{Born} , \tag{7.11}$$

where δ_{corr} is the sum of internal and external corrections to the Born cross section

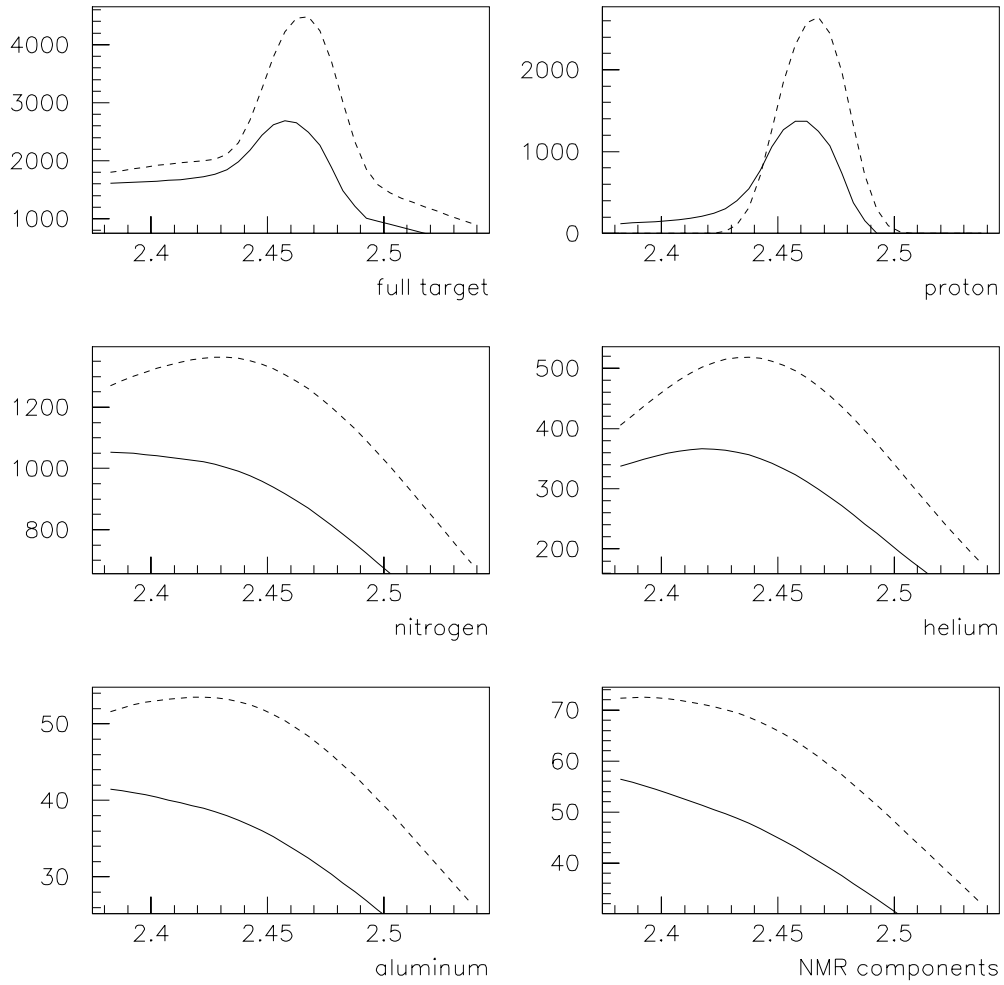

Figure 7.9: Target material rates, radiated (solid line) and unradiated (dashed). These modelled rates have the HMS acceptance function built in so as to be able to compare them directly to data. The width of the proton peak is therefore exaggerated since it includes contributions from a wide range of scattering angles.

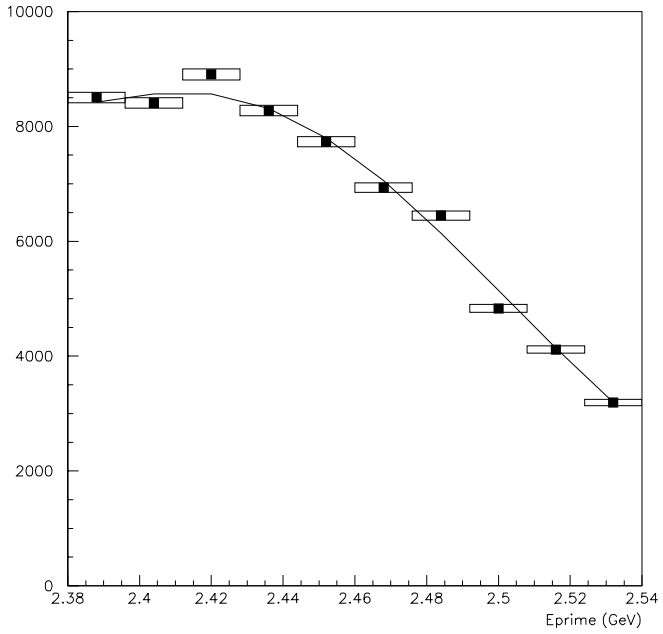

Figure 7.10: Event distribution for the carbon target from model (solid line) and E93026 data (solid squares). The data is from run 22279 and covers an angular range of 1.0 degree about the central angle. The data is binned in 16 MeV bins. An overall normalization factor was applied to the model distribution to match the same relative scale as the data. Uncertainty in the data is represented by the open rectangles about each data point. Uncertainty in E' is the half the bin width, while uncertainty in the number of counts is the statistical uncertainty.

[96]. Higher order radiative corrections can be incorporated by exponentiating δ_{corr}:

$$\frac{d\sigma}{d\Omega}_{rad} = e^{\delta_{corr}} \frac{d\sigma}{d\Omega}_{Born} \quad . \tag{7.12}$$

Exponentiation is only valid for the infrared divergent terms, however the inaccuracy induced in the non-infrared divergent terms due to exponentiation is negligible [41].

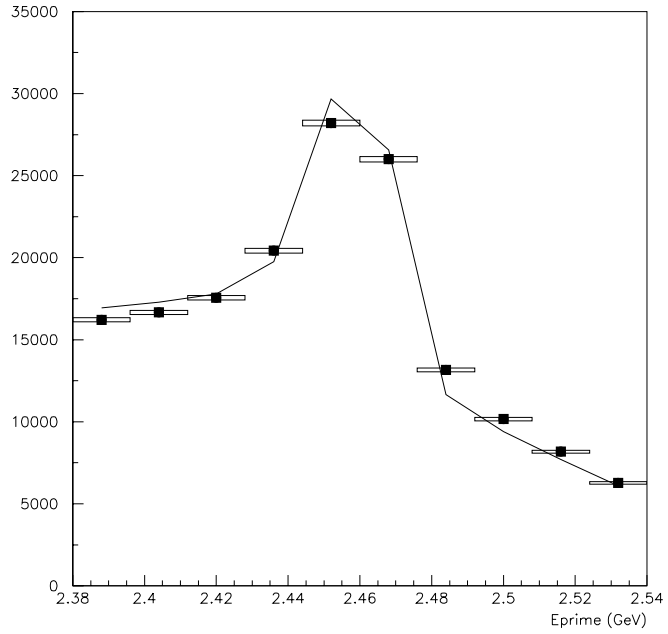

Figure 7.11: Event distribution for the proton target from model (solid line) and E93026 data (solid squares). The data is from run 21690 and covers an angular range of 1.0 degree about the central angle. The data is binned in 16 MeV bins. An overall normalization factor was applied to the model distribution to match the same relative scale as the data. The model assumes a packing fraction of 55%. Uncertainty in the data is represented by the open rectangles about each data point. Uncertainty in E' is the half the bin width, while uncertainty in the number of counts is the statistical uncertainty.

7.5.1 Internal Corrections

Internal corrections to the cross section included processes such as vacuum polarization, vertex corrections, and internal bremsstrahlung. Internal corrections were based on the work of Mo and Tsai [96] and Tsai [97]. In their work it was assumed that the photons emitted are either along the direction of the incident electron or the scattered electron. This is known as the peaking approximation. The peaking approximation allows a double integral to be broken down into two single integrals, reducing the computational strain. Internal bremsstrahlung was approximated by an equivalent

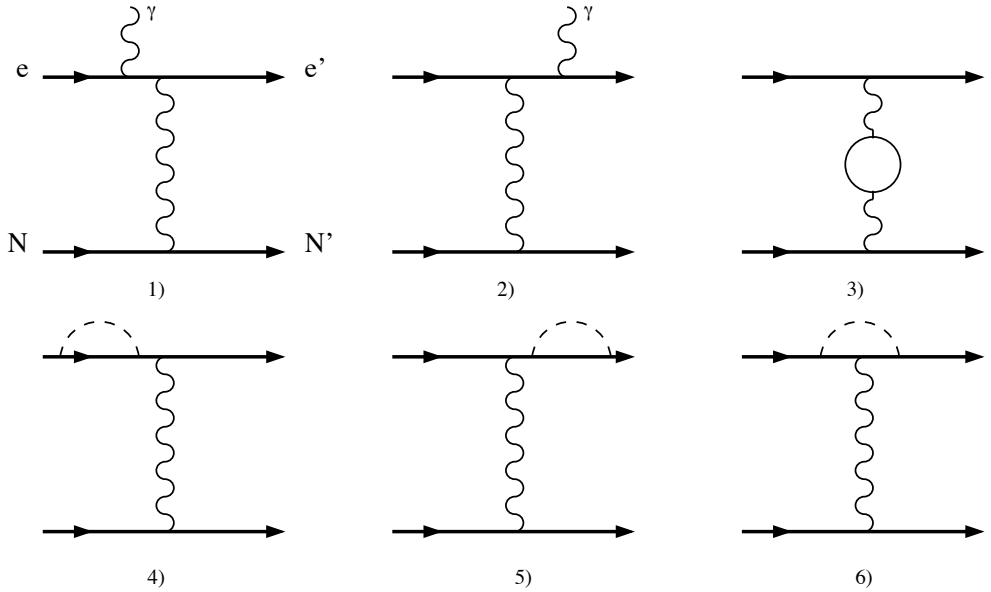

Figure 7.12: Feynman diagrams of radiative processes: 1) and 2) bremsstrahlung, 3) vacuum polarization, 4) and 5) self-energy, and 6) vertex correction.

radiator placed before and after the scattering point:

$$t_r = \left(\frac{\alpha}{b\pi}\right)\left[ln\left(\frac{Q^2}{m_e^2}\right) - 1\right] \tag{7.13}$$

The magnitude of the equivalent radiator is determined by Q^2 and b, a term dependent upon the Z of the material, which has a value of approximately 4/3. This equivalent radiator length was added to the total radiation length of the material, before and after scattering, when computing external corrections (see Equation 7.16).

7.5.2 External Corrections

External corrections to the scattering were calculated explicitly with a single integral for the initial electron energy, a single integral for the scattered electron energy, and a double integral incorporating energy loss in both variables.

Electrons emit bremsstrahlung photons when in the presence of the field of a nearby nucleus. Bremsstrahlung from "hard" photons (photons whose energy is

greater than the bin resolution) was the main source of external corrections. A small contribution from ionization loss was included, but the bremsstrahlung term dominated the external correction. The critical energy, E_c, which Leo [102] defines as the energy at which the radiation loss equals the collision-ionization loss is,

$$E_c = \frac{1600 m_e c^2}{Z} \ . \tag{7.14}$$

For scattering from $^{15}NH_3$, this critical energy is $E_c = 81.8$ MeV. For electrons below this critical energy, collision-ionization dominates. Above this critical energy, bremsstrahlung dominates the radiation. For E93026, the incident electron energy of 2729 MeV was well above the critical energy.

The full correction to the Born cross section included four corrections: a constant soft photon term, a term accounting for bremsstrahlung along the incoming electron, a term for bremsstrahlung along the outgoing electron, and a term including bremsstrahlung along the incoming and outgoing electron. The constant term, RAD1, is written:

$$\begin{aligned} RAD1 &= \sigma_0(E_0, E', \theta_e) f_{Tsai} F(b_{tb_i}) F(b_{ta_i}) \left(\frac{R\Delta}{E_0}\right)^{b_{tb}} \left(\frac{\Delta}{E'}\right)^{b_{ta}} \\ &\quad \left(1 - \frac{X0_{ATB}}{(1 - b_{tb_i}) R\Delta}\right) \left(1 - \frac{X0_{ATA}}{(1 - b_{ta_i})\Delta}\right) \ . \end{aligned} \tag{7.15}$$

$\sigma_0(E_0, E', \theta_e)$ is the Born cross section, as provided by QFS, and the function $f_{\rm Tsai}$ contains the internal corrections and is defined as

$$f_{\rm Tsai} = 1 + \sum \delta_{internal} \ . \tag{7.16}$$

The other variables in RAD1 are defined as follows:

$$\begin{aligned} F(X) &= 1 + 0.5772X - 0.62X^2 \\ b_{tb_i} &= b \cdot t_b + b_a \cdot t_{ba} \end{aligned}$$

$$
\begin{aligned}
b_{ta_i} &= b \cdot t_a + b_a \cdot t_{aa} \\
X0_{ATB} &= X_0 \cdot t_b + X_{0_a} \cdot t_{ba} \\
X0_{ATA} &= X_0 \cdot t_a + X_{0_a} \cdot t_{aa} \\
b_{tb} &= b(t_b + t_r) + b_a \cdot t_{ba} \\
b_{ta} &= b(t_a + t_r) + b_a \cdot t_{aa} \\
R &= \frac{M_p + E_0(1 - \cos\theta)}{M_p - E'(1 - \cos\theta)} \ ,
\end{aligned}
\tag{7.17}
$$

where t_b and t_a are the amount of target material before and after the scattering point, t_{ba} and t_{aa} are the amounts of other material before and after the scattering point, X_0 and X_{0_a} are the radiation length parameters for the target material and the other material outside the target (assumed to be aluminum). b_a is the b-value of aluminum and Δ is the bin resolution value (set to be 10 MeV).

Integration along the incoming electron yields RAD2:

$$
\begin{aligned}
RAD2 &= \int_{E'_{low}}^{E'_{high}} \sigma_0(E_0, E', \theta_e) f_{Tsai} F(b_{tb_i}) \left(\frac{R\Delta}{E_0}\right)^{b_{tb}} \left(1 - \frac{X0_{ATB}}{(1 - b_{tb_i})R\Delta}\right) \\
&\quad F(b_{ta_i}) \left(\frac{E'' - E'}{E''}\right)^{b_{ta}} \frac{b_{ta}}{E'' - E'} \cdot \phi(\frac{E'' - E'}{E''}) \ dE' \ ,
\end{aligned}
\tag{7.18}
$$

where $\phi(x) = 1 - x + 0.75x^2$. Likewise, integration along the scattered electron provides RAD3:

$$
\begin{aligned}
RAD3 &= \int_{E_{0_{low}}}^{E_{0_{high}}} \sigma_0(E_0, E', \theta_e) f_{Tsai} F(b_{ta_i}) \left(\frac{\Delta}{E'}\right)^{b_{ta}} \left(1 - \frac{X0_{ATA}}{(1 - b_{ta_i})\Delta}\right) \\
&\quad F(b_{tb_i}) \left(\frac{E_0 - E'_0}{E_0}\right)^{b_{tb}} \frac{b_{tb}}{E_0 - E'_0} \cdot \phi(\frac{E_0 - E'_0}{E_0}) \ dE_0 \ .
\end{aligned}
\tag{7.19}
$$

The double integral accounts for those electrons that lost energy on the way in and on the way out of the target.

$$
RAD4 = \int_{E_{0_{low}}}^{E_{0_{high}}} \int_{E'_{low}}^{E'_{high}} \sigma_0(E_0, E', \theta_e) f_{Tsai} F(b_{tb_i}) F(b_{ta_i}) \left(\frac{E_0 - E'_0}{E_0}\right)^{b_{tb}} \left(\frac{E'' - E'}{E''}\right)^{b_{ta}}
$$

$$\frac{b_{tb}}{E_0 - E_0'}\frac{b_{ta}}{E'' - E'}\phi(\frac{E_0 - E_0'}{E_0})\phi(\frac{E'' - E'}{E''})\; dE_0 dE' \; . \tag{7.20}$$

The fully radiated cross section is then $\frac{d\sigma}{d\Omega}_{rad} = RAD1 + RAD2 + RAD3 + RAD4$.

Comparisons were made against reported corrections from Mo and Tsai [96], and Stein [103] in order to test our procedure. Stein published Born and radiated cross sections from elastic electron-proton scattering. Both the Born and radiated cross sections from our code were compared to those from Stein and were found to be in reasonable agreement (to 5%). Mo and Tsai have calculated internal (zero target thickness) radiative tails from elastic $e - p$ scattering. The values from the 5 GeV calculations are shown in Figure 7.13. Using the same kinematics (E_0=5.0 GeV, θ=5°), our routine generated radiated cross sections across the same range of scattered electron energy (1.0 - 4.8 GeV). Our model compares very well to that of Mo and Tsai. At very large energy loss, the results begin to deviate, but this is well out of our kinematic region of interest.

7.5.3 Interaction Point

The assumption was made that the scattering within the target cell occurred, on average, at the center of the target, along the direction of the beam. Calculations of target material thicknesses before and after the interaction point were based on this assumption. A test was performed to determine the scale of possible error induced in the model from this assumption.

Two target composition files were produced, one where all scattering of target material took place at the front face of the target, and the other where all scattering took place at the back plane of the target cell. This would give an upper bound to the possible error from the center target assumption. Rates for these two target composition files were compared to rates from a "normal" target composition file (where all scattering occurs at the center of the target), and the difference was less than 1% in both cases. Furthermore, the differences were fairly consistent across

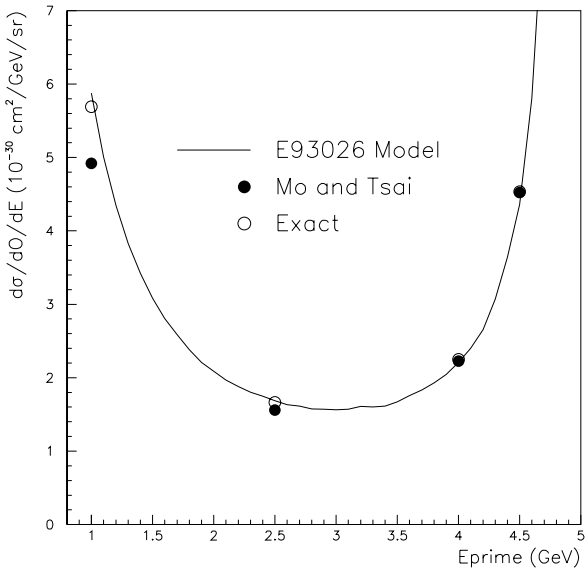

Figure 7.13: Mo and Tsai radiative tails for proton for incident energy of 5 GeV and scattering angle of 5°. The open circles represent the calculated value for the radiative tail of the *ep* elastic peak calculated by the exact formula, whereas the solid circles are the values calculated by the Mo and Tsai approximation for the radiative tail. The line represents the values determined from the E93026 model.

the scattered energy range. We expect that the polarized target and carbon target scatter in the same way and the error induced in the rate ratio from the center target assumption would be completely negligible. Materials before and after the target cell were all foils of sufficiently small thickness that there was no scattering position dependence.

7.6 $^{15}ND_3$ Packing Fractions

Polarized target data was also combined in groupings by target cell within anneal periods to reduce the uncertainty in rates. $^{15}ND_3$ target runs were grouped by top and bottom cavity within each anneal period. The packing fractions for all individual runs were calculated to make sure all runs within a group gave similar results. It

was believed that the packing fraction within an anneal period would change little as there was no mechanism for shifting around of the target material. Even after an anneal, which can potentially cause shifting of the target material, there was not much evidence of settling of the target material. The absence of settling or shifting of the material was determined by inspection of spectrometer rates over time as a function of target position and by the visual inspection at insert changes.

Table 7.3: Deuteron packing fractions by run numbers.

Range of Run Numbers	Packing Fraction	Target Cell
21816 - 21876	0.505 ± 0.004	top
21881 - 21922	0.489 ± 0.003	top
21927 - 21979	0.480 ± 0.003	top
21986 - 22020	0.474 ± 0.003	top
22046 - 22080	0.471 ± 0.003	top
22100 - 22124	0.498 ± 0.004	top
22125 - 22137	0.560 ± 0.004	bottom
22138 - 22156	0.489 ± 0.003	top
22157 - 22172	0.532 ± 0.004	bottom
22180 - 22198	0.482 ± 0.004	top
22199 - 22213	0.539 ± 0.004	bottom
22218 - 22239	0.532 ± 0.004	bottom
22240 - 22244	0.487 ± 0.004	top
22250 - 22272	0.532 ± 0.004	bottom
22278 - 22288	0.494 ± 0.004	top

Table 7.3 lists the packing fraction values and statistical uncertainty for each grouping of $^{15}ND_3$ runs. For the earlier running for Q^2=0.5, in the top target only, deuteron packing fraction was roughly 50%. For the later Q^2=0.5 deuteron running, the top target had a packing fraction of 50% again, while the bottom target had a 54% packing fraction. Figure 7.14 shows the packing fraction as a function of E' for runs 22199-22213 (a subset of the entire set of runs used).

The errors listed are only statistical. This 1% statistical uncertainty must be combined with the uncertainty in the model, which was estimated at 4-5%, to get the total uncertainty in the packing fraction determination.

Table 7.4: Relative number densities in the $^{15}ND_3$ target composition file

Material	Ratio of N_X to N_D
Deuterium	1.0
Nitrogen	0.3333
Carbon	0.2860
Target Helium	0.2403
External Helium	0.0801
Aluminum	0.0146
Copper	0.0031
Nickel	0.0014

Table 7.5: Relative number densities in the $^{15}NH_3$ target composition file

Material	Ratio of N_X to N_P
Proton	1.0
Nitrogen	0.3333
Carbon	0.2822
Target Helium	0.2373
External Helium	0.0792
Aluminum	0.0144
Copper	0.0031
Nickel	0.0013

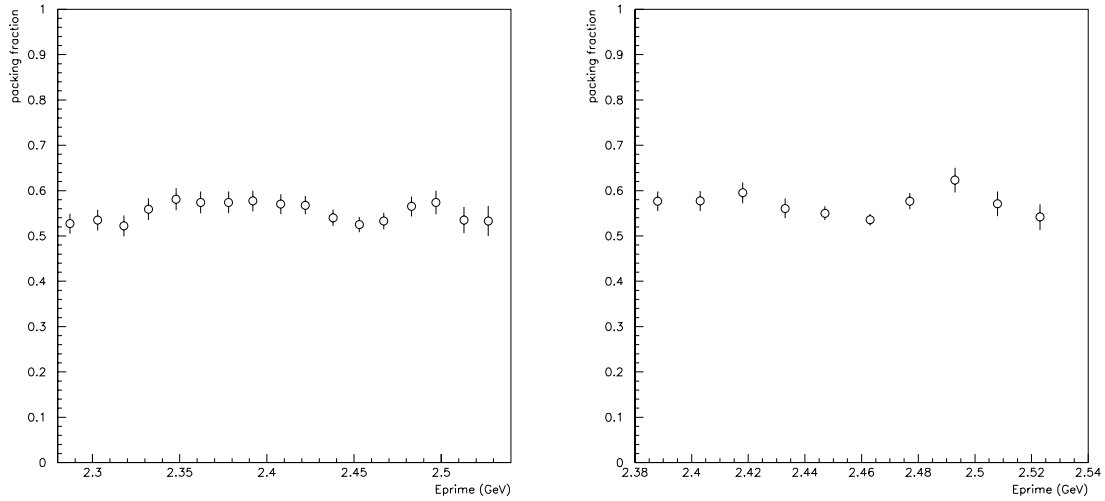

Figure 7.14: $^{15}ND_3$ (left) and $^{15}NH_3$ (right) packing fractions as a function of E′. The $^{15}ND_3$ data is from the set of runs 22199-22213. The $^{15}NH_3$ packing fraction is from all 22 proton runs.

7.7 $^{15}NH_3$ Packing Fractions

Packing fractions for the proton targets were calculated in a similar fashion. More attention to the details of the model was necessary due to the sharp elastic proton peak. Errors introduced into the model of the cross section as a function of scattering energy or angle, or mistreatment of radiative corrections could result in large deviations from the data. Including a large angular range is also more difficult with the $^{15}NH_3$ target. The sharp elastic peak at the central angle was broadened in E' as the elastic peak falls at different scattered energies for different scattering angles. The model had to have the appropriate angular dependence in order to match the data. The model was calculated for all θ bins across the angular range of the data used for packing fraction determination (nominally $\pm$ 0.5° from the central angle of 15.72°). For completeness and consistency, the calculation of the modelled rates was calculated over all θ bins for all materials in the $^{15}NH_3$ target.

Table 7.6 lists the packing fraction values for $^{15}NH_3$ run groupings. Proton packing fractions were consistent over all run periods, and all packing fraction values for

Table 7.6: Proton packing fractions by run numbers

Range of Run Numbers	Packing Fraction	Target Cell
21592 - 21607	0.564 ± 0.007	top
21613 - 21614	0.570 ± 0.013	top
21621 - 21624	0.572 ± 0.013	top
21690 - 21696	0.571 ± 0.008	top

different runs were consistent within error. Again, errors listed are purely statistical. Figure 7.14 shows the packing fraction as a function of E' for both $^{15}ND_3$ and $^{15}NH_3$ runs. Values of packing fraction are consistent across E', and supports taking an average of the packing fraction across E'.

7.8 Dilution Factor

If the packing fraction is known, the single arm dilution factor is readily calculable. The dilution factor is the ratio of rates from polarized materials in the target to rates from all materials (polarized and unpolarized) in the target.

$$f = \frac{R_X \cdot pf}{R_X \cdot pf + R_{^{15}N} \cdot pf + R_{tgthe}(1 - pf) + R_{hex} + R_{Al} + R_{Cu} + R_{Ni}} \ . \qquad (7.21)$$

Rates listed are radiated rates. The subscript X represents either proton or deuteron, depending on the target.

The dilution factor was computed as a function of E' and θ in the same bins as the data was collected. Since dilution factor is a ratio of rates, all phase space dependence factored out. The dilution factors shown in Figure 7.15 are for $^{15}ND_3$ and $^{15}NH_3$ with packing fractions of 50% and 55% respectively. Small changes in packing fraction have a negligible impact on the dilution factor.

The Born dilution factor was produced from Born rates using the same method. The Born dilution factors for $^{15}ND_3$ and $^{15}NH_3$ are shown in Figure 7.16. Packing fractions are the same as in the radiated plots.

Uncertainty in the dilution factor is determined from the uncertainty in the packing fraction and from the uncertainty in the model. Uncertainty in the packing fraction propagates into a smaller uncertainty in dilution factor due to the nature of the equation for the dilution factor (Equation 7.14). Since the uncertainty in the model (4-5%) is already larger than the uncertainty in the packing fraction, it dominates the overall uncertainty in the dilution factor. Total uncertainty in the dilution factor is estimated to be 5%.

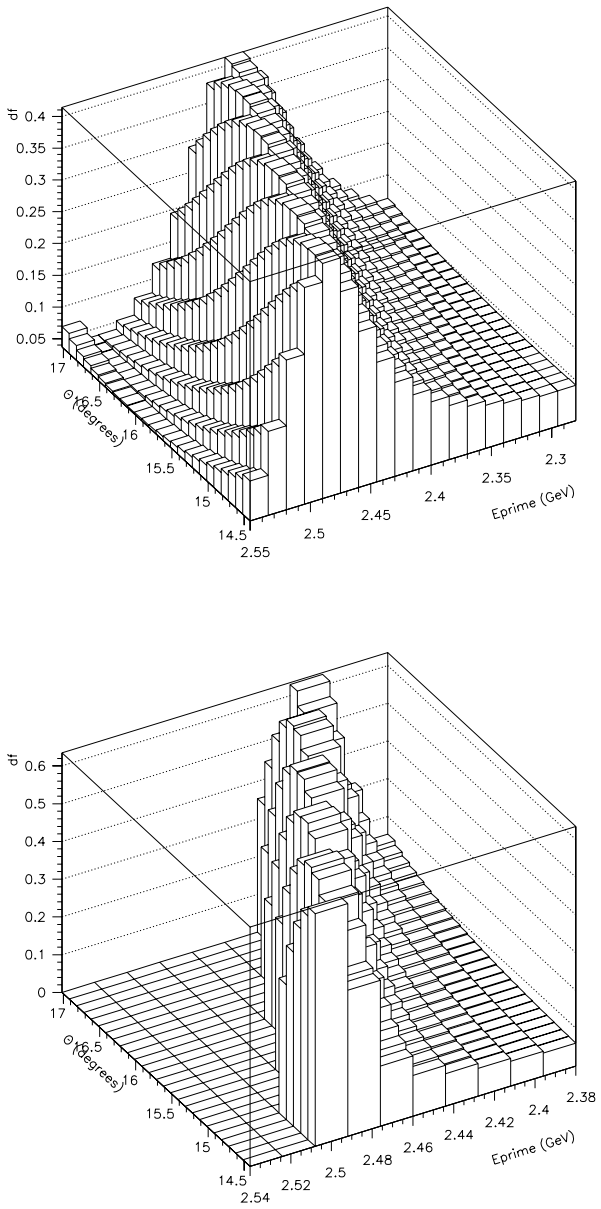

Figure 7.15: Single arm radiated dilution factor for $^{15}ND_3$ and $^{15}NH_3$. Radiated dilution factors can be used in calculating asymmetries from radiated counting asymmetries.

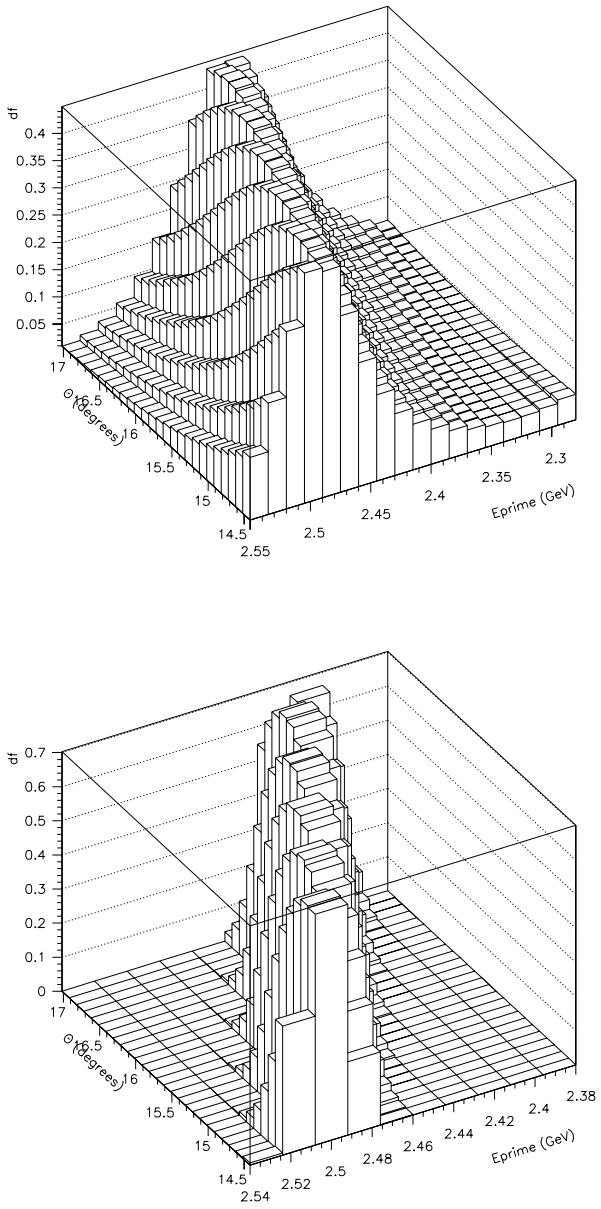

Figure 7.16: Single arm Born dilution factor for $^{15}ND_3$ and $^{15}NH_3$. Born dilution factors are used in asymmetry calculations where the counting asymmetry has been radiatively corrected.

Chapter 8 Analysis

8.1 Introduction

In this chapter, the details of converting the data into an asymmetry, and ultimately into a value for G_{Ep}, will be outlined. Corrections applied to the raw counting asymmetry take into account the dilution factor, the nitrogen background, unpolarized radiative corrections, and polarized radiative corrections. Error analysis for the asymmetries and the form factor are also discussed.

8.2 Raw Single Arm Asymmetry Calculation

The counting asymmetry is the difference in counts between the two helicities divided by the total number of counts. This counting asymmetry can be related to the theoretical asymmetry by calculable and measurable factors. These factors are the dilution factor, accounting for events scattered from non-target material, the target polarization, and the beam polarization,

$$\epsilon = \frac{N_+ - N_-}{N_+ + N_-} = f P_t P_b A_p \ , \tag{8.1}$$

where A_p is the physics asymmetry from Equation 2.18. N_+ and N_- are the counting rates for each helicity scaled by the appropriate scaling factors (ps and C), and divided by charge (Q),

$$N_+(_-) = \frac{L(R) \cdot ps \cdot C^{\pm}}{Q^{\pm}} \ . \tag{8.2}$$

L and R are the raw $+$ and $-$ helicity counts, ps is the prescale factor, and C is a deadtime and efficiency correction factor. Each C and Q factor were determined for

each helicity and each event type. The correction factor, C, was written,

$$C = \frac{1}{(1 - cdt) \cdot t_{eff} \cdot fe} \ , \tag{8.3}$$

where cdt was computer deadtime, t_{eff} was trigger efficiency, and fe was the fiducial efficiency. Computer deadtime and trigger efficiency were helicity dependent and applied to each helicity separately. Including the different helicities and separate event types (where the subscripts 1 and 3 denote event types 1, singles events, and 3, coincidence events), the sum of all events (the denominator of the counting asymmetry equation) is as follows:

$$N_+ + N_- = \frac{L_1 \cdot ps_1 \cdot C_1^+}{Q^+} + \frac{L_3 \cdot C_3^+}{Q^+} + \frac{R_1 \cdot ps_1 \cdot C_1^-}{Q^-} + \frac{R_3 \cdot C_3^-}{Q^-} \ . \tag{8.4}$$

The prescale for event type 3 is omitted as it was always set to 1.

The raw asymmetry was extracted as a function of E' and θ and was scaled by the polarization factors and the dilution factor on a run-by-run basis, before being combined with other runs. With variables as defined above, the measured asymmetry becomes:

$$A_p(E', \theta) = \frac{\epsilon(E', \theta)}{f(E', \theta) P_t P_b} \ . \tag{8.5}$$

8.3 Estimation of Uncertainty in the Raw Asymmetry

The expression for the error for the simple definition of counting asymmetry is derived from

$$\delta\epsilon = \sqrt{\left(\frac{\partial\epsilon}{\partial N_+}\delta N_+\right)^2 + \left(\frac{\partial\epsilon}{\partial N_-}\delta N_-\right)^2} \ , \tag{8.6}$$

where $\delta L = \sqrt{L}$ and $\delta R = \sqrt{R}$. After partial differentiation of the equation for the counting asymmetry with respect to the positive and negative helicity counts, and

making these substitutions for δL and δR, we arrive at the following equation for the uncertainty in the counting asymmetry:

$$\delta\epsilon = \frac{2\sqrt{N_+ N_-}}{(N_+ + N_-)^{\frac{3}{2}}} \ . \tag{8.7}$$

As N_+ and N_- are roughly equal, $N_+ \simeq N_- = N/2$, then the error reduces even further to

$$\delta\epsilon \simeq \frac{1}{\sqrt{N}} \ . \tag{8.8}$$

However, the error calculation gets more complicated when accounting for the prescale factors. If the prescale factor for event type 1 was 4, and X event type 1 (non-coincidence) events were recorded, then, ignoring deadtimes and other efficiencies, $4{\cdot}X$ non-coincidence events were obtained. However, the uncertainty in the measurement, then, is that associated with the value of X. This uncertainty is then multiplied by the prescale factor, which makes it larger, rather than the smaller, which would be expected from the uncertainty from $4{\cdot}X$ counts. So the error analysis must be done on the actual events counted, X, which is not the overall N value. Consider the full equation for the counting asymmetry:

$$\epsilon = \frac{(L_1 \cdot ps \cdot C_1^+ \cdot Q_N + L_3 \cdot C_3^+ \cdot Q_N) - (R_1 \cdot ps \cdot C_1^- + R_3 \cdot C_3^-)}{(L_1 \cdot ps \cdot C_1^+ \cdot Q_N + L_3 \cdot C_3^+ \cdot Q_N) + (R_1 \cdot ps \cdot C_1^- + R_3 \cdot C_3^-)} \ . \tag{8.9}$$

In this equation, L_1 and L_3 represent event type 1 and 3, respectively, of one helicity, while R_1 and R_3 represent the same for the opposite helicity. C^+ and C^- are the composite deadtime and efficiency factors for the two helicities (subscripts represent event types). The term Q_N is the charge normalization of the two helicities ($Q_N = Q^-/Q^+$). The error in the asymmetry is then

$$\delta^2\epsilon = \left(\frac{\partial\epsilon}{\partial L_1}\right)^2 \delta^2 L_1 + \left(\frac{\partial\epsilon}{\partial L_3}\right)^2 \delta^2 L_3 + \left(\frac{\partial\epsilon}{\partial R_1}\right)^2 \delta^2 R_1 + \left(\frac{\partial\epsilon}{\partial R_3}\right)^2 \delta^2 R_3 \ , \tag{8.10}$$

where the individual contributions from each helicity dependent event type can be written as follows:

$$\left(\frac{\partial\epsilon}{\partial L_1}\right) = \frac{ps\cdot C_1^+\cdot Q_N}{\Sigma} - ps\cdot C_1^+\cdot Q_N\left(\frac{\Delta}{\Sigma^2}\right) , \tag{8.11}$$

$$\left(\frac{\partial\epsilon}{\partial L_3}\right) = \frac{C_3^+\cdot Q_N}{\Sigma} - C_3^+\cdot Q_N\left(\frac{\Delta}{\Sigma^2}\right) , \tag{8.12}$$

$$\left(\frac{\partial\epsilon}{\partial R_1}\right) = -\frac{ps\cdot C_1^-}{\Sigma} - ps\cdot C_1^-\left(\frac{\Delta}{\Sigma^2}\right) , \tag{8.13}$$

$$\left(\frac{\partial\epsilon}{\partial R_3}\right) = -\frac{C_3^-}{\Sigma} - C_3^-\left(\frac{\Delta}{\Sigma^2}\right) , \tag{8.14}$$

where Δ is the numerator of the asymmetry, and Σ is the denominator. If we count only the non-prescale adjusted counts in the error, then $\delta L_1 = \sqrt{L_1} \rightarrow (\delta L_1)^2 = L_1$; similarly for the other terms. Inserting into Equation 8.10,

$$\begin{aligned}
\delta^2\epsilon &= \left[ps\cdot C_1^+\cdot Q_N\left(\frac{1}{\Sigma}-\frac{\Delta}{\Sigma^2}\right)\right]^2\cdot L_1 + \left[C_3^+\cdot Q_N\left(\frac{1}{\Sigma}-\frac{\Delta}{\Sigma^2}\right)\right]^2\cdot L_3 \\
&\quad + \left[-ps\cdot C_1^-\left(\frac{1}{\Sigma}+\frac{\Delta}{\Sigma^2}\right)\right]^2\cdot R_1 + \left[-C_3^-\left(\frac{1}{\Sigma}+\frac{\Delta}{\Sigma^2}\right)\right]^2\cdot R_3 \\
&= (ps\cdot C_1^+\cdot Q_N)^2\left[\frac{\Sigma-\Delta}{\Sigma^2}\right]^2\cdot L_1 + (C_3^+\cdot Q_N)^2\left[\frac{\Sigma-\Delta}{\Sigma^2}\right]^2\cdot L_3 \\
&\quad + (-ps\cdot C_1^-)^2\left[\frac{\Sigma+\Delta}{\Sigma^2}\right]^2\cdot R_1 + (-C_3^-)^2\left[\frac{\Sigma+\Delta}{\Sigma^2}\right]^2\cdot R_3 \ .
\end{aligned}$$

Utilizing the fact that

$$\begin{aligned}
\Sigma-\Delta &= 2(R_1\cdot ps\cdot C_1^- + R_3\cdot C_3^-) \\
\Sigma+\Delta &= 2(L_1\cdot ps\cdot C_1^+\cdot Q_N + L_3\cdot C_3^+\cdot Q_N),
\end{aligned}$$

we find the result for the square of the error in the raw asymmetry to be

$$\begin{aligned}
\delta^2\epsilon &= 4[(ps\cdot C_1^+\cdot Q_N)^2 L_1 + (C_3^+\cdot Q_N)^2 L_3]\cdot\frac{(R_1\cdot ps\cdot C_1^- + R_3\cdot C_3^-)^2}{\Sigma^4} \\
&\quad + 4[(ps\cdot C_1^-)^2 R_1 + (C_3^-)^2 R_3]\cdot\frac{(L_1\cdot ps\cdot C_1^+\cdot Q_N + L_3\cdot C_3^+\cdot Q_N)^2}{\Sigma^4} \ .
\end{aligned} \tag{8.15}$$

This result is similar to that found in the thesis of TJ Liu [104] and in work by Oscar Rondon [105] (albeit for simpler cases).

8.4 Nitrogen Correction to the Asymmetry

Since the nitrogen in $^{15}NH_3$ is partially polarized, we must account for it in the measured asymmetry. The presence of polarized protons in ^{15}N means that the measured asymmetry is a mix of asymmetries from polarized protons in hydrogen and polarized protons in nitrogen. The polarization of each of these sources will be different and will therefore contribute differently to the asymmetry. Considering only the polarizable components, the equation for the number of counts is

$$N_+(N_-)(E',\theta) = N_h\sigma_h(E',\theta)(1\pm A_h(E',\theta)P_BP_h)+N_{15}\sigma_{15}(E',\theta)(1\pm A_{15}(E',\theta)P_BP_{15}) \ . \tag{8.16}$$

N_+ and N_- are defined as before, N_h and N_{15} are the number densities of hydrogen and ^{15}N respectively, σ_h and σ_{15} are the cross sections[1] for hydrogen and ^{15}N, A_h and A_{15} are the asymmetries due to both spin species, P_h and P_{15} are the respective polarizations, and P_B is the beam polarization. The difference between counts can then be written as

$$N_+(E',\theta) - N_-(E',\theta) = 2P_B[N_h\sigma_h(E',\theta)A_h(E',\theta)P_h + N_{15}\sigma_{15}(E',\theta)A_{15}(E',\theta)P_{15}] \ , \tag{8.17}$$

and the raw asymmetry becomes,

$$\begin{aligned} \epsilon(E',\theta) &= \frac{N_+(E',\theta) - N_-(E',\theta)}{N_+(E',\theta) + N_-(E',\theta)} \\ &= \frac{P_B[N_h\sigma_h(E',\theta)A_h(E',\theta)P_h + N_{15}\sigma_{15}(E',\theta)A_{15}(E',\theta)P_{15}]}{N_h\sigma_h(E',\theta) + N_{15}\sigma_{15}(E',\theta) + \sum(N\sigma(E',\theta))_{unpol}} \ . \end{aligned} \tag{8.18}$$

[1] The symbol σ is used to represent $\frac{d\sigma}{d\Omega dE'} \cdot \Delta\Omega \cdot \Delta E' \cdot \mathrm{I}$ throughout this chapter.

The denominator includes the sum of rates from all unpolarized materials. Remembering that the dilution factor is defined as the rate from hydrogen divided by the total rate,

$$f_h(E',\theta) = \frac{N_h\sigma_h(E',\theta)}{N_h\sigma_h(E',\theta) + N_{15}\sigma_{15}(E',\theta) + \sum(N\sigma(E',\theta))_{unpol}} \ , \tag{8.19}$$

we can write a dilution factor for ^{15}N as well:

$$f_{15}(E',\theta) = \frac{N_{15}\sigma_{15}(E',\theta)}{N_h\sigma_h(E',\theta) + N_{15}\sigma_{15}(E',\theta) + \sum(N\sigma(E',\theta))_{unpol}} \ . \tag{8.20}$$

This dilution factor for ^{15}N was determined from the model of radiated rates just as the dilution factor for hydrogen was determined. The expression for the raw asymmetry can then be written:

$$\epsilon(E',\theta) = P_B[f_h(E',\theta)A_h(E',\theta)P_h + f_{15}(E',\theta)A_{15}(E',\theta)P_{15}] \ , \tag{8.21}$$

and the hydrogen asymmetry can be solved,

$$A_h(E',\theta) = \frac{\epsilon(E',\theta) - f_{15}(E',\theta)A_{15}(E',\theta)P_{15}P_B}{f_h(E',\theta)P_hP_B} \tag{8.22}$$

The asymmetry from nitrogen can be determined directly from the data if a cut on W is made below the elastic peak from hydrogen. The Fermi-broadened nitrogen cross section extends below the hydrogen peak and is the only source of asymmetry in this region. Figure 8.1 shows the W dependence of the measured asymmetry, which is the raw count asymmetry divided by the beam and target (hydrogen) polarization.

The asymmetry in the lowest 3 W bins is of opposite sign from the hydrogen asymmetry and is the result of the polarized nitrogen. Since there is no scattering from hydrogen in this region ($\sigma_h = 0$, so $f_h = 0$), we can write

$$A_m(E',\theta) = \frac{\epsilon(E',\theta)}{P_BP_h} = \frac{f_{15}(E',\theta)A_{15}(E',\theta)P_{15}}{P_h} \ , \tag{8.23}$$

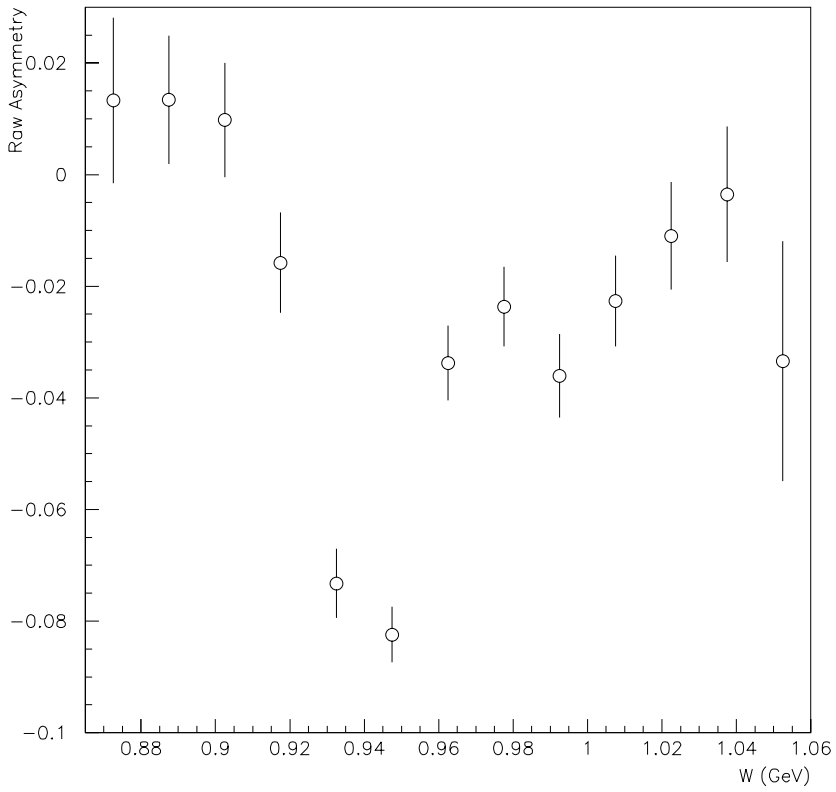

Figure 8.1: Measured asymmetry as a function of W for all $^{15}NH_3$ runs. The measured asymmetry is defined below as the count rate asymmetry (ϵ) divided by the beam and hydrogen polarization.

and

$$< A_{15} > \;=\; \left\langle \frac{\epsilon(E',\theta)}{f_{15}(E',\theta)P_B P_{15}} \right\rangle \quad \text{for W} < 0.915 \text{ GeV} \; . \tag{8.24}$$

One caveat to this method is that the asymmetry from nitrogen at low W is from the outer edge of the Fermi-broadened distribution of nitrogen events. These events towards the limit of the Fermi distribution may in fact be from different orbital shells than events in the middle of the Fermi distribution, and therefore may have a different asymmetry than those events. However, any difference in asymmetry would

most likely be small and, given the uncertainty in this data, a weighting by dilution factor only should be sufficient.

Both nitrogen and hydrogen polarizations can be measured directly. However, measurement of both polarization values at the same time was not possible and therefore a parameterization of the nitrogen polarization for a given hydrogen polarization was used. This parameterization was derived for experiment E143 at SLAC for the purposes of background subtraction [78]. The parameterization is as follows:

$$P_{15} = -(0.136P_h - 0.183P_h^2 + 0.335P_h^3) \ . \tag{8.25}$$

For a measured hydrogen polarization of 57%, this parameterization yields a nitrogen polarization of $\sim$ -8%. Parameterizations based on the theory of Equal Spin Temperature (EST) [106] have been developed since E143. This theory states that the spins of both the hydrogen and the nitrogen are connected by a common spin temperature when saturated by the microwave radiation which flips the spins of the electrons. If the polarization of the hydrogen is known, the spin temperature can be determined and used to calculate the polarization of the nitrogen. Values of the polarization determined by EST are not significantly different than those determined by the E143 parameterization. Using EST, hydrogen polarization of 57% yields a nitrogen polarization of $\sim$ -7%.

A systematic study of the asymmetry below the hydrogen peak was performed. The width (FWHM) of the hydrogen peak was determined experimentally to be 16.5 MeV, and the hydrogen cross section at W=0.915 GeV is 3.5 standard deviations from the peak at W=0.938 GeV. This value of W was set as the cutoff for calculating the nitrogen asymmetry. Specific values of target polarization and dilution factor for each run and each bin were used to obtain a weighted average value for A_{15} of -0.02659 $\pm$ 0.04735. This value was then used for each run as the nitrogen correction, scaled by the nitrogen dilution factor for the bin in question, and by the ratio of run

specific nitrogen to hydrogen polarization,

$$Ncorr_i(E',\theta) = f_{15}(E',\theta)\frac{P_{15_i}}{P_{h_i}} \cdot < A_{15} > \quad . \tag{8.26}$$

The subscript i represents individual runs. $Ncorr_i(E',\theta)$ is the nitrogen correction to the measured asymmetry for each run. The hydrogen asymmetry for each run can then be determined using the following equation:

$$A_{h_i}(E',\theta) = \frac{\frac{\epsilon_i(E',\theta)}{P_h P_B} - Ncorr_i(E',\theta)}{f_h(E',\theta)} \tag{8.27}$$

8.5 Unpolarized Radiative Corrections to the Asymmetry

The raw asymmetry, corrected for polarized protons in nitrogen, must be radiatively corrected for comparison to the Born value of the asymmetry. The effects of radiation moves events from the elastic peak into lower E' bins. This can be corrected by applying the unpolarized radiative correction factor, which we will designate, RC_u. If we assume that the only contributions to the numerator of the asymmetry (Equation 2.17) come from hydrogen after the nitrogen correction, we may write the asymmetry as follows:

$$\epsilon(E',\theta) = \frac{L^{rad}(E',\theta) - R^{rad}(E',\theta)}{L^{rad}(E',\theta) + R^{rad}(E',\theta) + X^{rad}(E',\theta)} \tag{8.28}$$

where L and R represent positive and negative helicity hydrogen counts, X represents the sum of all unpolarized counts (which cancels out in the numerator), and the superscript *rad* indicates that these are counts from radiated cross sections, since the data is naturally radiated.

Since the numerator has contributions only from hydrogen, while the denominator has contributions from all materials, the unpolarized radiative correction factor is the ratio of conversion factors from radiated to Born rates for hydrogen and the full

target,

$$RC_u(E',\theta) = \frac{N_h^0(E',\theta)/N_h^{rad}(E',\theta)}{N_{all}^0(E',\theta)/N_{all}^{rad}(E',\theta)} \ , \tag{8.29}$$

where N_h is the rate from hydrogen, and N_{all} is the total rate from all target materials (superscripts 0 and *rad* indicate Born and radiated values). We can then relate the measured asymmetry to the Born asymmetry through

$$\epsilon(E',\theta) \cdot RC_u(E',\theta) = \epsilon^0(E',\theta) \ . \tag{8.30}$$

Figure 8.2 illustrates the value of this unpolarized radiative correction factor over the range of E' and θ of interest. RC_u is zero where the hydrogen cross section is zero.

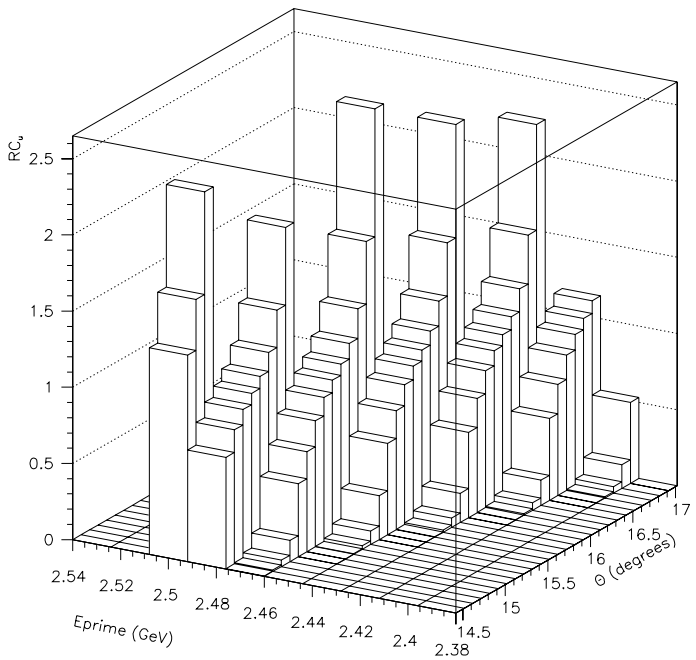

Figure 8.2: Unpolarized radiative correction factors as a function of E' and θ.

8.6 Polarized Radiative Corrections to the Asymmetry

In addition to unpolarized radiative corrections, *polarized* radiative corrections must also be made to the asymmetry. The cross section from polarized $e-p$ scattering is made up of both an unpolarized part (σ^u) and a polarized part (σ^p) [107],

$$\sigma^{\uparrow} = \sigma^u + \sigma^p \quad and \quad \sigma^{\downarrow} = \sigma^u - \sigma^p \ . \tag{8.31}$$

Each radiated cross section (σ_{rad}) has contributions from virtual processes and from real bremsstrahlung,

$$\sigma^{u,p}_{rad} = \sigma^{u,p}_0(1+\delta_V) + \sigma^{u,p}_R \ . \tag{8.32}$$

δ_V represents the correction in the cross section due to the virtual processes, while σ_R is the cross section from real bremsstrahlung. The subscript "0" indicates a Born cross section. Using these two equations, an equation can be derived linking the measured asymmetry to the Born asymmetry. The raw Born asymmetry[2], ϵ^0, written in detail, is as follows:

$$\epsilon^0 = \epsilon \cdot \frac{N^0_h/N^{rad}_h}{N^0_{all}/N^{rad}_{all}} \tag{8.33}$$

$$= \epsilon \cdot \frac{\dfrac{L^0+R^0}{L^0(1+\delta_V+\delta^u_R+\delta^L_R)+R^0(1+\delta_V+\delta^u_R+\delta^R_R)}}{\dfrac{\Sigma^0}{\Sigma^0(1+\delta_V+\delta_{R-unpol})}} \tag{8.34}$$

where δ^u_R is the correction due to real bremsstrahlung which is not polarization dependent, and $\delta^{L/R}_R$ are the corrections from real bremsstrahlung for a given helicity state, L or R. Σ is the sum of all cross sections in the target, and $\delta_{R-unpol}$ is the

[2]All asymmetries, cross sections, dilution factors, and radiative corrections are implied to be functions of E' and θ, but are written without the functional dependence, in most places, for ease of reading.

correction factor for all materials combined:

$$\delta_{R-unpol} = \frac{L^0(\delta_R^u + \delta_R^L) + R^0(\delta_R^u + \delta_R^R) + X^0\delta_R^X}{L^0 + R^0 + X^0} \tag{8.35}$$

The Σ^0s cancel, leaving

$$\epsilon^0 = \epsilon \cdot \frac{(L^0 + R^0)(1 + \delta_V + \delta_{R-unpol})}{L^0(1 + \delta_V + \delta_R^u + \delta_R^L) + R^0(1 + \delta_V + \delta_R^u + \delta_R^R)} \ , \tag{8.36}$$

where,

$$\epsilon = \frac{L^0(1 + \delta_V + \delta_R^u + \delta_R^L) - R^0(1 + \delta_V + \delta_R^u + \delta_R^R)}{\Sigma^0(1 + \delta_V + \delta_{R-unpol})} \ . \tag{8.37}$$

The terms containing $\delta_{R-unpol}$ cancel, and the equation can be simplified to

$$\epsilon^0 = \frac{L^0 + R^0}{\Sigma^0} \cdot \frac{(L^0 - R^0)(1 + \delta_V) + L^0(\delta_R^u + \delta_R^L) - R^0(\delta_R^u + \delta_R^R)}{(L^0 + R^0)(1 + \delta_V) + (L^0(\delta_R^u + \delta_R^L) + R^0(\delta_R^u + \delta_R^R))} \ , \tag{8.38}$$

where the term in front is simply the Born dilution factor, which is calculable from the model. The Born asymmetry, $(L^0 - R^0)/(L^0 + R^0)$, can be factored out of the numerator, leaving an expression containing the Born asymmetry times a multiplicative correction factor, plus an additive correction factor,

$$\frac{\epsilon^0}{f^0} = \frac{A^0}{1 + \frac{L^0(\delta_R^u + \delta_R^L) + R^0(\delta_R^u + \delta_R^L)}{(L^0 + R^0)(1 + \delta_V)}} + \frac{L^0(\delta_R^u + \delta_R^L) - R^0(\delta_R^u + \delta_R^R)}{L^{rad} + R^{rad}} \ . \tag{8.39}$$

The terms remaining on the right hand side of the equation are only dependent upon hydrogen counts and radiative corrections to hydrogen. The effects of all other materials has been factored out by the unpolarized radiative correction RC_u and the dilution factor, f^0.

The factor multiplied by A^0 in the first term on the right hand side of the equation, we shall call f_{RC} for historical reasons [108, 109]. It can be easily determined from

the following identity:

$$L^0(\delta_R^u + \delta_R^L) + R^0(\delta_R^u + \delta_R^R) = \sigma_h^0 \delta_R^T \tag{8.40}$$

where δ_R^T is the total correction to the cross section from real bremsstrahlung. δ_R^T is an unpolarized term since it contains the sum of corrections to both helicities. Since the rate for hydrogen scattering is proportional to the cross section, we can express the hydrogen Born unpolarized cross section in terms of the left helicity and right helicity counts,

$$\sigma_h^0 = L^0 + R^0 \ , \tag{8.41}$$

knowing that the constants of proportionality will cancel out of the equations for the polarized radiative correction factors. The expression for f_{RC} then reduces to

$$f_{RC} = \frac{1}{1 + \dfrac{\sigma_h^0 \delta_R^T}{\sigma_h^0(1+\delta_V)}} \tag{8.42}$$

The hydrogen Born cross sections cancel, leaving only a ratio of *unpolarized* radiative correction factors.

$$f_{RC} = \frac{1+\delta_V}{1+\delta_V+\delta_R^T} \ . \tag{8.43}$$

The additive term, A_{RC}, contains polarized radiative correction factors. Similar to the derivation in f_{RC}, the term $(L^0(\delta_R^u+\delta_R^L) - R^0(\delta_R^u+\delta_R^R))$ is equal to the *polarized* hydrogen cross section times the polarized correction to the tails:

$$L^0(\delta_R^u + \delta_R^L) - R^0(\delta_R^u + \delta_R^R) = \sigma_h^p \delta_R^p \ . \tag{8.44}$$

Using this identity, the additive correction factor is

$$A_{RC} = \frac{\sigma_h^p \delta_R^p}{\sigma_h^0(1+\delta_V+\delta_R^T)} \tag{8.45}$$

leaving a combination of polarized and unpolarized cross sections and radiative corrections to hydrogen.

The code MASCARAD [110] was used to determine these two corrections to the measured asymmetry, f_{RC} and A_{RC}. MASCARAD calculates radiative corrections for elastic electron-proton scattering with a polarized hydrogen target. Calculations were made for each E' and θ bin of the data, and from these correction factors, f_{RC} and A_{RC} were determined. The term f_{RC} had very little effect on the asymmetry as it was very nearly 1.0 in all bins. The range of f_{RC} was 0.999 to 1.000. A_{RC} was typically near zero, ranging from 0.002 to 0.000.

The sample output from MASCARAD can be seen in Table 8.1. This output file is for a one point input file. Values of f_{RC} and A_{RC} were then determined from the output values shown in the table.

bmom =	2.729	lepton momentum			
tmom =	0.000	proton momentum			
lepton =	1	1 = electron			
cutv =	0.000				
nev =	1	# of loops			
iy =	333522	random seed			
npoi =	1	# of points			
σ_h^0	$1+\delta_V$	δ_R^T	$1+\delta_V+\delta_R^T$	mean value	est. stat. error
0.1821E-03	0.842	0.000	0.843	0.843	0.000
σ_h^p	$1+\delta_V$	δ_R^p	$1+\delta_V+\delta_R^p$	mean value	est. stat. error
-0.3486E-04	0.842	-0.004	0.838	0.838	0.000

Table 8.1: Sample MASCARAD output file. For any one point ($npoi$) there are two rows of data. The first row contains the unpolarized cross section and radiative corrections. The second row contains the polarized cross section and radiative corrections. The last two columns of each row are meaningful only for MASCARAD runs of greater than one iteration (nev).

The full equation for the experimentally determined Born hydrogen asymmetry, incorporating the nitrogen correction and polarized and unpolarized radiative corrections, becomes

$$A_h(E',\theta) = \left(\frac{\epsilon(E',\theta)}{f^0(E',\theta)P_B P_T} - \frac{f_{15}(E',\theta) < A_{15} > P_{15}}{f^0(E',\theta)P_T}\right) \cdot RC_u(E',\theta) \quad (8.46)$$
$$= A_h^0(E',\theta) f_{RC}(E',\theta) + A_{RC}(E',\theta) \ .$$

The Born asymmetry can then be solved,

$$A_h^0(E',\theta) = \frac{\left(\frac{\epsilon(E',\theta)}{f^0(E',\theta)P_B P_T} - \frac{f_{15}(E',\theta)<A_{15}>P_{15}}{f^0(E',\theta)P_T}\right) \cdot RC_u(E',\theta) - A_{RC}(E',\theta)}{f_{RC}(E',\theta)} \ . \quad (8.47)$$

8.7 Determination of G_{Ep}

To obtain G_{Ep} from the asymmetry[3], one must rearrange the previous equation. Making the assumption that the magnetic field axis is exactly perpendicular to the q-vector for all events, and in the plane, the asymmetry is written:

$$A_h^0 = \frac{-2\sqrt{\tau(1+\tau)}\tan(\theta/2)(G_{Ep}/G_{Mp})}{(G_{Ep}/G_{Mp})^2 + \tau(1+2(1+\tau)\tan^2(\theta/2))} \ , \quad (8.48)$$

and we obtain the quadratic equation

$$\left(\frac{G_{Ep}}{G_{Mp}}\right)^2 + \frac{f(\tau,\theta)}{A_h^0}\left(\frac{G_{Ep}}{G_{Mp}}\right) + g(\tau,\theta) = 0 \ , \quad (8.49)$$

where $f(\tau,\theta)=2\sqrt{\tau(1+\tau)}\tan(\theta/2)$, and $g(\tau,\theta) = \tau(1+2(1+\tau)\tan^2(\theta/2))$. The solutions are

$$\frac{G_{Ep}}{G_{Mp}} = \frac{-f(\tau,\theta)}{2A_h^0} \pm \sqrt{\left(\frac{-f(\tau,\theta)}{2A_h^0}\right)^2 - g(\tau,\theta)} \ . \quad (8.50)$$

The positive root of this quadratic produces the value of G_{Ep}. Therefore, G_{Ep} can be written

$$G_{Ep} = C(1-R) \ , \quad (8.51)$$

[3]Again, form factors and asymmetries are functions of E' and θ.

where

$$C = \frac{-f(\tau,\theta)G_{Mp}}{2A_h^0} \quad \text{and,} \quad R = \sqrt{1 - \frac{4A_h^{0^2} g(\tau,\theta)}{f(\tau,\theta)^2}} \ .$$

Values of the form factor can now be determined for each E' and θ bin of the data. The value of G_{Ep} will eventually be combined into a single value of G_{Ep} for each run, and ultimately into a single value of G_{Ep} for all the data at this momentum transfer.

The statistical uncertainty in this measurement of G_{Ep} comes from the statistical uncertainty in A_h^0. Using Equation (8.50) and performing standard error propagation, taking only G_{Mp} and A_h^0 as sources of uncertainty, we arrive at the equation for the uncertainty in G_{Ep}:

$$\delta^2 G_{Ep} = \left(\frac{\partial G_{Ep}}{\partial G_{Mp}}\right)^2 \delta^2 G_{Mp} + \left(\frac{\partial G_{Ep}}{\partial A_h^0}\right)^2 \delta^2 A_h^0 \ . \tag{8.52}$$

Uncertainty in kinematic values have been ignored since the statistical uncertainty in the asymmetry dominates the overall uncertainty[4]. It can then be shown [11] that

$$\left(\frac{\partial G_{Ep}}{\partial G_{Mp}}\right)^2 = \left(\frac{G_{Ep}}{G_{Mp}}\right)^2 \ , \tag{8.53}$$

and

$$\left(\frac{\partial G_{Ep}}{\partial A_h^0}\right)^2 = \left[\frac{C^2}{A_h^{0^2}}\left(1 - \frac{1}{R}\right)^2\right] \ . \tag{8.54}$$

These yield a relative error,

$$\left(\frac{\delta G_{Ep}}{G_{Ep}}\right)^2 = \left(\frac{\delta G_{Mp}}{G_{Mp}}\right)^2 + \left(\frac{\delta A_h^0}{A_h^0}\right)^2 \left[C^2\left(1 - \frac{1}{R}\right)^2 \frac{1}{G_{Ep}^2}\right] \ , \tag{8.55}$$

which further reduces, given Equation (8.51), to

$$\left(\frac{\delta G_{Ep}}{G_{Ep}}\right)^2 = \left(\frac{\delta G_{Mp}}{G_{Mp}}\right)^2 + \left(\frac{\delta A_h^0}{A_h^0}\right)^2 \left(\frac{1}{R}\right)^2 \ , \tag{8.56}$$

[4] An estimate of the error in G_{Ep} from the uncertainty in τ was less than 1%.

where $(1/R)^2$ is the magnification factor, M. The relative error of the asymmetry, multiplied by M, dominates the error in G_{Ep} at these kinematics.

8.7.1 Inclusion of Polarization Angles

The equations for G_{Ep} from the previous section are for the case when the magnetic field axis is exactly perpendicular with the direction of $\vec{q}$ and the polarization is completely in the plane. However, because of the finite acceptance of the spectrometer and the fact that the direction of the target field is held constant, the angles θ^* and ϕ^* deviate from the ideal, the effects of which must be taken into account in determining G_{Ep}.

The mathematics is tedious, but the result is that G_{Ep} can still be written as $C(1-R)$, with changes to C and R:

$$C = \frac{-f(\tau,\theta)G_{Mp}}{2A_h^0} \cdot \sin\theta^* \cdot \cos\phi^* \ , \tag{8.57}$$

and,

$$R = \sqrt{1 - \frac{4A_h^0 \kappa(\tau,\theta)\cos\theta^*}{f(\tau,\theta)\sin^2\theta^*\cos^2\phi^*} - \frac{4A_h^{0^2} g(\tau,\theta)}{f(\tau,\theta)^2\sin^2\theta^*\cos^2\phi^*}} \ , \tag{8.58}$$

where $\kappa(\tau,\theta) = \sqrt{\tau(1+(1+\tau)\tan^2(\theta/2))}$. The kinematic factors $f(\tau,\theta)$ and $g(\tau,\theta)$ are unchanged.

The relative error in G_{Ep} is also affected by the inclusion of these two angles and can now be written:

$$\left(\frac{\delta G_{Ep}}{G_{Ep}}\right)^2 = \left(\frac{\delta G_{Mp}}{G_{Mp}}\right)^2 + \left(\frac{\delta A_h^0}{A_h^0}\right)^2 \left[C\left(1-\frac{1}{R}\right) + \frac{\kappa(\tau,\theta)G_{Mp}}{R\tan\theta^*\cos\phi^*}\right]^2 \frac{1}{G_{Ep}^2} \ . \tag{8.59}$$

Polarization angles were determined from a Monte Carlo routine (MCEEP), modified by Hongguo Zhu for this experiment [85]. A distribution of events from inclusive scattering, for a composite $^{15}NH_3$ target (including hydrogen, nitrogen, helium, and aluminum), was generated and compared to the data in variables E' (see Figure 8.3)

and θ (see Figure 8.4) to determine if MCEEP accurately represents the data. The composite distributions of Figures 8.3 and 8.4 compare very well to the data. The distribution of θ^*, ϕ^*, and $\cos\phi^*$ from Monte Carlo can be seen in Figures 8.5 - 8.7. The average value of $\cos\phi^*$ was determined since the contribution from ϕ^* to G_{Ep} is always in a cosine. This average value of $\cos\phi^*$ is substituted into Equation 8.59 wherever $\cos\phi^*$ appears. Since $\phi^* \sim 180°$, this value is $\sim$ -1.0. The average value of θ^* is used because the weighted average value of G_{Ep} for a range of values for θ^* is equal to the value of G_{Ep} from a weighted average value of θ^*.

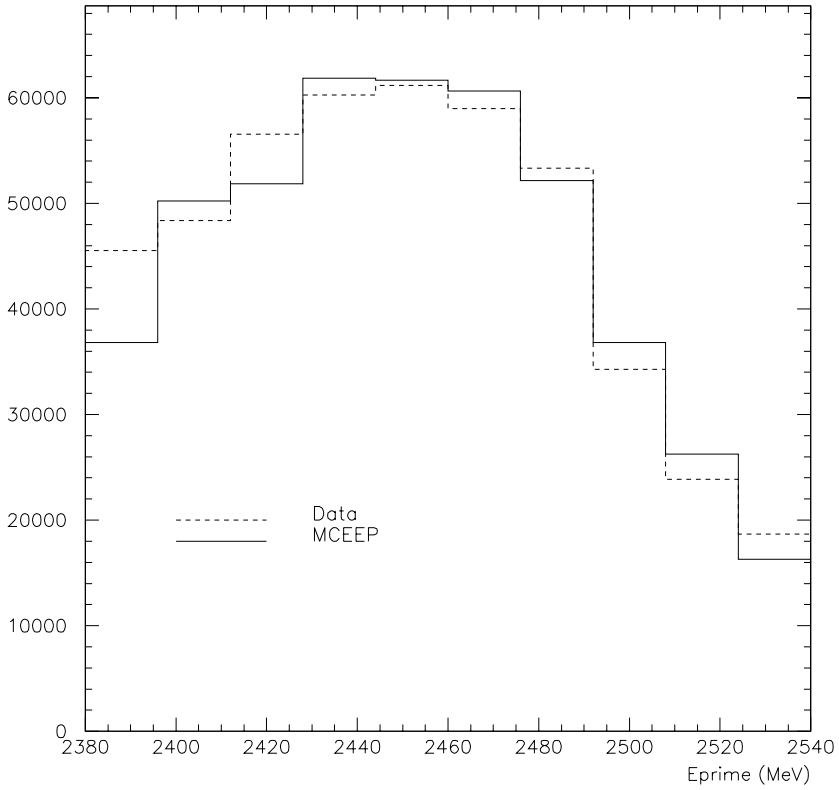

Figure 8.3: MCEEP composite target event distribution in E' vs. data at Q^2=0.5 $(\mathrm{GeV}/c)^2$. Composite target includes hydrogen, nitrogen, helium, and aluminum at densities found in the target model. The data distribution comes from run 21690. An overall normalization factor was applied to the MCEEP distribution to match the same relative scale as the data.

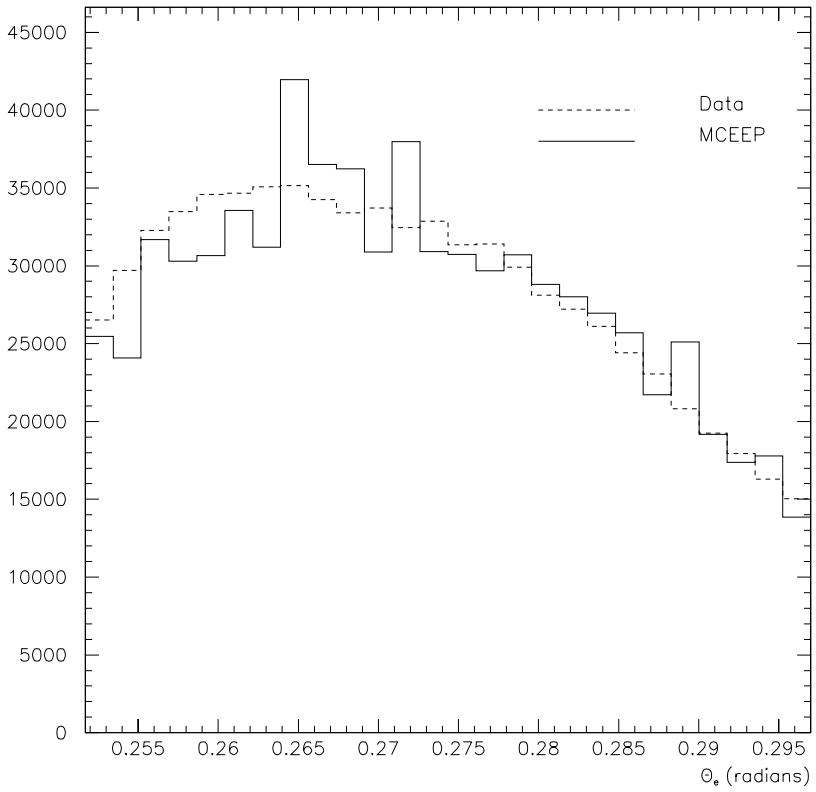

Figure 8.4: MCEEP composite target event distribution in scattering angle vs. data at Q^2=0.5 (GeV/c)^2. Composite target includes hydrogen, nitrogen, helium, and aluminum at densities found in the target model. Data rate comes from run 21690. An overall normalization factor was applied to the MCEEP distribution to match the same relative scale as the data.

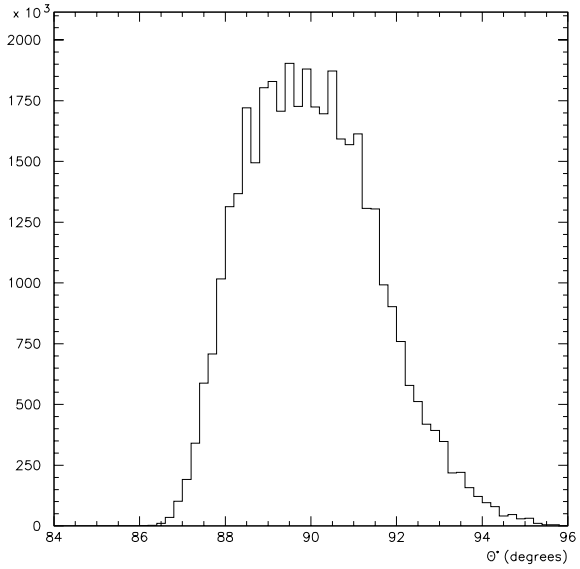

Figure 8.5: θ^* values from MCEEP at Q^2=0.5 (GeV/c)^2. The average value of θ^* is 90.09°.

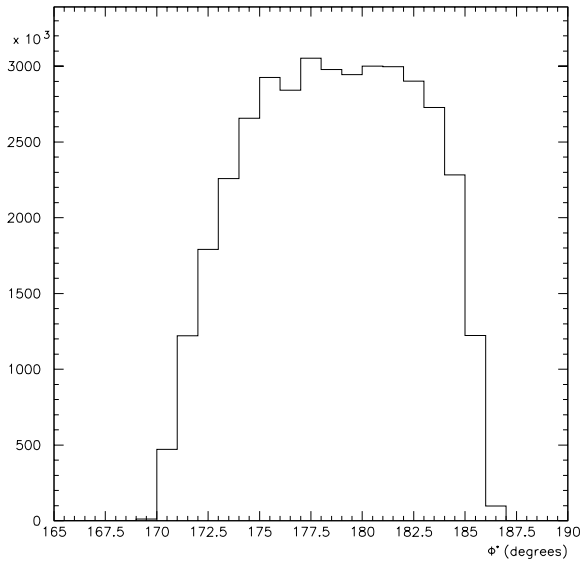

Figure 8.6: ϕ^* values from MCEEP at Q^2=0.5 (GeV/c)^2. The value of ϕ^* is centered around 178.5°, rather than 180°, reflecting the average tilt in the scattering plane.

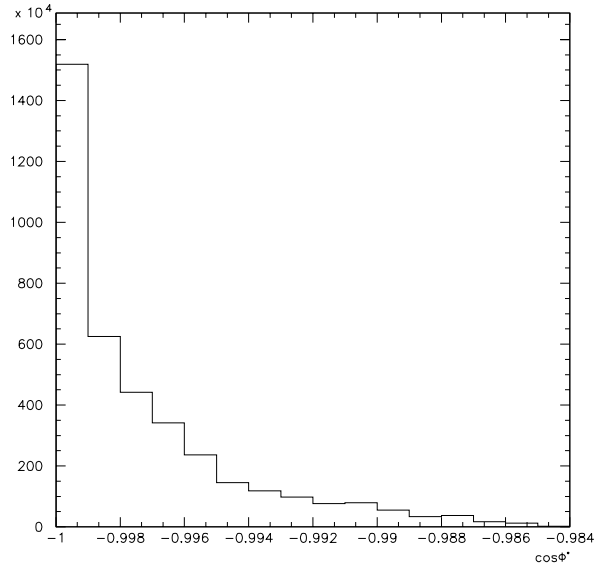

Figure 8.7: $\cos\phi^*$ values from MCEEP at Q^2=0.5 (GeV/c)^2. The average value of $\cos\phi^*$ is -.9973.

Chapter 9 Results

9.1 Experimental Results

Data from twenty-one $^{15}NH_3$ runs were analyzed and asymmetries were calculated for E' bins ranging from 2.380 GeV to 2.540 GeV, in bins of 16 MeV. Bins in θ ranged from 14.42° to 17.02° with bin widths of 0.10°, giving a total of 260 bins. Each bin resulted in an independent asymmetry measurement with an associated error. Due to the multitude of bins, a single bin did not include many events, resulting in large error bars for that particular bin. However, data from all bins could be combined to get an average asymmetry value for the entire set of data. The weighted average asymmetry for a given run was determined from the value of the asymmetry in each bin and the associated statistical uncertainty for each bin as follows:

$$A_i = \frac{\sum_j \sum_k A(E',\theta) \cdot wt(E',\theta)}{\sum_j \sum_k wt(E',\theta)} \ . \tag{9.1}$$

The subscript i represents each run. The function $wt(E',\theta)$ is the inverse of the statistical uncertainty squared, $1/(\delta A(E',\theta))^2$.

The asymmetry was subject to a series of corrections, as described in the previous chapter, before it could be compared to theoretical predictions. This process occurred in several stages (which are represented by subscripts a, b and c). The first stage (stage a) was to correct the raw counting asymmetry for the dilution factor, target polarization, and beam polarization:

$$A_a(E',\theta) = \frac{\epsilon(E',\theta)}{f(E',\theta)P_t P_b} \ . \tag{9.2}$$

This is identical to Equation (8.5). The next step (stage b) is to correct for the

nitrogen asymmetry, by subtracting the nitrogen correction (divided by the hydrogen dilution factor), as shown in Equation (8.27):

$$A_b(E',\theta) = \frac{\frac{\epsilon_i(E',\theta)}{P_h P_B} - Ncorr_i(E',\theta)}{f_h^0(E',\theta)} = A_a(E',\theta) - \frac{Ncorr_i(E',\theta)}{f_h(E',\theta)} \ . \tag{9.3}$$

After the nitrogen correction was applied, the unpolarized radiative correction could be applied (stage c). This correction assumes that only protons from hydrogen contribute to the numerator of the asymmetry (see Equation 2.18). The unpolarized radiative correction was calculated as described in the previous chapter, and is a multiplicative factor applied to the asymmetry:

$$A_c(E',\theta) = \frac{\frac{\epsilon_i(E',\theta)}{P_h P_B} - Ncorr_i(E',\theta)}{f_h^0(E',\theta)} \cdot RC_u = A_b(E',\theta) \cdot RC_u \ . \tag{9.4}$$

The final step is applying the polarized radiative corrections. This correction, as described in the previous chapter, has two components - a multiplicative factor (f_{RC}) and an additive factor (A_{RC}),

$$A_h^0(E',\theta) = \frac{\frac{\frac{\epsilon_i(E',\theta)}{P_h P_B} - Ncorr_i(E',\theta)}{f_h^0(E',\theta)} \cdot RC_u - A_{RC}}{f_{RC}} = \frac{A_c(E',\theta) - A_{RC}}{f_{RC}} \ . \tag{9.5}$$

Using Equation (9.1), an average asymmetry for each run was produced at each stage of correction. Plots of the individual asymmetries at each stage can be seen in Figure 9.1. An experiment average asymmetry was then determined using the individual asymmetries (and corresponding statistical uncertainties),

$$< A_h^0 >= \frac{\sum_i A_i \cdot wt_i}{\sum_i wt_i} \ . \tag{9.6}$$

The experiment averaged asymmetry at each stage of correction was as follows:

$$< A_a > \ = \ -0.12933 \pm 0.00684$$

$$
\begin{aligned}
< A_b > &= -0.13156 \pm 0.00686 \\
< A_c > &= -0.14190 \pm 0.00746 \\
< A_h^0 > &= -0.14203 \pm 0.00746 \ .
\end{aligned}
$$

The nitrogen correction and unpolarized radiative corrections are the largest corrections, while the unpolarized radiative correction is very small.

A weighted average value of the scattered energy ($< E' > = 2.4588$ GeV) and scattering angle ($< \theta > = 15.5852°$) produced an average $Q^2 = 0.4934$ (GeV/c)^2.

After all corrections are performed, and the asymmetry is summed over all bins and all runs, the data point at Q^2=0.4934 (GeV/c)^2 overlaps all the models, albeit with large error bars. A plot of the modelled Born asymmetries compared to the experimental value is shown in Figure 9.2.

At this momentum transfer, the dipole approximation yields $G_{Mp} = \mu_p G_D$=0.97217. With an asymmetry value of A_h^0 = -0.14203 $\pm$ 0.00746 and average values of θ^*=90.09° and cos ϕ^*=0.9973, a value of G_{Ep} was determined to be $G_{Ep} = 0.34335 \pm 0.22399$. This compares favorably to the value from the dipole model, $G_D = 0.34807$, albeit with very large error bars, due to the insensitivity of the asymmetry to G_{Ep} at these kinematics. A plot of G_{Ep}/G_D is shown in Figure 9.3, compared to the values predicted by various models. The error bars on the measurement extend well beyond the boundaries of the plot, which demonstrates the insensitivity of the measurement at this momentum transfer. Table 9.1 summarizes the experimental results from this kinematic point. Uncertainty in G_{Mp} is assumed to be 2%. Similarly, Figures 9.4 and 9.5 show this experimental point against previous data. The error bars are large, but this is due to the magnification of the asymmetry error at this momentum transfer. This factor drops off dramatically at higher Q^2 values.

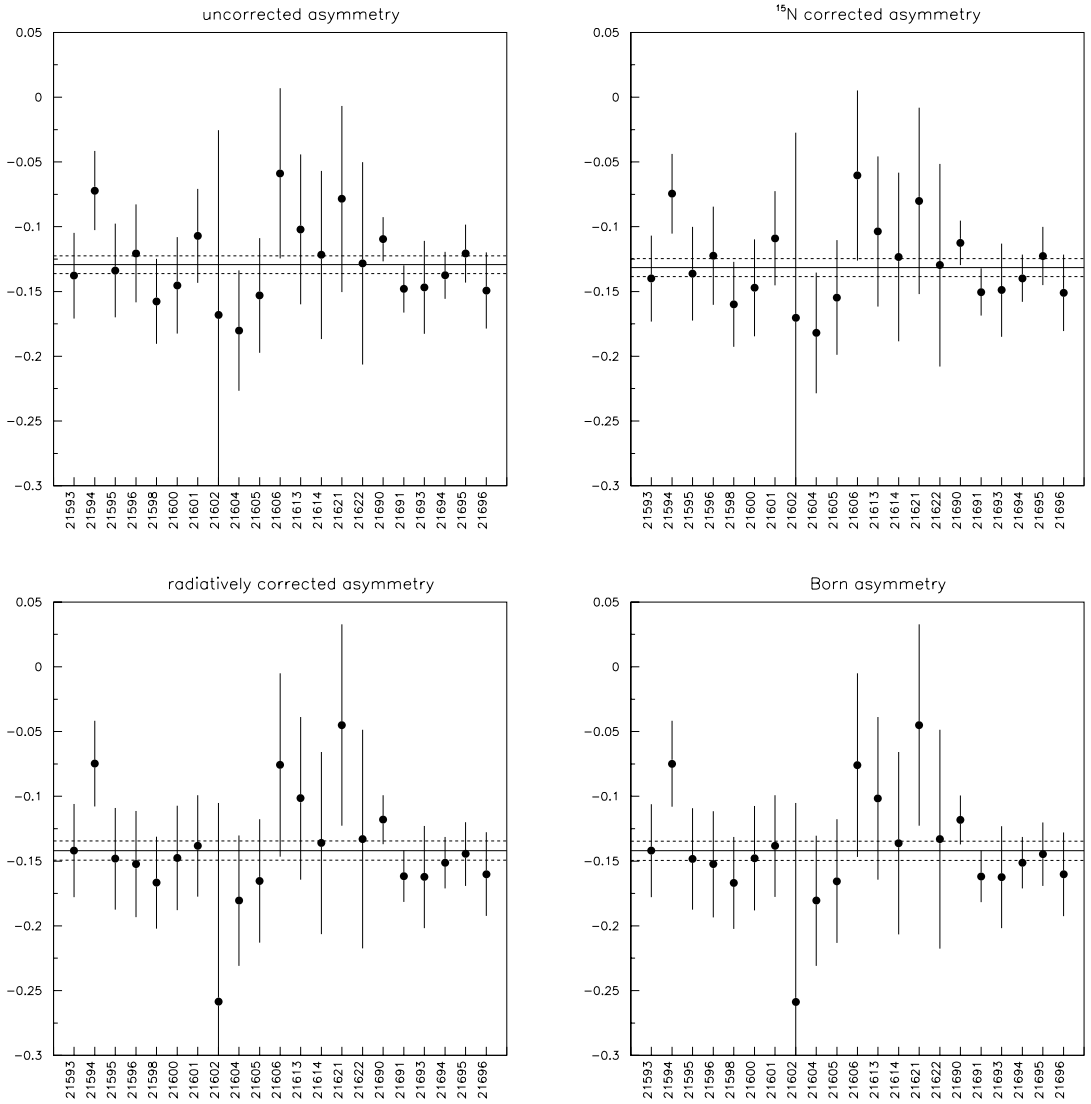

Figure 9.1: Evolution of individual asymmetries through various corrections. The top left plot is the raw asymmetry corrected for only the dilution factor, target polarization, and beam polarization. The top right plot is that raw asymmetry corrected for the nitrogen content. The bottom left plot illustrates the effect of unpolarized radiative corrections on the asymmetry. The bottom right plot is of the fully corrected asymmetries, including polarized radiative corrections. All points are plotted against run number.

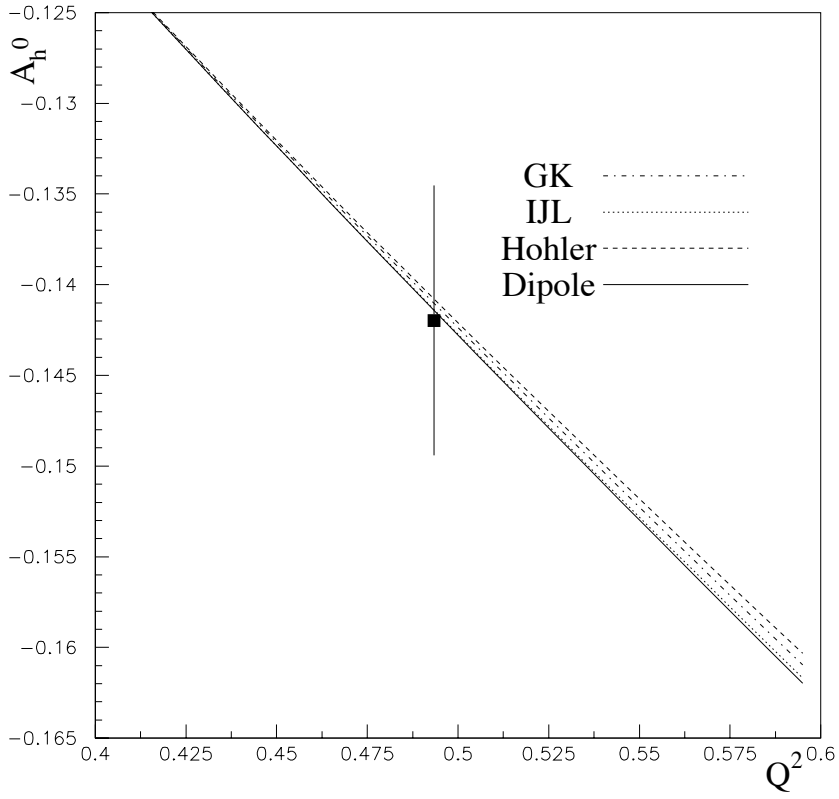

Figure 9.2: Experimentally determined Born asymmetry plotted with models of the asymmetry [17, 21, 26].

Table 9.1: Average values for Q^2=0.5 (GeV/c)^2 data

E'	2.4588 GeV
θ_{scat}	15.5852°
Q^2	0.4934 (GeV/c)^2
A_h^0	-0.14203 ± 0.00746
θ^*	90.09°
$\cos\phi^*$	-0.9973
G_{Mp}	0.97217 ± 0.01944
G_{Ep}	0.34335 ± 0.22399
G_D	0.34807
G_{Ep}/G_D	0.98643 ± 0.64352

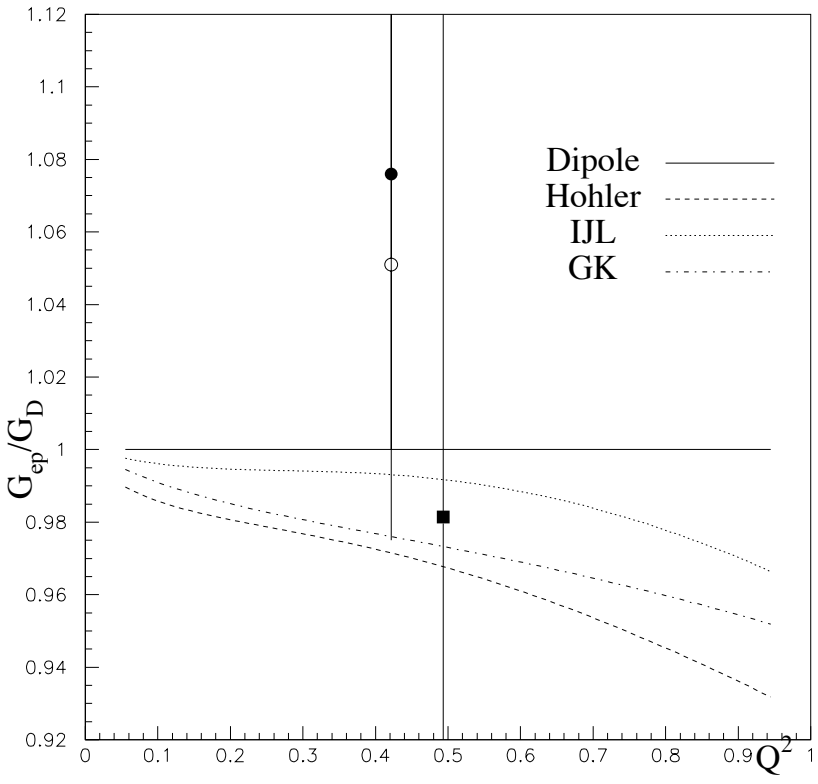

Figure 9.3: Experimentally determined charge form factor divided by the dipole charge form factor, plotted with models of the form factor. Data from E93026 is represented by the solid square. Models by Hohler [17], Iachello, Jackson and Lande [21] and Gari and Krümpelmann [26] are represented by lines. Lattice calculations are represented by the closed (with sea contribution) and open circles (without sea contribution) [28].

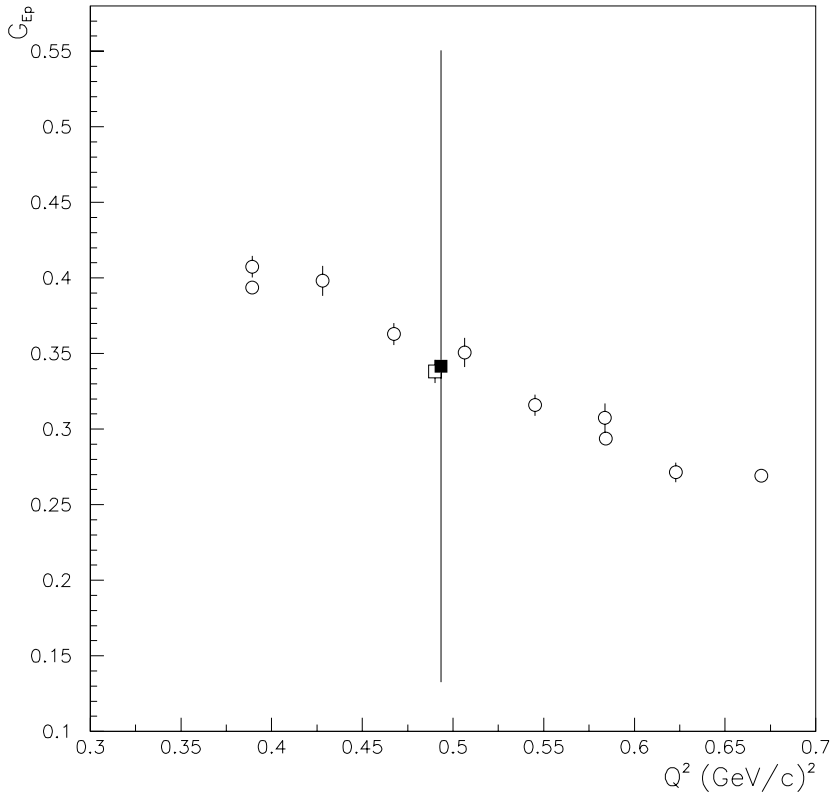

Figure 9.4: Experimentally determined charge form factor, plotted with previous data. The open circles are from Rosenbluth separation [32, 34, 35] and the open square is from recoil polarimetry [43]. The solid square is from this experiment.

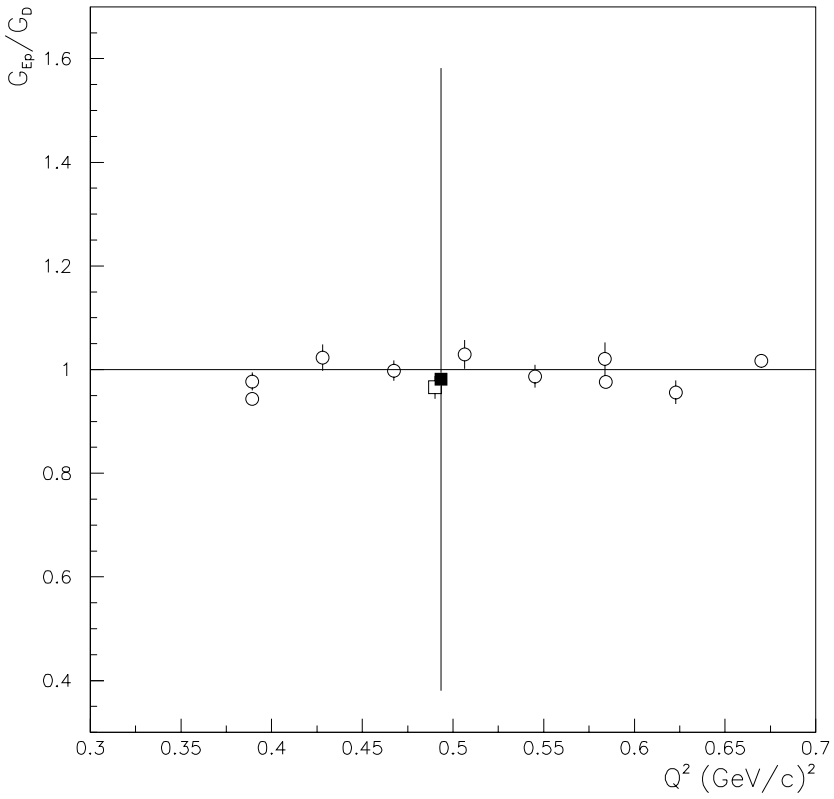

Figure 9.5: Experimentally determined charge form factor divided by the dipole charge form factor, plotted with previous data [32, 34, 35]. The open circles are from Rosenbluth separation and the solid square is from this experiment.

Figure 9.6 shows the relationship between the momentum transfer and the magnification factor. It is evident from the plot that magnification of the asymmetry uncertainty is very sensitive to the Q^2 value. This sensitivity is extended to the choice of kinematics for a given Q^2 value as can be seen in Figure 9.7, which shows the fluctuation in the magnification at a fixed Q^2 across a range of scattering angles. Error in the asymmetry was fixed at 10% for all data points.

Figure 9.8 shows the behavior of the magnification factor at a fixed Q^2 value as the value of G_{Ep} changes with respect to G_D. The value of the magnification factor blows up as the square-root term in the quadratic equation approaches zero (at $\sim$1.08 G_D for the kinematics in the figure). It is clear that the magnification of the error in the asymmetry is affected not only by the scattered electron energy and scattering angle, and not even simply on the resulting Q^2 value, but it also depends on the value of G_{Ep} determined from the asymmetry.

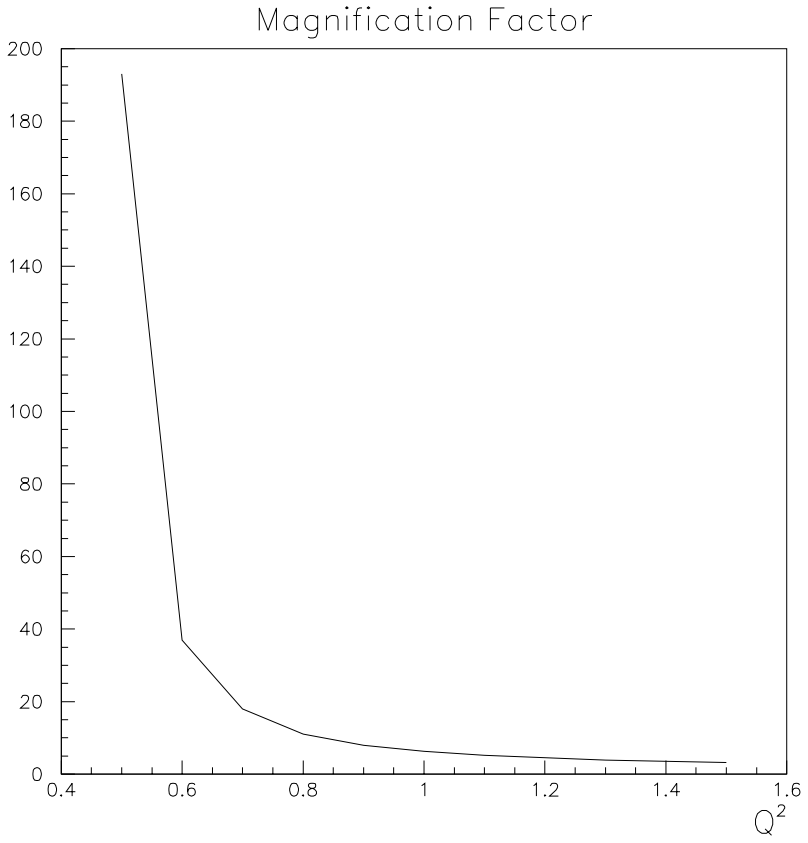

Figure 9.6: Magnification factor as a function of Q^2. For each Q^2, the value of G_{Ep} was assumed to be equal to the value of G_D. The value of θ was held fixed. E' was determined from θ and the incident energy, E_0, which was varied to change the value of Q^2.

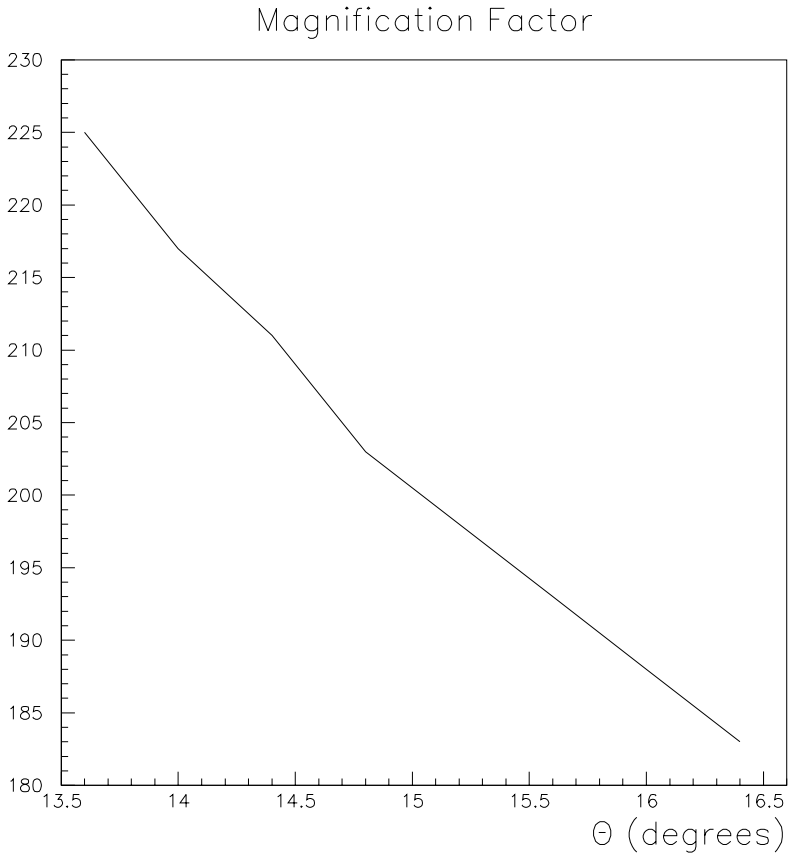

Figure 9.7: Magnification factor as a function of θ. For each θ, the value of E' was adjusted to fix the Q^2 value at 0.50 $(\mathrm{GeV}/c)^2$. The value of G_{Ep} was assumed to be equal to the value of G_D.

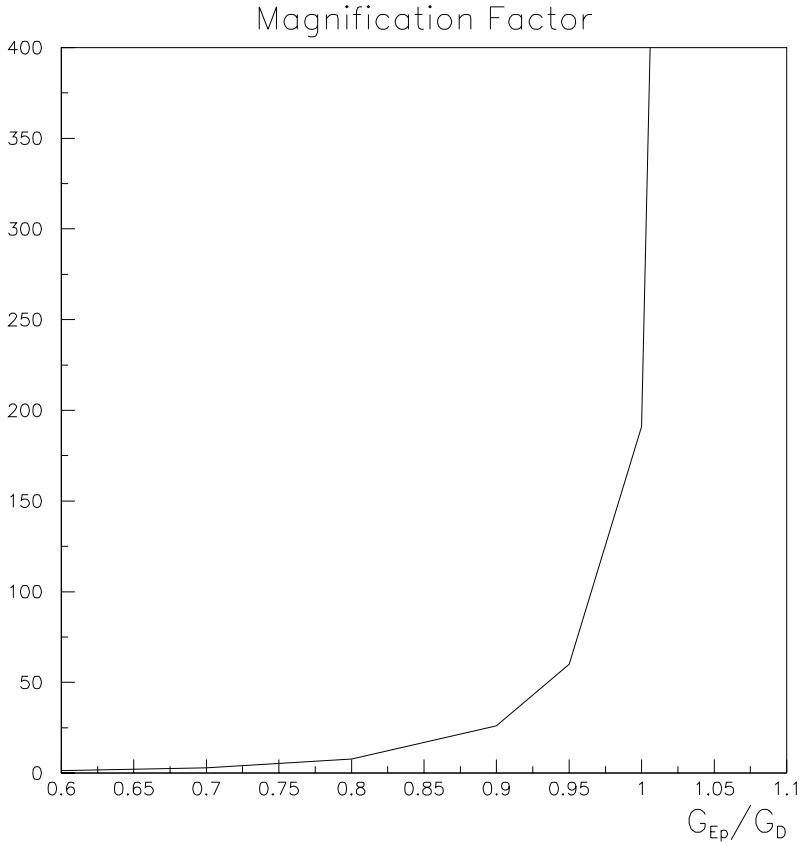

Figure 9.8: Magnification factor as a function of G_{Ep}/G_D. Kinematics are fixed at E_0=2.729 GeV, E' = 2.462 GeV, θ = 15.68°, and Q^2=0.50 (GeV/c)^2. The magnification factor approaches ∞ at G_{Ep}/G_D=1.08 at these kinematics.

9.1.1 Results at Q^2=1.0 (GeV/c)^2

Despite the lack of experiment time dedicated to NH_3 running at Q^2=1.0 (GeV/c)^2, a rough determination of the asymmetry at this momentum transfer was made with the four runs available. A packing fraction of 55% was assumed based on the packing fractions of other runs throughout the experiment. Error in this value would not contribute significantly to the statistical uncertainty. A nitrogen correction was done in the same manner as for the Q^2=0.5 (GeV/c)^2 data, yielding a weighted average value of $< A_{15} >$ = -0.51144 $\pm$ 0.26879. Unpolarized radiative corrections were obtained from the model, as before. However, polarized radiative corrections were not performed as they had little impact on the measurement at Q^2=0.5 (GeV/c)^2. The values of θ^* and $\cos\phi^*$ were assumed to be the same as for Q^2=0.5 (GeV/c)^2, 90.09° and -0.9973 respectively.

With all the stated corrections, the value of the asymmetry at Q^2=1.0 (GeV/c)^2 was A_h^0 = -0.13165 $\pm$ 0.04628 (a 35% statistical uncertainty). The weighted average Q^2 value was found to be Q^2 = 0.9625 (GeV/c)^2 from an average E' = 3.715 GeV and an average θ = 14.2°. At these kinematics and for this asymmetry value, the magnification factor was calculated to be only 12.5, far smaller than at the lower Q^2 point. This yielded a value for the form factor of G_{Ep} = 0.20076 $\pm$ 0.24933. The 124% uncertainty is misleading when comparing to the 61% error from the lower momentum transfer, as much of this is due to the difference in statistical uncertainty. If the Q^2=1.0 (GeV/c)^2 asymmetry had the same uncertainty as the Q^2=0.5 (GeV/c)^2 asymmetry (5.2%), this would give a final value of G_{Ep}=.20076 $\pm$ 0.03696, for only a 18% uncertainty.

Table 9.2 shows the average experimental results at this momentum transfer. Uncertainty in G_{Mp} is again assumed to be 2%.

Table 9.2: Average values for Q^2=1.0 (GeV/c)^2 data

E'	3.7147 GeV
θ_{scat}	14.2032°
Q^2	0.9625 (GeV/c)^2
A_h^0	-0.13165 ± 0.04628
θ^*	90.09°
$\cos\phi^*$	-0.9973
G_{Mp}	0.50335 ± 0.01007
G_{Ep}	0.20076 ± 0.24933
G_D	0.18022
G_{Ep}/G_D	1.114 ± 1.384

Chapter 10 Summary and Conclusions

The proton electric form factor, G_{Ep} has been measured at momentum transfer squared values of Q^2=0.5 (GeV/c)^2 and Q^2=1.0 (GeV/c)^2. Although the statistical errors are large, the measurements are in agreement with previous results from other experiments and are in line with the dipole approximation. The charge form factor is relatively well known and in most cases has been seen to follow the dipole approximation. The results of this analysis provides a validation of this *new technique* more than it confirms a well known quantity.

This experiment has improved upon the theoretical basis for determing the form factors over the Rosenbluth separation method. With sufficient statistics at kinematics optimized for the measurement, this new method could provide a precise measurement of the form factor dependence as a function of Q^2. Experiment E93026 was never optimized for G_{Ep} data taking, and as a result, the choice of kinematics is poor for obtaining a precise result. The magnification factor at Q^2=0.5 (GeV/c)^2 is too large to obtain form factor values of sufficient precision. However, it has been shown in this analysis that the conditions are much better at Q^2 = 1.0 (GeV/c)^2 and higher.

The choice of kinematics also influenced the method with which we analyzed the data. The θ^* and ϕ^* dependence of the form factor has been approximated by using average values of θ^* and $\cos\phi^*$. This was done to avoid a problem in the calculation of G_{Ep} at Q^2=0.5 (GeV/c)^2. Nearly half of the θ^* values produce a value of G_{Ep} that is imaginary. This is illustrated by Figure 10.1, which shows the calculated value of G_{Ep} across a range of θ^* and ϕ^* values. The plot assumes the same value of the asymmetry in each bin (the value stated in Table 9.1. These imaginary results for

G_{Ep} are a result of a negative number in the root:

$$R = \sqrt{1 - \frac{4A_h^0 \kappa(\tau,\theta)\cos\theta^*}{f(\tau,\theta)\sin^2\theta^*\cos^2\phi^*} - \frac{4A_h^{0^2} g(\tau,\theta)}{f(\tau,\theta)^2\sin^2\theta^*\cos^2\phi^*}} \ . \tag{10.1}$$

In all likelihood, the asymmetry has some dependence on θ^* and ϕ^*. An attempt was made to extract the asymmetry from the data for each bin and calculate G_{Ep} for each bin as well. However, since the value of G_{Ep} is imaginary at high θ^* and extreme ϕ^*, and depends on the value of the asymmetry as well, the resulting average, non-imaginary G_{Ep} value would be calculated from only half the data and would be the result of a smaller asymmetry value than was actually measured (the larger the asymmetry, the greater the chance of an imaginary G_{Ep} value). This problem was avoided by taking an average of θ^* and $\cos\phi^*$. However, it is still fortunate that we were able to maintain θ^* at nearly 90°. Had the distribution been shifted to 90.2°, then even this method of using the average θ^* and $\cos\phi^*$ values would have yielded an imaginary G_{Ep}.

The ideal analysis method would be to bin the data as a function of θ^* and ϕ^*. Each bin could have an associated asymmetry and G_{Ep} value, which could be compared to results produced by a monte carlo. An alternative approach is to compare the asymmetry, binned in θ^* and ϕ^*, to the asymmetry predicted from different values of G_{Ep}. Hopefully future experiments will be able to take advantage of the lessons learned in E93026.

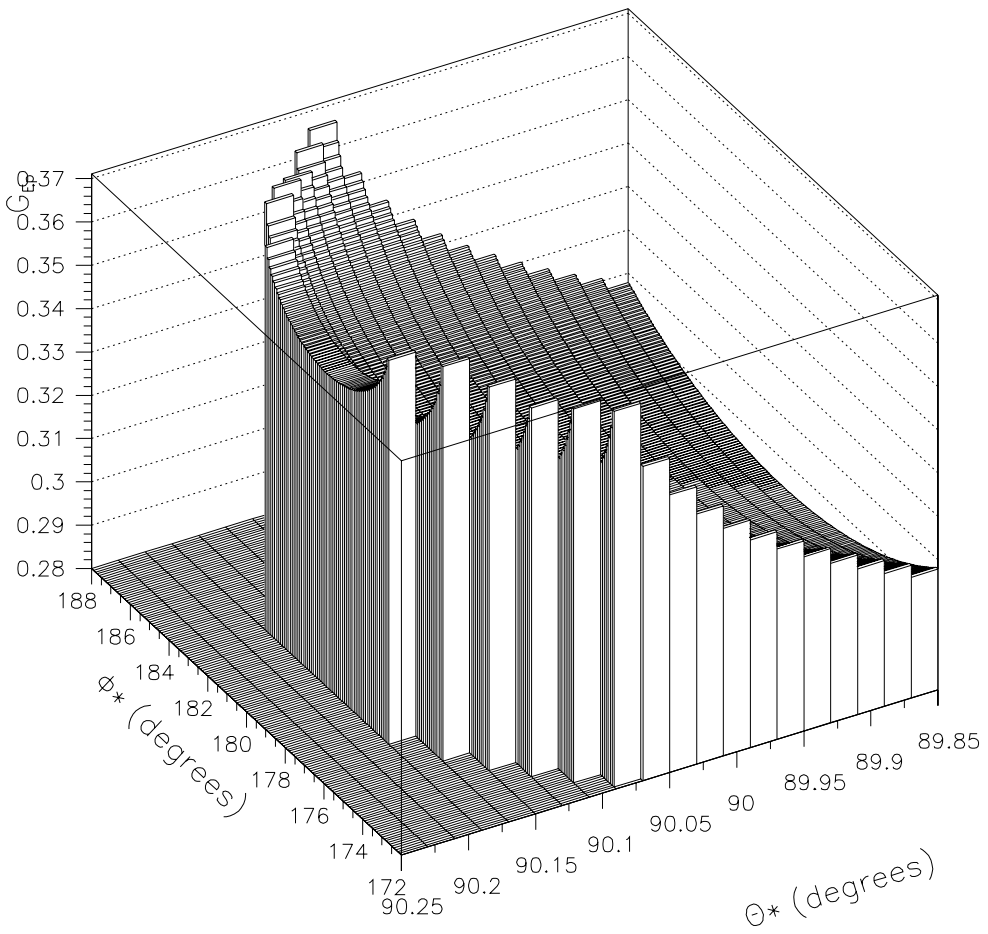

Figure 10.1: Theoretical dependence of G_{Ep} as a function of θ^* and ϕ^*. At certain values of θ^* and ϕ^*, the calculated value of G_{Ep} from the asymmetry value measured in E93026 is imaginary. At θ^* values higher than 90.05°, the calculated value of G_{Ep} is imaginary for some values of ϕ^*, starting at the extremes of the range of ϕ^* values. Above 90.20°, all values of G_{Ep} are imaginary, regardless of the value of ϕ^*.

Appendix A Asymmetry Lists

Table A.1: The list of $^{15}NH_3$ asymmetries at $Q^2 = 0.5$ (GeV/c)^2.

Run	A_h^0	δA_h^0
21593	-0.14196	0.03579
21594	-0.07478	0.03297
21595	-0.14832	0.03912
21596	-0.15252	0.04088
21598	-0.16677	0.03535
21600	-0.14770	0.04024
21601	-0.13850	0.03906
21602	-0.25867	0.15348
21604	-0.18064	0.05021
21605	-0.16553	0.04756
21606	-0.07596	0.07079
21613	-0.10152	0.06271
21614	-0.13607	0.07026
21621	-0.04488	0.07762
21622	-0.13311	0.08433
21690	-0.11812	0.01879
21691	-0.16173	0.01987
21693	-0.16245	0.03934
21694	-0.15122	0.01978
21695	-0.14474	0.02449
21696	-0.16012	0.03221

Table A.2: The list of $^{15}NH_3$ asymmetries at $Q^2 = 1.0$ (GeV/c)^2.

Run	A_h^0	δA_h^0
22320	-0.06695	0.07551
22325	-0.51907	0.25861
22328	-0.13732	0.13758
22329	-0.15514	0.06687

Appendix B Target Runlists

Table B.1: A list of good $^{15}ND_3$ runs at $Q^2 = 0.5$ (GeV/c)^2.

Run Number	Date [1998]	N_{coin} [k]	P_t [%]	Charge [μC]	P_b [%]	I_b [nA]	PS Factor
21820	09/01	200.9	22.12	102.4	76.43±0.73	89.1	2
21825		222.7	21.78	113.5		84.5	
21827		203.6	21.31	102.2		84.2	
21829		218.5	20.55	111.9		90.7	
21830		201.1	20.20	103.0		95.0	
21832		206.3	19.66	106.4		92.7	
21833		200.0	19.71	102.9		73.3	
21839		198.9	19.74	102.8		79.8	
21849		200.7	19.06	102.7		95.6	
21850		119.8	18.91	61.7		83.5	
21852		203.1	18.34	106.2		93.2	
21853		205.4	18.33	105.7		99.4	
21854		239.2	18.20	123.7		99.8	
21855		199.3	17.52	102.3	76.43±0.73	89.8	2
21856	09/02	203.5	17.25	104.9		96.8	
21857		207.7	17.17	107.6		96.6	
21870		197.7	16.21	101.9		96.2	
21871		198.2	16.11	102.1		90.0	
21872		195.9	16.02	100.5		86.0	
21873		196.8	15.98	102.0		83.4	
21875		195.5	15.71	100.2		84.6	
21876		193.7	15.64	100.0		81.0	
21881		123.1	- 3.76	60.1		95.6	1
21885		281.2	-14.25	140.0		94.1	4
21888		280.3	-20.72	138.6		87.8	4
21889		279.7	-21.60	138.6		81.8	
21890		280.1	-21.54	139.0		87.3	

21891		281.0	-21.37	138.9		88.5	
21898	09/03	280.1	-21.85	139.5		67.8	
21899		279.4	-21.12	138.2		85.1	
21900		280.0	-21.00	141.4		81.8	
21901		281.0	-21.07	139.1		87.9	
21902		281.2	-20.83	139.5		91.0	
21903		280.3	-20.66	139.5		89.2	
21904		279.3	-20.60	142.1		83.9	
21905		279.4	-20.53	142.6		86.0	
21906		279.7	-20.48	138.4		77.9	
21907		279.8	-20.29	138.3		81.2	
21908		280.9	-19.95	139.7		86.3	
21909		280.6	-19.87	139.4		86.6	
21910		282.3	-19.68	139.6	76.43±0.73	87.4	4
21911		280.3	-19.33	140.8		92.7	
21912		279.6	-19.29	140.3		86.7	
21913		280.1	-19.17	140.9		87.9	
21914		279.9	-19.00	141.6		87.0	
21915		278.8	-18.71	140.1		85.0	
21916		243.0	-18.48	121.9		84.4	
21917		278.9	-18.21	140.5		86.5	
21918		278.6	-18.12	140.3		84.1	
21920		278.7	-17.75	140.8		88.4	
21921		279.3	-17.53	240.3		88.3	
21922		185.5	-17.30	93.8		86.6	
21931		224.7	20.19	115.0	76.69±0.51	71.7	
21932		278.1	22.17	142.2		79.3	
21934		279.1	23.59	142.2		95.2	
21936		278.8	23.60	142.1		84.9	
21937		278.2	23.31	142.6		92.1	
21938		279.0	23.07	142.3		90.7	
21939		278.4	22.78	148.1		89.9	
21940		278.9	22.55	143.0		94.5	
21941		280.0	22.07	143.2		98.8	
21945	09/04	278.9	21.65	140.8		93.0	
21946		279.7	21.21	140.5		86.0	
21947		280.8	20.95	144.4		92.4	
21954		280.7	20.34	140.5		79.2	
21955		280.9	20.01	140.9		92.8	
21957		280.6	19.40	140.3		93.3	
21958		280.1	19.19	140.5		92.2	
21959		280.4	18.85	140.4		93.1	

21960		280.0	18.65	144.1		94.6	
21964		280.2	18.37	140.9		93.4	
21967		280.4	17.95	141.0		85.5	
21968		166.3	18.20	83.8	76.43±0.73	91.7	4
21969		280.2	17.88	140.6		95.4	
21970		279.5	17.73	140.2		85.8	
21971		279.3	17.33	140.9		96.3	
21972		280.1	17.13	141.0		94.4	
21975		277.7	16.64	140.1		92.0	
21978		278.8	16.28	140.1		88.5	
21979		278.5	16.04	140.4		92.8	
21986		311.9	26.06	156.9		87.8	
21987		280.4	25.53	142.0		90.0	
21988		286.7	24.83	145.5		93.1	
21989		293.7	24.32	148.9		95.0	
21990	09/05	279.4	24.07	141.4		84.5	
21991		186.3	23.50	94.5		93.2	
21995		278.9	22.53	142.0		91.4	
21996		279.4	22.42	141.8		89.5	
21997		279.6	21.96	141.9		93.1	
21998		279.5	21.66	142.1		93.6	
21999		280.4	21.50	143.2		90.4	
22000		279.5	21.12	141.8		93.7	
22001		278.7	20.93	142.3		89.6	
22002		280.5	20.50	143.0		93.8	
22003		281.3	20.18	142.7		94.0	
22012		279.2	19.08	142.3		94.6	
22013		278.7	18.75	142.1		92.3	
22014		278.4	18.40	142.0		92.0	
22047		266.4	-21.31	145.9		90.1	
22048		266.6	-21.33	145.7	77.49±0.51	93.8	4
22050		278.8	-20.80	142.9		89.1	
22051		279.1	-20.88	143.1		92.7	
22052		278.1	-20.99	142.7		90.7	
22054		277.4	-21.19	142.3		89.3	
22055		278.6	-21.12	143.0		94.2	
22056		278.0	-21.25	142.7		91.3	
22057		139.1	-21.08	71.7		92.6	
22058		277.8	-20.96	148.9		92.6	
22063		276.3	-20.38	142.5		88.0	
22064		270.0	-20.13	144.4		90.4	

22066		277.4	-19.89	142.8		92.2	
22067		277.0	-19.74	142.5		91.5	
22068		179.4	-19.54	94.7		91.2	
22069		275.5	-19.58	142.0		74.2	
22073		276.5	-19.03	142.9		88.9	
22074		276.0	-18.70	142.9		92.1	
22075		277.5	-18.49	144.7		92.3	
22076		274.9	-18.41	143.7		85.3	
22077		277.2	-18.19	143.2		90.7	
22078		275.4	-18.03	142.6		86.3	
22080		276.0	-17.65	143.2		91.6	
22102		283.5	15.29	141.1		109.5	
22103		283.8	15.89	143.4		110.4	
22104		283.7	15.76	142.1		110.7	
22105		283.7	15.55	143.0		110.5	
22106		280.2	15.65	144.5		93.6	
22111		275.9	19.08	139.4		87.5	
22117		274.3	18.14	137.6		87.8	
22118		274.6	18.14	137.8		89.6	
22119		275.6	18.07	137.8		84.6	
22120		275.6	17.77	138.0		85.0	
22121		191.4	17.61	95.8	78.07±0.42	88.4	4
22122		280.9	17.29	142.3		105.5	
22123		280.4	16.92	141.3		107.2	
22126		422.2	15.63	200.1		108.6	
22127		423.2	19.56	206.1		104.7	
22129		422.7	19.27	201.0		111.5	
22130		423.0	18.60	201.3		107.7	
22131		424.0	16.50	201.4		106.9	
22132		423.3	14.85	200.7		106.8	
22133	09/10	424.8	12.40	202.2		106.3	
22142		421.6	29.35	215.9		110.6	
22143		421.4	28.48	216.7		104.5	
22144		421.9	27.41	216.4		113.4	
22145		421.3	26.81	216.3		106.4	
22146		108.6	26.17	55.4		112.2	
22147		420.7	25.84	214.7		110.2	
22148		420.4	25.35	215.1		109.0	
22149		420.3	24.90	215.2		106.1	
22150		421.0	24.27	215.9		110.8	
22151		420.9	23.90	216.5		109.7	

22152		421.0	23.48	216.8		107.7	
22153		420.6	22.80	216.0		112.3	
22154		421.5	22.38	215.7		111.6	
22155		432.1	21.36	222.2		142.1	
22156		429.6	21.32	222.0		131.9	
22157		433.0	11.72	212.7		136.9	
22159		64.1	22.62	31.8		124.8	
22160		502.6	22.63	241.2		131.2	6
22161		502.6	21.54	241.2		139.1	
22162		502.8	20.11	242.0		140.8	
22163		505.3	22.44	242.7	78.07±0.42	143.3	6
22164		505.4	19.84	242.4		144.4	
22165		503.0	16.89	241.4		131.0	
22166		502.3	13.60	241.1		131.2	
22167		504.9	18.43	243.5		144.6	
22169		502.4	17.50	241.6		134.7	
22170	09/11	504.7	16.71	243.0		141.8	
22171		503.1	16.12	244.1		141.6	
22172		629.3	15.48	302.3		142.0	
22180		629.0	39.23	319.1	77.40±0.37	116.8	
22181		630.3	34.31	322.3		115.0	
22182		623.0	31.07	315.7		116.8	
22183		306.3	28.93	153.4		109.3	
22185		636.3	27.39	316.9		107.7	
22186		677.4	25.91	338.4		118.8	
22192		676.9	24.45	337.4		112.9	8
22195		677.1	22.84	339.1		110.2	
22196		677.7	21.63	340.5		115.7	
22197		678.9	20.92	340.5		114.9	
22199		676.5	-9.90	324.8		113.4	
22200		412.2	-18.48	198.6		141.5	
22201		675.9	-19.88	327.1		142.3	
22202		675.6	-20.91	326.6		142.1	
22204		675.2	-19.03	326.7		135.4	
22205		676.8	-18.07	327.7		139.5	
22206		676.4	-16.83	326.8		137.7	
22207		676.2	-15.84	327.6		138.9	
22209	09/12	674.6	-15.59	331.3		141.2	
22212		674.4	-17.99	328.3		133.8	
22213		676.7	-16.72	328.8		142.2	
22219		676.9	-20.28	328.2		138.3	

22220		675.7	-23.56	327.6		140.7	
22221		675.6	-24.13	327.4		144.4	
22222		674.2	-23.90	327.6		144.8	
22223		612.5	-23.41	298.5		134.0	
22229		673.8	-22.46	329.8	78.22±0.50	139.5	8
22230		298.5	-20.79	145.9		142.4	
22233		672.3	-20.40	329.2		136.4	
22234		673.1	-19.48	329.8		135.3	
22237		672.7	-18.18	328.8		140.9	
22238		675.7	-17.71	330.0		138.5	
22239		673.6	-17.15	329.5		139.4	
22240		673.7	-32.14	351.5		135.3	
22241		674.2	-25.64	350.7		136.1	
22244		674.4	-24.17	351.6		128.2	
22250	09/13	670.0	-26.74	328.8		140.0	
22264		640.7	-24.14	314.9		105.9	
22265		672.3	-22.71	330.8		118.4	
22266		211.8	-22.39	116.7		114.0	
22268		672.5	-21.63	330.9		114.4	
22269		671.4	-20.64	330.4		114.0	
22271		673.4	-20.19	332.2		113.8	
22278		469.2	36.88	248.4		109.3	
22282		674.0	28.44	352.0		92.7	
22283	09/16	677.7	25.83	352.7		89.0	
22284		677.5	24.35	351.5		88.7	
22285		677.7	23.37	351.7		86.3	
22286		678.8	22.16	351.9		94.0	
22287		679.1	21.32	351.8		92.1	
22288		231.3	20.49	120.2		85.4	

Table B.2: A list of good $^{15}NH_3$ runs at $Q^2 = 0.5$ (GeV/c)^2.

Run Number	Date [1998]	$N_{singles}$ [k]	N_{coin} [k]	P_t [%]	Charge [μC]	P_b [%]	I_b [nA]	PS Factor	Comments
21593	08/23	65.9	109.0	68.92	164.4	34.40	74.1	4	
21594		66.8	109.4	74.57	162.7		67.4		
21595		45.7	73.6	74.61	120.4		66.7		
21596		65.3	110.4	60.60	161.5		82.0		
21598		65.5	110.8	70.07	161.9		82.4		
21600		65.4	110.0	61.81	162.5		65.8		
21601		72.9	124.3	60.01	182.0				
21602		4.3	7.4	61.95	10.8		87.4		
21604		53.5	90.4	54.75	133.1		86.0		
21605		66.3	112.8	51.77	166.0		86.4		
21606		31.8	54.1	49.98	80.4		81.5		
21613		65.9	111.6	39.25	164.2		85.4		
21614		63.4	107.3	35.79	158.3		84.1		
21621		71.7	121.1	30.46	179.5		63.2		
21622		67.3	113.0	29.00	165.8		83.0		no target info
21690	08/25	59.3	97.7	80.00	147.7	59.73	88.8		no target info
21691		65.6	107.0	72.00	161.1		80.0		no target info
21693		18.7	30.6	67.80	46.1		82.1		
21694		77.8	128.2	66.20	192.3		90.2		
21695		66.1	108.6	58.07	161.9		82.8		
21696		52.1	84.6	50.01	127.2		83.6		

Table B.3: A list of good $^{15}NH_3$ runs at $Q^2 = 1.0$ (GeV/c)^2.

Run Number	Date [1998]	$N_{singles}$ [k]	N_{coin} [k]	P_t [%]	Charge [μC]	P_b [%]	I_b [nA]	PS Factor	Comments
22320		44.8	23.5	30.0	140.4		39.5		
22325		2.8	2.6	30.0	11.5		65.5		
22328		10.6	9.5	30.0	43.4		65.4		
22329		45.5	40.4	30.0	183.5		61.8		

Table B.4: A list of good carbon target runs at $Q^2 = 0.5$ (GeV/c)^2.

Run Number	Date [1998]	$N_{singles}$ [k]	N_{coin} [k]	Charge [μC]	P_b [%]	I_b [nA]	PS Factor	Comments
21577	08/22	9.2	11.8	7.2	34.4	106.6	4	
21578		106.7	136.3	84.1		106.9	4	
21579		75.5	95.3	59.6		92.0	4	
21581		11.1	12.5	8.0		73.4	4	
21587		178.4	203.3	130.6		75.2	4	
21590		297.4	89.0	65.9		78.8	1	
21591		300.4	86.1	62.3		75.9	1	
21801	09/01	11.7	12.8	8.2	76.43	61.2	4	
21803		54.0	27.3	19.5		67.9	2	
21804		18.6	9.7	6.6		66.5	2	
22116	09/09	179.0	202.6	139.7	78.07	125.6	4	
22279	09/15	65.5	130.8	90.3	78.22	82.5	8	

Appendix C Target Composition

Table C.1: Target composition file for $^{15}ND_3$

matl	thick	unit	density (g/cm^3)	X0	conc.	flag	Z	A	MW	Z-coord. (cm)
1.beam exit	0.0150	in	1.850	65.190	1.00	w	4	9	9.012	
2.air gap	3.0000	cm	.00129	36.660	1.000	w	7	14	14.421	
3.OVC entr	0.0080	in	2.700	24.011	1.000	w	13	27	26.982	
4.LN2 can	0.0015	in	2.700	24.011	1.000	w	13	27	26.982	-42.0
5.4K shield	0.0015	in	2.700	24.011	1.000	w	13	27	26.982	-4.0
6.tailpiece	0.0020	in	2.700	24.011	1.000	w	13	27	26.982	-2.0
7.LHe	0.5000	cm	0.145	94.322	1.000	w	2	4	4.003	-1.75
8.endcap	0.0015	in	2.700	24.011	1.000	w	13	27	26.982	-1.50
9.tgt 15N	3.0000	cm	0.917	43.255	0.010	t	7	15	15.000	0.00
10.tgt H3	3.0000	cm	0.917	43.255	0.010	t	1	1	1.008	0.00
11.tgt 14N	3.0000	cm	0.867	40.862	0.000	t	7	14	14.003	0.00
12.tgt H3	3.0000	cm	0.867	40.862	0.000	t	1	1	1.008	0.00
13.tgt 15N	3.0000	cm	1.056	50.500	0.970	t	7	15	15.000	0.00
14.tgt D3	3.0000	cm	1.056	50.500	2.970	t	1	2	2.014	0.00
15.tgt 14N	3.0000	cm	1.056	48.107	0.020	t	7	14	14.003	0.00
16.tgt D3	3.0000	cm	1.056	48.107	0.020	t	1	2	2.014	0.00
17.tgt He	3.0000	cm	0.145	94.322	1.000	t	2	4	4.003	0.00
18.NMR Cu	0.01008	cm	8.960	12.860	1.000	t	29	64	63.546	0.00
19.NMR Ni	0.00433	cm	8.760	12.680	1.000	t	28	59	58.693	0.00
20.endcap	0.0015	in	2.700	24.011	1.000	w	13	27	26.982	1.50
21.LHe	0.5000	cm	0.145	94.322	1.000	w	2	4	4.003	1.75
22.tailpiece	0.0020	in	2.700	24.011	1.000	w	13	27	26.982	2.00
23.4K shield	0.0015	in	2.700	24.011	1.000	w	13	27	26.982	4.00
24.LN2 can	0.0015	in	2.700	24.011	1.000	w	13	27	26.982	42.0
25.OVC entr	0.0080	in	2.700	24.011	1.000	w	13	27	26.982	
26.air gap	3.0000	cm	.00129	36.660	1.000	w	7	14	14.421	
27.beam exit	0.0150	in	1.850	65.190	1.00	w	4	9	9.012	

Table C.2: Target composition file for $^{15}NH_3$

matl	thick	unit	density (g/cm^3)	X0	conc.	flag	Z	A	MW	Z range (cm)
1.beam exit	0.0150	in	1.850	65.190	1.00	w	4	9	9.012	
2.air gap	3.0000	cm	.00129	36.660	1.000	w	7	14	14.421	
3.OVC entr	0.0080	in	2.700	24.011	1.000	w	13	27	26.982	
4.LN2 can	0.0015	in	2.700	24.011	1.000	w	13	27	26.982	-42.0
5.4K shield	0.0015	in	2.700	24.011	1.000	w	13	27	26.982	-4.0
6.tailpiece	0.0020	in	2.700	24.011	1.000	w	13	27	26.982	-2.0
7.LHe	0.5000	cm	0.145	94.322	1.000	w	2	4	4.003	-1.75
8.endcap	0.0015	in	2.700	24.011	1.000	w	13	27	26.982	-1.50
9.tgt 15N	3.0000	cm	0.917	43.255	0.980	t	7	15	15.000	0.00
10.tgt H3	3.0000	cm	0.917	43.255	2.940	t	1	1	1.008	0.00
11.tgt 14N	3.0000	cm	0.867	40.862	0.020	t	7	14	14.003	0.00
12.tgt H3	3.0000	cm	0.867	40.862	0.060	t	1	1	1.008	0.00
13.tgt 15N	3.0000	cm	1.056	50.500	0.000	t	7	15	15.000	0.00
14.tgt D3	3.0000	cm	1.056	50.500	0.000	t	1	2	2.014	0.00
15.tgt 14N	3.0000	cm	1.056	48.107	0.000	t	7	14	14.003	0.00
16.tgt D3	3.0000	cm	1.056	48.107	0.000	t	1	2	2.014	0.00
17.tgt He	3.0000	cm	0.145	94.322	1.000	t	2	4	4.003	0.00
18.NMR Cu	0.01008	cm	8.960	12.860	1.000	t	29	64	63.546	0.00
19.NMR Ni	0.00433	cm	8.760	12.680	1.000	t	28	59	58.693	0.00
20.endcap	0.0015	in	2.700	24.011	1.000	w	13	27	26.982	1.50
21.LHe	0.5000	cm	0.145	94.322	1.000	w	2	4	4.003	1.75
22.tailpiece	0.0020	in	2.700	24.011	1.000	w	13	27	26.982	2.00
23.4K shield	0.0015	in	2.700	24.011	1.000	w	13	27	26.982	4.00
24.LN2 can	0.0015	in	2.700	24.011	1.000	w	13	27	26.982	42.0
25.OVC entr	0.0080	in	2.700	24.011	1.000	w	13	27	26.982	
26.air gap	3.0000	cm	.00129	36.660	1.000	w	7	14	14.421	
27.beam exit	0.0150	in	1.850	65.190	1.00	w	4	9	9.012	

Table C.3: Target composition file for carbon

matl	thick	unit	density (g/cm^3)	X0	conc.	flag	Z	A	MW	Z range (cm)
1.beam exit	0.0150	in	1.850	65.190	1.00	w	4	9	9.012	
2.air gap	3.0000	cm	.00129	36.660	1.000	w	7	14	14.421	
3.OVC entr	0.0080	in	2.700	24.011	1.000	w	13	27	26.982	
4.LN2 can	0.0015	in	2.700	24.011	1.000	w	13	27	26.982	-42.0
5.4K shield	0.0015	in	2.700	24.011	1.000	w	13	27	26.982	-4.00
6.tailpiece	0.0020	in	2.700	24.011	1.000	w	13	27	26.982	-2.00
7.LHe	0.5000	cm	0.145	94.322	1.000	w	2	4	4.003	-1.75
8.endcap	0.0015	in	2.700	24.011	1.000	w	13	27	26.982	-1.50
9.Carbon	3.0000	cm	2.265	42.700	1.000	t	6	12	12.011	-1.16
10.tgt LHe	3.0000	cm	0.145	94.322	1.000	t	2	4	4.003	0.34
11.endcap	0.0015	in	2.700	24.011	1.000	w	13	27	26.982	1.50
12.LHe	0.5000	cm	0.145	94.322	1.000	w	2	4	4.003	1.75
13.tailpiece	0.0020	in	2.700	24.011	1.000	w	13	27	26.982	2.00
14.4K shield	0.0015	in	2.700	24.011	1.000	w	13	27	26.982	4.00
15.LN2 can	0.0015	in	2.700	24.011	1.000	w	13	27	26.982	42.0
16.OVC entr	0.0080	in	2.700	24.011	1.000	w	13	27	26.982	
17.air gap	3.0000	cm	.00129	36.660	1.000	w	7	14	14.421	
18.beam exit	0.0150	in	1.850	65.190	1.00	w	4	9	9.012	

Appendix D TE and Calibration Constant Lists

D.1 $^{15}ND_3$ Thermal Equilibrium Measurements

Table D.1: Top deuteron target thermal equilibrium measurements

date stamp (mmdd_hhmm)	B-field (Tesla)	Area	δA	Temp K	δT K	CC	δCC
0901_1202	5.0400	0.01509	0.00013	1.436	0.001	0.7421	0.0065
0906_0237	5.0400	0.01361	0.00008	1.449	0.001	0.8153	0.0048
0908_0818	5.0400	0.01257	0.00010	1.445	0.001	0.8854	0.0073
1006_0409	5.0043	0.01210	0.00012	1.432	0.001	0.9222	0.0090
1006_1347	5.0043	0.01255	0.00027	1.446	0.001	0.8805	0.0190
1006_1631	5.0043	0.01197	0.00011	1.450	0.001	0.9204	0.0083

Table D.2: Bottom deuteron target thermal equilibrium measurements

date stamp (mmdd_hhmm)	B-field (Tesla)	Area	δA	Temp K	δT K	CC	δCC
0908_1803	5.0400	0.00815	0.00010	1.481	0.001	1.3331	0.0167
1006_1154	5.0043	0.01361	0.00008	1.481	0.002	0.8975	0.0174

D.2 $^{15}ND_3$ Target Calibration Constants

Table D.3: Top deuteron target calibration constants and correction factors

Era	Epoch	CC taken	CC used	CC to use	Corfac
Preliminary	2	6.4683	6.2683	6.9353	1.0722
	3	7.2408	7.2408	6.7698	0.9350
	4	6.9938	6.9938	6.0543	0.8657
	5		0.9870	0.9239	0.9361
	6		0.9870	0.9239	0.9361
Q^2=0.5	7	0.7621	0.7621	0.7421	0.9738
	8		0.7621	0.7421	0.9738
	9		0.7621	0.7421	0.9738
	10		0.7621	0.7421	0.9738
	11	0.7496	0.7621	0.8153	1.0698
	12	0.8400	0.8400	0.8854	1.0540
	13		0.8400	0.8854	1.0540
	14		0.8400	0.8854	1.0540
	15		0.8400	0.8854	1.0540
	16		0.8400	0.8854	1.0540
Q^2=1.0	19		0.8400	0.9188	1.0938
	20		0.8400	0.9188	1.0938
	21		0.8400	0.9188	1.0938
	22		0.8400	0.9188	1.0938
	23		0.8400	0.9188	1.0938

Table D.4: Bottom deuteron target calibration constants and correction factors

Era	Epoch	CC taken	CC used	CC to use	Corfac
Q^2=0.5	12	1.3900	1.3900	1.3331	0.9590
	13		1.3900	1.3331	0.9590
	14		1.3900	1.3331	0.9590
	15		1.3900	1.3331	0.9590
	16		1.3900	1.3331	0.9590
Q^2=1.0	19		1.3900	0.8975	0.6457
	20		1.3900	0.8975	0.6457
	21		1.3900	0.8975	0.6457
	22		1.3900	0.8975	0.6457
	23		1.3900	0.8975	0.6457

D.3 $^{15}NH_3$ Thermal Equilibrium Measurements

Table D.5: Top proton target thermal equilibrium measurements

date stamp (mmdd_hhmm)	B-field (Tesla)	Area	δA	Temp K	δT K	CC	δCC
1107_0201	5.0043	0.43710	0.00015	1.378	0.001	0.8486	0.0004
1109_1831	5.0043	0.43081	0.00016	1.381	0.001	0.8595	0.0004
1109_2315	5.0043	0.44008	0.00015	1.379	0.001	0.8425	0.0003
1110_0445	5.0043	0.46088	0.00026	1.349	0.001	0.8222	0.0005

Table D.6: Bottom proton target thermal equilibrium measurements

date stamp (mmdd_hhmm)	B-field (Tesla)	Area	δA	Temp K	δT K	CC	δCC
0729_0219	5.0400	0.36600	0.00020	1.447	0.001	0.9526	0.0009
0729_1909	5.0400	0.36700	0.00009	1.500	0.001	0.9352	0.0001
0730_0643	5.0400	0.38929	0.00026	1.483	0.001	0.8918	0.0008
0809_1632	5.0400	0.38457	0.00016	1.474	0.001	0.9081	0.0006

D.4 $^{15}NH_3$ Target Calibration Constants

Table D.7: Proton target calibration constants and correction factors

Era	Epoch	CC taken	CC used	CC to use	Corfac
Q^2=0.5	2	0.90409	0.90409	0.8918	0.9864
	3	0.92406	0.92406	0.9081	0.9827
	4	1.0438	1.0438	0.9941	0.9524
	5	0.15927	0.15927	0.15170	0.9524

Appendix E Deuteron TE Data Lists

E.1 Deuteron Thermal Equilibrium Data Points

date stamp (mmdd_hhmm)	Area	Temperature K
0901_1202	0.106739	1.442605
	0.093564	1.442275
	0.100267	1.437550
	0.089947	1.446714
	0.098393	1.437467
	0.093501	1.440953
	0.095816	1.442358
	0.096085	1.435464
	0.092383	1.444499
	0.095359	1.437383
	0.091672	1.441863
	0.101443	1.437883
	0.101551	1.436383
	0.099914	1.440539
	0.091506	1.428903
	0.092223	1.437383
	0.098777	1.425848
	0.097528	1.433622
	0.096027	1.431015
	0.096690	1.439793
	0.102490	1.426783
	0.091923	1.439213
	0.091791	1.421146
	0.090711	1.432866
	0.088581	1.432194
	0.091227	1.440953
	0.093674	1.424570
	0.092314	1.437966
	0.092034	1.431605

date stamp (mmdd_hhmm)	Area	Temperature K
	0.098394	1.443924
	0.094137	1.435965
	0.102320	1.436216
	0.102960	1.439793
	0.102128	1.428819
	0.108942	1.440374
	0.105957	1.435129
	0.101988	1.438382
	0.103269	1.441780
	0.100849	1.446141
	0.102630	1.443430
	0.105133	1.436383
	0.107739	1.434962
	0.104267	1.434627
	0.109079	1.440705
	0.109758	1.431099
	0.106067	1.430762
	0.106208	1.430256
	0.106042	1.428141
0906_0237	0.086504	1.444828
	0.081908	1.449735
	0.082833	1.441945
	0.082625	1.443430
	0.082250	1.447205
	0.085291	1.444499
	0.086105	1.443512
	0.083787	1.447777
	0.082187	1.448920
	0.082484	1.441697
	0.087259	1.444746
	0.084617	1.451198
	0.089799	1.444499
	0.088756	1.447532
	0.087078	1.451198
	0.088439	1.445649
	0.092203	1.445895

date stamp (mmdd_hhmm)	Area	Temperature K
	0.093996	1.444253
	0.090903	1.442523
	0.093612	1.445977
	0.089424	1.450954
	0.088984	1.442605
	0.091176	1.444417
	0.089179	1.448594
	0.091364	1.451847
	0.089302	1.445567
	0.091610	1.449409
	0.087576	1.452414
	0.089121	1.447941
	0.091300	1.451847
	0.086160	1.453304
	0.090709	1.448594
	0.089727	1.451441
	0.091187	1.454274
	0.085567	1.454032
	0.092182	1.449490
	0.093712	1.453304
	0.089229	1.455403
	0.089413	1.455403
	0.090511	1.452333
	0.092626	1.456449
	0.092363	1.456530
	0.092892	1.451766
	0.093005	1.456931
	0.090778	1.457894
0908_0818	0.085013	1.439628
	0.088286	1.445567
	0.086324	1.455483
	0.082174	1.450629
	0.082036	1.447123
	0.089131	1.443347
	0.085821	1.438631

date stamp (mmdd_hhmm)	Area	Temperature K
	0.079001	1.438049
	0.082337	1.440788
	0.080435	1.444746
	0.080451	1.454516
	0.081000	1.451685
	0.082821	1.449897
	0.082208	1.442523
	0.082429	1.441615
	0.079301	1.438714
	0.080719	1.438382
	0.079844	1.452414
	0.081613	1.454919
	0.076493	1.445157
	0.083074	1.436216
0908_1803	0.054895	1.476110
	0.051749	1.481668
	0.059687	1.473623
	0.056677	1.486257
	0.060752	1.475878
	0.050004	1.483508
	0.052398	1.470967
	0.055591	1.484579
	0.050309	1.470262
	0.051256	1.486028
	0.047359	1.485952
	0.049974	1.479282
	0.054087	1.479513
	0.053284	1.484196
	0.057809	1.478510
	0.057984	1.487931
	0.048597	1.476188
	0.058689	1.484960
	0.051467	1.485571
	0.058988	1.475412
	0.052376	1.482665

date stamp (mmdd_hhmm)	Area	Temperature K
	0.048179	1.477969
	0.050254	1.479821
	0.052228	1.474168
	0.053976	1.476808
	0.049544	1.484502
	0.055102	1.473934
	0.050340	1.480514
	0.049255	1.486181
	0.047926	1.473778
	0.054277	1.483431
	0.051090	1.473389
	0.055064	1.481053
	0.046343	1.490507
	0.060102	1.493449
1006_0409	0.091001	1.438964
	0.077156	1.430846
	0.082071	1.429326
	0.082831	1.432446
	0.077918	1.438132
	0.080820	1.431183
	0.079893	1.429157
	0.078164	1.430593
	0.072907	1.433873
	0.081029	1.429411
	0.072722	1.428649
	0.078968	1.432530
	0.078121	1.436716
	0.080411	1.429073
	0.080173	1.428480
	0.076494	1.430762
	0.080696	1.436883
	0.086574	1.432614
	0.075204	1.428226

date stamp (mmdd_hhmm)	Area	Temperature K
	0.074428	1.428734
	0.077775	1.432866
	0.077333	1.433957
	0.079853	1.428395
	0.082916	1.427378
	0.079260	1.431773
	0.077233	1.437050
1006_1154	0.073348	1.486409
	0.067574	1.491263
	0.082209	1.482512
	0.080689	1.482818
	0.075725	1.477273
	0.069770	1.477040
	0.091455	1.476343
	0.084761	1.488234
	0.085149	1.480206
	0.076438	1.478510
	0.073945	1.476653
	0.078798	1.469477
	0.075881	1.477273
	0.083268	1.477892
	0.079970	1.489372
	0.079211	1.491716
1006_1347	0.087900	1.446550
	0.087529	1.444664
	0.089021	1.446305
	0.086645	1.445567
	0.079936	1.443594
	0.078302	1.445239
	0.073648	1.446550
	0.079422	1.447042
	0.076297	1.444253
	0.086885	1.445485
1006_1631	0.078404	1.451198
	0.076809	1.451928

date stamp (mmdd_hhmm)	Area	Temperature K
	0.082951	1.451279
	0.080318	1.445649
	0.083776	1.446141
	0.082136	1.450141
	0.088575	1.449735
	0.081794	1.452090
	0.075155	1.451928
	0.076835	1.449409
	0.075534	1.450873
	0.083592	1.450629
	0.077203	1.450792
	0.084333	1.449409
	0.082784	1.450141
	0.076905	1.450954
	0.073947	1.451604
	0.075846	1.450060
	0.074820	1.449897
	0.080407	1.450873
	0.080027	1.452819
	0.080842	1.454516
	0.080130	1.453709
	0.076739	1.451035
	0.080572	1.450385
	0.070489	1.450141
	0.074111	1.453062
	0.083394	1.450873
	0.074578	1.446059
	0.077907	1.447042
	0.076651	1.446469
	0.073573	1.444499

Appendix F Proton TE Data Lists

F.1 Proton Thermal Equilibrium Data Points

date stamp (mmdd_hhmm)	Area	Temperature K
0729_0219	0.000367	1.481053
	0.000366	1.476576
	0.000365	1.474946
	0.000367	1.487475
	0.000367	1.471358
	0.000365	1.481360
	0.000366	1.474401
	0.000366	1.485495
	0.000366	1.470575
	0.000367	1.482588
	0.000366	1.472140
	0.000366	1.473700
	0.000367	1.483508
	0.000367	1.471280
	0.000366	1.485113
	0.000367	1.469477
	0.000366	1.474712
	0.000367	1.478046
	0.000366	1.470262
	0.000367	1.484196
	0.000368	1.469713
	0.000367	1.472999
	0.000369	1.470262
	0.000369	1.484808
0729_1909	0.000368	1.489902
	0.000368	1.496824
	0.000369	1.488993
	0.000369	1.500552

date stamp (mmdd_hhmm)	Area	Temperature K
	0.000367	1.494050
	0.000369	1.492093
	0.000368	1.501591
	0.000367	1.492771
	0.000368	1.497572
	0.000367	1.500552
	0.000368	1.493900
	0.000367	1.501220
	0.000367	1.498094
	0.000368	1.494125
	0.000366	1.504108
	0.000370	1.497572
	0.000368	1.493975
	0.000368	1.502481
	0.000368	1.496899
	0.000368	1.496899
	0.000369	1.502925
	0.000369	1.498542
	0.000368	1.497870
	0.000370	1.504477
	0.000367	1.499436
	0.000367	1.499138
	0.000368	1.500849
	0.000368	1.491565
	0.000368	1.501814
	0.000367	1.495402
	0.000367	1.495551
	0.000367	1.502036
	0.000368	1.497049
	0.000368	1.498318
	0.000367	1.503813
	0.000368	1.500998
	0.000369	1.504330
	0.000369	1.498840
	0.000368	1.500701
	0.000369	1.505657

date stamp (mmdd_hhmm)	Area	Temperature K
	0.000366	1.500701
	0.000368	1.500923
	0.000367	1.506614
	0.000368	1.507349
	0.000369	1.505583
	0.000368	1.501369
	0.000368	1.513631
	0.000368	1.507202
	0.000368	1.504108
	0.000368	1.514575
	0.000370	1.507936
	0.000368	1.507863
	0.000368	1.517469
	0.000368	1.511447
	0.000367	1.509328
	0.000367	1.518046
	0.000368	1.512467
	0.000368	1.500552
	0.000367	1.512030
	0.000368	1.499734
	0.000368	1.505952
	0.000367	1.506320
	0.000368	1.503147
	0.000366	1.512540
	0.000366	1.506761
	0.000368	1.501146
	0.000366	1.509475
	0.000368	1.500626
	0.000367	1.506614
	0.000368	1.501146
	0.000368	1.497721
	0.000368	1.502333
	0.000368	1.496600
	0.000368	1.501591
	0.000366	1.498244
	0.000368	1.492470

date stamp (mmdd_hhmm)	Area	Temperature K
	0.000367	1.499064
	0.000367	1.494201
	0.000367	1.498318
	0.000367	1.493223
	0.000366	1.488614
	0.000366	1.491791
	0.000367	1.490356
	0.000366	1.492319
	0.000367	1.488993
	0.000367	1.482358
	0.000367	1.485418
	0.000366	1.486562
0730_0643	0.393128	1.473389
	0.390502	1.485723
	0.390495	1.479898
	0.390003	1.487931
	0.390521	1.479975
	0.389166	1.488082
	0.389743	1.482512
	0.390122	1.485113
	0.390562	1.483431
	0.390568	1.472921
	0.390466	1.483967
	0.388971	1.474168
	0.390156	1.489978
	0.390472	1.480899
	0.388964	1.478278
	0.391192	1.485495
	0.390161	1.482512
	0.389589	1.487475
	0.389190	1.483431
	0.390001	1.480822
	0.390156	1.490507
	0.389888	1.481821

date stamp (mmdd_hhmm)	Area	Temperature K
	0.391820	1.492771
	0.389758	1.485571
	0.390706	1.480283
	0.395270	1.488082
0809_1632	0.384719	1.470889
	0.386791	1.469556
	0.385968	1.468770
	0.386992	1.480514
	0.388913	1.475334
	0.386404	1.467905
	0.386561	1.466960
	0.384862	1.481130
	0.387198	1.478355
	0.385895	1.472687
	0.386964	1.466407
	0.388003	1.470889
	0.386080	1.481821
	0.386766	1.478355
	0.385147	1.471358
	0.385687	1.469399
	0.386813	1.468770
	0.385446	1.480976
	0.386690	1.478587
	0.387568	1.470105
	0.383664	1.471984
	0.388289	1.468613
	0.387092	1.482665
	0.385668	1.478664
	0.386090	1.474479
	0.385931	1.467511
	0.387086	1.467669
	0.386229	1.477660
	0.385821	1.480591
	0.386020	1.477505
	0.386433	1.473311
	0.385358	1.467196

date stamp (mmdd_hhmm)	Area	Temperature K
	0.387438	1.476808
	0.385244	1.481821
	0.386769	1.478201
	0.385200	1.472374
	0.385129	1.471984
	0.388212	1.469870
	0.386416	1.482895
	0.383995	1.478896
	0.385802	1.474479
	0.385244	1.470732
	0.385366	1.467826
	0.387030	1.483278
	0.386286	1.483661
1107_0201	2.875495	1.378702
	2.858744	1.375059
	2.867700	1.382966
	2.861927	1.376089
	2.875953	1.376650
	2.870751	1.376182
	2.873924	1.383981
	2.875352	1.376089
	2.876037	1.381949
	2.878320	1.376276
	2.874316	1.379446
	2.868673	1.377024
	2.874045	1.377957
	2.878565	1.377863
	2.869232	1.375621
	2.874548	1.383151
	2.876939	1.376556
	2.869074	1.380931
	2.869476	1.376837
	2.881465	1.377677
	2.874327	1.382504
	2.872017	1.375153

date stamp (mmdd_hhmm)	Area	Temperature K
	2.875636	1.383058
	2.876618	1.376370
	2.878760	1.380560
	2.871854	1.377490
	2.870666	1.375340
1109_1831	2.822451	1.374965
	2.847459	1.375808
	2.852229	1.376182
	2.849087	1.376650
	2.833692	1.374965
	2.850228	1.375808
	2.814948	1.376089
	2.825912	1.376463
	2.862131	1.374778
	2.822796	1.375902
	2.842321	1.376930
	2.841129	1.376370
	2.838094	1.375527
	2.810303	1.375902
	2.847122	1.376370
	2.807444	1.376370
	2.819115	1.375434
	2.823275	1.376182
	2.816957	1.376182
	2.823658	1.376837
	2.833289	1.375902
	2.834542	1.375902
	2.817572	1.375995
	2.848341	1.376556
	2.843387	1.376370
	2.825851	1.375340
	2.817484	1.375434
	2.838085	1.376463
	2.840921	1.377210
	2.822427	1.375621
	2.823155	1.376182

date stamp (mmdd_hhmm)	Area	Temperature K
	2.824689	1.376556
	2.823178	1.376930
	2.857708	1.375340
	2.835390	1.376463
	2.854469	1.376837
	2.841343	1.376743
	2.848082	1.375715
	2.858694	1.376743
	2.814201	1.376930
	2.841866	1.377304
	2.831909	1.375527
	2.849619	1.376370
	2.850152	1.376370
	2.833236	1.377024
	2.852428	1.376837
	2.860485	1.376182
	2.835806	1.377304
	2.857748	1.376930
	2.819870	1.377304
	2.824199	1.375715
	2.847321	1.376743
	2.836086	1.376650
	2.825773	1.377304
	2.799803	1.376556
	2.823785	1.376463
	2.856125	1.377490
	2.827747	1.377210
	2.828831	1.376370
	2.829876	1.376089
	2.807326	1.377304
	2.828943	1.377863
	2.822145	1.376556
	2.841310	1.376930
	2.862700	1.376930
	2.800398	1.377584
	2.843093	1.377117

date stamp (mmdd_hhmm)	Area	Temperature K
	2.836865	1.376370
	2.807409	1.376556
	2.846040	1.377770
	2.843654	1.377863
	2.842048	1.376370
	2.857540	1.377677
	2.845117	1.377677
	2.844513	1.377584
	2.835408	1.376370
	2.820956	1.377584
	2.835144	1.377584
	2.842520	1.377490
	2.825180	1.377304
	2.840823	1.377397
	2.849180	1.378236
	2.882357	1.377397
	2.826458	1.376743
	2.843732	1.377117
	2.844537	1.377863
	2.822016	1.377677
	2.815548	1.376837
	2.812526	1.377863
	2.853800	1.377584
	2.830513	1.378329
	2.815622	1.377024
	2.856974	1.377304
	2.838298	1.377677
	2.819515	1.377770
	2.848367	1.378236
	2.806447	1.376650
	2.837873	1.378050
	2.827693	1.377770
	2.820550	1.378516
	2.824325	1.376743
	2.859226	1.377490
	2.838622	1.377397

date stamp (mmdd_hhmm)	Area	Temperature K
	2.850821	1.378050
	2.826192	1.377957
	2.837985	1.377117
	2.812847	1.378143
	2.824430	1.378143
	2.842848	1.378422
	2.830730	1.376930
	2.839511	1.377957
	2.860240	1.377770
	2.806773	1.378422
	2.841188	1.378050
	2.838098	1.378422
	2.820229	1.379910
	2.840979	1.379818
	2.823268	1.379632
	2.827796	1.379353
	2.831831	1.380467
	2.826355	1.381209
	2.831650	1.380560
	2.818588	1.380375
	2.822361	1.380375
	2.862392	1.381302
	2.857145	1.380746
	2.814456	1.380003
	2.838139	1.380375
	2.828954	1.381116
	2.815520	1.380653
	2.853674	1.380003
	2.831934	1.380189
	2.818219	1.381024
	2.839613	1.381857
	2.828283	1.380003
	2.838520	1.381024
	2.856277	1.382689
	2.829825	1.384717
	2.849132	1.384533

date stamp (mmdd_hhmm)	Area	Temperature K
	2.841372	1.385269
	2.871533	1.386187
	2.808687	1.387470
	2.830889	1.388110
	2.816148	1.387012
	2.813998	1.388385
	2.837685	1.388750
	2.862633	1.389571
	2.845472	1.388385
	2.853294	1.389206
	2.858122	1.389571
	2.825777	1.390118
	2.854290	1.389024
	2.844884	1.389297
	2.827593	1.390118
	2.824953	1.390209
	2.850257	1.389753
	2.837820	1.389206
	2.846912	1.389844
	2.845974	1.389753
	2.831499	1.390026
	2.836306	1.388750
	2.814232	1.389297
	2.829631	1.390026
	2.825346	1.389844
	2.845430	1.388932
	2.804290	1.388932
	2.823614	1.389753
	2.825508	1.389297
	2.849955	1.388659
	2.831287	1.388841
	2.815061	1.389297
	2.819485	1.389571
	2.833524	1.388659
	2.848705	1.388476
	2.834780	1.388567

date stamp (mmdd_hhmm)	Area	Temperature K
	2.829588	1.389206
	2.828671	1.388293
	2.827076	1.387653
	2.836897	1.388202
	2.845274	1.388476
	2.869119	1.388202
	2.815875	1.387104
	2.862777	1.387745
	2.820825	1.387836
	2.828444	1.388019
	2.839754	1.386646
	2.807351	1.387104
	2.828262	1.387653
	2.830280	1.387836
	2.843332	1.386462
	2.809265	1.385820
	2.824451	1.386646
	2.836929	1.386462
	2.850413	1.386371
	2.829535	1.385177
	2.831338	1.385820
	2.838194	1.386004
	2.818941	1.385820
	2.845334	1.384533
	2.825896	1.384533
	2.819352	1.385361
	2.836656	1.385085

Appendix G Cross Section Derivation

Derivation of Elastic Cross Sections and Asymmetry

G.1 Elastic Scattering

Elastic scattering implies that the proton remains bound after scattering from an electron. A virtual photon exchanged between the electron and proton probes the constituent quarks without changing the final state of the proton. The Feynman diagram shows this reaction.

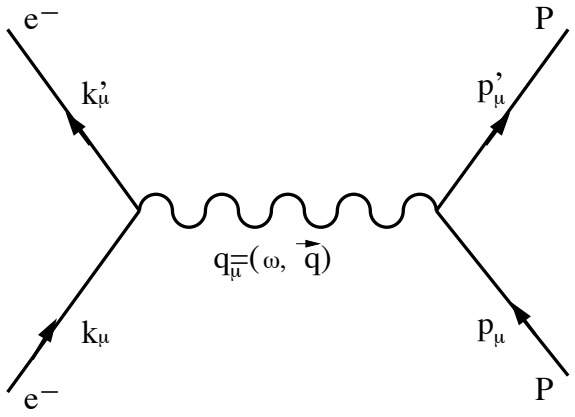

Figure G.1: Feynman diagram of elastic electron-proton scattering.

An electron with incident four momenta k and final four momenta k' scatters elastically from a proton initially at rest within the nucleus with four momenta p. The scattered proton four momenta is p'. The four momentum transfer, q, is the difference between the initial and final scattered electron four momenta, $k - k'$. The square of the four momentum transfer is a Lorentz invariant and can be described in

terms of kinematic variables,

$$Q^2 \equiv -q^2 = 4EE' \sin^2(\frac{\theta}{2}) \ , \tag{G.1}$$

where E is the initial electron energy (beam energy), E' is the scattered electron energy, and θ is the scattering angle.

G.2 Breit Frame

The Breit frame, also called the 'brick wall' frame is a convenient frame in which to evaluate the cross section from elastic scattering. In this frame the hadron incident momentum is equal to the final hadron momentum, but opposite in direction ($\vec{p} = -\vec{p'}$), and the direction of q in this frame (q_B) is along the direction of hadron momentum. Also, there is no energy transfer, so $Q^2 = |\vec{q}_B|^2$ and $q_B^2 = -4|\vec{p}|^2$. Choosing the z-axis along $\vec{q}_B$ with scattering in the x-z plane, the electron four momenta are:

$$\begin{aligned} k &= \frac{|\vec{q}_B|}{2}(\csc\frac{\theta_B}{2}, \cot\frac{\theta_B}{2}, 0, 1) \ , \\ k' &= \frac{|\vec{q}_B|}{2}(\csc\frac{\theta_B}{2}, \cot\frac{\theta_B}{2}, 0, -1) \ . \end{aligned} \tag{G.2}$$

The Lorentz transformation from lab frame to Breit frame is completely along the z-axis, so we can use the fact that the x-axis is the same in both frames to determine the relationship between θ_B and θ (See Brian Milbrath's thesis [15] for the complete derivation):

$$\cot^2\frac{\theta_B}{2} = \frac{\cot^2\frac{\theta}{2}}{1+\tau} \ , \tag{G.3}$$

where $\tau = \frac{Q^2}{4M^2}$. The four-component Dirac spinors in the Breit frame are defined as:

$$u^{(s)} = \sqrt{E+m}\begin{bmatrix} \chi^{(s)} \\ \frac{\vec{\sigma}\cdot\vec{p}}{E+m}\chi^{(s)} \end{bmatrix} \tag{G.4}$$

$$\bar{u}^{(s')} = \sqrt{E+m}\begin{bmatrix} \chi^{(s')\dagger} & -\frac{\vec{\sigma}\cdot\vec{p'}}{E+m}\chi^{(s')\dagger} \end{bmatrix} . \tag{G.5}$$

s=1,2 and χ is a two-component spinor where $\chi_i^\dagger \chi_j = \delta_{ij}$.

G.3 Cross Section Derivation

The differential cross section for this reaction can be written in terms of the Lorentz invariant amplitude, M, which can be derived from the lepton and hadron currents for the reaction. The basic expression for the cross section is as follows:

$$d\sigma = \frac{|M|^2}{4[(k\cdot p)^2 - m_e^2 M_p^2]^{\frac{1}{2}}}\delta^{(4)}(k'+p'-k-p)\frac{d^3k'}{2E'}\frac{d^3p'}{2(M_p+\nu)} , \tag{G.6}$$

where

$$M = \frac{-e^2}{q^2}[j^\mu(k,k')]\cdot[J_\mu(p,p')] \tag{G.7}$$

and

$$|M|^2 = \frac{e^4}{q^4}L^{\mu\nu}W_{\mu\nu} . \tag{G.8}$$

where $L^{\mu\nu}$ and $W_{\mu\nu}$ are the leptonic and hadronic tensors, respectively.

G.3.1 Symmetric Terms

The electron current is defined by

$$j_\mu = \bar{u}(k')\gamma_\mu u(k) , \tag{G.9}$$

where $\bar{u}(k')$ and $u(k)$ are Dirac spinors and γ_μ is the point-like interaction coupling. It can then be shown that the symmetric part of the lepton tensor is

$$L_S^{\mu\nu} = 2(k'^\mu k^\nu + k'^\nu k^\mu - (k'\cdot k - m^2)g^{\mu\nu}) . \tag{G.10}$$

Using the incident and scattered electron momenta given in the Breit frame, we find that the non-zero terms of the lepton tensor are:

$$\begin{aligned} L^{00} &= Q^2 \cot^2(\frac{\theta_B}{2}) \ , \\ L^{01} &= L^{10} = Q^2 \cot(\frac{\theta_B}{2}) \csc(\frac{\theta_B}{2}) \ , \\ L^{11} &= Q^2 \csc^2(\frac{\theta_B}{2}) \ , \\ L^{22} &= Q^2 \ . \end{aligned} \tag{G.11}$$

The hadronic current, however, is not well defined. Since the proton has internal structure, its coupling is more complex. Given in terms of Dirac and Pauli form factors, the hadron current is

$$J_\mu = \bar{u}(k') \left(F_1(Q^2)\gamma_\mu + \frac{i\kappa}{2M} F_2(Q^2)\sigma_{\mu\nu}q^\nu \right) u(k) \ . \tag{G.12}$$

Using the identities $\bar{u}_f \gamma_0 u_i = 2M$ and $\bar{u}_f \gamma_k u_i = \chi^\dagger i(\vec{\sigma} \times \vec{q})_k \chi$, each J_μ component can be determined. Then the proton tensor,

$$W^S_{\mu\nu} = \frac{1}{2} Tr(J_\mu J^\dagger_\nu) \ , \tag{G.13}$$

can be fully evaluated. The math is straightforward, and converting from Dirac and Pauli form factors to the Sachs form factors ($G_E = F_1 + \frac{\kappa q^2}{4M^2} F_2$ and $G_M = F_1 + \kappa F_2$), I arrive at symmetric proton tensor components along the diagonal:

$$\begin{aligned} W_{00} &= 4M^2 G_E^2 \ , \\ W_{11} &= Q^2 G_M^2 \ , \\ W_{22} &= Q^2 G_M^2 \ . \end{aligned} \tag{G.14}$$

Contracting the two tensors, I can solve for the differential cross section,

$$\frac{d\sigma}{d\Omega} = \frac{e^4}{64\pi^2 M^2 Q^4}\left(\frac{E'}{E}\right)^2 L_S^{\mu\nu} W_{\mu\nu}^S \ . \tag{G.15}$$

Using the knowledge that $\tau = Q^2/4M^2$, and the relations between Breit frame angles and laboratory frame angles, I find that the unpolarized differential cross section is the same as the proposal,

$$\frac{d\sigma}{d\Omega} = \sigma_{Mott}\left(\frac{E'}{E}\right)\left(\frac{G_{E_p}^2(Q^2) + \tau G_{M_p}^2(Q^2)}{1+\tau} + 2\tau G_{M_p}^2(Q^2)\tan^2(\theta/2)\right) \ . \tag{G.16}$$

This is the denominator (Σ) of the expression for the asymmetry,

$$A_p = \frac{\sigma_+ - \sigma_-}{\sigma_+ + \sigma_-} = \frac{\Delta}{\Sigma} \ . \tag{G.17}$$

G.3.2 Antisymmetric Terms

The polarized part of the asymmetry (Δ) comes from the antisymmetric parts of the lepton and hadron currents. Mixtures of symmetric and antisymmetric terms cancel so we are only left with the antisymmetric lepton tensor contracted with the antisymmetric hadron tensor. These antisymmetric tensors are written as follows:

$$L_A^{\mu\nu} = -2i\epsilon^{\mu\nu\rho\sigma} q_\rho s_\sigma \ , \tag{G.18}$$

$$W_{\mu\nu}^A = \frac{1}{2} Tr[J_\mu(\vec{\sigma}\cdot\hat{n})J_\nu^\dagger] \ , \tag{G.19}$$

where s_σ is the spin of the electron ($\pm$ 1/2), $\hat{n}$ is the direction proton polarization and $\vec{\sigma}$ is the set of Pauli matrices, making

$$\vec{\sigma}\cdot\hat{n} = \begin{bmatrix} n_z & n_x - in_y \\ n_x + in_y & -n_z \end{bmatrix} \ . \tag{G.20}$$

Using the same identities as before, each tensor component for the antisymmetric terms can be determined. In terms of θ_B, G_E and G_M, the two antisymmetric tensors are as follows:

$$L_A = \begin{bmatrix} 0 & 0 & -iQ^2\cot(\theta_B/2) & 0 \\ 0 & 0 & -iQ^2\csc(\theta_B/2) & 0 \\ iQ^2\cot(\theta_B/2) & iQ^2\csc(\theta_B/2) & 0 & 0 \\ 0 & 0 & 0 & 0 \end{bmatrix} \tag{G.21}$$

$$W^A = \begin{bmatrix} 0 & -2iqMG_EG_M\sin\theta^*\sin\phi^* & 2iqMG_EG_M\sin\theta^*\cos\phi^* & 0 \\ 2iqMG_EG_M\sin\theta^*\sin\phi^* & 0 & iQ^2G_M^2\cos\theta^* & 0 \\ -2iqMG_EG_M\sin\theta^*\cos\phi^* & -iQ^2G_M^2\cos\theta^* & 0 & 0 \\ 0 & 0 & 0 & 0 \end{bmatrix} \tag{G.22}$$

Angles θ^* and ϕ^* account for the direction of the hadron polarization. Specifically, θ^* is the angle from the z-direction in the x-z plane and ϕ^* is the angle from the x-direction in the x-y plane. Contracting the two tensors and converting out of the Breit frame we have

$$L_AW^A = 2Q^2\left[2MqG_EG_M\frac{\cot(\theta/2)}{\sqrt{1+\tau}}\sin\theta^*\cos\phi^* + Q^2G_M^2\sqrt{1+\frac{\cot^2(\theta/2)}{1+\tau}}\cos\theta^*\right]. \tag{G.23}$$

Plugging this result into the cross section and using the same tricks and conversions as before, I again get (save for a minus sign) the same result as the proposal for the differential cross section difference.

$$\begin{aligned} \frac{d\Delta\sigma}{d\Omega} &= 2\sigma_{Mott}\left(\frac{E'}{E}\right)\tan(\theta/2)\sqrt{\frac{\tau}{1+\tau}} \\ &\quad\cdot\left[G_EG_M\sin\theta^*\cos\phi^* + G_M^2\sqrt{\tau(1+(1+\tau)\tan^2(\theta/2))}\cos\theta^*\right] \end{aligned} \tag{G.24}$$

G.4 Proof of Lepton Tensor Terms

G.4.1 Symmetric Terms

$$L_S^{\mu\nu} = 2(k'^{\mu}k^{\nu} + k'^{\nu}k^{\mu} - (k' \cdot k - m^2)g^{\mu\nu}) \tag{G.25}$$

Assuming that the m^2 term is negligible, the lepton tensor reduces to

$$L_S^{\mu\nu} = 2(k'^{\mu}k^{\nu} + k'^{\nu}k^{\mu} - (k' \cdot k)g^{\mu\nu}). \tag{G.26}$$

We can now use the fact that $-q^2 = Q^2 \approx 2(k \cdot k')$ to reduce it even further to

$$L_S^{\mu\nu} = 2(k'^{\mu}k^{\nu} + k'^{\nu}k^{\mu}) + q^2 g^{\mu\nu}. \tag{G.27}$$

Remembering our lepton four momenta:

$$\begin{aligned} k &= \frac{|\vec{q}_B|}{2}(\csc\frac{\theta_B}{2}, \cot\frac{\theta_B}{2}, 0, 1)\ , \\ k' &= \frac{|\vec{q}_B|}{2}(\csc\frac{\theta_B}{2}, \cot\frac{\theta_B}{2}, 0, -1)\ , \end{aligned} \tag{G.28}$$

we can compute any of the lepton tensor terms.

Take for example L_S^{00}:

$$\begin{aligned} L_S^{00} &= 2(k'^0k^0 + k'^0k^0) + q^2 g^{00} \\ &= 4(\frac{|q_B|^2}{2}\csc\frac{\theta_B}{2})^2 + q^2 \\ &= Q^2\csc^2(\frac{\theta_B}{2}) - Q^2 \\ &= Q^2(1 + \frac{\cot^2(\theta/2)}{1+\tau}) - Q^2 \\ &= Q^2\frac{\cot^2(\theta/2)}{1+\tau} \\ &= Q^2\cot^2(\frac{\theta_B}{2})\ , \end{aligned}$$

where I have used the fact that $Q^2 = |q_B|^2$ and the angle relations between Breit and lab frames. The other symmetric lepton tensor terms can all be derived in a similar fashion.

G.4.2 Antisymmetric Terms

$$L_A^{\mu\nu} = \frac{1}{2} Tr(\gamma_\mu k' \gamma^\mu \gamma^5 \gamma_\nu k \gamma^\nu) = 2i\epsilon^{\rho\mu\sigma\nu} k'_\rho k_\sigma \tag{G.29}$$

Solve for L_A^{02} for an example. With L_A^{02}, there are two possibilities for the indices ρ and σ, 1 and 3. The complete value for this tensor term is the sum of all possibilities. So the value of L_A^{02} is then

$$\begin{aligned}
L_A^{\mu\nu} &= 2i\epsilon^{1032} k'_1 k_3 + 2i\epsilon^{3012} k'_3 k_1 \\
&= 2i(+1)(\frac{|q_B|}{2}\cot\frac{\theta_B}{2})(\frac{|q_B|}{2}) + 2i(-1)(-\frac{|q_B|}{2})(\frac{|q_B|}{2}\cot\frac{\theta_B}{2}) \\
&= 2 \times (i\frac{Q^2}{2}\cot\frac{\theta_B}{2}) \\
&= iQ^2 \cot\frac{\theta_B}{2} \ .
\end{aligned}$$

The rest of the antisymmetric terms can be done similarly.

G.5 Proof of Hadron Tensor Terms

G.5.1 Symmetric Terms

$$W^S_{\mu\nu} = \frac{1}{2} Tr(J_\mu J^\dagger_\nu) \tag{G.30}$$

and

$$J_{\mu\nu} = \bar{u}(k') \left(F_1(Q^2)\gamma_\mu + \frac{i\kappa}{2M} F_2(Q^2)\sigma_{\mu\nu}q^\nu \right) u(k). \tag{G.31}$$

In the Gordon decomposition,

$$\bar{u}(\sigma_{\mu\nu}q^\nu)u = -2iM(\bar{u}\gamma_\mu u) + \bar{u}(p_\mu + p'_\mu)u. \tag{G.32}$$

Using this substition,

$$\begin{aligned} J_\mu &= \bar{u}_f \left[F_1\gamma_\mu + \frac{i\kappa}{2M} F_2(-2iM\gamma_\mu + i(p_\mu + p'_\mu)) \right] u_i \\ &= \bar{u}_f \left[\gamma_\mu(F_1 + \kappa F_2) - \frac{\kappa}{2M}(p_\mu + p'_\mu) \right] u_i \ . \end{aligned}$$

So all terms will be some combination of $\bar{u}u$, $\bar{u}\gamma_0 u$, and $\bar{u}\gamma_k u$. It can be shown that $\bar{u}u = 2E$, $\bar{u}\gamma_0 u = 2M$, and $\bar{u}\gamma_k u = i(\vec{\sigma} \times \vec{q})_k$.

$$\begin{aligned} \bar{u}u &= (E+M) \begin{pmatrix} \chi^\dagger & \frac{-\vec{\sigma}\cdot\vec{p'}}{E+M}\chi^\dagger \end{pmatrix} \begin{pmatrix} \chi \\ \frac{\vec{\sigma}\cdot\vec{p}}{E+M}\chi \end{pmatrix} \\ &= (E+M)\left(1 + \frac{(\sigma\cdot p)^2}{(E+M)^2}\right) \\ &= (E+M)\left(1 + \frac{E^2 - M^2}{(E+M)^2}\right) \\ &= 2E \ . \end{aligned}$$

$$\bar{u}\gamma_0 u = (E+M) \begin{pmatrix} \chi^\dagger & \frac{-\vec{\sigma}\cdot\vec{p'}}{E+M}\chi^\dagger \end{pmatrix} \begin{pmatrix} 1 & 0 \\ 0 & -1 \end{pmatrix} \begin{pmatrix} \chi \\ \frac{\vec{\sigma}\cdot\vec{p}}{E+M}\chi \end{pmatrix}$$

$$
\begin{aligned}
&= (E+M)\left(1-\frac{(\sigma\cdot p)^2}{(E+M)^2}\right)\\
&= (E+M)\left(1-\frac{E^2-M^2}{(E+M)^2}\right)\\
&= 2M\ .
\end{aligned}
$$

$$
\begin{aligned}
\bar{u}\gamma_k u &= (E+M)\begin{pmatrix}\chi^\dagger & \frac{-\vec{\sigma}\cdot\vec{p'}}{E+M}\chi^\dagger\end{pmatrix}\gamma_k\begin{pmatrix}\chi\\ \frac{\vec{\sigma}\cdot\vec{p}}{E+M}\chi\end{pmatrix}\\
&= (E+M)\begin{pmatrix}\chi^\dagger & \frac{-\vec{\sigma}\cdot\vec{p'}}{E+M}\chi^\dagger\end{pmatrix}\begin{pmatrix}0 & \sigma_k\\ -\sigma_k & 0\end{pmatrix}\begin{pmatrix}\chi\\ \frac{\vec{\sigma}\cdot\vec{p}}{E+M}\chi\end{pmatrix}\\
&= (E+M)\begin{pmatrix}\chi^\dagger & \frac{-\vec{\sigma}\cdot\vec{p'}}{E+M}\chi^\dagger\end{pmatrix}\begin{pmatrix}\sigma_k\frac{\vec{\sigma}\cdot\vec{p}}{E+M}\chi\\ -\sigma_k\chi\end{pmatrix}\\
&= \chi^\dagger\left(\sigma_k(\sigma\cdot p)+(\sigma\cdot p'\sigma_k)\right)\chi\\
&= \chi^\dagger\left[(\sigma\cdot\hat{(}n)_k)(\sigma\cdot p)+(\sigma\cdot p')(\sigma\cdot\hat{n}_k)\right]\chi\\
&= \chi^\dagger\left[(\hat{n}_k\cdot p)+i\vec{\sigma}\cdot(\hat{n}_k\times p)+(p'\cdot\hat{n}_k)+i\vec{\sigma}\cdot(p'\times\hat{n}_k)\right]\chi\\
&= \chi^\dagger i\vec{\sigma}\left[(p'-p)\times\hat{n}_k\right]\chi\\
&= \chi^\dagger i(\vec{\sigma}\times\vec{q})_k\chi\ .
\end{aligned}
$$

Using these, $J_0 = 2MG_E$, $J_1 = iqG_M\sigma_2$, $J_2 = iqG_M\sigma_1$, and $J_3 = 0$.

Solve for W_{11} as an example:

$$
\begin{aligned}
W_{11} &= \frac{1}{2}Tr(J_1J_1^\dagger)\\
&= \frac{-G_M^2}{2}Tr(q^2\sigma_2\sigma_2)\\
&= \frac{Q^2G_M^2}{2}Tr\left[\begin{pmatrix}0 & -i\\ i & 0\end{pmatrix}\begin{pmatrix}0 & -i\\ i & 0\end{pmatrix}\right]\\
&= \frac{Q^2G_M^2}{2}Tr\left[\begin{pmatrix}1 & 0\\ 0 & 1\end{pmatrix}\right]\\
&= Q^2G_M^2\ .
\end{aligned}
$$

The other terms on the diagonal can be done in the same fashion.

G.5.2 Antisymmetric Terms

The antisymmetric hadron tensor is very similar to the symmetric, with an additional $(\sigma \cdot \hat{n})$ term in the trace.

$$W^A_{\mu\nu} = \frac{1}{2} Tr[J_\mu (\vec{\sigma} \cdot \hat{n}) J^\dagger_\nu] \ . \tag{G.33}$$

Do W^A_{02} as an example:

$$\begin{aligned}
W_{02} &= \frac{1}{2} Tr\left[F_0 (\sigma \cdot \hat{n}) F_2^\dagger\right] \\
&= \frac{1}{2} Tr\left[(2MG_E)(\sigma \cdot \hat{n})(iqG_M \sigma_1)\right] \\
&= iqMG_E G_M Tr\left[(\sigma \cdot \hat{n})\sigma_1\right] \\
&= iqMG_E G_M Tr\left[\begin{pmatrix} n_z & n_x - in_y \\ n_x + in_y & -n_z \end{pmatrix} \begin{pmatrix} 0 & 1 \\ 1 & 0 \end{pmatrix}\right] \\
&= iqMG_E G_M [n_x - in_y + n_x + in_y] \\
&= 2iqMG_E G_M \hat{x} \ .
\end{aligned}$$

Other terms solved similarly.

Appendix H Alternate Methods of Polarization Measurement

Integration of the voltage response from the Q-meter circuit is the standard established method of measuring target polarization. However, there are alternative measurement techniques that can also be used. These methods are best employed in circumstances when the normal "area method" cannot be used, or as a redundant measurement to the area technique.

H.1 Peak Height Ratio

Normally, the nucleon polarization is measured by a process similar to that described in chapter 5. An NMR measurement is made at thermal equilibrium and used to calibrate the enhanced signals. However, in some instances a thermal equilibrium measurement is difficult or even impossible. Before high magnetic fields and temperatures near 1 Kelvin were used, thermal signal levels were amongst the noise. The measurement of a deuteron signal from ND_3 is extremely difficult under such conditions, as the wings of the signal can be completely lost in the noise. Under these conditions, it is possible to forego a measurement at thermal equilibrium, and take advantage of the unique signal shape of the deuteron in NH_3.

A spin-1 system in a homogeneous external field will have three magnetic sublevels [111], given by

$$E_m = -mh\nu_D + h\nu_Q(3\cos^2\theta - 1)(3m^2 - (I(I+1))) \ , \qquad \text{(H.1)}$$

where ν_D is the deuteron Larmor frequency, ν_Q is the frequency of the energy shift

due to the quadrupole moment interaction with the electrical field gradient inside the ammonia molecule, and θ is the angle between the external magnetic field and the electric field gradient. For deuteron, I=1, and m=-1,0,1. The two transitions are from the m=+1 state to the m=0 state, and from the m=0 state to the m=-1 state [112]. The corresponding transition energies are

$$E_{-10} = h\nu_D + 3h\nu_Q(3\cos^2\theta - 1) \ , \tag{H.2}$$

and

$$E_{01} = h\nu_D - 3h\nu_Q(3\cos^2\theta - 1) \ . \tag{H.3}$$

At θ=90°, the transition intensity is peaked and is offset from the central Larmor frequency by $\pm 3h\nu_Q$. At θ=0° we have the pedestal of the transition which is offset from the central Larmor frequency by $\pm 6h\nu_Q$. The right (higher frequency) peak and left (lower frequency) pedestal correspond to the m=+1 to m=0 transition and has a peak intensity of I_+ (See Figure H.1 for the deuteron lineshape). The left peak and right pedestal has a peak intensity of I_-. Assuming a Boltzman distribution among the magnetic sublevels, we can use this knowledge of transition intensity to determine the polarization

$$P = \frac{R^2 - 1}{R^2 + R + 1} \ , \tag{H.4}$$

where R is the ratio of transition intensities, I_+/I_-.

In reality, the signals of the two transitions overlap, so to get the intensities, one must subtract the pedestal of one transition from the peak of the other transition. $I_+ = \text{Peak}_{01} - \text{Ped}_{-10}$ and $I_- = \text{Peak}_{-10} - \text{Ped}_{01}$. Since each pedestal can be clearly discerned from the other transition, this ratio of intensities is fairly easy to measure [111].

This proves to be a useful method when the area of the thermal signal is impossible to measure, and was the principle method for determining polarization before the use of the Liverpool Q-meter detection circuit. However, the accuracy of this mea-

surement technique is not nearly as good as that of measuring a thermal equilibrium calibration. Also, it only works for signals of significant size. A small natural asymmetry between the peak heights in ND_3 leads to erroneous measurements at TE and low polarization levels. However, for signals above 20% polarization, it can provide a good redundancy check on the area measurement or can be used if the calibration constant is called into question.

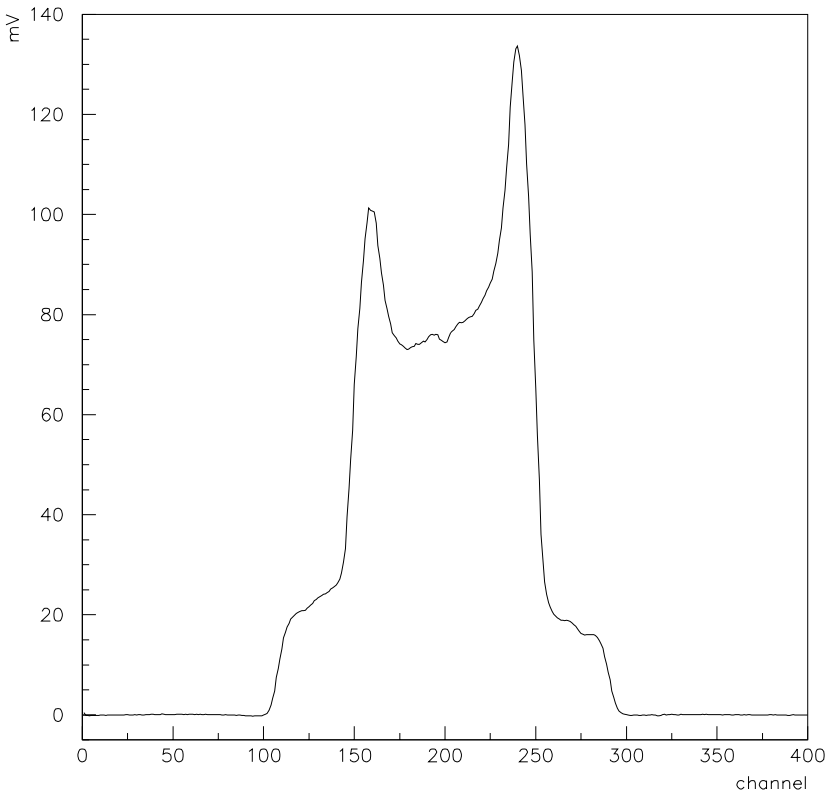

Figure H.1: Deuteron signal with enhanced polarization. Peak and pedestal heights can be used to determine the magnitude of the polarization.

H.2 Midpoint Method

In the proton signal, where there is no interaction with an electric field gradient, there is no splitting of the line shape. It is well known that, for the proton signal, not only the area but also the height of the signal itself is proportional to the polarization. If one assumes a symmetric spreading of the signal from about the central frequency, then the value of the response function at that central value is a measure of the signal strength, which is a measure of the difference of populations of two energy states. This also holds true for the deuteron. If the signal is properly centered with the two ND_3 deuteron peaks symmetrically placed on either side of the central Larmor frequency, then the value of the strength at the central frequency must also be proportional to the polarization.

I will not go into the details of the lineshape function, but rather refer you to reference [113]. There all the theory is worked out at great length. The purpose of this is not to try to recreate the lineshape, but use information about the theoretical lineshape to gain an alternative method for determining polarization.

The intensity function, which is a combination of the lineshapes of the two deuteron peaks, can be described as follows:

$$I_{Q,n,\sigma} = C \cdot (P - A)g^{+}(\nu - \nu_{zee}) + (P + A)g^{-}(\nu - \nu_{zee}) \ , \tag{H.5}$$

where P is the vector polarization, A is the tensor polarization, C is a constant, ν is the frequency, and ν_{zee} is the Zeeman central frequency. $g^{\pm}$ are functions describing the deuteron peaks above and below the central frequency. At the midpoint, $\nu = \nu_{zee}$, and using $g^{+}(x) = g^{-}(-x)$, we see that the tensor polarization drops out of the intensity function, and we are left with

$$I_{Q,n,\sigma} = 2CPg(0) \ . \tag{H.6}$$

The value of $g(0)$ is determined from physical constants of the material only, and is

the same for both g^+ and g^-. It is clear that I is directly proportional to P.

The main drawback of this method is that it only uses one point on the curve and depends on the signal being well centered. It also requires a calibration at thermal equilibrium like the standard area method. However, calibrations can be easily taken at the same time as the area calibrations, and it can provide nice redundancy in the polarization measurement.

Bibliography

[1] P.A. Tipler, Physics, 2nd Edition (1982).

[2] A. Minten, *Electron Scattering, Form Factors, Vector Mesons*, CERN Lectures, (1969).

[3] N.F. Mott, Proc. Roy. Soc. (London) **A124**, 425 (1929).

[4] P.A.M. Dirac, Proc. Roy. Soc. (London) **A117**, 610 (1928).

[5] M.E. Rose, Phys. Rev. **73**, 279 (1948).

[6] M.N. Rosenbluth, Phys. Rev. **79**, 615 (1950).

[7] F.J. Ernst, R.G. Sachs and K.C. Wali, Phys. Rev. **119**, 1105 (1960).

[8] R.G. Sachs, Phys. Rev. **126**, 2256 (1962).

[9] R.G. Arnold, C.E. Carlson, F. Gross, Phys. Rev. **C23**, 363 (1981).

[10] R. Madey, T. Eden, Fizika **B8**, 35-40 (1999).

[11] D.B. Day *et al.*, CEBAF Proposal E93-026, "The Charge Form Factor of the Neutron", (1993).

[12] N. Dombey, Rev. Mod. Phys. **41**, 236 (1969).

[13] T. Pussieux and R. Windmolders, *A Collection of Formulas for Spin Dependent Deep Inelastic Scattering*, in New Haven 1994, Internal Spin Structure of the Nucleon, 212-234 (1995).

[14] F. Halzen and A.D. Martin, *Quarks and Leptons*, (1984).

[15] B. Milbrath, Ph.D. thesis, University of Virginia, 1996.

[16] H. Frauenfelder and E.M. Henley, Subatomic Physics, 2nd Edition, (1991).

[17] G. Höhler *et al.*, Nucl. Phys. **B114**, 505 (1976).

[18] R.A. Williams and S. Krewald, CEBAF Theory Group Preprint (CEBAF-TH-94_06), (1994).

[19] Y. Nambu, Phys. Rev. **106**, 1366 (1957).

[20] H.B. O'Connell, B.C. Pearce, A.W. Thomas, and A.G. Williams, Prog. Nucl. Part. Phys. **39**, 201-252 (1997).

[21] F. Iachello, A.D. Jackson, and A. Lande, Phys. Lett. **B43**, 191 (1973).

[22] S.J. Brodsky and G.R. Farrar, Phys. Rev. Lett. **31**, 1153 (1973). S.J. Brodsky and G.R. Farrar, Phys. Rev. **D11**, 1309 (1975).

[23] L. Andivahis, *et al.*, Phys. Rev. **D50**, 5491 (1994).

[24] A.V. Radyushkin, Few Body Systems Suppl. **99**, 1 (2000).

[25] P.E. Bosted *et al.*, Phys. Rev. Lett. **68**, 3841 (1992).

[26] M. Gari and W. Krümpelmann, Z. Phys. **A322**, 689 (1985).

[27] M. Gari and U. Kaulfuss, Nucl. Phys. **A408**, 507 (1983).

[28] S.J. Dong, K.F. Liu, and A.G. Williams, Phys. Rev. **D58**, 074504 (1998).

[29] J. Ashman *et al.*, Nucl. Phys. **B328**, 1 (1989).

[30] B. Adeva *et al.*, Phys. Lett. **B329**, 399 (1994).

[31] K. Abe *et al.*, Phys. Rev. Lett. **74**, 346 (1995).

[32] T. Janssens *et al.*, Phys. Rev. **142**, 922 (1966).

[33] J. Litt *et al.*, Phys. Rev. **31B**, 40 (1970).

[34] Ch. Berger *et al.*, Phys. Lett. **35B**, 87 (1971).

[35] W. Bartel *et al.*, Nucl. Phys. **58**, 429 (1973).

[36] A. Sill, *et al.*, Phys. Rev. **D48**, 29 (1993).

[37] A. Sill, PhD Thesis, American University (1986).

[38] R.G. Arnold *et al.*, Phys. Rev. Lett. **57**, 174 (1986).

[39] A.T. Katramatou *et al.*, Ncul. Inst. Meth.??? (1987??).

[40] G.G. Petratos, PhD Thesis, American University (1988).

[41] R. Walker, *et al.*, Phys. Rev. **D49**, 5671 (1994).

[42] R.C.D. Walker, Ph.D. thesis, Cal. Tech., 1989.

[43] M.K. Jones *et al.*, Phys. Rev. Lett. **84**, 1398 (2000).

[44] Private communication with M. Zeier, (2000).

[45] B. Zihlmann *et al.*, submitted to Nucl. Instrum. Method (1999).

[46] J. Arrington *et al.*, Nucl. Instrum. Method **A311**,39-48 (1992).

[47] L.G. Levchuk, Nucl. Instrum. Method **A345**, 496-499 (1994).

[48] Private communication with B. Zihlmann, (2000).

[49] C. Yan *et al.*, Nucl. Instr. Meth. **A365**, 261 (1995).

[50] C. Yan, Hall C Chicane Beam Line for $G_e n$ 98, JLab Tech Note **97-036**.

[51] C. Yan, Hall C Raster System - The Second Generation, JLab Tech Note **97-004**.

[52] G. Krafft and A. Hofler, *How the Linac Beam Position Monitors Work,* CEBAF-TN-93-004 (1993).

[53] M. Steinacher and I. Sick, Nucl. Instr. Meth. **A455**, 759 (2000).

[54] C. Armstrong, Beam Current Measurement in Hall C, JLab Internal Report(unpublished).

[55] K. B. Unser, The Parametric Current Transformer, a Beam Curent Monitor Developed for LEP, CERN SL/**91-42**(unpublished).

[56] Private communication with D. Mack, (1999).

[57] D.C. Crabb, D.B. Day, The Virginia/Basel/SLAC Polarized Target: Operation and Performance during Experiment E143 at SLAC, NIM **A356**, 9-19 (1995).

[58] J. R. Arrington, Ph.D. thesis, Caltech, 1998.

[59] M. Berz, "COSY Infinity Version 7 Reference Manual", NSCL Tech Report, MSUCL-977, MSU, 1995.

[60] Experimental and Physics Industrial Control System(EPICS), Los Alamos National Laboratory, 1984.

[61] Private communication with O. Rondon, (2000).

[62] E.L. Garwin *et al.*, Nucl. Instr. Meth. **107**, 365 (1973).

[63] Private communication with T. Eden, (1998).

[64] Madey, *et al.*, NIM **214**, 401-413 (1983).

[65] O.A. Rondon, *Absorption of Neutrons in the Neutron Detector Pb Shielf in Expt. 93-026 - G_{En}*, unpublished technical note, (2000).

[66] A. Abragam, *Principles of Nuclear Magnetism.* Oxford: Clarenden, 1961.

[67] M. Goldman, J. Magn. Reson. **17**, 393 (1975).

[68] M. Borghini, J. Phys. Lett. **26A**, 242 (1968).

[69] G.R. Court, *et al.*, Nucl. Instr. Meth. **324A**, 433-440 (1993).

[70] I. Sick, Tech Note, "E93-026 Field Direction Measurements", September 7, 1999.

[71] Data Sheets from Trident Plastics, manufactured by Daikin America.

[72] S. Bultmann *et al.*, Nucl. Instrum. Meth. **A425**, 23 (1999).

[73] D.C. Crabb and W. Meyer, Annu. Rev. Nucl. Part. Sci. **47**, 67-109 (1997).

[74] O.A. Rondon, Phys. Rev. **C60**, 35201, (1999).

[75] Private communication with D. Zimmermann, (1996).

[76] CIL gas bottle data sheets.

[77] O.A. Rondon, E143 Tech note.

[78] The E143 Collaboration, Phys. Rev. **D58**, 112003 (1998).

[79] C.R. Gregory and C.W. Nuttall, Explosion Risks in Cryogenic Liquids Exposed to Inionizing Radiation, CERN Report CERNAT/95-06 (DI), 1995.

[80] D.C. Crabb and O. Rondon, Proposal to Irradiate Target Material at JLab FEL Facility(unpublished), (1998).

[81] A. Rijllart, Microprocessorized NMR Measurement, Proc. 4th Int. Workshop on Polarized Target Materials and Techniques, Bad Honnef, p. 155 (1984).

[82] P.M. McKee, Proceedings from the Workshop on Polarized Solid Targets, (1998).

[83] C.M. Harris, Proceedings from the International Workshop on Polarized Sources and Targets, (1999).

[84] Private communication with D. Crabb, (2000).

[85] H. Zhu, Ph.D. thesis, University of Virginia, 2000.

[86] D. Dutta, Ph.D. thesis, Northwestern University, 1999.

[87] M. Muehlbauer, "E93-026 Target Field Optics Studies", E93026 internal report, 1998. Data from this report can currently be found at jazz.physik.unibas.ch/ markus/gen/prog.html.

[88] P. Ulmer, Monte Carlo for Electro-Nuclear Coincidence Experiment(MCEEP), version 3.0, September 12, 1999.

[89] M. Zeier and T. Petitjean, Electronics Deadtime (G_{EN}), JLab Internal Report(unpublished).

[90] M. Zeier, Electronics Deadtime and Asymmetry, E93-026 Technical Note, (2000).

[91] J.W. Lightbody and J.S. O'Connell, Computers in Physics, May/June 1997, 57-64.

[92] R.R. Whitney *et al.*, Phys. Rev. **C9**, 2230 (1974).

[93] F. Krautschneider, Ph.D. thesis, Bonn University, BONN-IR-76-37 (1976).

[94] F.W. Brasse *et al.*, Phys Rev. Lett. **17**, 1192 (1966).

[95] T.C. Petitjean, Ph.D. thesis, Basel University, 2000.

[96] L. W. Mo and Y. S. Tsai, Rev. Mod. Phys. **41**, 205 (1969).

[97] Y. S. Tsai, SLAC-PUB-**848**, SLAC Report(unpublished).

[98] S. Sobottka, Phys. Rev. **118**, 831 (1960).

[99] B. Parker *et al.*, Phys. Rev. **C34**, 2354 (1986).

[100] B. Grossetete, S. Jullian, and P. Lehmann, Phys. Rev. **141**, 1435 (1966).

[101] D.B. Day *et al.*, Phys. Rev. **C48**, 1849 (1993).

[102] W.R. Leo, Techniques for Nuclear and Particle Physics Experiments, (1987).

[103] S. Stein, *et al.*, Phys. Rev. **D12**, 1884 (1975).

[104] T.J. Liu, Ph.D. thesis, University of Virginia, 1996.

[105] O. Rondon, E143 internal memo on asymmetry error, unpublished (1994).

[106] A. Abragam and M. Goldman, Rep. Prog. Phys. **41**, 395 (1978).

[107] T.V. Kuchto and N.M. Shumeiko, Nucl. Phys. **B219**, 412-436 (1983).

[108] M. Romalis and Y. Kolomensky, E154 Technical Note 54.

[109] S. Kuhn and F. Wesselmann, E155 Technical Note 59, (1998).

[110] A. Afanasev, I. Akushevich, N. Merenkov, Preliminary Report on Model Independent Radiative Corrections to Polarized Electron-Nucleon Elastic Scattering, (unpublished).

[111] W. Meyer and E. Schilling, Proceedings of the 4th International Workshop on Polarized Target Materials and Techniques, (1984).

[112] F. Sperisen, Nucl. Instr. Meth. **A260**, 455-462 (1987).

[113] Kielhorn, Ph.D. thesis, University of Texas at Austin, 1991.